2018

Customizable Phased Array Antenna Using Reconfigurable Antenna Elements

Mahmoud Shirazi
University of Central Florida

CUSTOMIZABLE ANTENNA ARRAY USING RECOFIGURABLE ANTENNA ELEMENTS

by

MAHMOUD SHIRAZI
M.S Amirkabir University of Technology, 2012

A dissertation submitted in partial fulfillment of the requirements
for the degree of Doctor of Philosophy
in the Department of Electrical and Computer Engineering
in the College of Engineering and Computer Science
at the University of Central Florida
Orlando, Florida

Fall Term
2018

Major Professor: Xun Gong

ABSTRACT

A shared-aperture reconfigurable dual-polarized slot-ring antenna array switching between different frequency bands is presented for phased array applications. PIN diode switches are incorporated into the slots of the antenna to change the state of the reconfigurable slot-ring antenna array. Each frequency band has its own feeding lines which allows for the use of high-performance narrow-band transmit/receive (T/R) modules instead of Low-performance ultra wideband (UWB) T/R modules. Furthermore, the spacing between the elements in each frequency band is less than half free-space wavelength (λ_0) over the frequency band of operation which enables grating-lobe-free beam scanning. This is the first shared-aperture reconfigurable dual-polarized antenna array with separate feeding which is scalable to a larger array with element spacing of less than $0.5\lambda_0$ in all frequency bands.

First, a switchable-band reconfigurable antenna array switching between *L* and *C* bands is presented. This antenna operates at 1.76/5.71 GHz with a fractional bandwidth (FBW) of 8.6%/11.5%, realized gain of 0.1/4.2 dBi and radiation efficiency of 66.6%/80.7% in the *L*-/*C*-band operating states, respectively. Second, a reconfigurable dual-polarized slot-ring antenna element switching between *S* and *C* bands with wide bandwidth in each operating state is presented. Fractal shapes are incorporated into the slot-ring antenna structure to significantly enhance bandwidth. In the *S*-/*C*-band operating state, this antenna shows 69.1%/58.3% FBW with a measured maximum realized gain of 2.4/3.1 dBi. Third, a reconfigurable dual-polarized antenna array which is able to switch between *S*- and *C*-band operating states with full-band coverage is

developed. A 2×2 *S*-band antenna array can be reconfigured to a 4×4 *C*-band antenna array by activating/deactivating PIN diode switches. This antenna array shows 64.3%/66.7% FBW with 8.4/14.3 dBi maximum realized gain in the *S*-/*C*-band operating states, respectively.

To my mother, father, brother and sister

ACKNOWLEDGMENTS

This work was supported in part by the Defense Advanced Research Projects Agency (DARPA) Arrays at Commercial Timescale (ACT) Program under Grant HR0011-14-1-0003.

TABLE OF CONTENTS

LIST OF FIGURES

LIST OF TABLES

CHAPTER 1: INTRODUCTION

Phased array antennas are widely used for military applications such as advanced radar and electronic warfare (EW) or civilian applications such as cellular networks. For example, there has been an increasing interest in designing phased array antennas for future 5G networks and 5G Internet of Things (IoT) applications. Unfortunately, due to the vastly different personalities required for these applications, an antenna array designed and developed for one project cannot be easily adapted to another one. As a result, multifunctional antenna arrays have attracted much attention in the last decade because they can be easily adapted to different applications. These antenna arrays are flexible in changing multiple antenna properties such as frequency, bandwidth, polarization, and radiation pattern. Designing a multi-functional phased array antenna is even more challenging because a tradeoff should be considered between the number of transmit/receive (T/R) modules and the spacing between antenna elements to avoid grating lobes while scanning the main beam. In this dissertation, reconfigurable antenna arrays with proper element spacing for narrow band and wideband applications are demonstrated.

The EM interface of a multi-functional communication system that operates in multiple frequency bands can be realized by multi-band antenna arrays, switchable-band antenna arrays, ultra-wideband antenna arrays, or switchable wideband antenna arrays. A brief summary of each category is provided in the following sections.

1.1 Multiband Antenna Arrays

Multiband antenna arrays have been used in various applications such as WLAN [1, 2], WiMAX [3], 2G/3G/LTE base stations [4], satellite communications [5, 6, 7, 8], phased array [9], and radar [10]. There has been a strong interest in developing multiband antenna arrays since they are compact, lightweight and low cost compared with multiple single-frequency-band antenna arrays.

Radiators of the multi-frequency-band antenna arrays that share the same aperture can be on different layers [11, 12] or the same layer [5, 8, 9, 13, 14]; although antenna arrays with multi-layer radiators usually provide better isolation between different frequency bands, they are not suitable for beam scanning due to blockage from radiators on the top layer.

Multi-band antenna arrays with radiators on the same layer can be divided into two categories: (1) common feeding for multiple frequency bands [2, 3, 9, 10, 13]; (2) separate feeding for each band [1, 4, 5, 7, 8, 14].

1.1.1 Common Feeding for Multiple Frequency Bands

In this category, the element spacing at the higher band is unavoidably large if the spacing at the lower band is maintained at $\lambda_0/2$. For example, in [3], a dual-band folded dipole antenna array is operating at 2.4/3.6 GHz in the lower/higher-band state with the element spacing of 0.65/0.93 λ_0, where λ_0 is the free space wavelength. The physical dimensions of the antenna

element are the same for both operating states; therefore, the element spacing at higher band is unavoidably large even though the lower band element spacing is relatively small. In [13], a patch antenna array that operates at 2.5/3.6 GHz in the lower/higher band states shows element spacing of 0.57/0.81 λ_0. A pixelated patch antenna array with a common feed for two bands, i.e. 4.7/7.5 GHz, using PIN diode switches was presented in [15]. This array exhibited an element spacing of 0.47/0.75λ_0 and FBW of 1.7%/4.0%.

If the element spacing is close to $\lambda_0/2$ at the higher band, then the spacing at the lower band is much smaller than $\lambda_0/2$ which results in stronger mutual coupling and an unnecessarily large number of electronics for the lower band. In [10], a dual-band slot-loaded patch antenna array operating at 1.3/3.1 GHz with element spacing of 0.23/0.55 λ_0 is demonstrated for radar applications. Another example in this category is a cavity-backed L-bar antenna array operating at 9.8/17 GHz with element spacing of 0.33/0.58 λ_0 [9]. These examples show that pushing the element spacing at higher band to be close to half wavelength results in the very-small element spacing at the lower band.

1.1.2 Separate Feeding for Each Frequency Band

In the second category, similar element spacing in terms of wavelength can be maintained in both frequency bands of a multi-band antenna array. In [6], a dual-band dual-polarized cavity-backed patch array was presented for satellite communication applications. This array operates at two frequencies, 12.2/17.6 GHz, with fractional bandwidth (FBW) of 5.2%/2.0% and element

spacing of 0.60/0.57 λ_0. The low frequency ratio of the folded dipole array in [14] enables maximum use of the radiating aperture to optimize the element spacing. The measured FBW of this antenna array is 5%/>22% at 1.0/2.0 GHz. As shown in Figure 1.1 (a), the spacing between the antenna elements is maintained at 0.50 λ_0 in both frequency bands. The placement of 2 GHz dipole elements inside the folded arms of the 1 GHz dipole elements reduces the dimensions of the array. A vertical coaxial transition for each antenna element as illustrated in Figure 1.1 (b) is needed in this array. This 3×3 *L*-band and 5×6 *S*-band array exhibits 12 and 17 dBi gain, respectively.

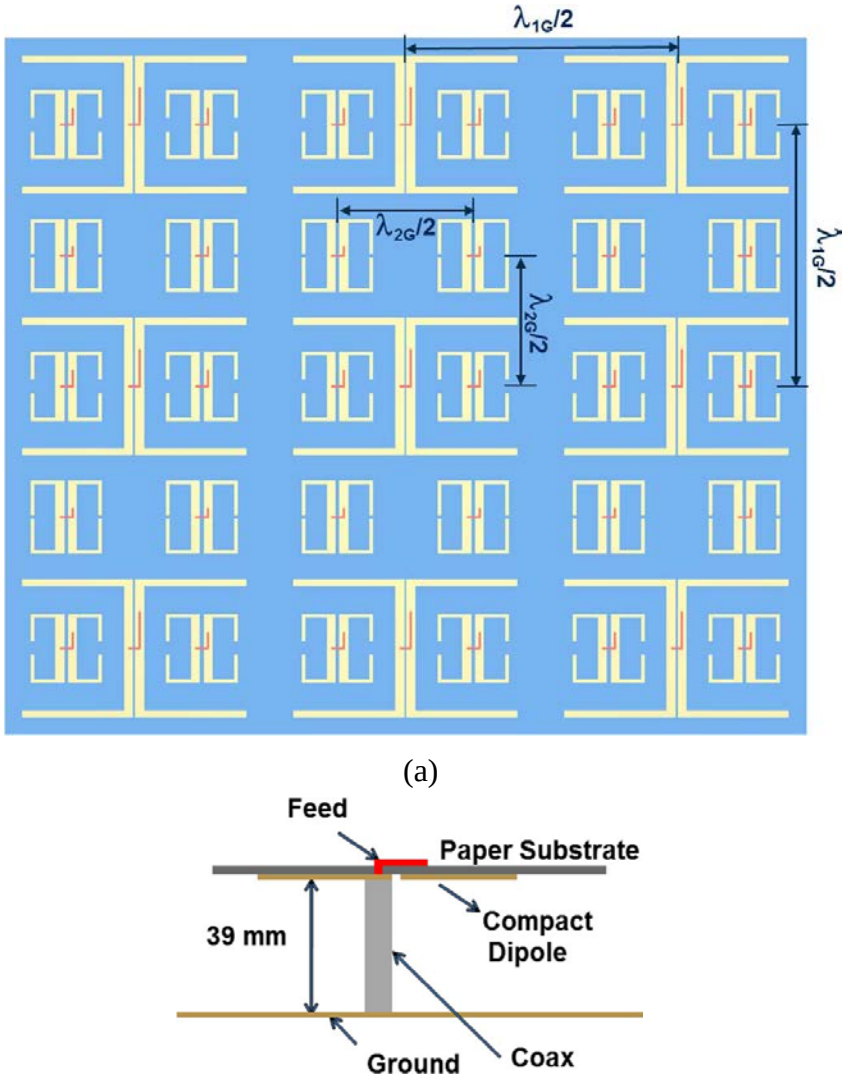

Figure 1.1 Shared-aperture dual-band folded dipole array. (a) 3×3 *L*-band array consists of 6×5 *S*-band array, (b) Coaxial vertical feeding for a single antenna element (reprinted from [14]).

1.2 Switchable-band Antenna Arrays

Multi-band antenna arrays can also be realized by reconfiguring the radiating aperture. The multiband antenna arrays in the previous section have no tuning elements. Most of the aforementioned multi-band antenna arrays with no tunability show narrow FBW in at least one band of operation. Furthermore, for the multi-band antenna arrays with low frequency ratio and large FBWs in both bands, it is challenging to realize good isolation between the two bands due to the limited space within the common radiating aperture.

The unused space in the radiating aperture of an antenna array can be effectively used by introducing switching elements inside or between the antenna elements [16, 17, 18, 19]. It is noted that switchable-band antenna arrays do not operate at multiple frequency bands simultaneously while multi-band antenna arrays in [1-14] do.

In [16], a planar pin-fed square-ring antenna was demonstrated for beamscanning applications. The antenna array in [16] operates in two frequency bands by turning PIN diode switches ON (*L* band state) or OFF (*S* band state). Due to the probe feeding, the impedance matching FBW is only 3.5%/5.5% in the *L*/*S* band. In addition, since both the *S*- and *L*-band radiators use the same physical area, the element spacing is larger at *S* band and therefore reduces the maximum scanning angle. A switchable tri-band bow-tie antenna array using PIN diodes was demonstrated in [17]. Each arm of the bow tie is divided into three sections with PIN diode switches between them. By turning on the switches in certain configurations, this bow tie antenna

can operate at 2.44/3.47/5.45 GHz with element spacing of 0.49/0.69/1.09 λ_0 in each respective frequency band. In this antenna, the large element spacing causes strong side lobes, especially at 5.45 GHz.

In [18], the radiating aperture of a patch antenna array is reconfigured by using PIN diode switches to maintain the element spacing in each band close to $\lambda_0/2$. As shown in Figure 1.2, an *L*-band element can be reconfigured to an *S*-band element by turning PIN diode switches OFF. Every other antenna element in the *S*-band array is designed to operate as a switchable *L*- and *S*-band antenna. Therefore, d_S and d_L in Figure 1.2 are $\lambda_{0S}/2$ and $\lambda_{0L}/2$, respectively. As a result, the element spacing is maintained at a half wavelength in both bands. It should be noted that 25% of the antenna elements have a common feed for both bands, which requires either one wideband T/R module or two narrowband T/R modules with an RF switch. The FBW of the patch antennas in [18] in the lower/higher band is merely 4.5%/2.4%.

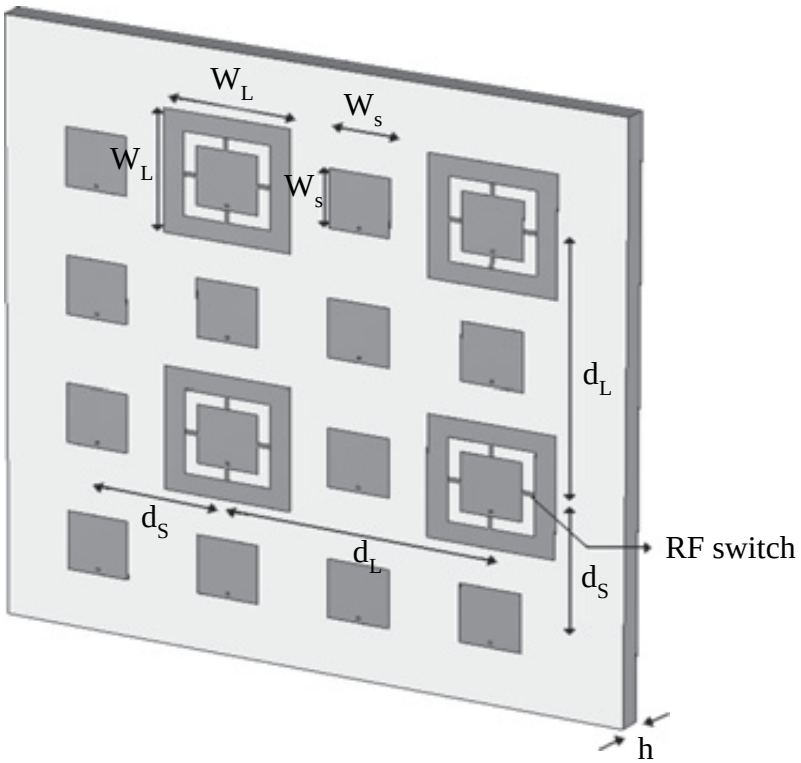

Figure 1.2 Geometry of the switchable-band patch antenna array in [18] with probe feeding for both *L* and *S* bands.

As mentioned in the previous section, multi-band antenna arrays with separate feeding for each band has an advantage over the ones with the same feeding because it does not need wideband electronics behind the antenna to cover all operating frequencies of the antenna array. The switchable-band antenna arrays in [16, 17, 18] share common feeding for some of the antenna elements. Therefore, either wideband T/R modules or narrowband T/R modules with an RF switch in required for each common feed. In [19], a reconfigurable slot-ring antenna array was presented with separate feeds for each frequency band. As shown in Figure 1.3, PIN diode switches are

placed strategically inside the slot of the large slot ring and also inside the slot of the four small slot rings to enable this antenna element to switch between 1.76 and 5.71 GHz with 8.6% and 11.5% FBW, respectively. It should be noted that each frequency band has its own feed and therefore only narrow-band T/R modules are needed. By extending this design to a larger array, the element spacing at both frequency bands can be designed to be less than $\lambda_0/2$, allowing for wide-angle beam scanning without grating lobes. Details of this antenna array with design procedure and simulation and measurement results are presented in Chapter 3 of this dissertation.

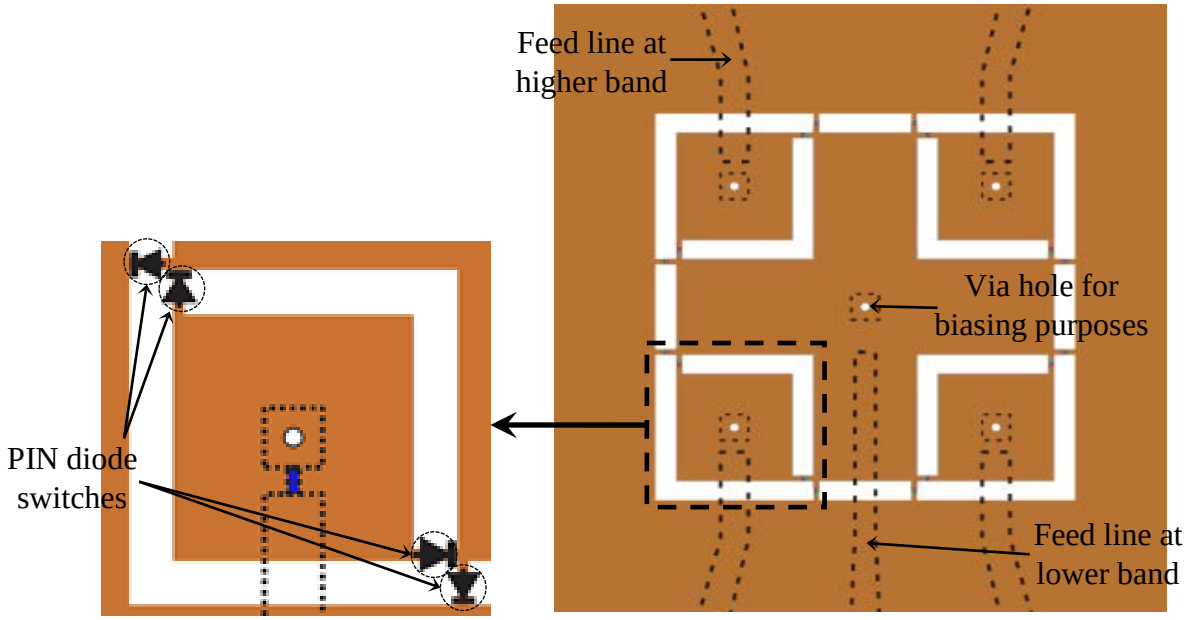

Figure 1.3 Switchable-band slot-ring antenna array with separate feed for *L*- and *S*-bands (reprinted from [19]).

1.3 Ultra Wideband Antenna Arrays

Phased array antennas with wide bandwidth and dual polarization are highly desirable in military applications, advanced radar and wireless communications because they can be easily adopted for different applications. Designing such an array is challenging because a tradeoff should be considered between the numbers of transmit/receive (T/R) modules and the spacing between antenna elements to avoid grating lobes while scanning the main beam. If the element spacing is maintained at $\lambda_0/2$ at the highest frequency of operation, then a large number of T/R modules are required. By increasing the element spacing, fewer T/R modules are needed but grating lobes will occur for large scan angles.

Ultra Wideband (UWB) phased array antennas that are realized by current sheet antennas (CSAs) [20] or Vivaldi antennas show more than 4:1 bandwidth. A single-polarized tightly-coupled dipole antenna (TCDA) with 136% FBW was demonstrated in [20]. For this antenna, the element spacing at 3.5/18.5 GHz is 0.09/0.46 λ_0. Another single-polarized TCDA with 144% FBW for VSWR < 3.2 at boresight was demonstrated in [21]. The element spacing for the antenna in [21] at 0.5/3.1 GHz is 0.08/0.5 λ_0 with 70^o main beam scanning range and more than 80% efficiency. However, for this antenna array, beam scanning is limited to 50^o at the lower end of frequency band due to the electrically small size of the antenna. In [22], a dual-polarized planar UWB CSA with 0.09/0.46 λ_0 element spacing at 1.1/5.3 GHz was shown with cross-polarization (X-pol.) levels as high as -7 dB in the principal planes. A dual-polarized TCDA array with 7.2:1 bandwidth for beam scanning applications was presented in [23]. As shown in Figure 1.4, each

element of the array consists of a pair of orthogonally placed dipole radiators with integrated folded Marchand baluns for matching purposes. Another version of this TCDA with higher port-to-port isolation was presented in [24]. The CSA arrays in [23] and [24] show 151% (VSWR < 2.8 at boresight) and 160% (VSWR < 3 at boresight) FBWs, less than $\lambda_0/2$ element spacing at the highest frequency of operation, 60^o beam scanning and 20 and 45 dB port-to-port isolations at boresight, respectively. These results were verified by simulations. High isolation in [7] is due to the use of one of the array polarizations for transmission and the other one for reception. Two versions of TCDAs at UHF and Ku frequency bands for space-borne applications were presented in [25]. The antenna array for the UHF/Ku band show 143% FBW with 0.07 λ_0 and 0.41 λ_0 element spacing at 0.6 GHz and 3.6 GHz, respectively.

A dual-polarized Vivaldi antenna array for remote sensing applications was demonstrated in [26] with 160% FBW and element spacing of 0.055/0.5 λ_0 at 2.0/18.0 GHz. This antenna array shows 30^o scanning range with no grating lobes. Despite their large FBWs, Vivaldi arrays are high profile and bulky. The long elements of the Vivaldi array lead to high X-pol. levels when it scans in the diagonal plane. Flared notch Vivaldi antenna arrays with 155% FBW and 45^o beam scanning were presented in [27] and [28]; the element count in [28] is reduced by a factor of 6.4 compared to [27]. It should be noted that the spacing between the Vivaldi elements in [27] and [28] is 0.067/0.54 λ_0 and 0.06/0.48 λ_0 at 1.0/8.0 GHz, receptively. In [29] and [30], bunny ear antenna arrays with 105% FBW, 0.17/0.56 λ_0 element spacing at 0.3/1.0 GHz and a beam scanning range of 45^o were shown. Although flared notch and bunny ear antenna arrays have shorter elements and wider-scan performance in the principal planes compared to Vivaldi arrays, they show high X-pol.

levels and poor VSWR when scanned in the diagonal plane. Other low-profile configurations with Banyan Tree Antenna (BTA) [31] or Balanced Antipodal Vivaldi Antenna (BAVA) [32, 33, 34] were demonstrated. In [31], the BTA array with a dimension of 0.56 λ_H was demonstrated as shown in Figure 1.5, where λ_H is the wavelength at the highest frequency of operation. At 2.0/7.5 GHz the antenna element spacing is 0.13/0.5 λ_0 and exhibits 45^o beam scanning even at the highest frequency of operation. It is noted that the BTA array in [31] shows degraded VSWR and X-pol. performance at large scan angles. The BAVA array in [32] with a height of 0.83 λ_H shows 120% FBW with element spacing of 0.17/0.67 λ_0 at 0.5/2.0 GHz, which is able to scan its main beam to 50^o in the principal planes. Two low-profile BAVA arrays with heights of 0.5 λ_H and more than 160% FBW are demonstrated in [33] and [34] with 45^o beam scanning in the principal planes. Furthermore, the BAVA arrays show poor VSWR when they scan in the H plane.

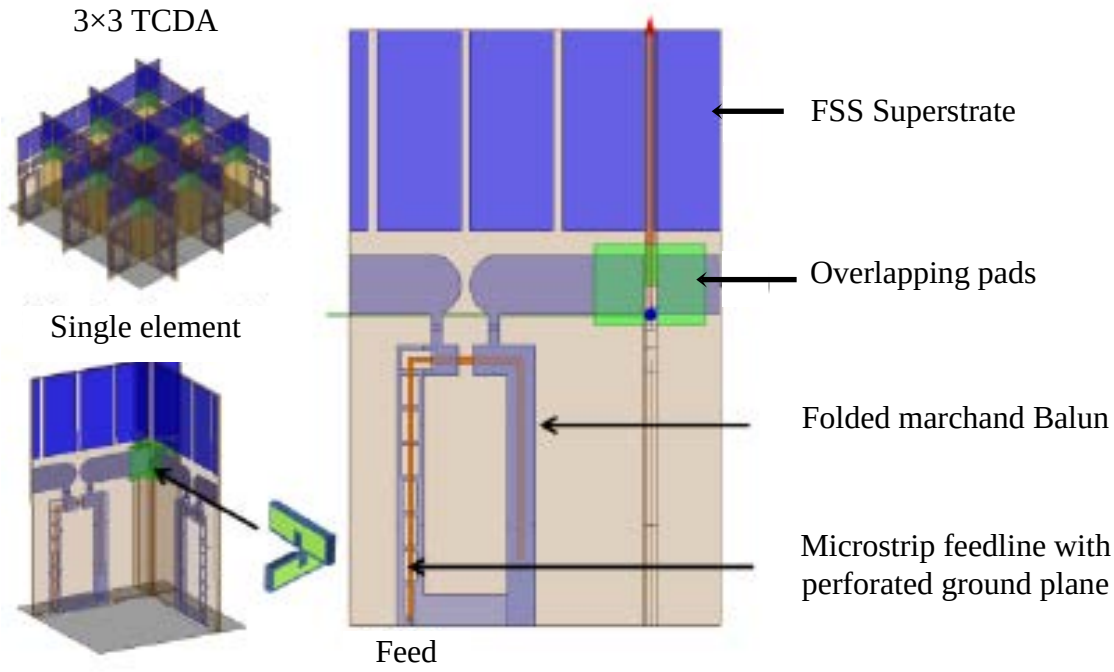

Figure 1.4 UWB dual-polarized TCDA antenna with microstrip feeding and marchand balun.

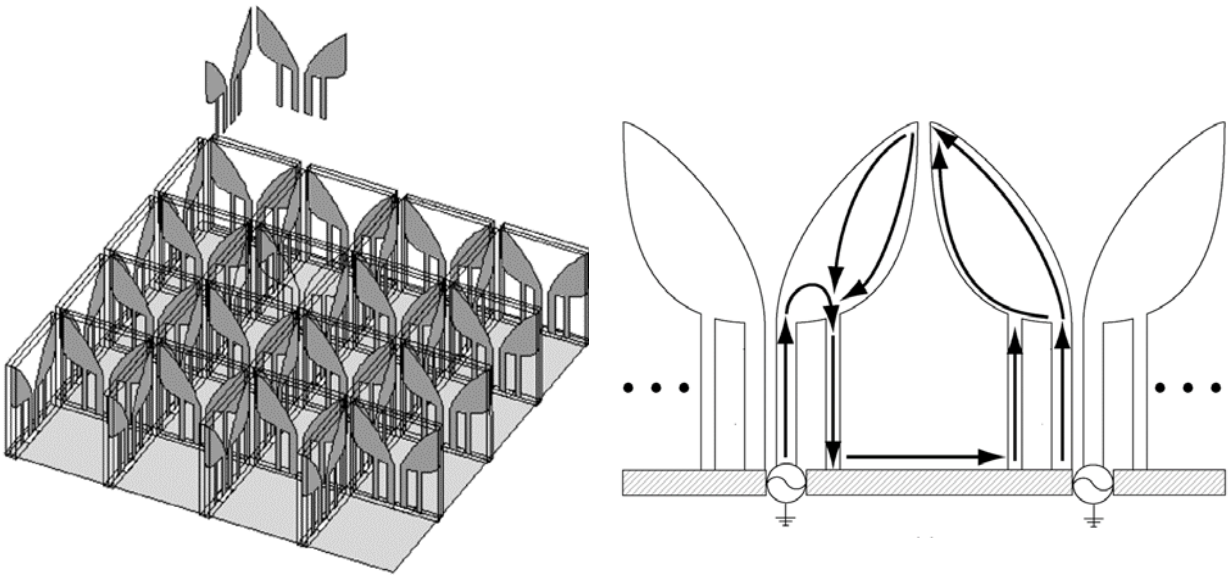

(a) (b)

Figure 1.5 (a) Dual-polarized BTA array. (b) Current distribution in two adjacent elements (reprinted from [31]).

Basically, for a wideband or UWB phased array antenna with frequency coverage from f_1 to f_2, if the element spacing at f_1 is maintained at $\lambda_{0f_1}/2$, then the spacing at f_2 is much larger than $\lambda_{0f_2}/2$, causing grating lobes at large scan angles. If the element spacing at f_2 is close to $\lambda_{0f_2}/2$, then the element spacing at f_1 is much smaller than $\lambda_{0f_1}/2$, resulting in an unnecessary-large number of T/R modules. Furthermore, UWB phased array antennas are very expensive to develop due to the potentially large number of low-performance UWB T/R modules. In order to form a shared-aperture phased array antenna operating at different frequency bands, it is highly desirable to have separate feeding for each band. A separate feeding mechanism allows for the use of high-

performance, narrow-band T/R modules instead of UWB T/R modules. By introducing a switchable band antenna array covering the full band in each operating state, the UWB frequency range is divided into two or more sections; therefore, T/R modules that cover the bandwidth of each operating state of the switchable-band antenna can be used.

In Chapter 4 of this dissertation, a reconfigurable antenna element with wide bandwidth in each operating state is presented. In this antenna element, fractal shapes are introduced to significantly extend the FBW as shown in Figure 1.6. Moreover, this antenna is switchable in terms of frequency band (between *S* and *C* band with full band coverage), polarization, and scan angle. To extend this concept to a large array, Chapter 5 introduces a reconfigurable antenna array covering two adjacent frequency bands. The schematic view of such an array is demonstrated in Figure 1.7. A 4×4 *S*-band array/8×8 C-band array is fabricated and tested. Details of the design procedure with the simulation and measurement results are presented Chapter 5.

In Chapter 6, a tri-band reconfigurable antenna array with wide bandwidth in three different frequency bands is demonstrated. An *S*-band antenna element which can be reconfigured to a 2×2 *C*-band antenna array or 4×4 *X*-band array is shown in Figure 1.8. Details of the simulation results for the antenna with microstrip feeding and vertical coaxial feeding are provided in Chapter 6.

Table 1-1 compares the different antenna arrays developed in this dissertation. The antenna array demonstrated in Chapter 3 operates in two frequency bands with narrow bandwidth in each operating state. The reconfigurable wideband antenna element in Chapter 4 operates in two

adjacent frequency bands with full-band coverage in each operating state. The antenna array presented in Chapter 5 is the full array demonstration of the antenna element in Chapter 4. Finally, a reconfigurable wideband antenna/array operating in three frequency bands is demonstrated in Chapter 6.

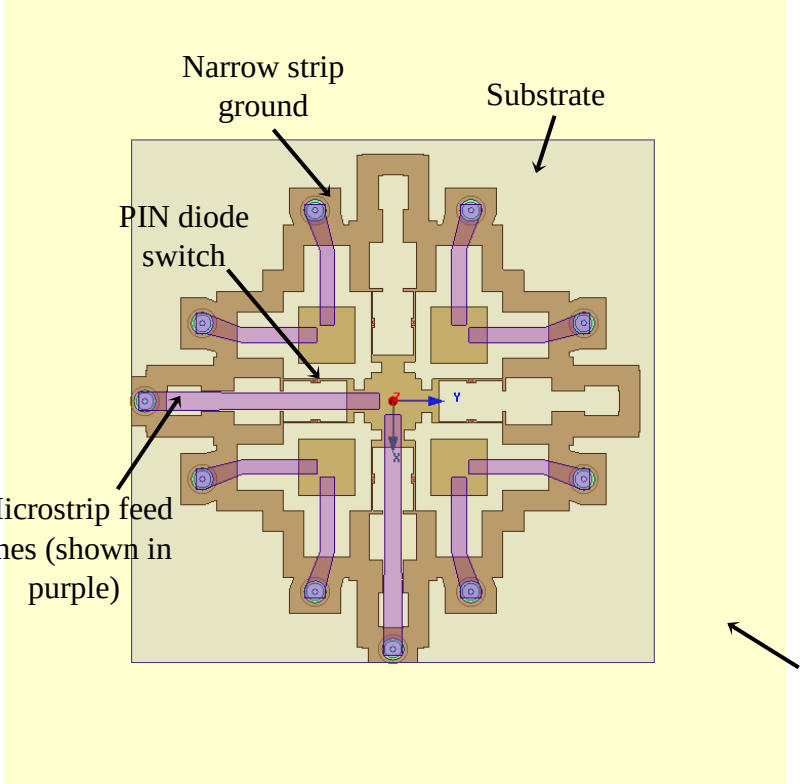

Figure 1.6. Wideband dual-polarized switchable-band antenna covering *S*- and *C*-bands. (a) *S*-band antenna element consists of four *C*-band elements and 8 PIN diode switches that are used to switch between the *S*- and *C*-bands.

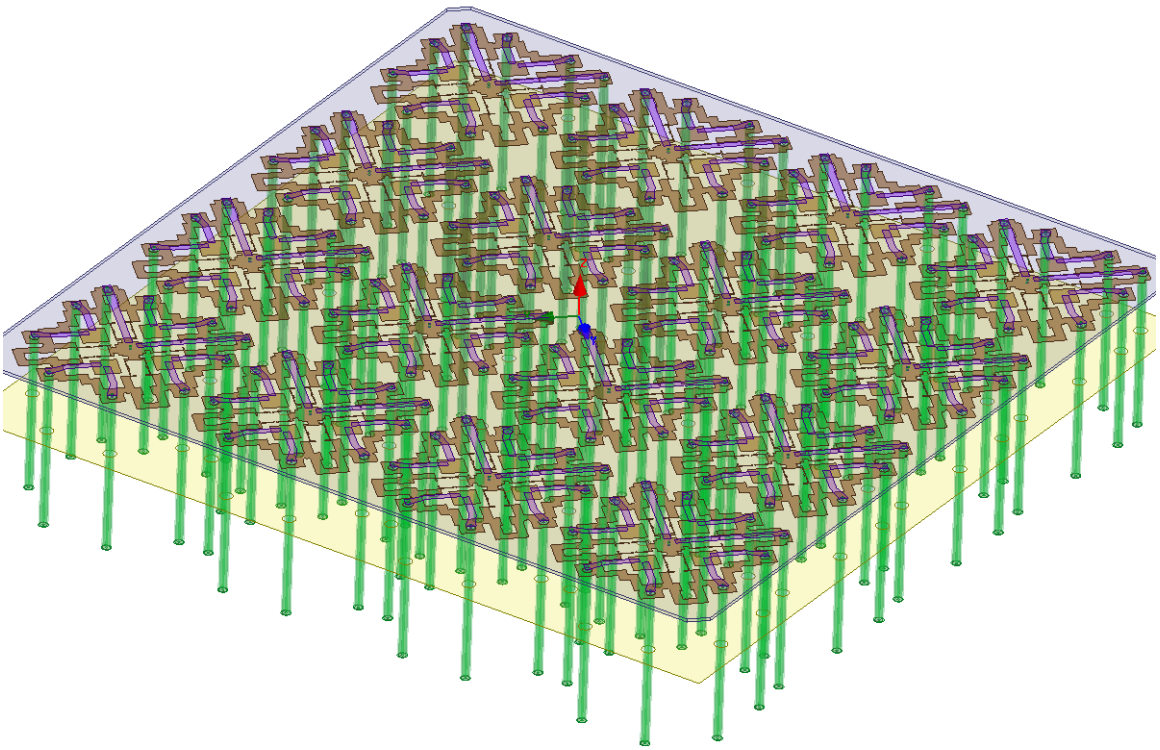

Figure 1.7. 4×4 *S*-band array/8×8 non-uniform *C*-band array (the element spacing between *S*-band antenna elements at 3.8 GHz is $0.62\lambda_0$).

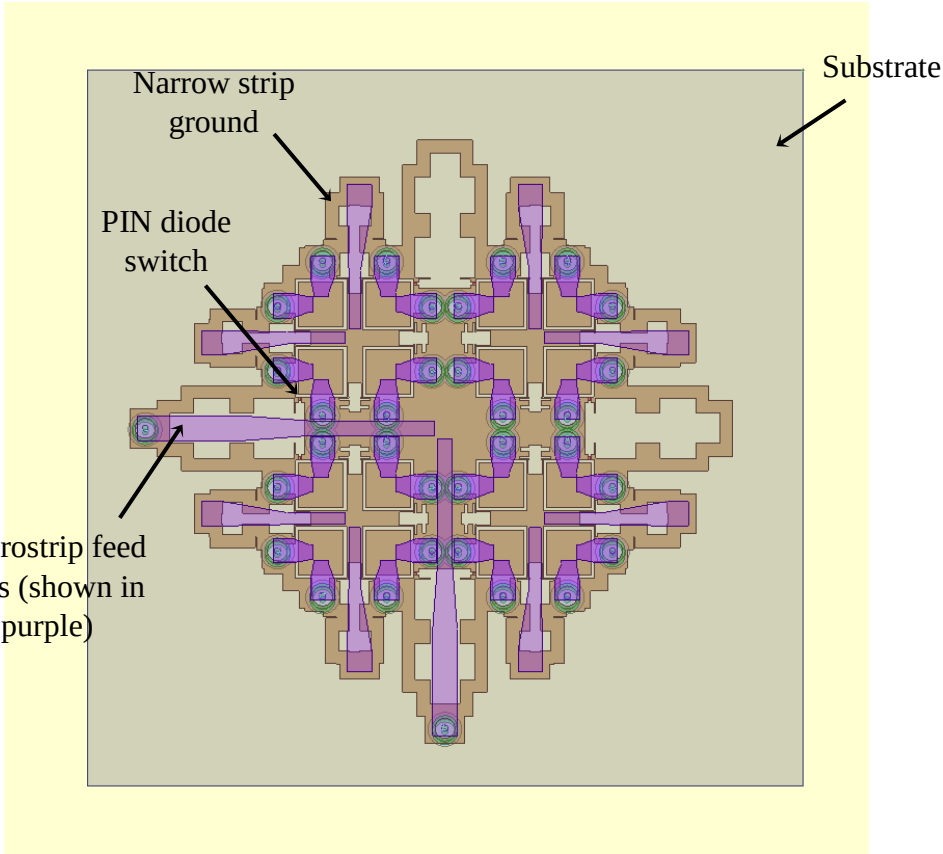

Figure 1.8. Dual-polarized tri-band antenna element covering *S*, *C*, and *X* bands (*S*-band antenna element consists of four *C*-band elements and 16 *X*-band elements).

Table 1-1. Comparison between the reconfigurable dual-polarized wideband slot-ring antenna/array in this paper and UWB or multi-band/switchable-band antenna arrays.

	Covered freq. bands	**FBW**	**Pol.**	**Scan volume in principal planes**	**Radiation efficiency**	**X-pol. in principal planes (dB)**	**T/R module**	**Comment**
Antenna array in Chapter 3	-	8.6%/11.5% in the *L*-/*C*-band state	Single LP	60º/60º in the *L*-/*C*-band state	67%/81% in the *L*-/*C*-band state	-15/-25 in the *S*-/*C*-band state	Narrow band	Limited bandwidth in each operating state

	Covered freq. bands	**FBW**	**Pol.**	**Scan volume in principal planes**	**Radiation efficiency**	**X-pol. in principal planes (dB)**	**T/R module**	**Comment**
Antenna array in Chapter 4	*S* and *C*	67%/64% in the *S*-/*C*-band state	Dual LP	Single element	67%/88% in the *S*-/*C*-band state	-12/-15 in the *S*-/*C*-band state	With only octave bandwidth	Vertical transition is needed for e0xpansion to larger array for beamscanning
Antenna array in Chapter 5	*S* and *C*	64%/67% in the *S*-/*C*-band state	Dual LP	60º/35º in the *S*-/*C*-band state	72%/85% in the *S*-/*C*-band state -	-15/-25 in the *S*-/*C*-band state	With only octave bandwidth	-
Antenna array in Chapter 6	*S* and *C* and *X*	64%/67%/40% in the *S*-/*C*-/*X*-band state	Dual LP	Single element	%/%/% in the *S*-/*C*-/*X*-band state	-/-/- in the *S*-/*C*-/*X*-band state	With only octave bandwidth	-

CHAPTER 2: CHARACTERIZING SWITCHING ELEMENTS

The most popular approaches for designing reconfigurable antennas are using electromechanical or electrical switches such as RF microelectromechanical systems (MEMS) [35], p-i-n (PIN) diodes [36], varactors [37], and field-effect transistors (FET) [38]. MEMS switches have the advantage of low loss and high Q compared to the PIN diodes and varactor diodes. Meanwhile, the RF PIN diodes are low cost and have a relatively high power-handling capability. On one hand, reconfigurable antennas using PIN diode switches are simpler to fabricate with low cost. On the other hand, PIN diodes need to be connected with forward bias DC current when in the ON state which will slightly degrade the power efficiency of the antenna.

For all versions of the reconfigurable antenna arrays in this dissertation, active elements such as varactors, PIN diode switches or MEMS switches are used to reconfigure the antenna array. These active elements are strategically placed inside the slots of the antenna elements to enable band selection. The tuning/switching mechanism for each antenna prototype is provided in the respective chapter. Overall. the switching mechanism for the antenna arrays developed in this project is far simpler than alternative techniques with similar level of reconfigurability.

Most antennas are passive elements, therefore they can realize high efficiency and linearity. When active elements are incorporated into the antenna structure, the efficiency and linearity of the antenna is degraded. New technologies have been continuously developed to maintain low-loss with high-linearity tuning/switching elements. For example, a GaAs varactor with a 9:1 tuning

range and output IP3 of 57 dBm was reported in [39]. Moreover, MEMS varactors and switches are known for very high linearity and low loss [40] but they are expensive with the current technology. The power handling capabilities and linearity of reconfigurable antenna arrays are limited by the varactors and switches. Therefore, characterization of these elements is important before designing a reconfigurable antenna array. In this chapter, a varactor diode and a PIN diode switch are characterized by measurements. It should be noted that the reconfigurable antenna arrays in this dissertation are flexible in terms of upgrading the tuning/switching elements without re-designing the entire antenna structure. In this case, if the state-of-the-art switches/varactors are improved upon, the power handling and linearity of the reconfigurable antenna array are automatically enhanced without a major redesign of the antenna array.

2.1 Varactor Diodes

Varactors or voltage-controlled capacitors are commonly used in VCOs, parametric amplifiers, frequency multipliers and so on. There are several types of commercially available varactors in different packages and for different purposes such as “varactor tuning diodes” or “varactor multiplier diodes”. In this section a GaAs varactor diode from Macom Company “MAVR-000120-1411” is characterized using probe measurements.

To characterize this varactor, a test fixture is designed and fabricated and the measurements are performed using a probe station with TRL calibration. A CPW line is used for the test fixture on a Rogers 5880 substrate with a thickness of 1.575 mm. Post processing will be done on the

measured Y-Parameters to calculate the capacitance of the varactor. Short-Open de-embedding method will also be used to de-embed the parasitic capacitances of the test fixture. Moreover, the nonlinearity performance and power handling capabilities of the varactor are studied. The P_{1dB} and IP_3 of the varactor will be measured and reported to know the power region in which this varactor operates linearly.

In this section, we will see:

- A figure which shows the capacitance of the varactor vs. reverse bias voltage
- The capacitance of the varactor over a wide range of frequencies from 2 to 12 GHz
- The nonlinearity performance of the varactor which can be determined by measuring the P_{1dB} or IP_3 of the varactor

2.1.1 Probe Measurement Method

The best way to characterize a passive device is to use a two-port configuration, since this analyses the behavior of the device in the most general way possible [41]. In addition, in the particular case of characterizing an integrated varactor, the two-port test obtains parameters related to the model of varactor that cannot be obtained with one-port measurements. With the configuration of the varactor in series between the two ports, exact characterization of a two-port device can be done [42].

The function of the test fixture is to make physical contact between the test probes and the DUT. It is important to know the parasitic effects of the test fixture to minimize its influence. The most commonly used geometrical shape for a test pad is the square as shown in Figure 2.1. The coupling (S_{12}) is an important parameter to be taken into account. The signal between ports 1 and 2, which passes through the DUT, should be at least 20 dB greater than the coupling value between ports at the frequency of interest.

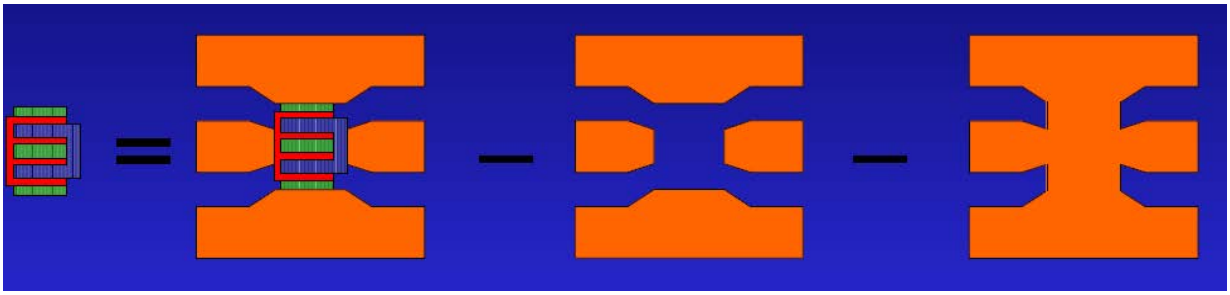

Figure 2.1. Square-shape test pad showing de-embedding from OPEN and SHORT

Using a Through, Reflect Line (TRL) calibration, the reference planes can be moved all the way to the ports of DUT. Dimensions of the test fixtures are selected based on the dimensions of several switches and varactors from different vendors. Measurement results for a varactor diode from MACOM (MAVR-000120-1411) is presented here. Figure 2.2 shows the dimensions of the TRL standards and test fixtures. The preview of a photomask with 24 copies of the test fixture is illustrated in Figure 2.3.

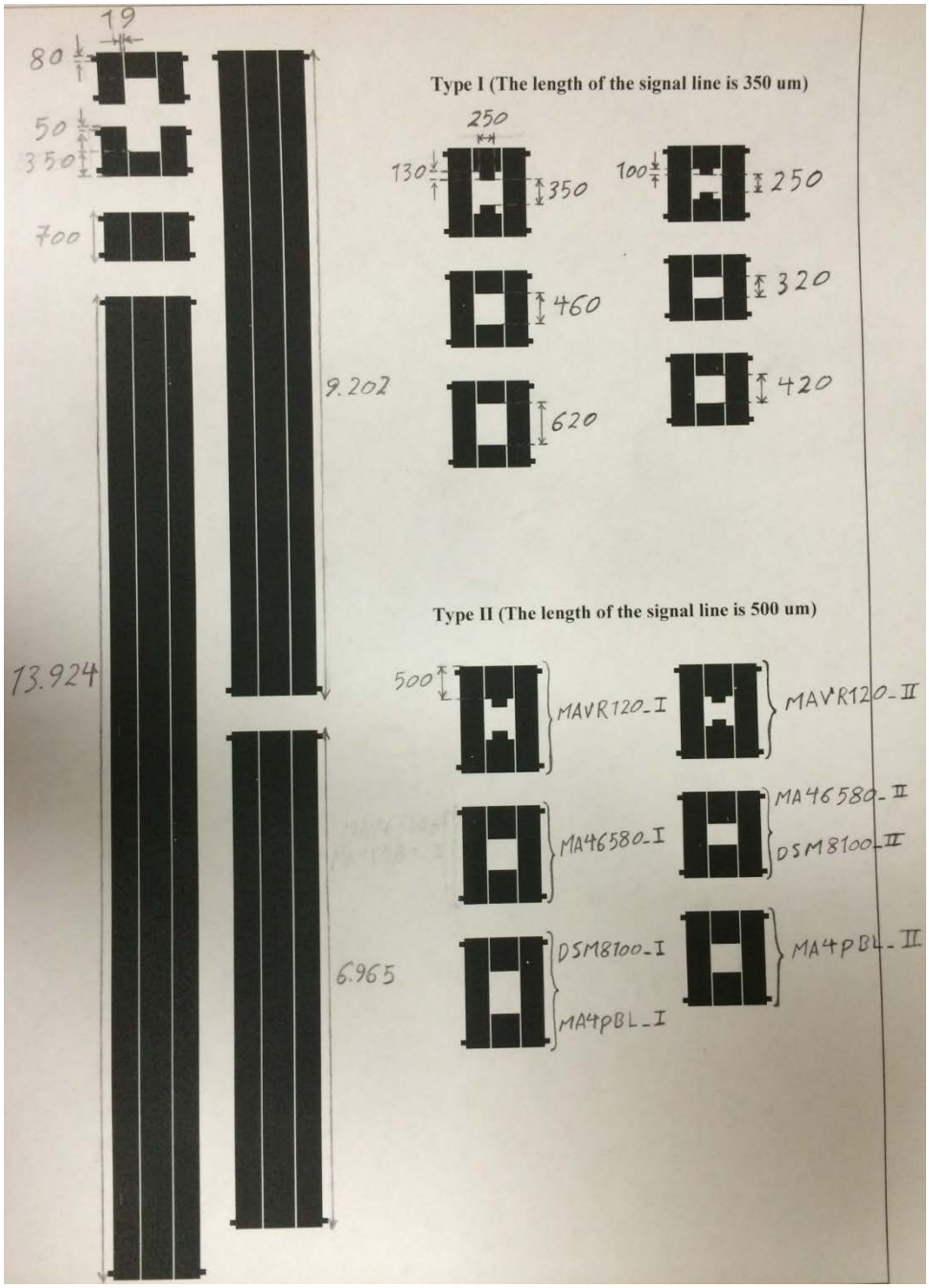

Figure 2.2 Dimensions of the TRL standards and test fixtures

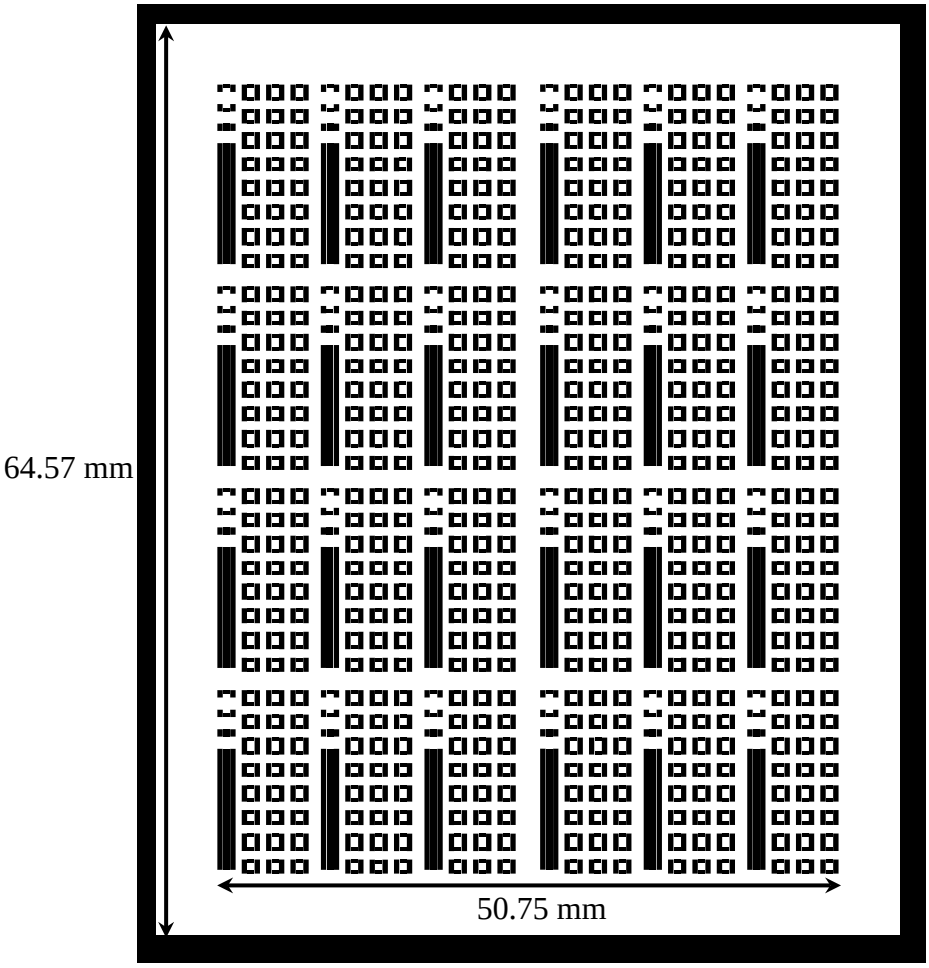

Figure 2.3 preview of the test fixtures with 24 copies.

The test fixture is fabricated using a photolithography process. The varactor diode are placed on the test fixture and conductive silver paint (SPI 05002-AB from Structure Probe, Inc.) is used to make the electrical connection between the switch and the pads of the text fixture. Figure 2.4 shows the varactor diode which is placed on the text fixture under the microscope. A probe station with the nonlinearity measurement setup of the varactor is shown in Figure 2.5. First,

the varactor is characterized to find the capacitance vs. bias voltage. Then, the nonlinearity of the varactor is tested.

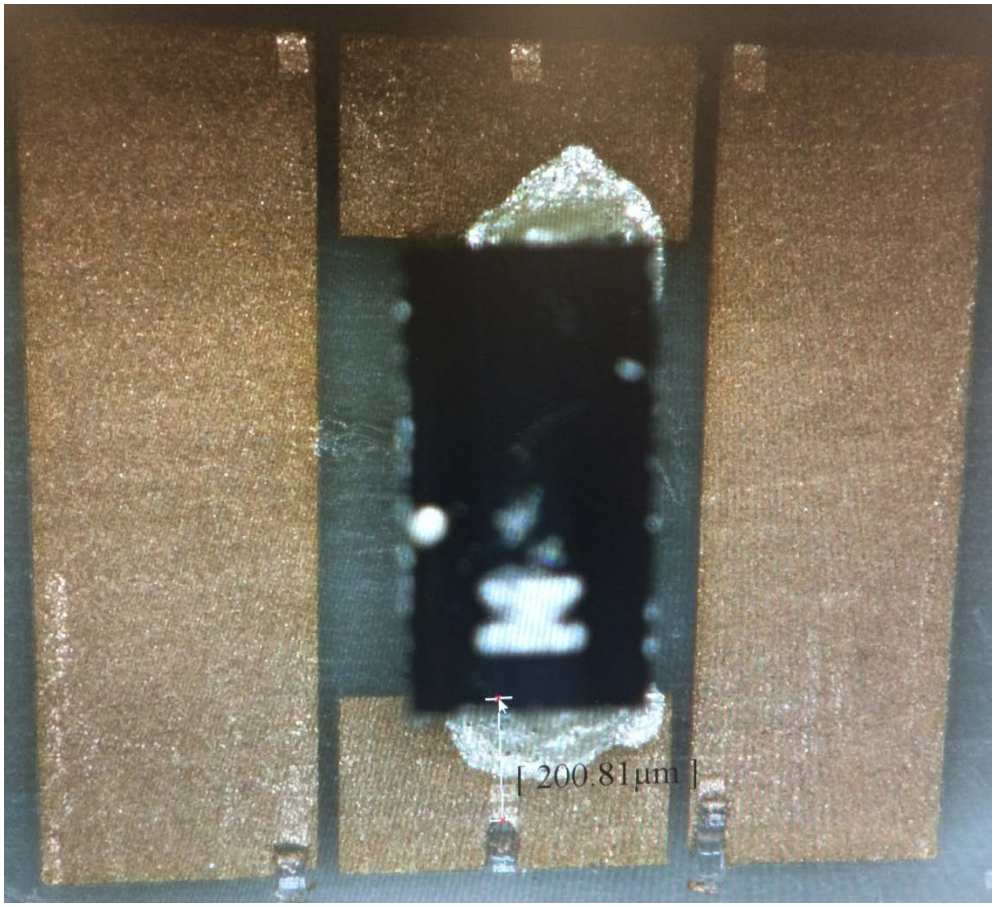

Figure 2.4 Varactor diode (MAVR-000120-1411) is placed on the text fixture using silver paint.

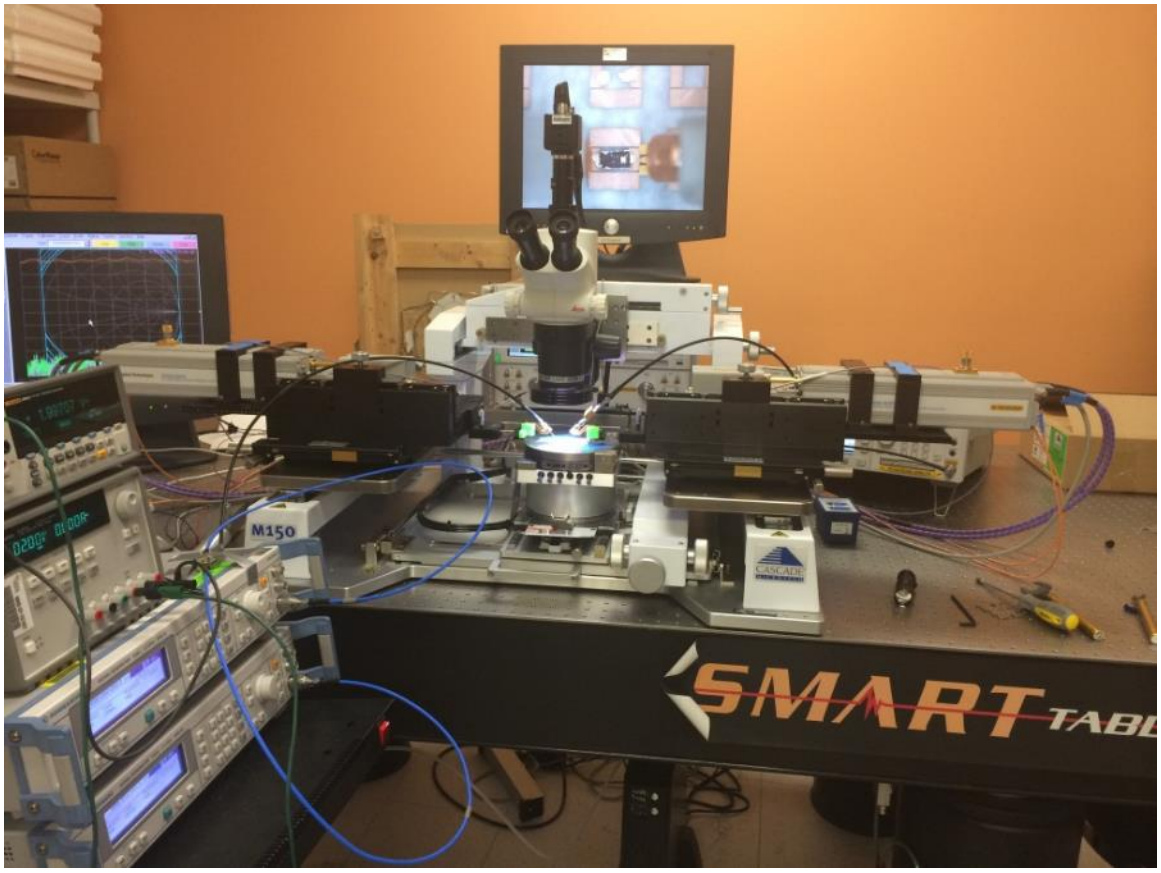

Figure 2.5 Probe station with the nonlinearity measurement setup for varactor characterization.

Figure 2.6 shows the circuit model for the test fixture. In this figure, it is assumed that a perfect TRL calibration was done which means that the reference planes are at the ports of DUT and there is no inductance, resistance or capacitance related to the signal line of the CPW line. For any length of the signal line that is not covered by the TRL calibration, a circuit model of the CPW line should be considered to obtain the capacitance of the varactor [43].

Two samples of MAVR-000120-1411 are measured and the results are provided in this section. Using Y-parameters, the capacitance of the varactor is calculated by (2-1)

$$C_s = \frac{1}{2\pi f . Im[{}^{1}/_{Y_{12}}]} \qquad (2\text{-}1)$$

Where C_S is the capacitance of DUT, f is the resonant frequency and Y_{12} is the measured admittance between port 1 and 2.

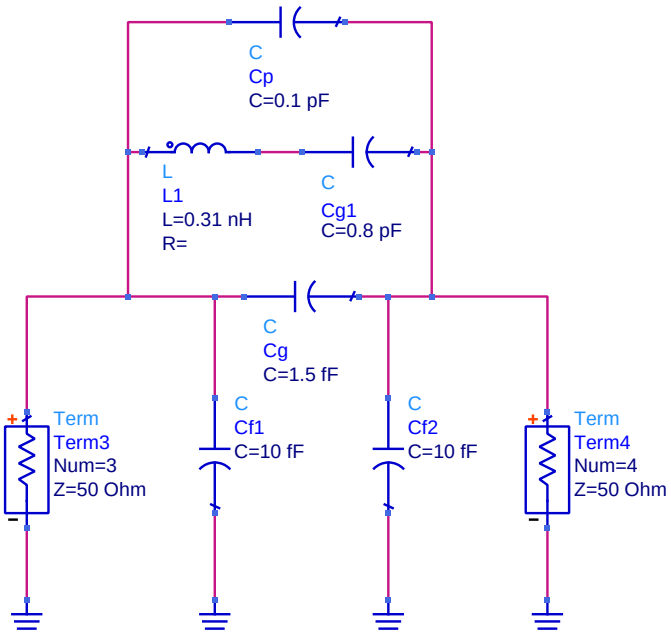

Figure 2.6 Circuit model of the test fixture.

Figure 2.7 illustrates the extracted capacitance from the measured Y-parameters for two samples of the varactor diodes. Consistent results over a wide frequency range for the two samples are obtained when the bias voltage (V_b) is 2, 4 and 12 V. From Figure 2.7, it is also noted that the resonant frequency increases as V_b increases.

The capacitance of the varactor (C_S) vs. reverse bias voltage (V_b) for the two samples is compared to the C_S vs. V_b from the datasheet of MAVR-000120-1411 [44] in Figure 2.8. It is seen that higher bias voltage results in lower capacitance. Moreover, the C-V_b curve for the two measured samples is consistent.

Nonlinearity measurements of the varactor are also performed using probe measurements. The measurement is done at 1 GHz with different bias voltages. The IP_3 of the varactor vs. V_b is depicted in Figure 2.9.To calculate the IP3 from the measurement results, all the losses from the cables, power combiners, connectors and probe feeds should be taken into account. The sum of the losses from the signal generator to the tip of probe is 5.06 dB. Furthermore, loss of the cables, connectors, and probe from the tip of probe to the signal generator is 0.77 dB. As illustrated in Figure 2.9, IP_3 of the varactor diode increases as the bias voltage increases with the worst IP_3 of 23 dBm at V_b = 2 V.

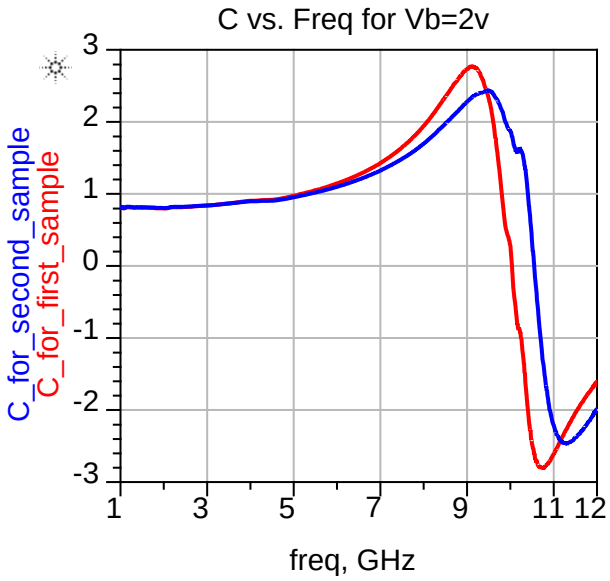

(a)

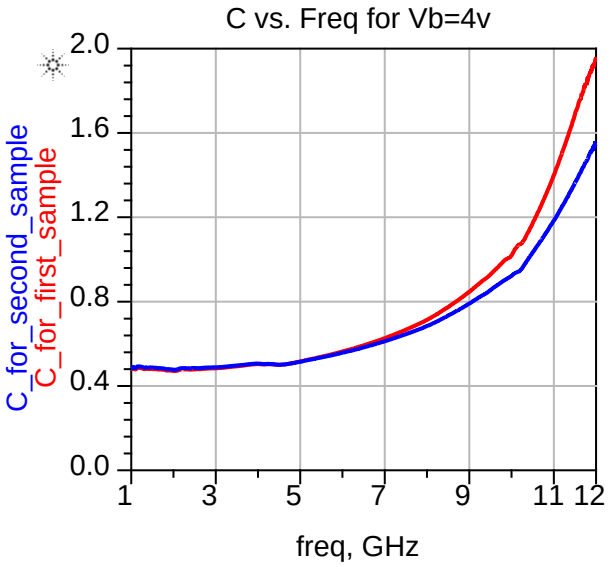

(b)

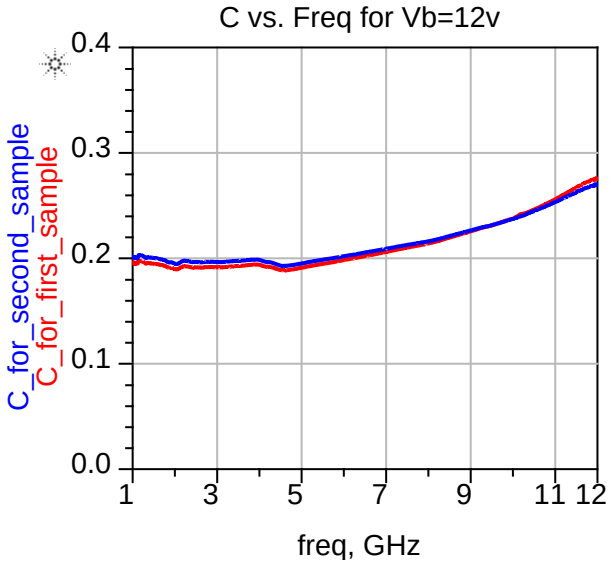

(c)

Figure 2.7 Extracted capacitance from Y-parameters for (a) V_b= 2 V, (b) V_b= 4 V and (c) V_b= 12 V.

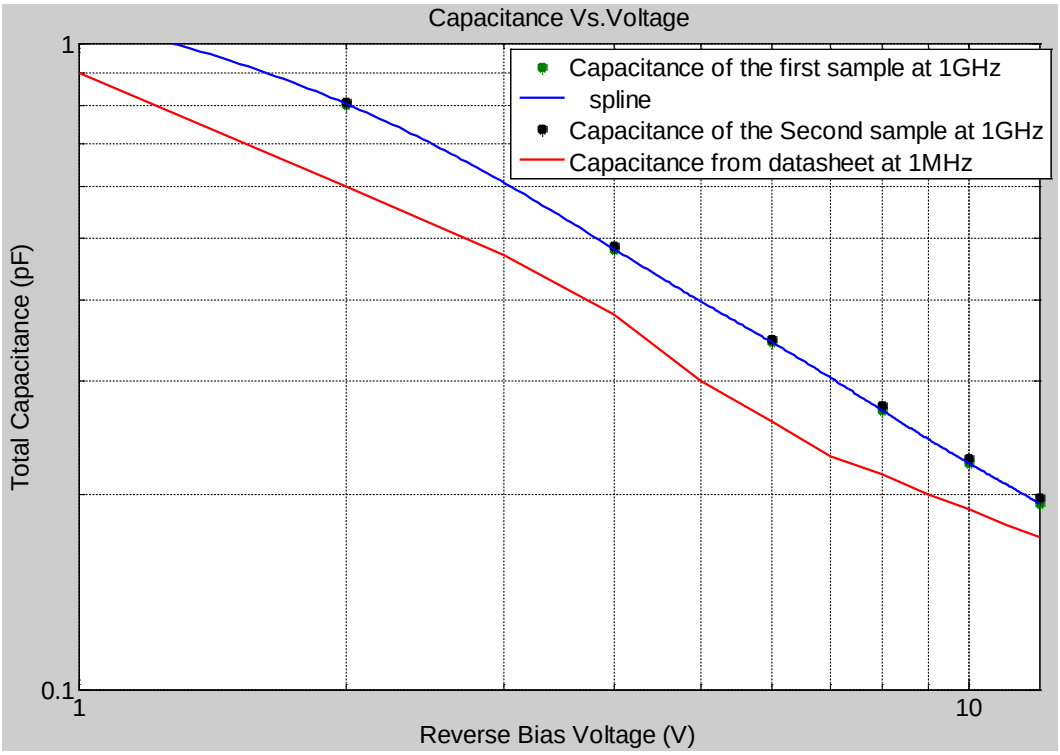

Figure 2.8 Total capacitance vs. reverse bias voltage.

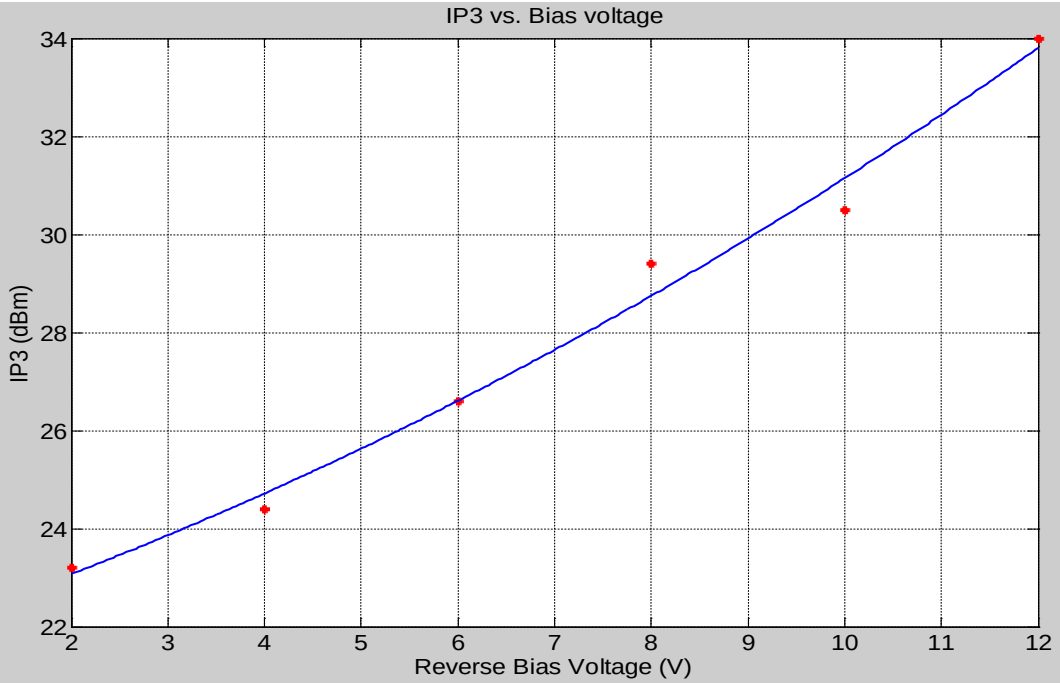

Figure 2.9 IP_3 vs. reverse bias voltage for the varactor diode.

2.2 PIN Diode Switches

PIN diode switches are widely used in reconfigurable RF/microwave devices such as filters, amplifiers and antennas. Reconfigurable antennas have significant potential in performing multiple roles by being able to reconfigure operating frequency, radiation pattern, or polarization in real time without changing the antenna structure. In this dissertation, reconfigurable antenna arrays with PIN diode switches are studied, therefore, PIN diodes that have been placed inside a slot-ring antenna are characterized.

In the literatures, it is seen that switches are modeled as short or open circuits in reconfigurable antennas. Although it provides a representation of the switch in the ON or OFF state, it can be further improved by using an equivalent circuit to model the PIN diode switch in the simulations. In [45], the effects of PIN diode switches on the impedance matching and radiation patterns of a reconfigurable leaky-wave antenna (LWA) was demonstrated.

In this section, first, the geometry of a reconfigurable slot-ring antenna is presented and an equivalent circuit model for the PIN diode in the ON and OFF states is developed based on the measurement results. Then, the effects of PIN diode switches on the performance of reconfigurable slot-ring antenna are demonstrated. Finally, parametric analyses of each element of the equivalent circuit model is also presented [46].

2.2.1 Antenna Configuration

A frequency reconfigurable slot-ring antenna switching between *S* and *C* bands is used in this study. Two slot-ring antennas with ideal and real switches are fabricated on a Rogers RT/Duroid 5880 substrate (ε_r=2.2 and tanδ=0.0009) with a thickness of h=0.79 mm. For the antenna with real switches, four PIN diodes (DSM8100-000 from Skyworks) are placed inside the slot-rings to enable switching between 2.18 GHz and 7 GHz. Figure 2.10 shows the geometry of the antenna. The big slot-ring operates in the *S* band while the small slot-ring, as shown in the inset in Figure 2.10, operates in the *C* band. Via holes for biasing purposes are placed near the center of the big and small slot-rings where the magnitude of electric field is minimum.

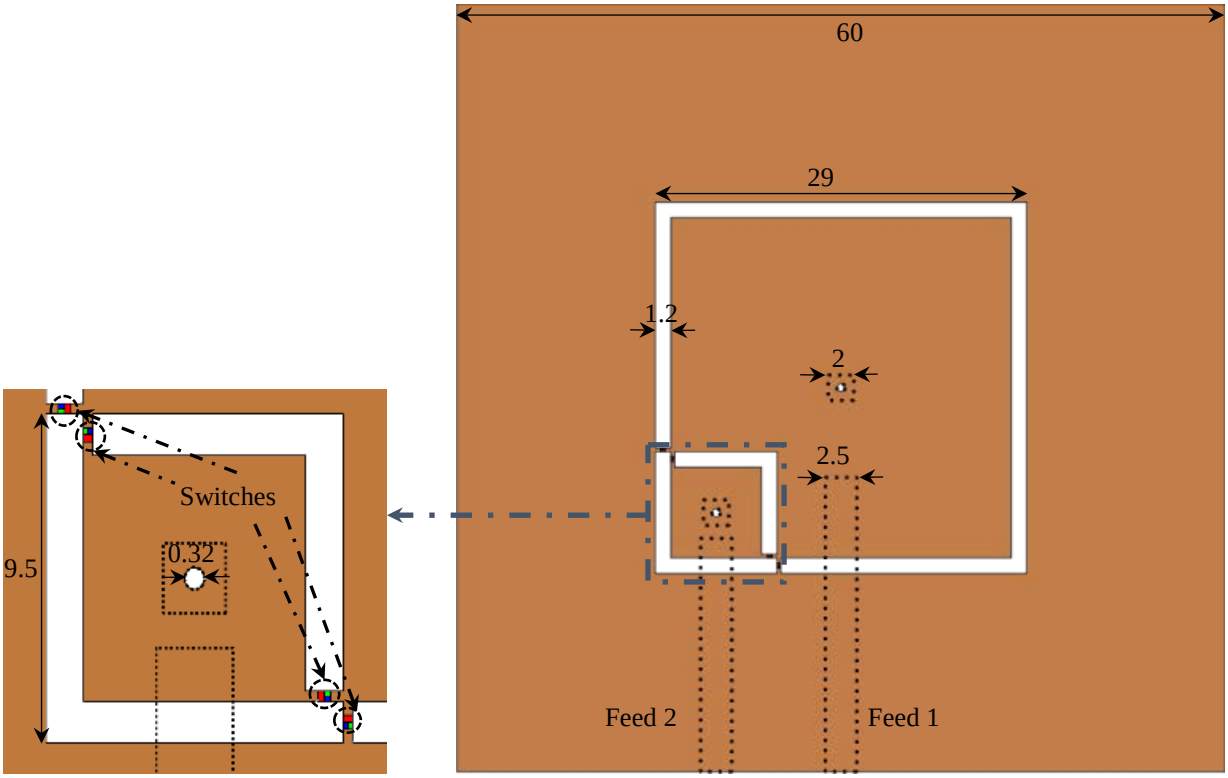

Figure 2.10 Schematic view of the switchable-frequency slot-ring antenna. The inset shows the close-up view of the *C*-band unit cell. (All dimensions are in mm).

2.2.2 Equivalent Circuit for The PIN Diode Switch

For comparison, the PIN diodes are modeled in two ways: An ideal model and a circuit model consiststing of *RLC* components. Figure 2.11 (a) and (b) depict the circuit model that is used for the Pin diode switch in the ON and OFF states, respectively. The inductance in the model is due to the packaging and it is similar in both states. The circuit element values are extracted from the measured S-parameters of the switch provided by the manufacturer (Skyworks). Table 2-1summarizes the extracted values in the ON and OFF states.

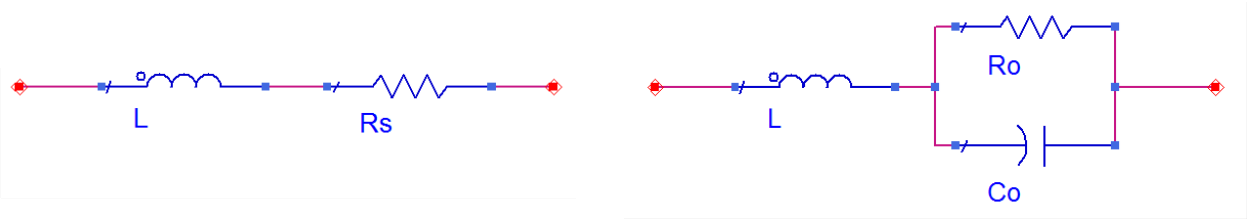

(a) (b)

Figure 2.11 Circuit model for the PIN diode switch when it is (a) ON or (b) OFF.

Table 2-1. Element values of the Equivalent circuit for the PIN diode switch in the ON and OFF states

State	Resistance	Capacitance	Inductance
ON	R_s=3 ohm	-	0.15 nH
OFF	R_o=15 Kohm	32 fF	0.15 nH

2.2.3 Simulation and Measurement Results

Figure 2.12 shows the fabricated antenna with four PIN diode switches. Two other slot-ring antennas with ideal switches (short circuit for the switch in the ON state and open circuit for the switch in the OFF state) are also fabricated to operate at 2.18 GHz and 7 GHz, respectively. The measured return losses of the antenna with real switches and the antenna with ideal switches at lower and higher bands are compared in Figure 2.13 (a) and (b), respectively. It is seen that the switches have a slight loading effects on the resonance frequency of the slot-ring antenna. It is noted that f_0 for the antenna with real switches is approximately 3.5% lower than f_0 for the antenna with ideal switches.

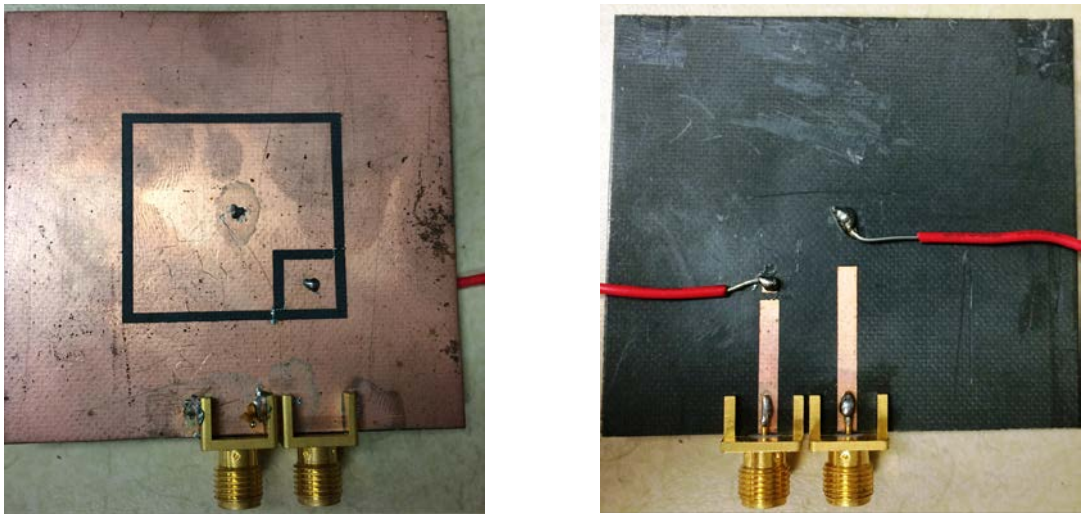

(a) (b)

Figure 2.12 Fabricated slot-ring antenna from the (a) top and (b) bottom view.

The gain and efficiency of the slot-ring antennas with ideal switches and real switches at 2.18 GHz and 7 GHz is summarized in Table 2-2. The equivalent circuit shown in Figure 2.11 is used to model the real switches in high-frequency structure simulator (HFSS). It is seen that the gain of the antenna with real switches is reduced and accordingly the efficiency of the antenna with real switches is less than the antenna with ideal switches.

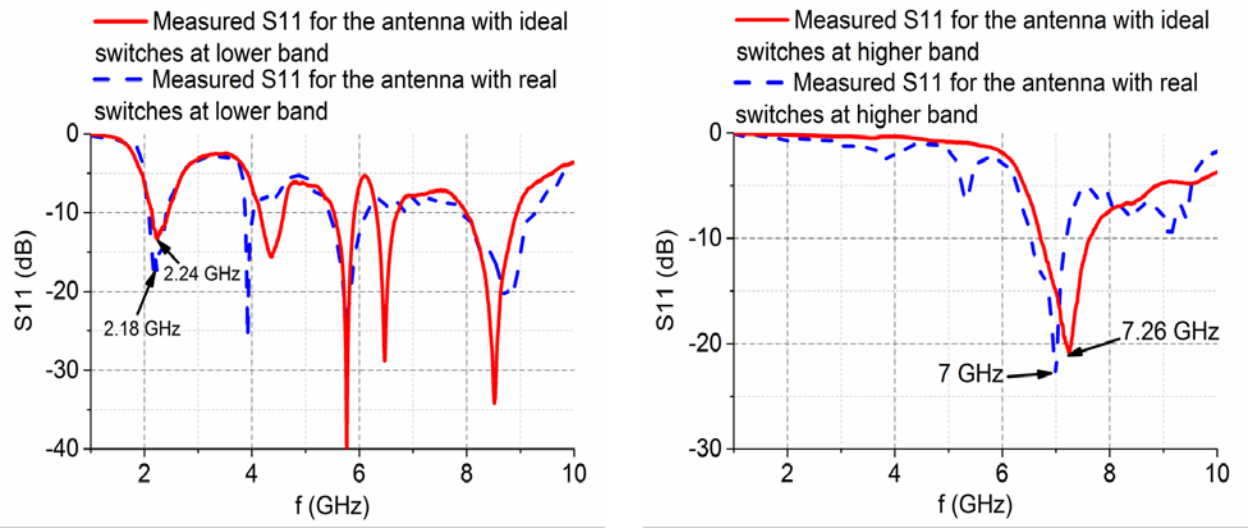

(a) (b)

Figure 2.13 Measured S_{11} for the antenna with ideal switches (red solid line) and real switches (blue dashed line) at (a) lower and (b) higher frequency bands.

Table 2-2. Gain and efficiency of the antenna with ideal switches and real switches in the lower and higher frequency bands.

Ideal switch/real switch	Frequency (measured)	Gain (dBi) (simulated)	Efficiency	Bandwidth
Ideal switch	2.24 GHz	0.01-	97%	13.5%
Real switch	2.18 GHz	-0.29-	93%	15.1%
Ideal switch	7.26 GHz	-5.72	98%	12.6%
Real switch*	7.00 GHz	5.23	91%	9.4%

2.2.4 Parametric Analysis

In this part, a parametric study on each circuit element of the Pin diode switch is performed. Figure 2.14 illustrates the effect of capacitance of the PIN diode (C_O) on the resonant frequency

of the antenna at the lower (f_{0L}) and higher (f_{0H}) bands. PIN diode switches with higher capacitances shift the resonant frequency of the reconfigurable antenna more. f_{0L} and f_{0H} vs. inductance of the switch (L) are shown in Figure 2.15. The effect of L on f_0 is similar at lower and higher frequency bands. From Figure 2.14 and Figure 2.15, it is seen that C_O has more effect on the resonant frequency of the slot-ring antenna than L.

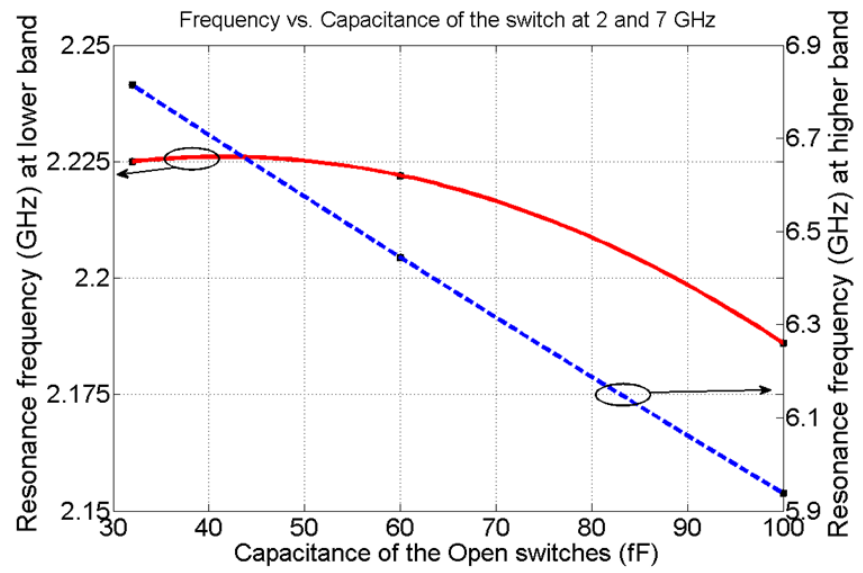

Figure 2.14 Resonance frequency of the slot-ring antenna vs. capacitance of the switch at lower (red solid line) and higher (blue dashed line) frequency bands.

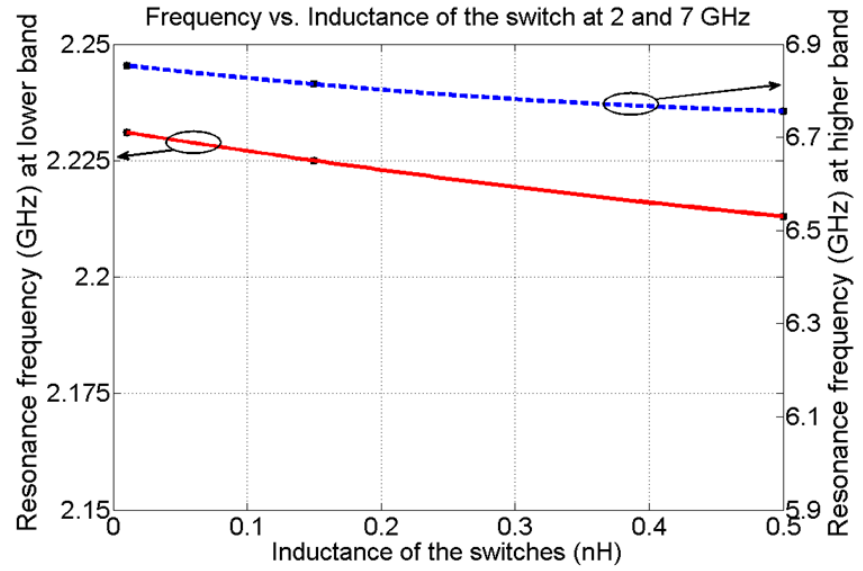

Figure 2.15 Resonance frequency of the slot-ring antenna vs. inductance of the switch at lower (red solid line) and higher (blue dashed line) frequency bands.

The gain of the slot-ring antenna vs. resistance of the switch in the ON state (R_S in Figure 2.11) is illustrated in Figure 2.16. For the antenna in the OFF state, the gain of the slot-ring antenna vs. resistance of the switch (R_O in Figure 2.11) is plotted in Figure 2.17. The effects of R_O on the antenna gain is much more than R_S.

The resistance of the Pin diode does not affect the resonant frequency of the slot-ring antenna. Moreover, the capacitance and inductance of the Pin diode switch do not change the antenna gain or efficiency. Therefore, no figures are provided in this section to show f_0 vs. R, or G vs. C_o, or G vs. L.

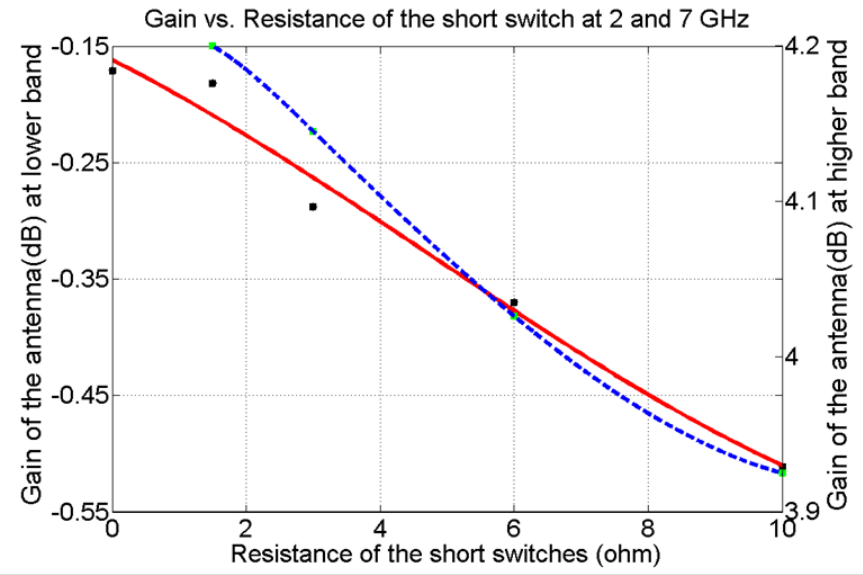

Figure 2.16 Gain of the slot-ring antenna vs. resistance of the switch in the ON state (R_S) at lower (red solid line) and higher (blue dashed line) frequency bands.

2.3 MEMS Switches

Varactors are currently implemented using reverse-biased semiconductor diodes. These devices have a number of performance drawbacks, including large energy losses and limited tuning range. Substantial research is now underway worldwide into the possibility of replacing these components with micromechanical capacitors fabricated using high-performance MEMS technology, although no such varactor has yet reached the commercial market.

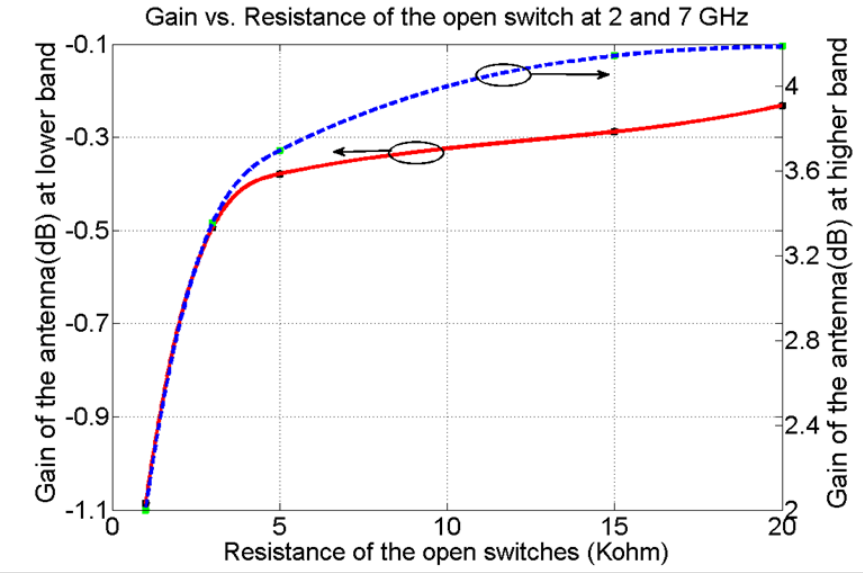

Figure 2.17 Gain of the antenna vs. resistance of the switch in the OFF state (R_O) at lower (red solid line) and higher (blue dashed line) frequency bands.

MEMS is a semiconductor-based technology that uses the selective deposition and etching of a series of thin films to create a range of micron-scale mechanical structures. MEMS varactors operate by using electrostatic forces to vary the separation between two plates and hence change the capacitance of the mechanical structure. Simulations show that MEMS devices are potentially able to offer tuning ranges of several hundred percent, together with high base capacitances and low energy losses. In comparison, most semiconductor diodes have a tuning range of a few tens of percent.

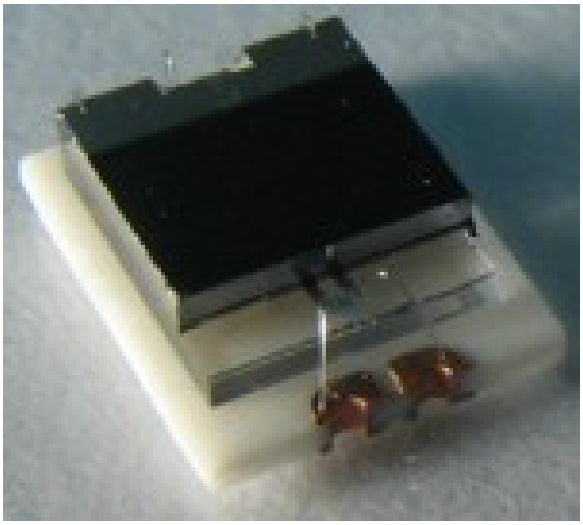

Figure 2.18 RF-MEMS varactor for high power applications (reprinted from [47]).

In Figure 2.18, a RF-MEMS varactor for high power applications is shown. A parallel plate, metal-air-metal capacitance is the main part of this high Q-factor RF-MEMS varactor. Continuous tunability and rather high RF capacitance values (required for UHF applications) are obtained [47].

Tyndall developed a RF MEMS Capacitive Switch illustrated in Figure 2.19 [48]. These surface micro-machined devices have the potential to offer substantial advantages over more conventional semiconductor switches, such as high isolation, low loss, and low power consumption. Although this technology is currently the subject of intensive worldwide research, no commercially available switch yet exists. This is largely due to the high operating voltages required by many MEMS switches, reliability concerns associated with the structures, and the high cost and complexity of packaging. The switch developed by Tyndall requires an operating voltage

of 10-15 V, which represents a substantial improvement on many current devices that require a voltage of up to 70 V. The RF performance is also promising, and the switches have shown an insertion loss of -0.2 dB at 30 GHz and an isolation of -19.3 dB at 30 GHz.

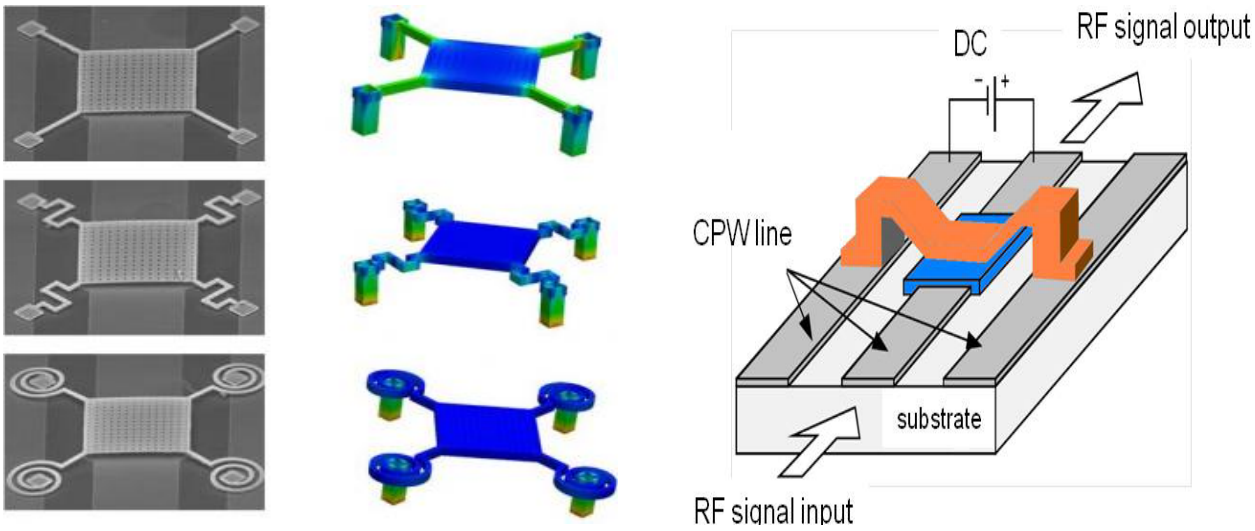

Figure 2.19 RF MEMS capacitive switch using post-CMOS surface micromachining process (reprinted from [48]).

As shown in Figure 2.19, the MEMS switch consists of a metallic electrode (membrane) suspended above a metallic coplanar waveguide (CPW) that is passivated with a dielectric (oxide). When a voltage is applied between the suspended electrode and the signal line the electrode collapses on the CPW due to electrostatic attraction. In the up-position, the capacitance between the electrode and the signal line is low (1-100 fF), allowing the RF signal to pass to the output port unimpeded. In the down-position the capacitance is high (1-10 pF) and the RF signal is coupled to the ground.

For mobile phones, MEMS will compete with BST (ferroelectric) varactors that entered serial production in 2010 for antenna tuning. While MEMS is better in terms of linearity, losses and tuning range, a strong BST manufacturing chain is already in place. Meanwhile, silicon-on-sapphire switches exhibit high linearity and although MEMS outperforms on losses, silicon-on-sapphire also benefits from a strong existing supply chain.

2.4 Conclusions

Varactor diodes, PIN diodes, and MEMS switches that are used in reconfigurable antennas have been presented in this chapter. First, a varactor diode (MAVR-000120-1411) has been characterized using probe measurements. The capacitance of the varactor vs. reverse bias voltage was obtained from the measurement results. Nonlinearity of the varactor was also investigated by measuring the IP_3 of the varactor diode. Then a PIN diode switch (DSM8100-000) has been characterized and an equivalent circuit has been presented to model the effects of PIN diode switches on a reconfigurable slot-ring antenna. An antenna with real switches has been compared to an antenna with ideal switches. Parametric analysis for each circuit element of the PIN diode switch have been provided. It is found that the capacitance of the switch is responsible for the shift in resonant frequency and the resistance of the switch in the ON state is responsible for the gain reduction. Finally, basics of RF MEMS switches and varactors with their advantages and disadvantages over PIN diodes, BSTs, and FET switches have been studied.

CHAPTER 3: SWITCHABLE BAND RECONFIGURABLE ANTENNA ARRAY

In many advanced communication systems, phased array antennas are highly desirable due to their high directivity and beam steering capability. These antennas have very wide applications in wireless networks [49, 50, 51, 52, 53], cognitive radio [54], bio and medical sciences [55, 56, 57] and IoT applications [58]. However, the development of antenna arrays is relatively time consuming and expensive. Multi-band and switchable-band antenna arrays are alternatives for designing multiple antenna arrays with single functionalities. As mentioned in Section 1.1, antenna arrays can be divided into two categories; (1) multi-band antenna arrays with common feeding for all frequency bands of operation, and (2) separate feeding for each band. In the first category, the element spacing at the higher band is unavoidably large if the spacing at the lower band is maintained at $\lambda_0/2$. If the element spacing is close to $\lambda_0/2$, at the higher band, then the spacing at the lower band is much smaller than $\lambda_0/2$ which results in stronger mutual coupling and an unnecessarily-large number of electronics for the lower band. In the second category, the element spacing in both frequency bands can be maintained at $0.5/0.5\lambda_0$ as demonstrated in this chapter.

First, a new slot-ring antenna which can be used as an element of a large phased array antenna with element spacing less than $0.5\lambda_0$ in multi frequency bands is presented. Then, a tunable version of this design is demonstrated to enhance the FBW in each operating state.

3.1 Switchable-Frequency Band Antenna Array

An *L*-band slot-ring antenna can be reconfigured to a 2×2 *C*-band slot ring antenna array in the same radiating aperture as shown in Figure 3.1. PIN diode switches are placed inside the slots of the antenna to dynamically change the antenna function and each frequency band has its own feeding lines. The operating frequencies of this antenna in the *L*-/*C*-band states are 1.76/5.71 GHz, representing a 3.2:1 ratio. The FBWs are shown to be 8.6%/11.5%, respectively. As a result, only narrow-band T/R modules are required for this antenna array. In addition, the element spacing at *C* band is $0.36\lambda_0$ within the antenna element shown in Figure 3.1(b).

3.1.1 Switchable-Frequency Antenna Element Configuration and Design

The schematic view of the multi-port switchable-frequency antenna is shown in Figure 3.1(b). By placing 16 PIN diode switches (DSM8100-000, 0201 package) inside the slots and properly turning them on and off, the 2×2 *C*-band slot-ring antenna array can also perform as an *L*-band slot-ring antenna. A *C*-band antenna array element is illustrated in Figure 3.1(c) to show the details of the switching. When switches 1 and 2 are closed and switches 3 and 4 are open (state I), this antenna is excited by port 1 and resonates at 1.76 GHz (*L*-band state). By closing switches 3 and 4 and opening switches 1 and 2 (state II), 4 smaller slot-rings are formed for *C*-band operation. In this state, the slot-ring antenna array is excited by ports 2 to 5 and resonates at 5.71 GHz (*C*-band state). Table 3-1 summarizes the relationship between the switch states and antenna frequency operating states. The resonant frequency in each operating state is determined by the perimeter of the square slot-ring (3-1):

$$f_r = \frac{c_0}{\lambda_g \sqrt{\varepsilon_{eff}}} \; ; \; \lambda_g = p = 4L \tag{3-1}$$

where c_o is the speed of light, λ_g is the guided wavelength at the resonant frequency, ε_{eff} is the effective dielectric constant (1.84 in this design), p is the perimeter of the slot-ring, and L is the lateral length of the square slot-ring. Since the lateral length of the slot-ring is $\lambda_g/4$ which is much smaller than $\lambda_0/2$, there is a lot of freedom in choosing the antenna element spacing in both operating states to avoid grating lobes at large scan angles.

Microstrip lines are used to feed this antenna as shown in Figure 3.1(c). The distance between the open end of the microstrip line and the slot is optimized to achieve the best impedance matching at each operating frequency. The width of the microstrip lines is slowly widened when they are extended to the edge of the antenna in order to achieve 50-Ω characteristic impedance. SMA connectors are soldered to the microstrip lines to provide access for measurement. Lumped ports are used in ANSYS HFSS to excite the antenna at both operating states.

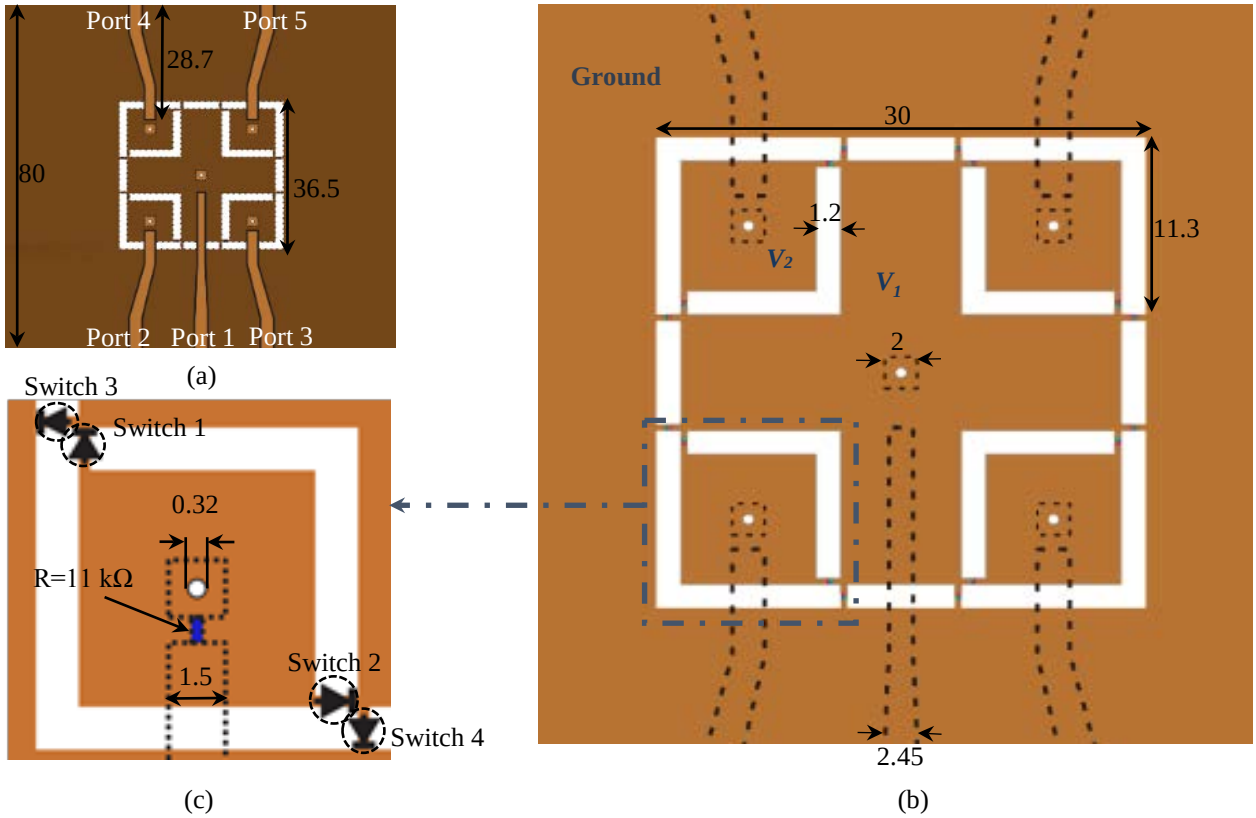

Figure 3.1 (a) Bottom and (b) top view of the switchable-frequency slot-ring antenna element. (c) Close-up view of the *C*-band unit cell. (All dimensions are in mm).

3.1.1.1 Loading Effects of PIN Diode Switches

As illustrated in Chapter 2, PIN diode switches do not behave as an ideal short or open in the ON or OFF state, respectively. An *RLC* equivalent circuit shown in Figure 3.2 is used in HFSS simulations to model the PIN diodes in the ON or OFF state. The element values for the ON and OFF states which were obtained from the PIN diode characterization in section are also illustrated in Figure 3.2. To verify the effect of each circuit element of the switch on the reconfigurable, an

antenna with an ideal switch is compared to an antenna containing switch models in HFSS simulations. It is observed that the resonant frequencies of the antenna in the *L*/*C* band decrease from 1.84/5.99 GHz to 1.76/5.71 GHz when the switch model is used compared with ideal switches. This 4.5% downshift in the resonant frequencies is primarily attributed to the parasitic capacitance of the PIN diode switches. The resistance of the switch is responsible for the reduction in the antenna gain as shown in section 2.2; the simulated realized gain in the *L*/*C* band decreases from 1.49/5.13 dBi to 0.78/4.95 dBi when the switch model is employed compared with lossless switches.

Table 3-1: Switch states in the *L*- and *C*-band operating states.

State	**Operating state**	**Switches 1 and 2**	**Switches 3 and 4**	V_1	V_2
I	*L*-band	ON	OFF	0V	2V
II	*C*-band	OFF	ON	2V	0V

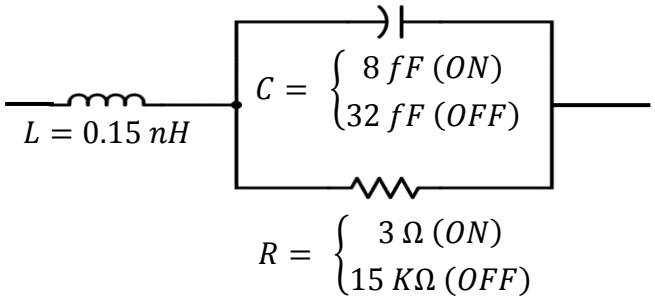

Figure 3.2 Circuit model for the PIN diode switch.

3.1.1.2 Biasing mechanism for the switches

In order to find the optimum location for DC biasing, the electric field distributions on the antenna aperture in both operating states are simulated and illustrated in Figure 3.3. It is observed that there is an electric field minimum at the center of this antenna; a metal wire is placed at this minimum location to provide a DC voltage (V_1) which is able to control switches 3 and 4 in Figure 3.1(c) without adversely affecting the RF performance. A 100-ohm resistor is connected in series with this metal wire to limit the current going through the switches. In order to control switches 1 and 2, a second DC voltage (V_2) is applied through a metallic via at the center of the *C*-band slot-ring antenna, which is itself connected to the microstrip feed line in series with a 11 kΩ resistor as shown in Figure 3.1(c). A coaxial bias-tee (ZX85-12G-S+ from Mini-Circuits) is used in each cable that connects to the *C*-band feed lines. At either State I or II, 8 switches are ON and the other 8 are OFF. The switches in OFF state do not consume DC power. In State I, the total DC power is 48 mW in which 44 mW is dissipated in four 11 kΩ resistors and 4 mW is consumed by the 8 PIN diodes. Smaller RF-blocking resistors can be used to decrease the DC power consumption to 8 mW without adversely affecting the RF performance. In State II, the total DC power is 4.8 mW in which 1.6 mW is dissipated in the 100-Ω resistor and 3.2 mW is consumed by the 8 PIN diodes. It should be mentioned that there is no DC current in the 11 kΩ resistors in this state.

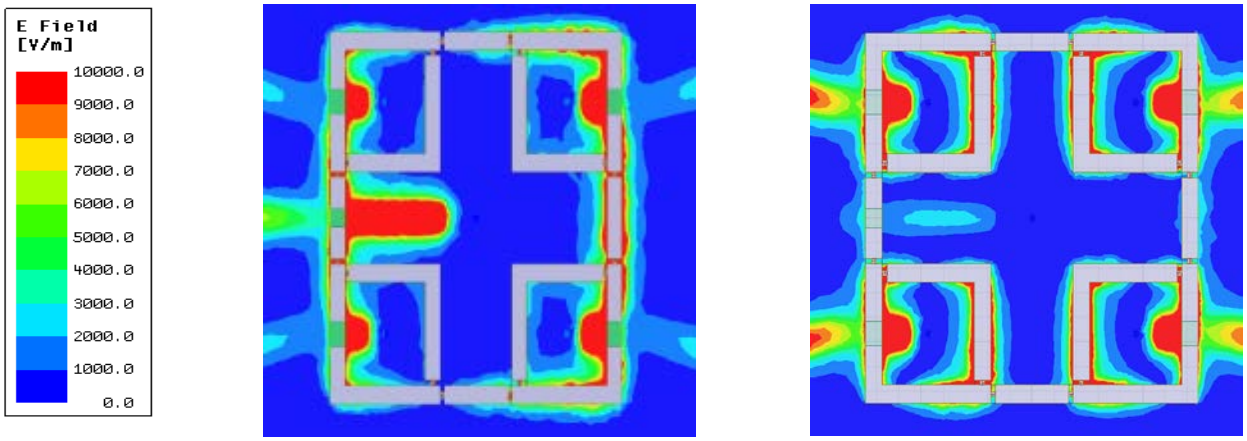

Figure 3.3 Magnitude of electric field on the top surface at (a) *L*-band operating state and (b) *C*-band operating state.

3.1.2 Simulation and Measurement Results

This switchable-band antenna element is fabricated on a Rogers RT/Duroid 5880 substrate (ε_r=2.2 and tanδ=0.0009) with a thickness of 0.79 mm as shown in Figure 3.4. Conductive silver paint (SPI 05002-AB from Structure Probe, Inc.) is used to make the electrical connection between the switch and the antenna.

(a) (b)

Figure 3.4 (a) Top and (b) bottom view of the fabricated antenna.

The simulated and measured return losses for the antenna at *L*- and *C*-band operating states are illustrated in Figure 3.5(a) and (b), respectively. At the lower-band operating state, a resonance at 1.76 GHz with 8.6% FBW is observed in Figure 3.5(a) when the antenna is in state I. When the antenna is reconfigured to state II, the energy at Port 1 is mostly reflected back. At the higher-band operating state, a resonance at 5.76 GHz with 11.5% FBW can be seen when the antenna is in state II. It is also shown in Figure 3.5(b) that the return loss at port 2 is much higher when the antenna is reconfigured to state I (a filter can be used to further improve the return loss at port 2 in state I). The return losses at Ports 3-5 are measured and found to be consistent with Figure 3.5(b).

Another important parameter for a multi-port antenna is the isolation between ports. Simulated S_{12} and S_{14} in the *L* band are compared to the measurement results in Figure 3.6(a). In

state II, the isolation between ports 1-2 (S_{12}) and between ports 2-3 (S_{23}) are shown in Figure 3.6(b). The isolation between any two ports is more than 10 dB in each operating state.

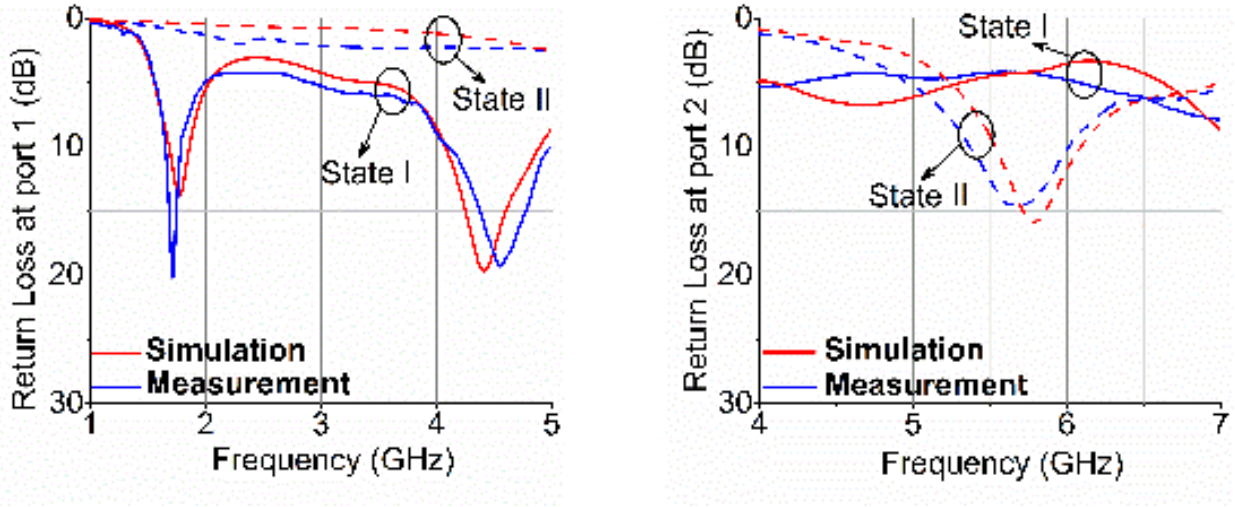

(a) (b)

Figure 3.5 Simulated and measured return loss for the slot-ring antenna at (a) *L*-band operating state and (b) *C*-band operating state.

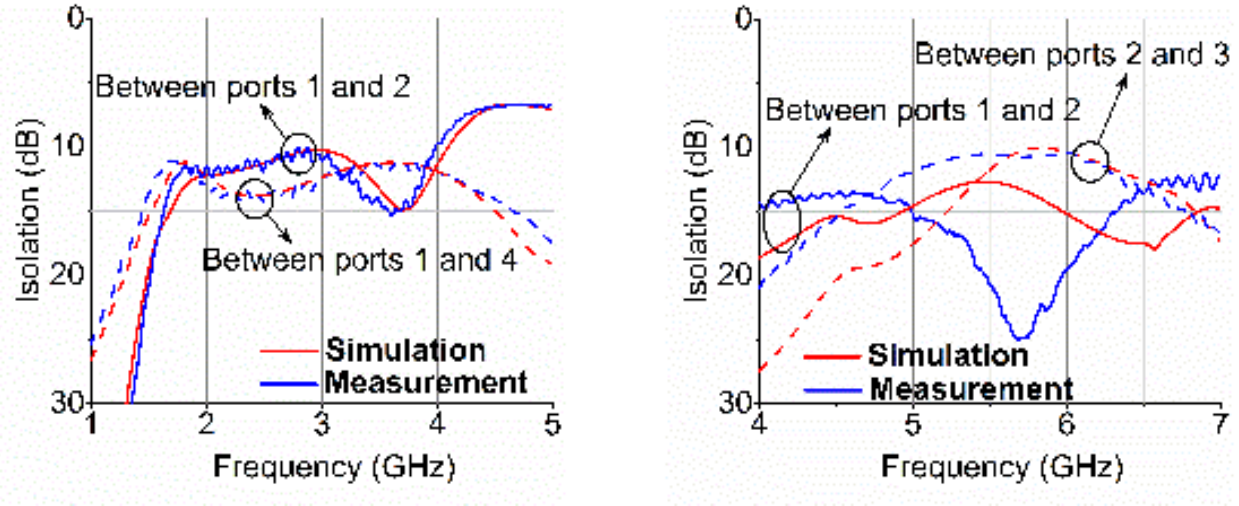

(a) (b)

Figure 3.6 Simulated and measured isolation between different ports of the slot-ring antenna at (a) *L*-band operating state and (b) *C*-band operating state.

The co-polarization (co-pol.) and cross-polarization (X-pol.) radiation patterns in the E- and H-planes are measured in an anechoic chamber. Figure 3.7 shows the H-plane measurement setup in the *C*-band state. In order to achieve the maximum radiation at boresight for the *C*-band array, a phase difference of 180^{o} is required between the feed ports on the opposite sides of the array, i.e. Ports 2-3 and Ports 4-5 are 180^{o} out of phase. A two-way power divider (RFLT2W2G08G from RF-lambda) with two 180^{o}-hybrids (RFHB02G08GPI from RF-lambda) is used to provide the required phase differences and feed the *C*-band antenna array. As illustrated in Figure 3.4(b), the biasing wire in the middle of the antenna should be perpendicular to the antenna to minimize the X-pol level. Figure 3.8(a) and (b) show the radiation patterns in the *L* and *C* bands, respectively. The measurement results agree well with simulation results, except for the

relatively-high measured X-pol. levels at *L* band. The antenna is larger in size and lower in gain at *L* band, therefore there is more scattering from the cable connected to Port 1 and the bias Tees connected to Ports 2-5, which are not included in simulations.

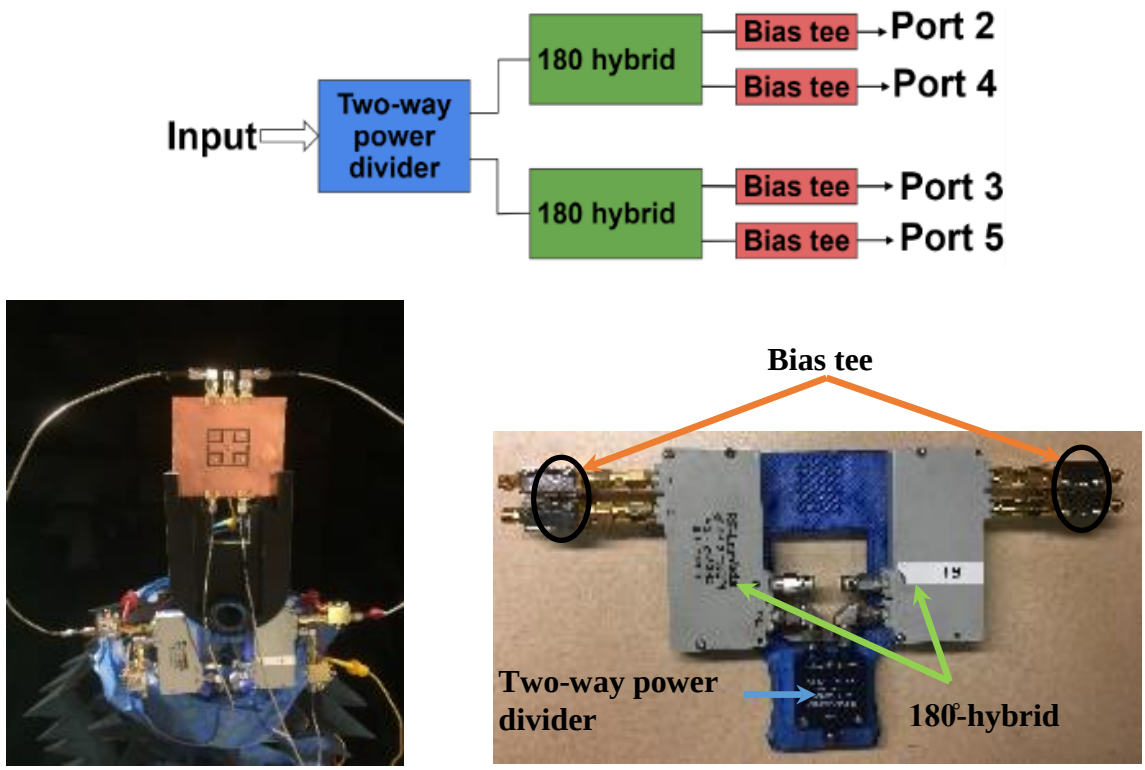

Figure 3.7 Radiation pattern measurement setup for the array at C-band state.

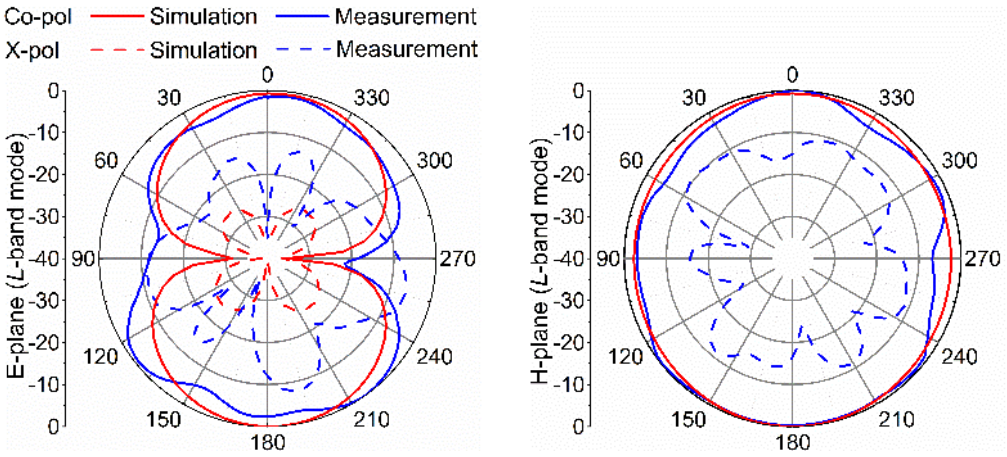

(a)

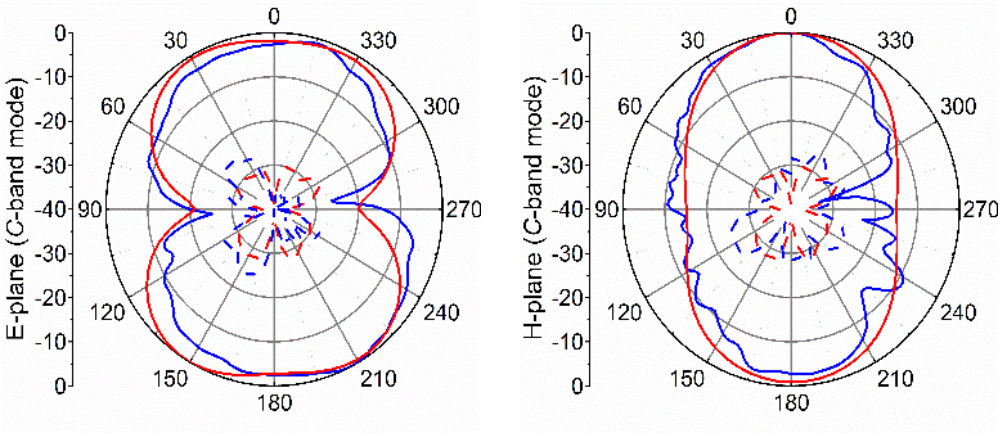

(b)

Figure 3.8 Simulated and measured radiation patterns of the slot-ring antenna for co- and X-pol. at (a) 1.76 GHz and (b) 5.71 GHz.

Figure 3.9 shows the simulated and measured realized gain at boresight in the *L*-/*C*-band operating states which is 0.1/4.2 dBi, respectively. This is a double-sided radiation antenna, so the gain is 3 dB lower than that of a single-sided radiation antenna. First, we assume all switches are

lossless in HFSS simulations, the radiation efficiency is found to be 96.2% and 99.5%, at *L*- and *C*-band operating states, respectively. When the switch loss is included, the radiation efficiency decreases to 66.6% and 80.7%, respectively. The radiation efficiency is obtained from the measured maximum absolute gain divided by the directivity. Note that, in the *L*-band state, all 16 PIN diodes are included in the electric current path (8 switches are in the open state and 8 switches are in the closed state). However, a fewer number of PIN diode switches are involved in forming an antenna element in the *C*-band state (two switches in the open state and two switches in the closed state). Therefore, antenna efficiency in the *C* band is higher than that at *L* band.

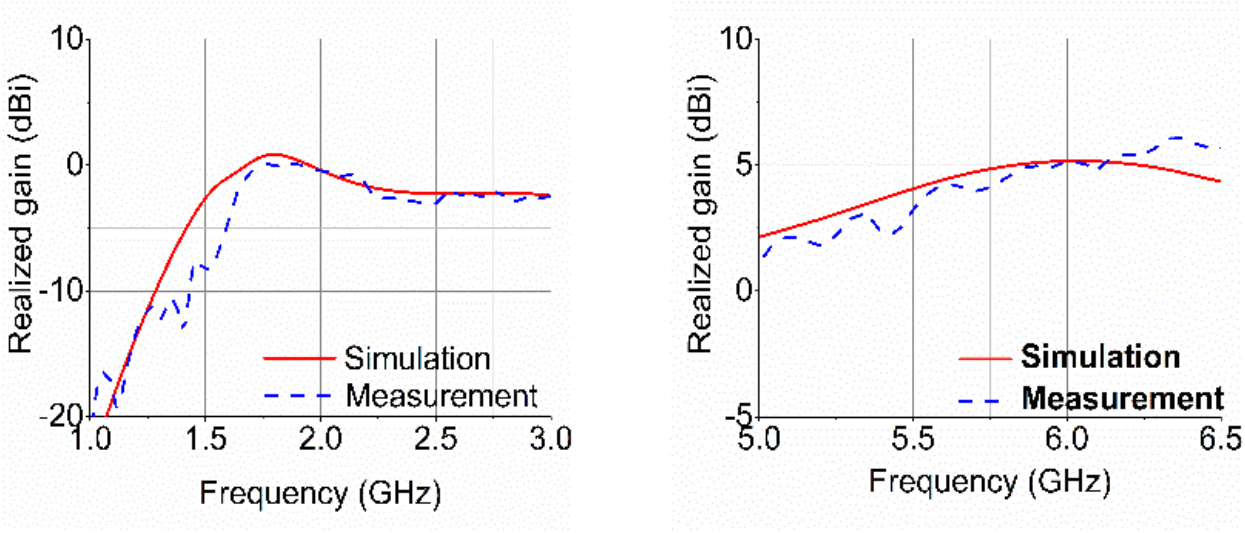

(a) (b)

Figure 3.9 Simulated and measured gain of the slot-ring antenna at (a) *L*-band operating state and (b) *C*-band operating state.

3.1.3 Switchable-Frequency Antenna Array Configuration

By extending the design of switchable-frequency antenna element to a larger array, the element spacing at both frequency bands can be designed to be less than $\lambda_0/2$, allowing for wide-angle beam scanning without grating lobes. The schematic view of a 3×3 *L*-band antenna array (6×6 *C*-band array) is shown in Figure 3.10. By controlling the DC bias voltage of PIN diode switches, the 3×3 *L*-band array can be reconfigured to a 6×6 *C*-band slot-ring antenna array. The center frequency in each band is 1.82/6.01 GHz, respectively, as illustrated in Figure 3.11. Figure 3.12 also demonstrates the simulated beamscanning up to ±60 degrees in the H plane for each operating state. No grating lobes are observed due to the fact that the antenna element spacing in both bands are less than $\lambda_0/2$. Table 3-2 compares the switchable-frequency slot-ring antenna presented in this section with other multi-band/switchable-band antenna arrays.

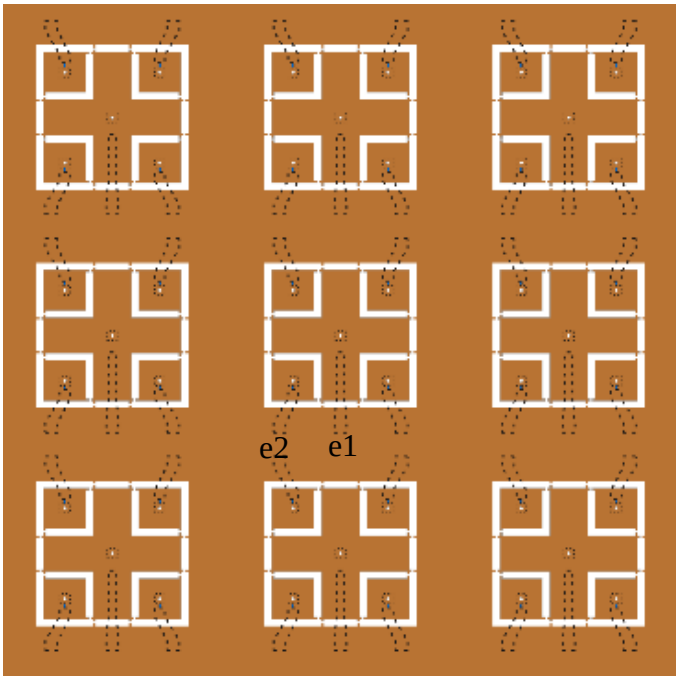

Figure 3.10. Switchable-frequency slot-ring antenna array.

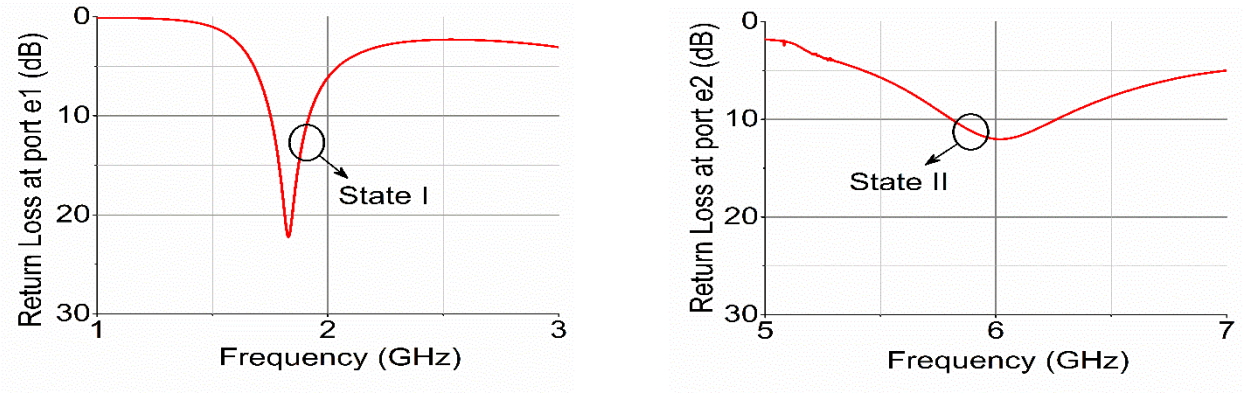

(a) (b)

Figure 3.11 Return losses of the switchable-frequency slot-ring antenna array at (a) *L* and (b) *C* bands.

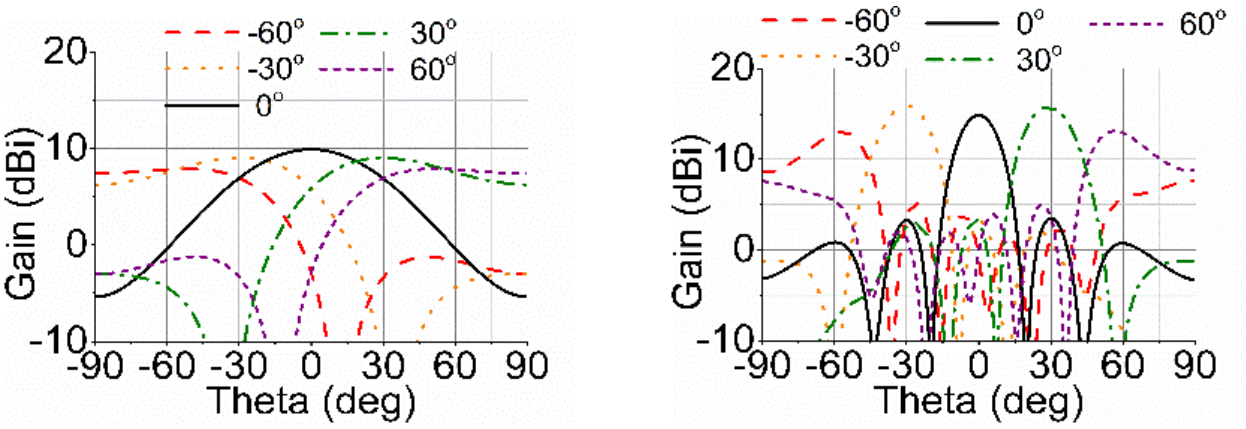

Figure 3.12. H-plane beam steering of the switchable-frequency slot-ring antenna array at (a) *L* and (b) *C* bands.

Table 3-2: Comparison of the switchable-frequency slot-ring antenna with other multi-band/switchable-band antenna arrays.

	f_1/f_2 (GHz)	**FBW_1/FBW_2**	**Feed**	**Polarization**	**Element spacing/λ_0**	**Comment**
[59]	1.2/9.6	6.0%/4.2%	Separate	Dual LP	0.67/0.67	Multi-layer radiators can cause problem when scanning
[13]	2.5/3.6	0.7%/0.6%	Same	LHCP/RHCP	0.57/0.81	Needs wide-band T/R module, large element spacing around f_2
[14]	1.0/2.0	5.0%/22.0%	Separate	Single LP	0.5/0.5	limited FBW at lower band
[18]	1.4/2.8	2.9%/5.3%	Same	Single LP	0.5/0.5	Needs wide-band T/R module for 25% of the elements
switchable-frequency antenna in Chapter 3	1.8/5.7	8.6%/11.5%	Separate	Single LP	<0.5/0.36	Wider FBW at lower band, suitable for beamscanning

3.2 Switchable-Band Frequency-Tunable Antenna Array

In this section, a tunable slot-ring antenna using varactors is presented. As shown in Figure 3.13, a tunable *L*-band slot-ring antenna contains four smaller *C*-band slot-ring antennas with PIN diode switches and varactors inside the slot-rings. The switching mechanism is similar to the one presented in section 3.1.1 for the switchable-frequency band antenna element. The varactors are able to continuously tune the center frequency of the slot-ring antenna within each respective frequency band. In this case, the antenna element is able to cover entire *L* and *C* bands in the *L*- and *C*-band operating states, respectively. A single-band antenna with continuous frequency tuning from 2.66 to 4.09 GHz with an instantaneous (FBW) of 1-3% and single polarization was experimentally verified in [60].

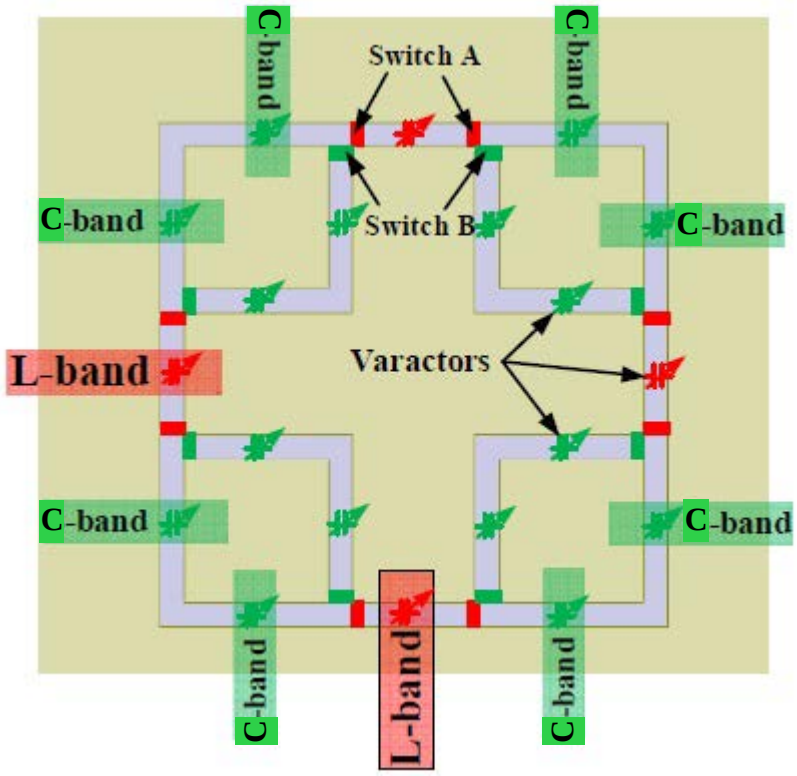

Figure 3.13 Switchable-band frequency tunable antenna element.

3.3 Conclusion

In the first section of this chapter, a novel reconfigurable slot-ring antenna element that can be used as an element of a large array has been demonstrated. This antenna is able to operate at two frequency bands, 1.76/5.71 GHz, based on the state of PIN diode switches, with FBW of 8.6%/11.5%, realized gain of 0.1/4.2 dBi, and radiation efficiency of 66.6%/80.7%, respectively. Then, a 3×3 *L*-band antenna array was formed; it is straightforward to maintain the element spacing around $\lambda_0/2$ at each operating frequency. In addition, due to the separate feeding for each band, only narrow-band T/R modules are needed. This particular multi-port antenna is designed to

exhibit a 3.2:1 operating frequency ratio; however, this ratio can be modified by simply varying the size of the smaller slot-ring antenna. Finally, to enhance more bandwidth in each operating state, varactor diodes were incorporated into the antenna element to tune the operating frequency of the antenna in each operating state.

CHAPTER 4: RECONFIGURABLE WIDEBAND ANTENNA ELEMENT OPERATING IN *S* AND *C* BANDS

Reconfigurable phased array antennas with wide bandwidth and dual polarization are highly desirable because they can be easily adopted for different applications to cope with changing system parameters. Bandwidth and power constraints are two important parameters in wireless networks [61]- [62]. As mentioned in the section 1.3, multi-band or switchable-band antenna arrays with separate feeding for each band allow for the use of high-performance narrow-band T/R modules instead of UWB T/R modules. In this case, the UWB frequency range is divided into two or more sections, therefore, T/R modules that cover the bandwidth of each operating state of the multi-band/switchable-band antenna can be used. In addition, due to their shared aperture design they can maintain the element spacing close to $\lambda_0/2$ at each band. In this chapter, first a reconfigurable slot-ring antenna with wide bandwidth in the *C*-band operating state is presented. Then, a reconfigurable antenna element with wide bandwidth in both *S*- and *C*-band operating states that shows double-sided radiation is demonstrated. Finally, a single-sided radiation antenna element with full coverage of *S* and *C* bands is studied.

4.1 Reconfigurable Double Slot-Ring Antenna Element for Bandwidth Enhancement in the *C*-Band Operating State

Planar slot antennas are good candidates for wireless systems due to their low profile, compact size, ease of fabrication, low cost and ease of integration with MMICs. But they are intrinsically narrow band. Several techniques have been reported in the literatures to increase the bandwidth of slot antenna such as wide-slot [63], fractal-shaped slot [64] and substrate removal

under the slot [65]. In [65], substrate removal under the slot can decrease the Q of the slot and enhance the bandwidth for cavity-backed slot antennas. A double-element annular slot-ring antenna for bandwidth enhancement was presented in [66]. In [67], a frequency-reconfigurable slot antenna using PIN diodes and with wide bandwidth was demonstrated. In this antenna, narrow slots are used to load the PIN diodes and wide slots are employed to increase the FBW.

The antenna element in this section is extended from the switchable-frequency band antenna element in section 3.1.1. With the four additional slots, a second resonance is formed from the inner slot-ring. Combined with the second harmonic frequency of the outer slot-ring, this antenna exhibits a relatively wide FBW at the lower band. The PIN diode switches are incorporated into the antenna element to switch between two frequency bands similar to the switchable-frequency band antenna element in section 3.1.1. It should be noted that this antenna configuration can be easily extended into antenna arrays, which is challenging for previously-reported reconfigurable slot antennas in [63]- [67].

4.1.1 Antenna Element Configuration

A microstrip-fed square slot-ring antenna as shown in Figure 3.1 is relatively narrow band. To increase the bandwidth of the antenna at lower band, a double slot-ring antenna shown in Figure 4.1(a) is developed. Four additional slots are added to the switchable-frequency band antenna element with several additional PIN diode switches. At the lower-band state, this antenna is composed of two concentric slot-rings, which are fed by a microstrip line with balanced stub

loading. The feed line is on the back side of the antenna as shown with dashed lines in Figure 4.1. The dimensions of the microstrip feed line and the distance between the two slot-rings can be designed so that the fundamental resonance of the inner slot-ring and the second harmonic of the outer slot-ring merge into a wider bandwidth. At the higher-band state, the switches can turn the antenna into a 2×2 slot-ring antenna array which is fed by microstrip lines. Figure 4.1(b) is the close-up view of one small slot-ring loaded with PIN diode switches. An equivalent circuit which was presented in section 2.2.2 is used to model PIN diode switches (DSM8100-000) in HFSS simulations. Biasing mechanism of the double slot-ring antenna is similar to the switchable-frequency antenna element provided in section 3.1.1.2.

4.1.2 Simulation Results

Figure 4.2 shows the simulation results for the antenna at lower band. The S_{11} is depicted in Figure 4.2(a). It is seen that the fundamental resonance of the outer ring occurs around 2 GHz and the second harmonic is around 4 GHz. The fundamental resonance of the inner ring is at 3.4 GHz which is close to the second harmonic of the outer ring. Therefore, a FBW of 28.2% is realized, compared to 11.4% for a switchable-frequency antenna element provided in section 3.1. In section 3.1.1, it was shown that the resonance frequency of the slot-ring is determined by its perimeter. Therefore, the inner ring has higher resonance frequency than the outer ring because it has shorter perimeter. At *C*-band state, the antenna element is a single slot-ring. Four slot-rings formed a 2×2 antenna array in this state. The antenna at higher band resonates at 7.74 GHz with a FBW of 9.1%, which is similar to that of the original switchable-frequency antenna element in

section 3.1. The radiation patterns in E and H planes in both operating states are shown in Figure 4.3. To simulate boresight radiation, the microstrip feed lines on the opposite sides of the array are fed with 180^{o} phase difference, i.e. ports 2-3 and ports 4-5 are 180^{o} out of phase. The antenna shows constant radiation patterns across the operating frequencies and radiates at boresight. The antenna gain vs. frequency in the *S* and *C* bands are shown in Figure 4.4(a) and (b), respectively.

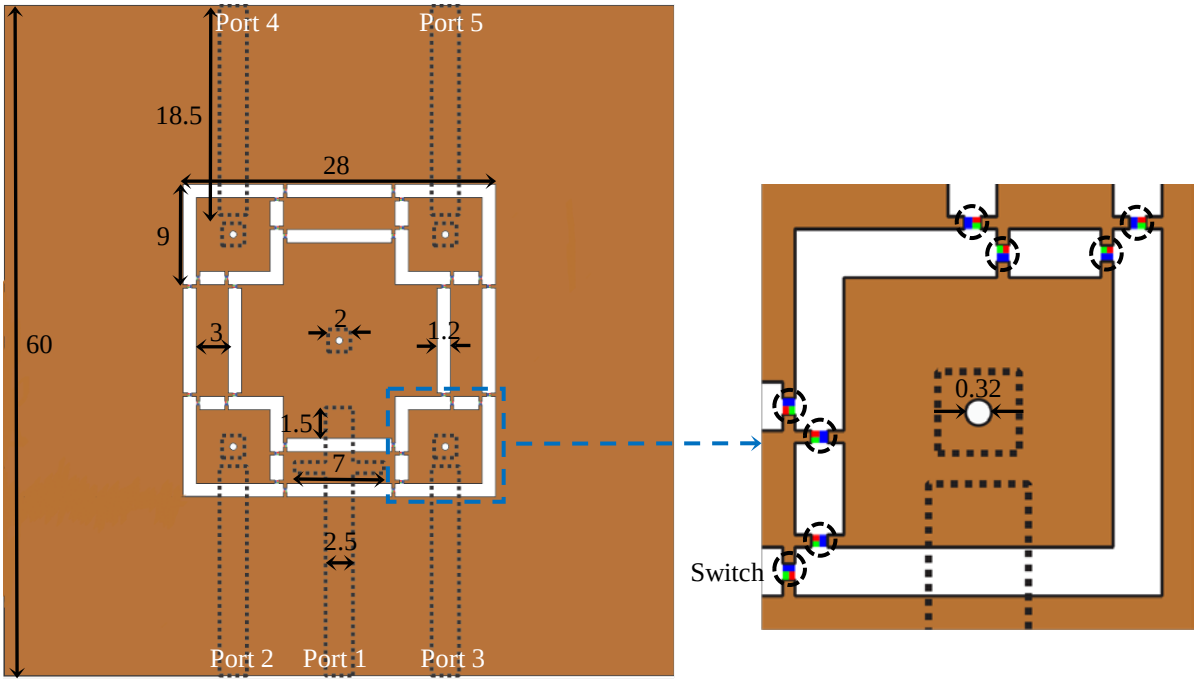

Figure 4.1 (a) Schematic view of the reconfigurable double slot-ring antenna element for bandwidth enhancement in the *C*-band operating state. (b) Close-up view of the *C*-band unit cell. (All dimensions are in mm).

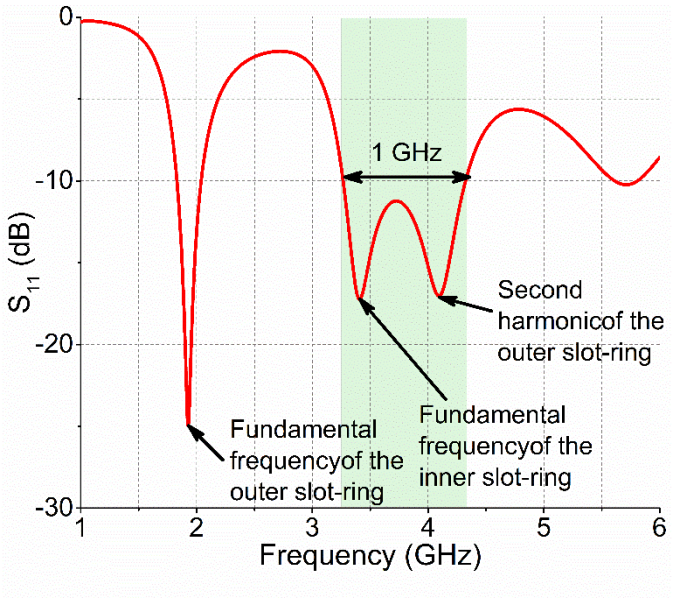

(a)

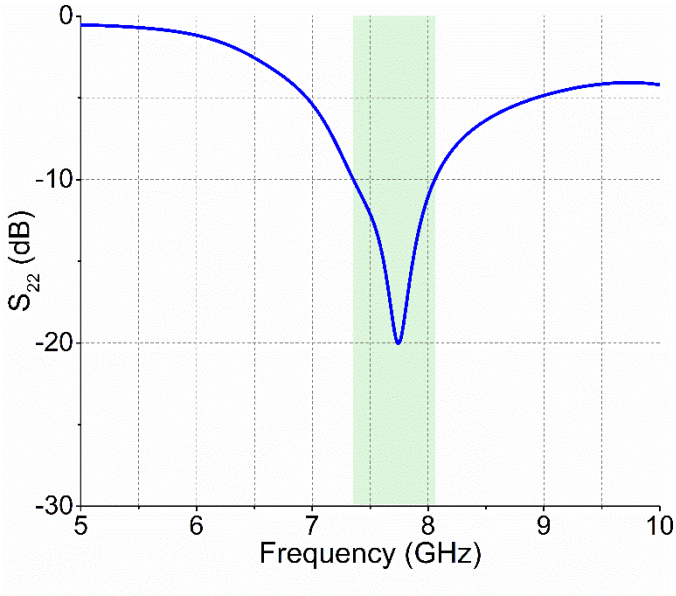

(b)

Figure 4.2. Simulated (a) S_{11} in the *S*-band operating state and (b) S_{22} in the *C*-band operating state for the reconfigurable double slot-ring antenna element.

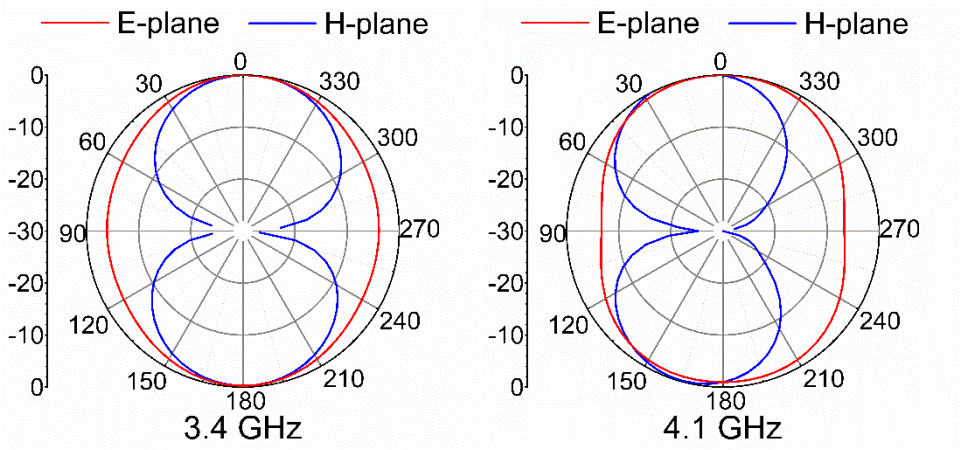

(a)

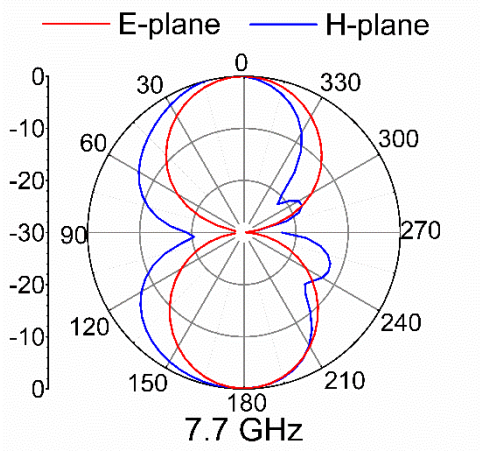

(b)

Figure 4.3. E- and H-plane radiation patterns of the reconfigurable double slot-ring antenna element at (a) *S*-band operating state at 3.4 and 4.1 GHz, and (b) *C*-band operating state at 7.7 GHz.

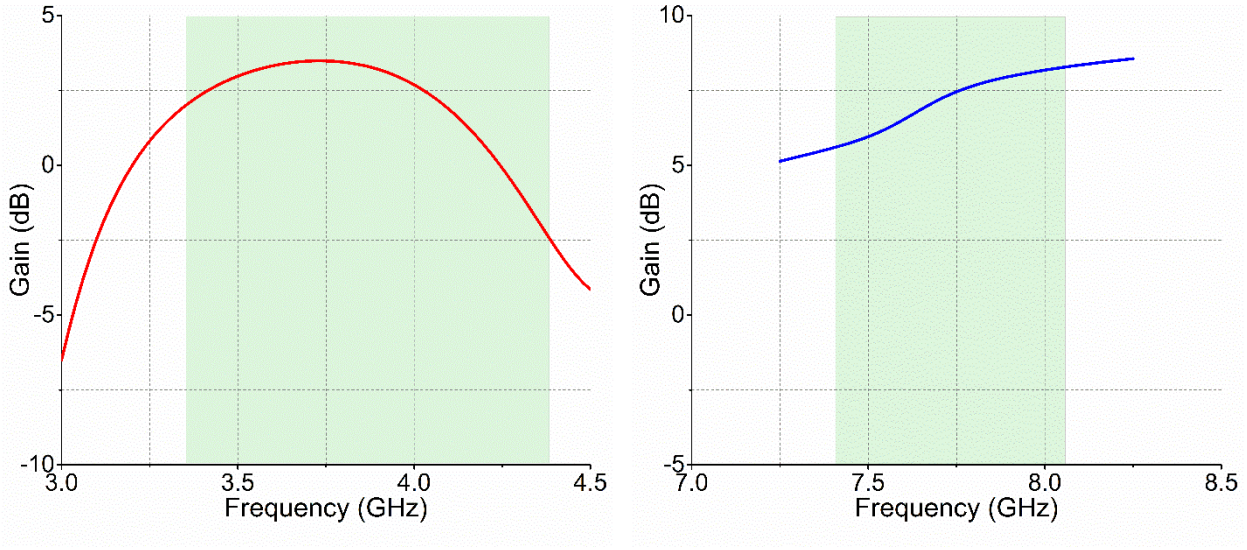

Figure 4.4. Simulated gain vs. frequency for the reconfigurable double slot-ring antenna element in the (a) *S*- and (b) *C*-band operating states.

Table 4-1 compares the original switchable-frequency antenna element in section 3.1 with the double slot-ring antenna in terms of center frequency, FBW, gain and radiation efficiency. At lower band, the FBW for the double slot-ring antenna is 2.5 times that of the original switchable-frequency antenna element, while the FBW at higher band is approximately the same for both antennas. The gain of the double slot-ring antenna is higher at lower band which is due to the fact that the resonant frequency of the double slot-ring antenna is higher with the same physical size. It is noted that the antenna efficiency is slightly reduced. It is mainly due to the fact that the number of switches is increased from 16 to 32 for the four additional slots. The resistance within each switch contributes to the reduction of antenna efficiency.

Table 4-1 Comparison between the single slot-ring antenna in Chapter 2 with the double slot-ring antenna.

		f_0 (GHz)	FBW (%)	Gain (dBi)	Radiation efficiency. (%)
S-band state	Single slot-ring antenna in Chapter 2	2.0	11.4	-1.5	93
	Double slot-ring antenna	3.4	28.2	1.8	80
C-band state	Single slot-ring antenna in Chapter 2	8.0	10.3	6.2	92
	Double slot-ring antenna	7.7	9.1	6.1	80

4.2 Reconfigurable Dual-Polarized Double-Sided Radiation Antenna Element with Wide Bandwidth in *S*- and *C*-band Operating States

Designing a wideband phased array antenna for beam scanning applications is challenging because the spacing between the antenna elements should be less than $\lambda_0/2$ to avoid grating lobes at wide scan angles. Typically, they are very costly to develop due to potentially large number of UWB T/R modules. If the element spacing at the lower end of the frequency band is maintained at $\lambda_0/2$, then the spacing at the higher end of the frequency band is unavoidably large. If the element spacing at the higher end of the frequency band is close to $\lambda_0/2$, then the spacing at the lower end of the frequency band is much smaller than $\lambda_0/2$ resulting in an unnecessary-large number of T/R modules.

In order to develop a phased array antenna with wide bandwidth and dual polarization, a reconfigurable dual-polarized fractal-shaped slot-ring antenna element covering *S* or *C* band in two operating states is introduced. The aperture of an *S*-band antenna can be reconfigured to a 2×2 *C*-band antenna array by turning on eight PIN diode switches. The FBW of this antenna/array in the *S*-/*C*-band state is 69.1%/58.3%, respectively. The element spacing in the 2×2 array is less than $\lambda_0/2$ over the entire *C* band. This antenna/array can be used as a unit cell of a larger phased array which will be discussed in Chapter 5.

4.2.1 Antenna Element Configuration and Design Procedure

The schematic view of the reconfigurable dual-polarized wideband antenna/array is shown in Figure 4.5. The aperture of an *S*-band fractal-shaped slot-ring can be reconfigured to a 2×2 *C*-band fractal-shaped slot-ring antenna array by turning on eight PIN diode switches (DSM8100-000, 0201 package). A *C*-band slot-ring array element with two PIN diode switches is illustrated in Figure 4.5(c). This design is developed from a switchable-frequency single-polarized slot-ring antenna element provided in section 3.1.1. It was mentioned in section 3.1.1 that the resonance frequency of a square slot-ring can be obtained from (3-1). As shown in Figure 4.5(a), $L_{S\text{-band}}/L_{C\text{-band}}$ is the lateral length of the square slot-ring in the *S*/*C* band. $L=\lambda_g/4$ is much smaller than $\lambda_0/2$, therefore it is easy to design the antenna spacing to be less than $\lambda_0/2$. To achieve wideband performance, modified Koch fractal geometry is incorporated into the slot-ring antenna as illustrated in Figure 4.5(b). The positions of eight PIN diode switches are shown with dashed circles in this figure and the effects these switches have on the antenna performance are discussed

in section 2.2.4. A metal wire is placed at the center of the antenna where the electric field is minimum to provide a DC bias voltage for all the PIN diodes. A 100-Ω resistor is connected in series with this wire to limit the DC current. When the switches are open (reverse-biased), the antenna is excited by port 1 (horizontal polarization) or port 2 (vertical polarization) and operates in the *S*-band state. By turning on the PIN diode switches (forward-biased), a 2×2 slot-ring antenna array is formed to operate in the *C*-band state. Ports 3 to 6 (horizontal polarization) or ports 7 to 10 (vertical polarization) are excited in this state. In the *S*-band state, the switches are OFF, so they do not consume DC power. In the *C*-band state, the total DC power consumption is 4.8 mW in which 1.6 mW is dissipated in the 100-Ω resistor and 3.2 mW is consumed by the eight PIN diodes in the ON state. Microstrip lines are used to feed this antenna/array. The width of the microstrip lines is gradually widened when they are extended to the edge of the antenna in order to achieve 50-Ω characteristic impedance. By optimizing the dimensions of the fractal geometries using HFSS, this antenna array is able to cover 1.8-3.7 GHz and 4.5-8.2 GHz in the *S*- and *C*-band operating states, respectively. The final geometrical parameters of the antenna/array with good broadband performance are summarized in Table 4-2.

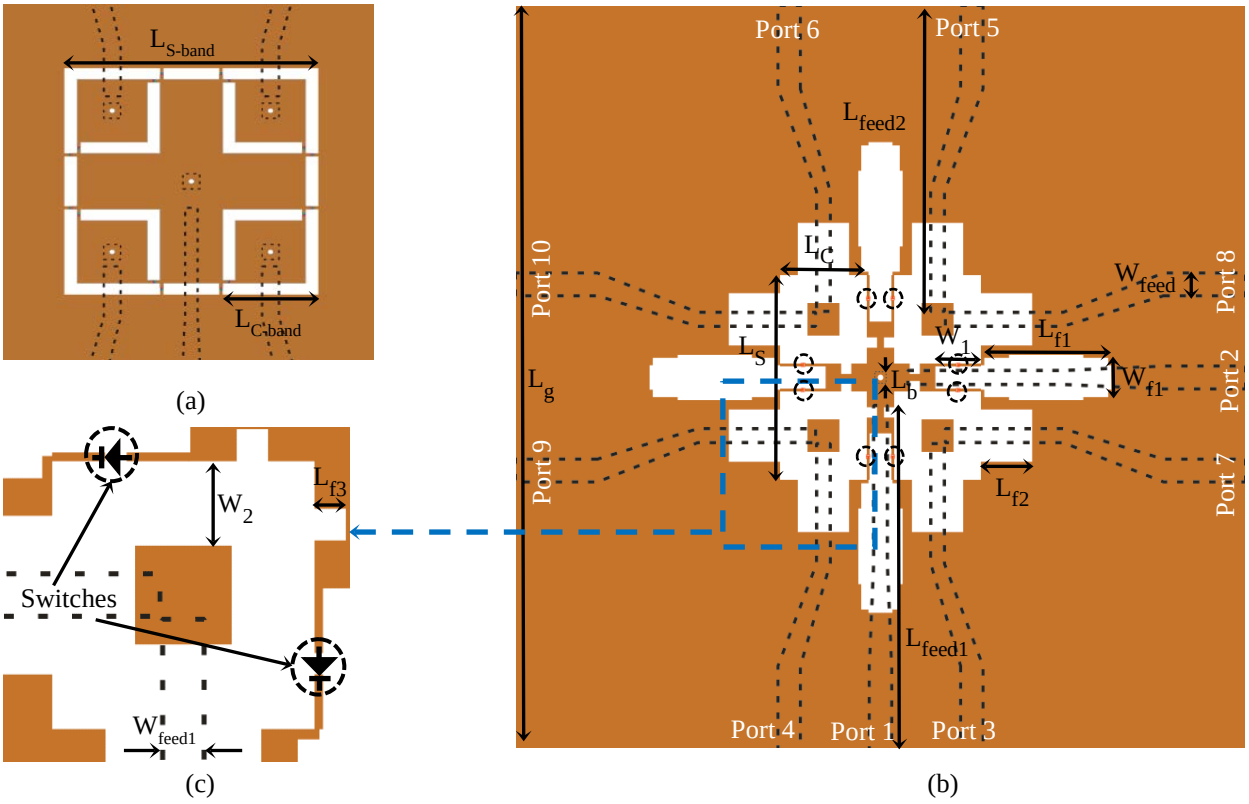

Figure 4.5. (a) Configuration of the switchable-frequency single-polarized slot-ring antenna [19]. (b) Configuration of the reconfigurable dual-polarized wideband slot-ring antenna/array. (c) Close-up view of the *C*-band unit cell.

Table 4-2 Geometrical parameters of the reconfigurable dual-polarized slot-ring antenna element with wide bandwidth in both operating states.

Symbol	Quantity (mm)	Symbol	Quantity (mm)
L_g	80	L_{f2}	5.6
L_S	22	L_{f3}	1.1
L_C	9.5	L_{feed1}	37

Symbol	Quantity (mm)	Symbol	Quantity (mm)
W_1	5	L_{feed2}	32.9
W_2	3	W_{feed}	2.5
L_{f1}	14	W_{feed1}	1.5
W_{f1}	4.2	L_b	1.2

In Figure 4.5(b), the *S*-band slot-ring with the lateral length of L_S provides the longest resonant path to generate a fundamental resonance. The fractals with the length of L_{f1} and L_{f2} provide other resonances which can be merged with the fundamental resonance to significantly increase the antenna bandwidth in the *S*-band operating state. Similarly, in the *C*-band state, the fundamental resonance is obtained from the *C*-band slot-rings with the lateral length of L_C, while the fractals with the length of L_{f2} and L_{f3} provide additional resonances to widen the bandwidth in the *C*-band operating state. In this state, the fractals with the length of L_{f1} act as parasitic elements.

4.2.1.1 Generation of Fractal Shapes

The generation of the fractal shapes for only one frequency band, e.g. *S* band, is studied here. Figure 4.6 shows the S_{11} for the slot-ring antenna with different iteration orders (IO = 0, 1, and 2) and iteration factor of 0.3. As the IO increases, the average electrical length of the slot-ring also increases, lowering the resonant frequency of the slot-ring antenna in the *S*-band operating state. Furthermore, with the incorporation of fractal geometries, the number of resonant bands increases, which in turn significantly increases the antenna bandwidth. IOs larger than 2 only slightly change the antenna bandwidth at the expense of complexity.

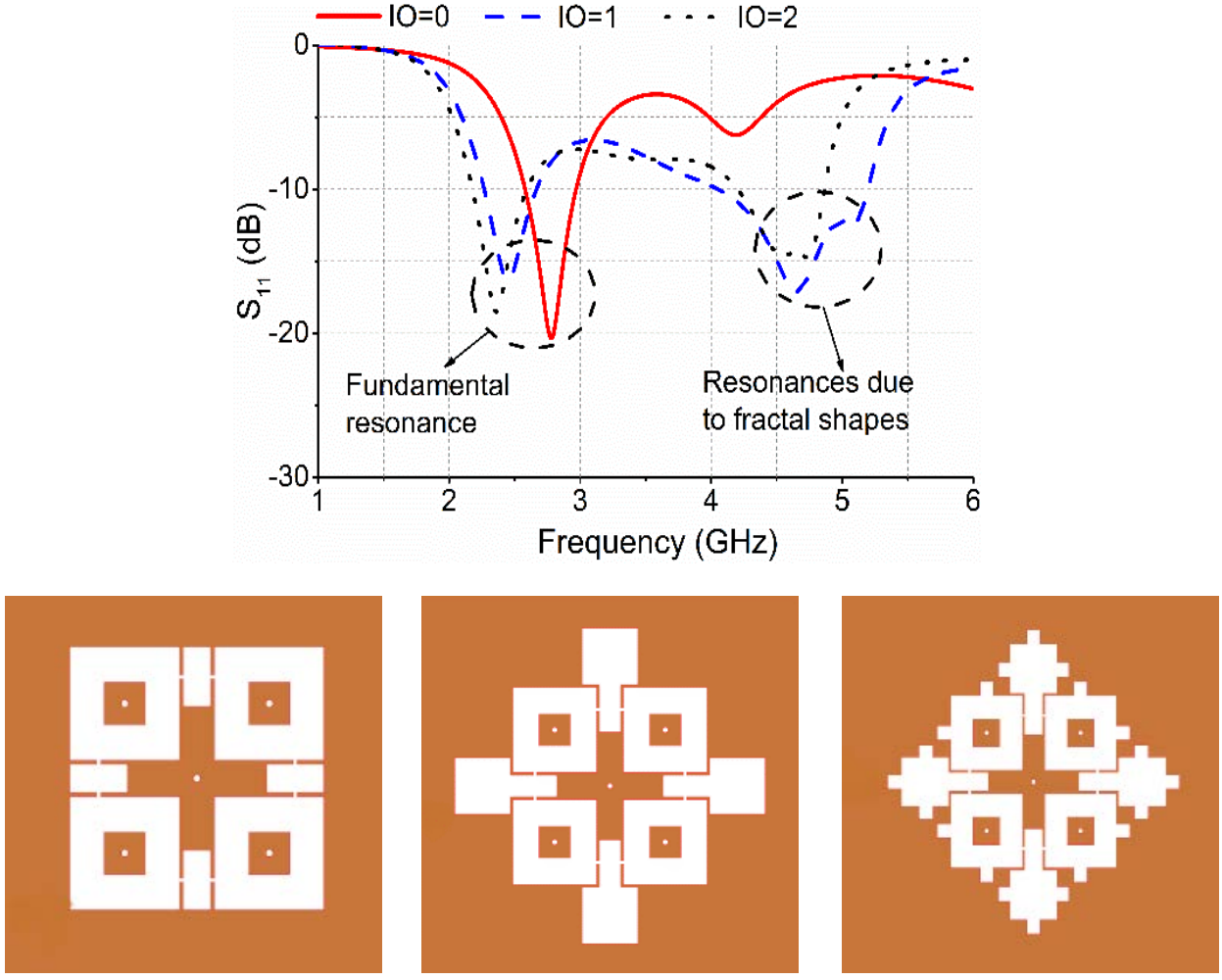

Figure 4.6. S_{11} of the fractal-shaped slot-ring antenna in the *S*-band operating state with different iteration orders (IO).

4.2.1.2 Parametric Study of Fractal Shapes

Figure 4.7(a) and (b) illustrate the variation of S_{11} and S_{44} with L_{f1} in the *S*- and *C*-band operating states, respectively. From Figure 4.7(a), it is seen that for longer L_{f1}, the effective length

of the fractal increases which results in lower resonant frequency for the fractal shapes with the length of L_{f1}. There needs to be a certain space between the fundamental resonance and resonances due to the fractal shapes to significantly improve bandwidth. Too much space between resonances, for example shorter L_{f1}, or closely spaced resonances, for example longer L_{f1}, results in poor matching. S_{11} and S_{44} for different values of L_{f2} are plotted in Figure 4.8(a) and (b), respectively. From Figure 4.7 and Figure 4.8, it is observed that L_{f1} mostly affects the bandwidth in the *S*-band state while L_{f2} is responsible for tuning the bandwidth in the *C*-band state. Furthermore, changing the dimensions of the fractal shapes does not affect the fundamental resonance which is dominated by the perimeter of the slot-ring. The bandwidth is enhanced because one resonant mode in the vicinity of the fundamental mode is excited by the fractal geometries. Guidelines are provided here for the design of a slot-ring antenna/array with wide FBW at two adjacent frequency bands:

1) Calculate the dimensions of the large slot-ring (L_S) as well as four small slot-rings (L_C) to operate in the desired frequency bands, based on (3-1).

2) Find the optimum dimensions of the fractal shapes to obtain the desired bandwidth in the low-frequency operating state regardless of the response in the higher-frequency operating state.

3) Adjust the slot width and dimensions of the fractal geometries to achieve the desired bandwidth in the high-frequency operating state regardless of the antenna response in the lower-band state.

4) Find an optimum point between the dimensions obtained from steps 2 and 3.

5) Adjust the dimensions of the feed network for wideband operation. Final dimensions should result in an antenna/array with wide bandwidth in both operating states.

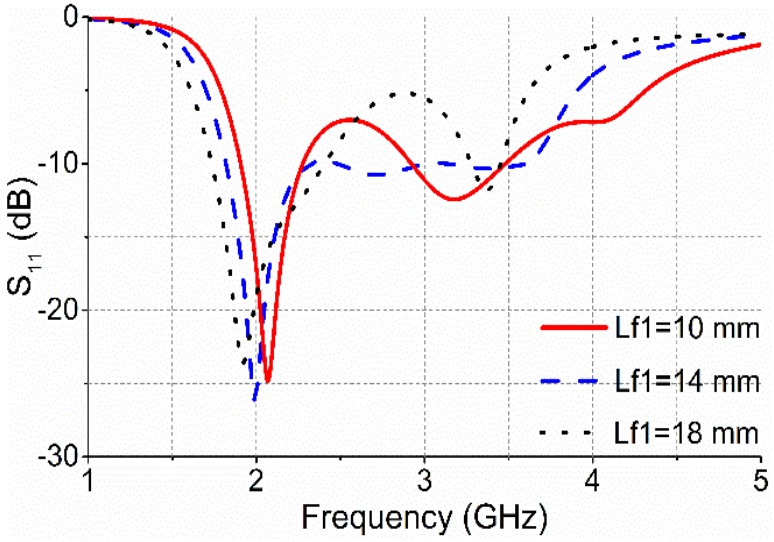

(a)

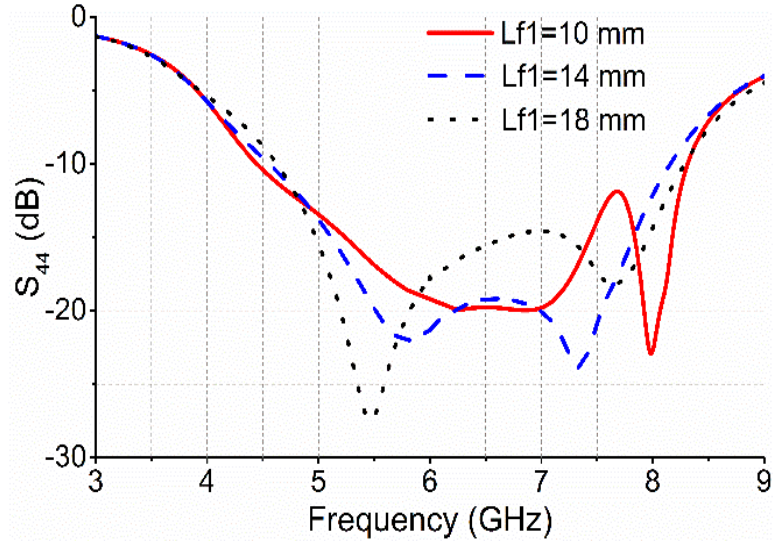

(b)

Figure 4.7. Effects of L_{f1} on the (a) S_{11} at *S*-band state and (b) S_{44} at *C*-band state.

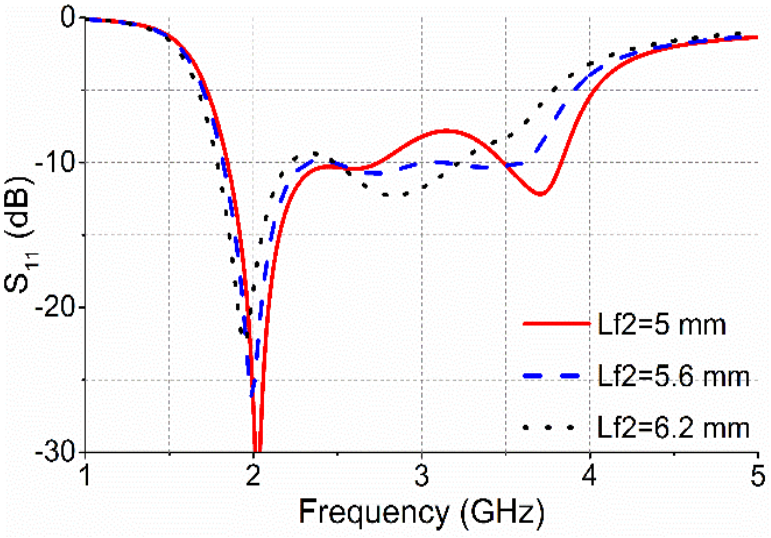

(a)

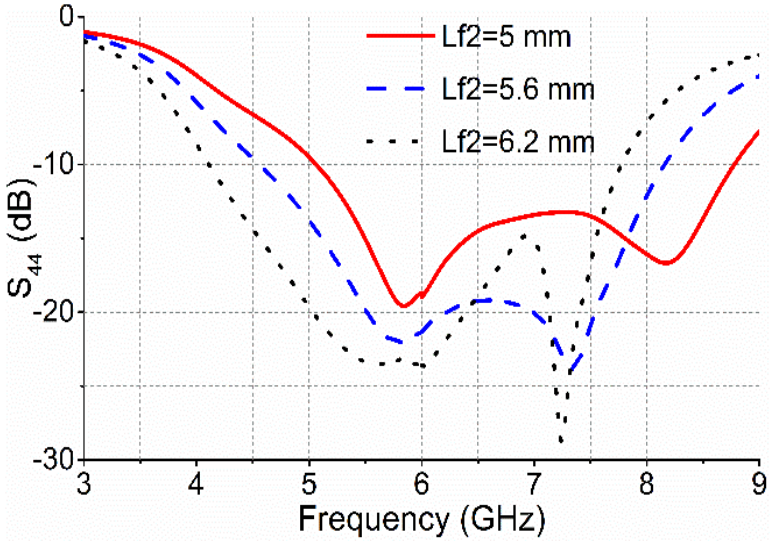

(b)

Figure 4.8. Effects of L_{f2} on the (a) S_{11} at *S*-band state and (b) S_{44} at *C*-band state.

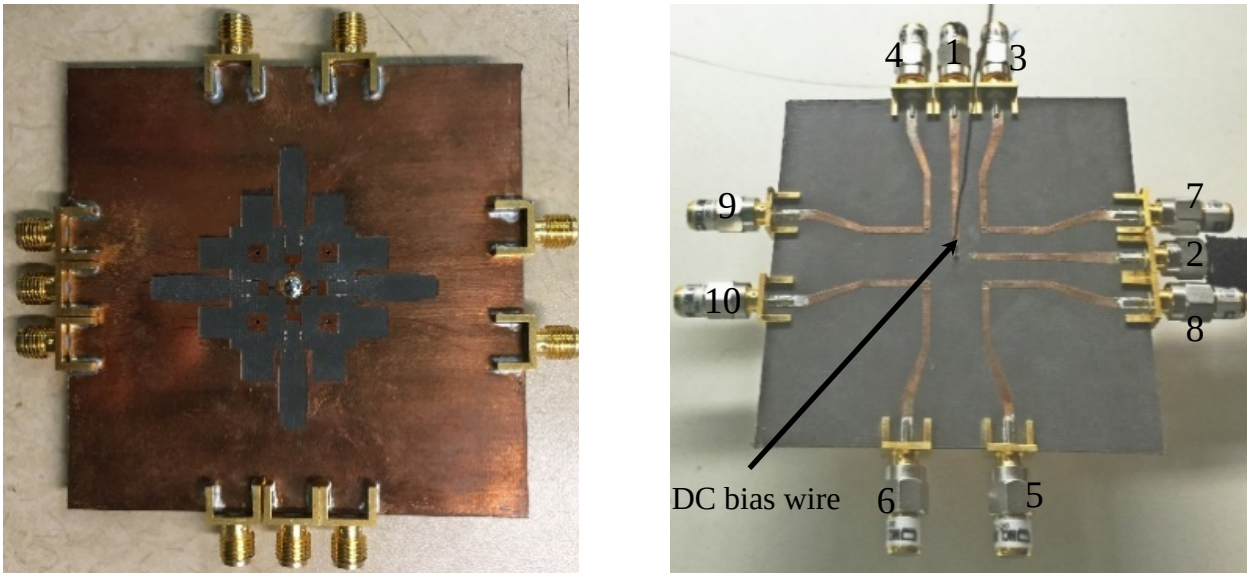

(a) (b)

Figure 4.9 (a) Top and (b) bottom view of the reconfigurable dual-polarized wideband slot-ring antenna/array (port numbers are shown in the right figure).

4.2.2 Simulation and Measurement Results

Figure 4.9(a) and (b) show the fabricated antenna from top and bottom view, respectively. Eight PIN diode switches are mounted on the radiating aperture on the top side of the antenna/array while the feed lines are on the bottom side. This antenna is fabricated on a Rogers RT/Duroid 5880 substrate (ε_r=2.2 and tanδ=0.0009) with a thickness of 0.79 mm. Conductive silver paint (SPI 05002-AB from Structure Probe, Inc.) is used to make the electrical connection between the switch and the antenna. The microstrip feed lines are slightly bent to provide enough space for the SMA

connectors. The port naming convention shown in Figure 4.9 is continued in further discussions of S-parameters and mutual coupling between the antenna ports.

4.2.2.1 S-Parameters

The simulated and measured S_{11} and S_{44} for the antenna/array in the *S*- and *C*-band operating states are illustrated in Figure 4.10 and Figure 4.11, respectively. In these figures, the reflection coefficients when the switches are ON or OFF are illustrated with solid or dashed lines, respectively. In the *S*-band state, the antenna shows 69.1% FBW as illustrated in Figure 4.10 when the switches are OFF. When the switches are ON, most of the energy is reflected back in the *S*-band state, i.e. S_{11} is higher than -1.5 dB. The measured S_{22} is consistent with Figure 4.10 due to the symmetric design of the antenna/array. In the *C*-band state, 58.3% FBW is obtained when the switches are ON. It is observed in Figure 4.11 that the antenna is significantly mismatched when the switches are turned off. However, it is noted that this mismatch is not as good as that in the *S*-band state. Figure 4.12(a) shows the measured reflection coefficients of all eight ports of the *C*-band array (four ports in the horizontal polarization and four ports in the vertical polarization) when the switches are ON or OFF. Consistency among the different ports and symmetry between V and H polarizations can be observed in Figure 4.12(a).

In an antenna array, the active S-parameters which consider all the mutual coupling between antenna elements are more important. Given an N-port device, let a_k denote the complex

excitation for the k_{th} port. Also let S denote the computed scattering matrix. If $a_m \neq 0$, define active-S_m, m = 1, 2… N by (4-1)

$$active - S_m \equiv \sum_{n=1}^{N} S_{mn} \frac{a_n}{a_m} \qquad m = 1, \ldots, N \tag{4-1}$$

If only one port is excited, $a_m = 0$ except for m=1, therefore according to (4-1), active-S_1 = S_{11}. For the 2×2 array in the *C*-band state, the active S-parameter for the maximum radiation at boresight is given by:

$$\text{active} - S_4 = S_{44} + S_{43}\frac{a_3}{a_4} + S_{45}\frac{a_5}{a_4} + S_{46}\frac{a_6}{a_4} = S_{44} + S_{43} - S_{45} - S_{46} \tag{4-2}$$

Figure 4.12(b) compares the S_{44} with the active-S_4 for the antenna/array in the *C*-band operating state. The antenna covers 4.5 to 8.2 GHz in the *C*-band state with the reflection coefficient less than -10 dB from the active-S_4.

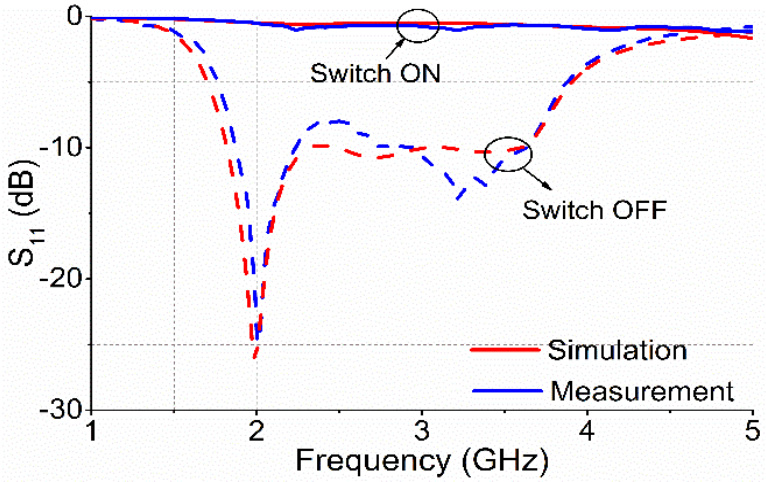

Figure 4.10. Simulated and measured S_{11} when the switches are ON (solid lines) or OFF (dash lines).

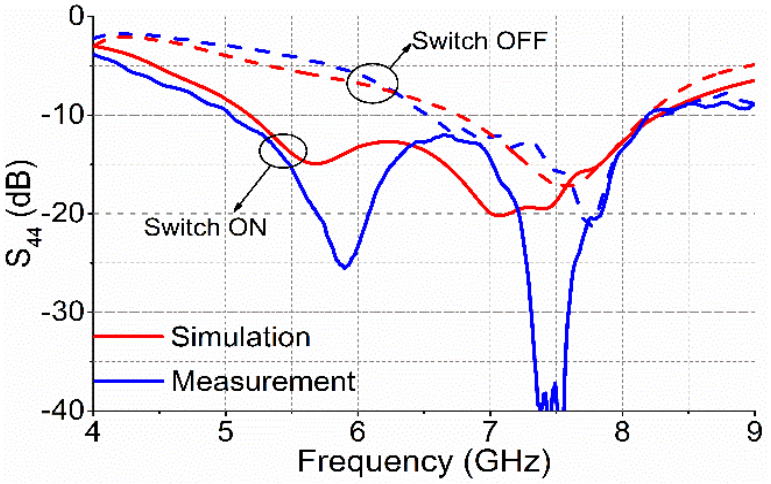

Figure 4.11. Simulated and measured S_{44} when the switches are ON (solid lines) or OFF (dash lines).

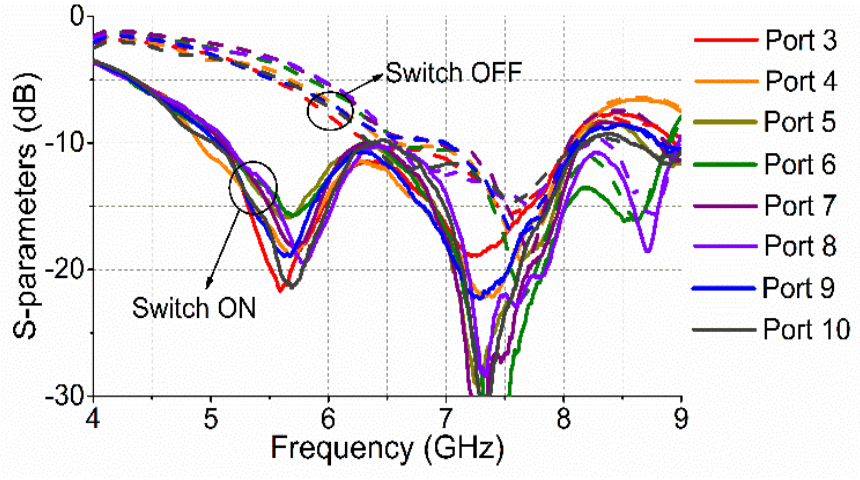

(a)

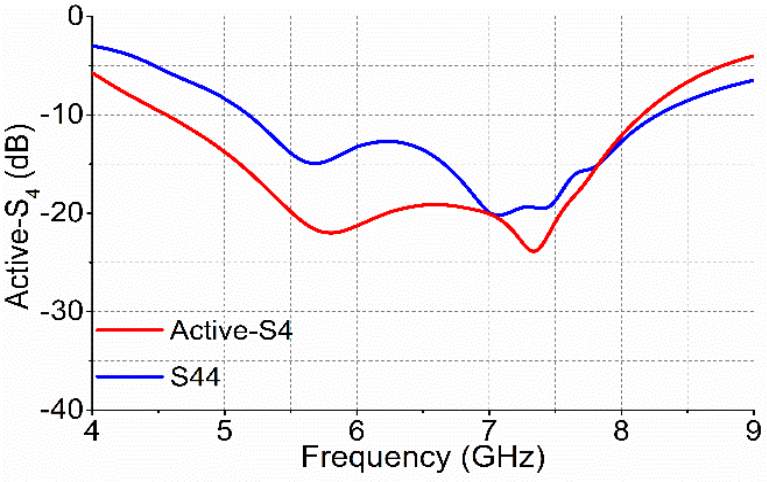

(b)

Figure 4.12. (a) Multi-color S-parameters for ports 3 to 8 when the switches are ON (solid lines) or OFF (dash lines). (b) Active-S_4 and S_{44} of the 2×2 *C*-band array in the *C*-band operating state.

Isolation between the 10 ports of the antena/array is another important parameter; the simulated and measured S_{12}, S_{13}, S_{34} and S_{37} are depicted in Figure 4.13(a), (b), (c), and (d), respectively. The mutual coupling between ports 1 and 2 (S_{12}) and ports 1 and 3 (S_{13}) in the *S* band

is lower than -8 dB and -18 dB, respectively. S_{13} and S_{34} are lower than -15 dB in the *C*-band state. The worst-case isolation is between ports 3 and 7 due to the closely-spaced feed lines of these two ports. S_{37} is less than -4 dB in the *C*-band operating state. Isolation between all other ports are better than 15 dB.

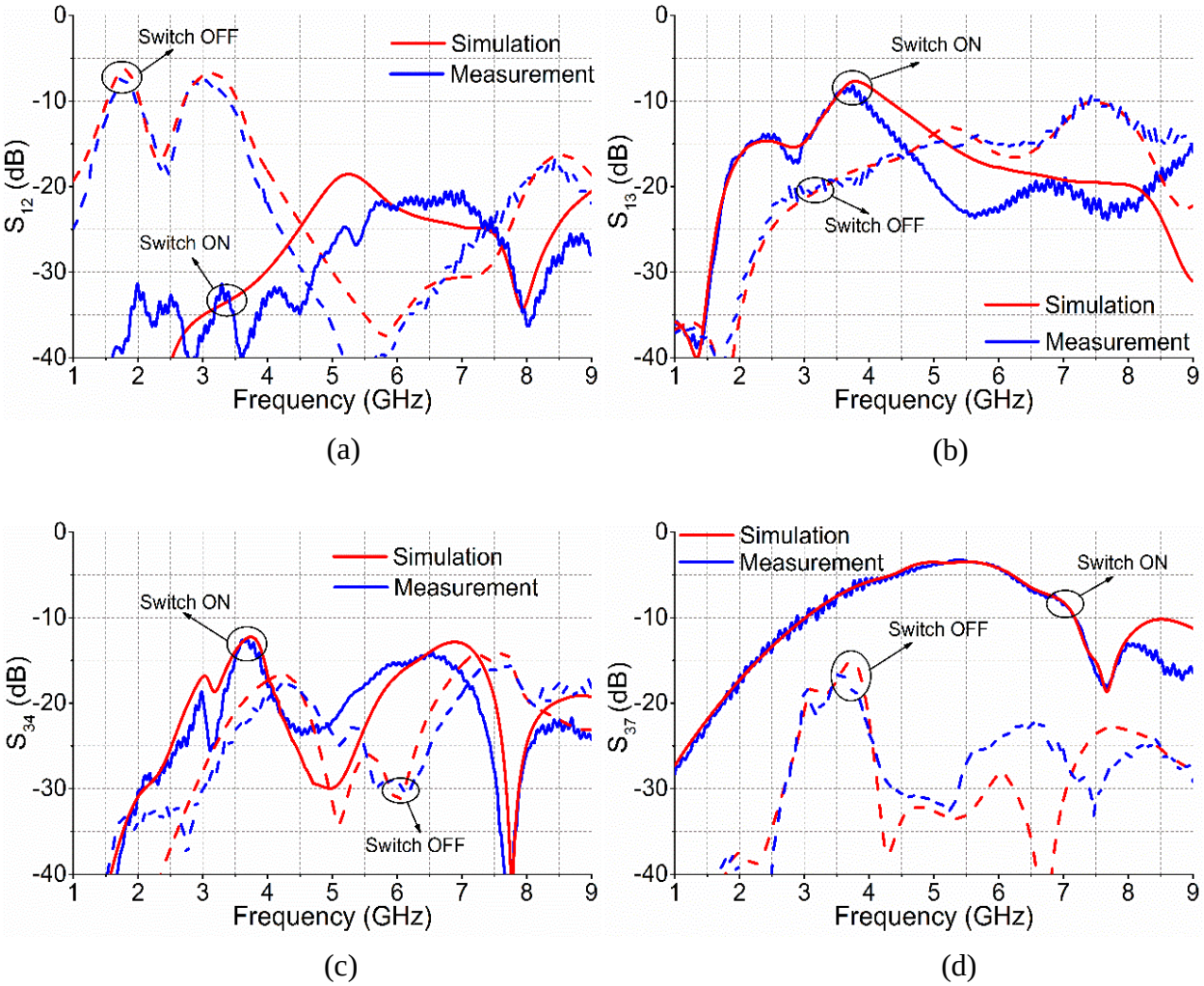

Figure 4.13. Simulated and measured mutual coupling between different ports. (a) S_{12}, (b) S_{13}, (c) S_{34} and (d) S_{37} when the switches are ON (solid lines) or OFF (dash lines).

4.2.2.2 Radiation Pattern

The co-pol. and X-pol. radiation patterns in the E-plane (y-z plane) and H-plane (x-z plane) are measured in an anechoic chamber at several frequency points in both operating states. Figure 4.14 shows the E-plane measurement setup of the 2×2 *C*-band array. In the *C*-band state, in order to achieve the maximum radiation at boresight, a phase difference of 180^{o} is required between the feeding ports on the opposite sides of the array, i.e. ports 3-4 and ports 5-6 are 180^{o} out of phase in the horizontal polarization. Similarly, ports 7-8 and ports 9-10 are 180^{o} out of phase in the vertical polarization. A two-way power divider (RFLT2W2G08G from RF-lambda) with two 180^{o} hybrids (RFHB02G08GPI from RF-lambda) are used to provide the required phase differences for the *C*-band array. Figure 4.15(a) and (b) show the simulated and measured radiation patterns in the *S*-band state at 2 and 3.5 GHz, respectively. In the *C*-band state, the radiation patterns are shown at 5 and 8 GHz in Figure 4.16(a) and (b), respectively; at each frequency the radiation patterns are normalized with respect to the maximum values and good agreement between the measured and simulated patterns is observed. For the *C*-band array, there are small dips in the E-plane at boresight due to the finite ground plane size [68]. In [69], the pattern distortion due to the edge diffractions for a finite ground plane is compared to an infinite ground plane. The pattern distortion can be avoided by using an infinite ground plane, for example a large antenna array. The measured X-pol. is as low as -12 and -15 dB in the *S*- and *C*-band operating states, respectively. As illustrated in Figure 4.9(b), the biasing wire in the middle of the antenna is perpendicular to the antenna to minimize the X-pol. level. Simulated X-pol. at 5 GHz is less than -30 dB, so it is not shown in Figure 4.16(b). Small discrepancies between the simulated and

measured X-pol. patterns are due to the effects of the semi-rigid coaxial cable and 50-ohm loads which were not included in the simulations. The induced currents on these components radiate and distort the radiation pattern of the antenna/array. Since the X-pol. component generated by the antenna is much weaker than its co-pol. component, the distortions affect the shape of the X-pol. pattern much more than the co-pol. Well-behaved linear polarization and broadside radiation patterns are observed in Figure 4.15 and Figure 4.16 over the entire *S* and *C* bands.

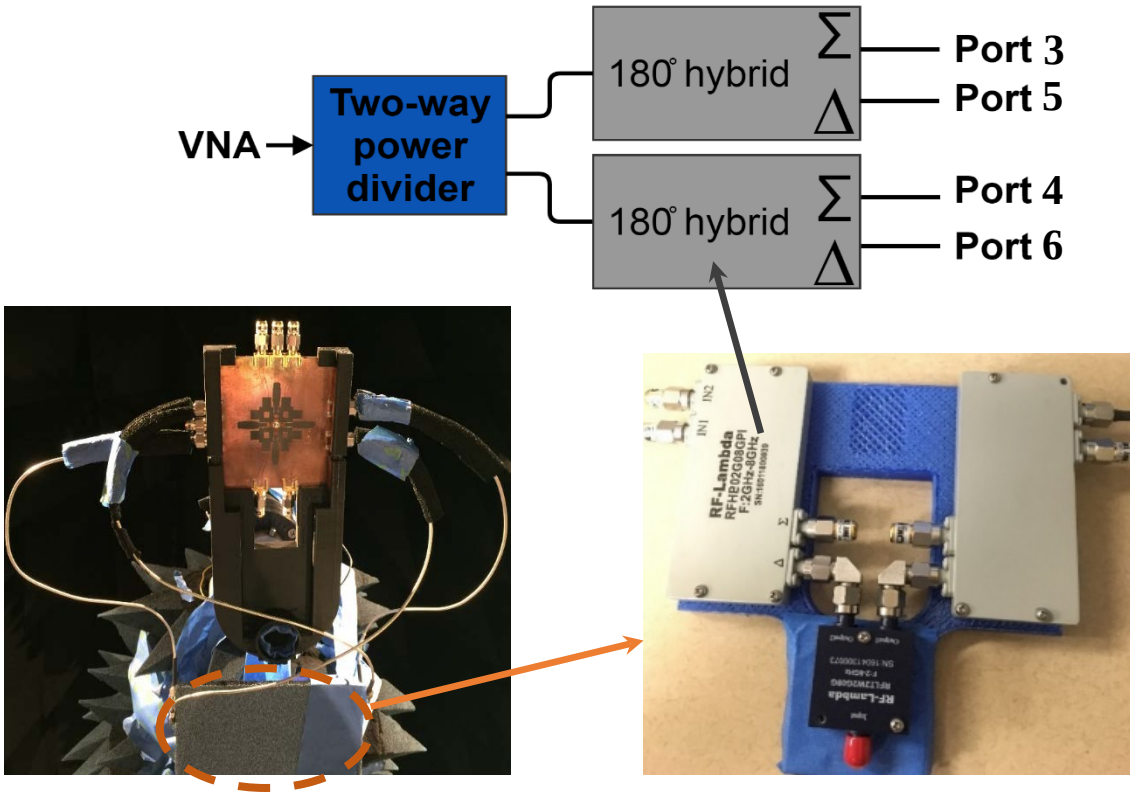

Figure 4.14. E-plane radiation pattern measurement setup of the 2×2 *C*-band array.

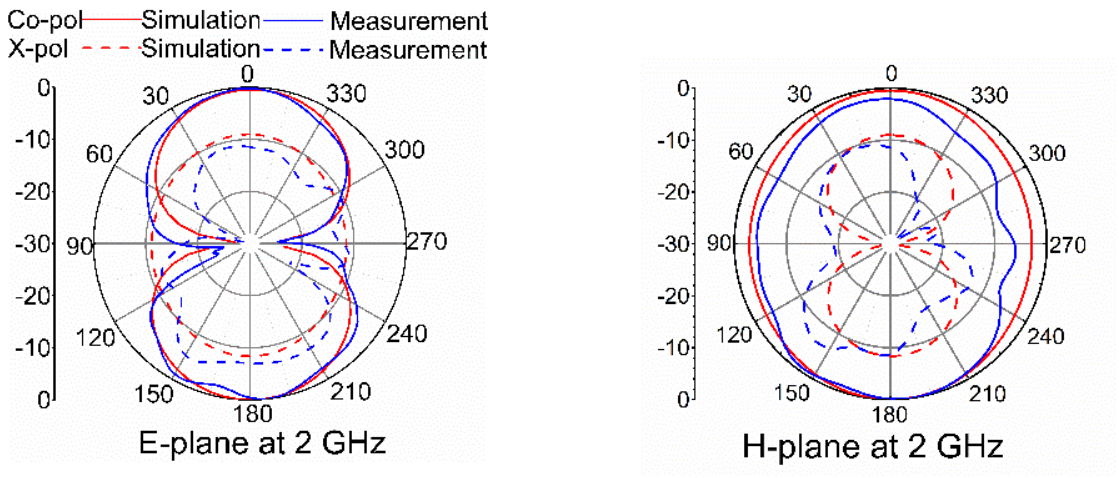

(a)

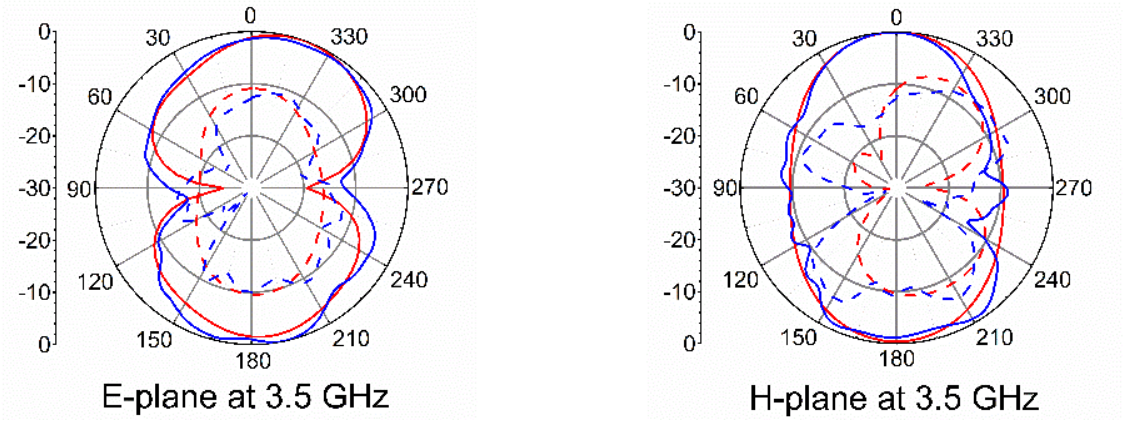

(b)

Figure 4.15. Co- and X-pol. radiation patterns of the reconfigurable dual-polarized double-sided radiation wideband antenna/array at (a) *S*-band operating state at 2 and 3.5 GHz.

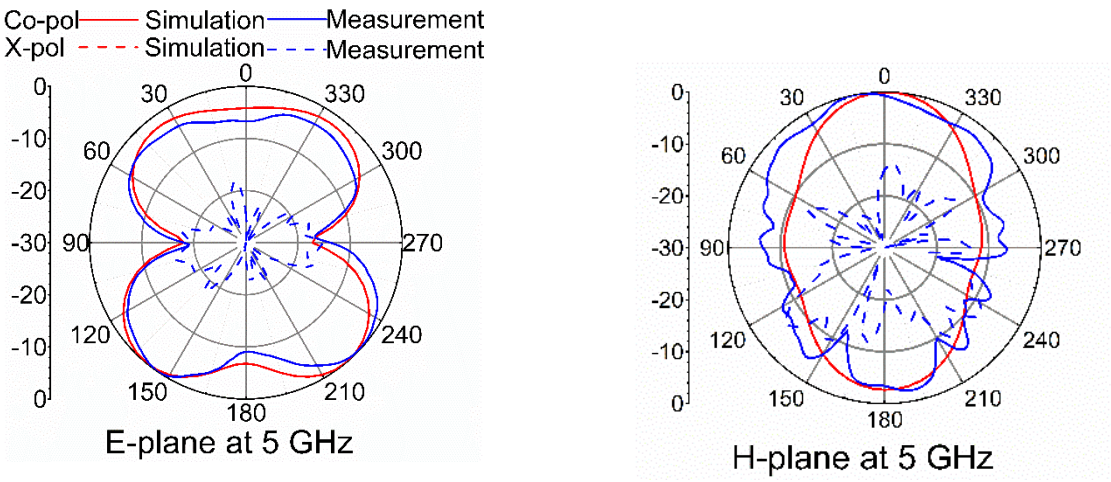

(a)

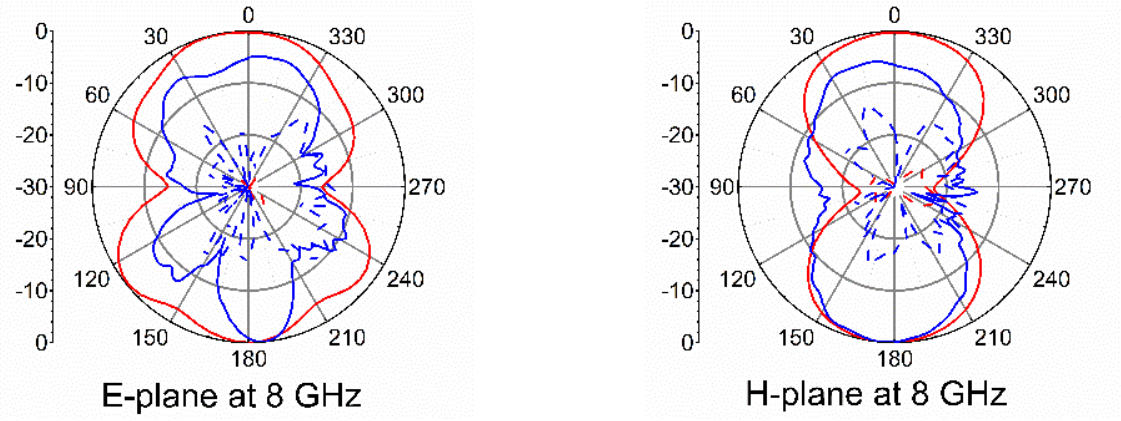

(b)

Figure 4.16. Co- and X-pol. radiation patterns of the reconfigurable dual-polarized double-sided radiation wideband antenna/array at *C*-band operating state at 5 and 8 GHz.

4.2.2.3 Realized Gain

Figure 4.17(a) and (b) demonstrate the simulated and measured realized gains versus frequency at *S*- and *C*-band operating states, respectively. It should be noted that the mismatch loss

and port isolations are considered in the realized gain which is stated as loss factor in (4-3). In fact, loss factor is the mismatch loss from the active ports plus the mutual coupling from the active ports to the non-active ports.

$$Realized\ gain = Absolute\ gain\ \times Loss\ factor \tag{4-3}$$

From Figure 4.17(a), it is seen that the realized gain is very low for frequencies below 1.8 GHz and above 3.6 GHz because S_{11} is very close to 0 dB at those frequencies. In the *C*-band operating state, the maximum realized gain of the 2×2 array is 3.4 dBi as shown in Figure 4.17(b). The element spacing for the *C*-band array is $0.19\lambda_0/0.33\lambda_0$ at 4.5/8.0 GHz and as a result the gain enhancement of the 2×2 array is approximately 1.0/3.0 dB, respectively. Moreover, as can be seen in Figure 4.16, the backside radiation is stronger in the *C*-band state, while the gain was measured at the front side. The dip in the realized gain around 5.5 GHz in Figure 4.17(b) is due to the large size of the antenna ground (L_g) [68] and also relatively poor isolation between ports 3 and 7 around 5.5 GHz (Figure 4.13(d)).

The radiation efficiency of an antenna (η) is equal to the absolute gain divided by the directivity while the total efficiency is the realized gain divided by the directivity. As shown in Figure 4.17, the radiation efficiency of the antenna/array in the *S*- and *C*-band states is better than 67% and 88%, respectively. Note that, in the *S*-band state, all eight PIN diodes are included in the electric current path but only two PIN diodes are involved in forming an antenna element in the *C*-band state. Therefore, antenna radiation efficiency in the *C*-band is higher than that at *S*-band.

In the *S*-band state when port 1 is excited, the loss factor is given by (4-4); it is the reflected power from port 1 plus the coupled power from port 1 to all other ports, i.e. ports 2-10. For the 2×2 antenna array at *C* band in the horizontal polarization, the loss factor is equal to the reflected power from ports 3 to 6, which can be calculated using Active-S parameters, plus the coupled power from ports 3-6 to other ports, i.e. ports 1, 2 and 7-10. The loss factor in the *C*-band state is given by (4-5). While calculating the coupled power from the active ports to the non-active ports, it should be noted that there is 180^o phase difference between ports 3-4 and ports 5-6. Therefore, a minus sign is needed for the coupled power from ports 5-6 to other ports.

$$Loss\ factor\ in\ the\ S\ band = |S_{i1}|^2 \quad i = 1, \dots, 10 \tag{4-4}$$

$$Loss\ factor\ in\ the\ C\ band = |Active\_S_3|^2 + |Active\_S_4|^2 + |Active\_S_5|^2 + |Active\_S_6|^2 + |S_{31} + S_{41} - S_{51} - S_{61}|^2 + |S_{32} + S_{42} - S_{52} - S_{62}|^2 + |S_{37} + S_{47} - S_{57} - S_{67}|^2 + |S_{38} + S_{48} - S_{58} - S_{68}|^2 + |S_{39} + S_{49} - S_{59} - S_{69}|^2 + |S_{310} + S_{410} - S_{510} - S_{610}|^2 \tag{4-5}$$

The total efficiency of the antenna/array versus frequency in the *S* and *C* bands are also shown in Figure 4.17(a) and (b), respectively.

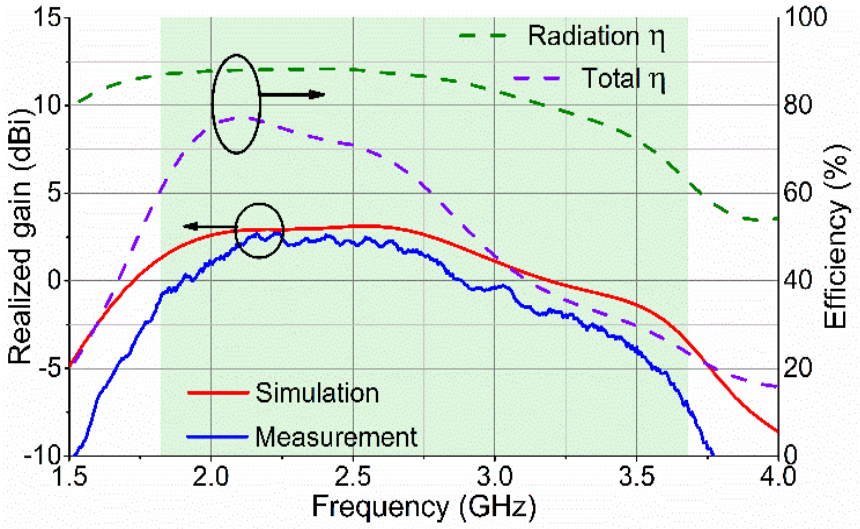

(a)

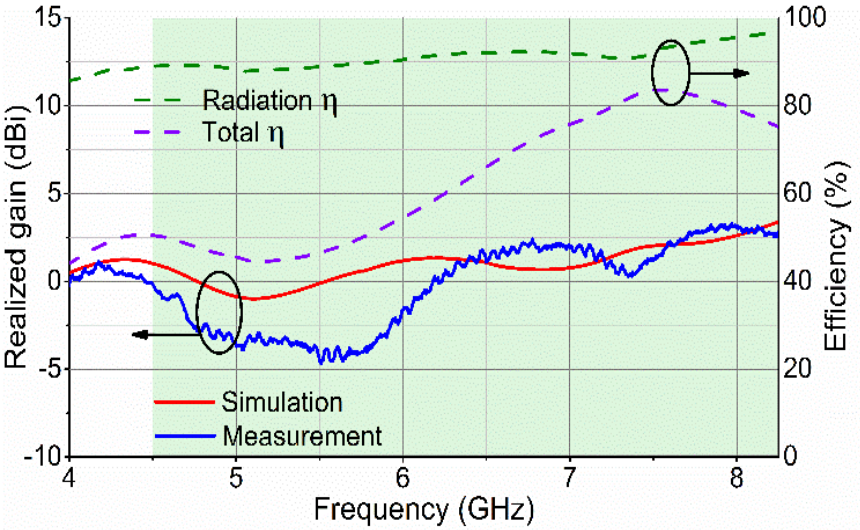

(b)

Figure 4.17. Simulated and measured realized gain, radiation efficiency and total efficiency of the reconfigurable dual-polarized double-sided radiation wideband antenna/array at (a) *S*- and (b) *C*-band operating states.

Table 4-3 compares the reconfigurable dual-polarized double-sided radiation wideband antenna/array in this section with UWB and multi-band/switchable-band antenna arrays. The most important parameters of a phased array antenna such as FBW, polarization, element spacing, efficiency, X-pol. level, and the type of T/R modules are considered in this table.

Table 4-3. Comparison between the reconfigurable dual-polarized double-sided radiation wideband antenna/array and UWB or multi-band/switchable-band antenna arrays.

	Freq. range (GHz)	**$f_{lower\text{-}band}$ / $f_{higher\text{-}band}$ (GHz)**	**FBW**	**Pol.**	**Element spacing/ λ_0**	**Efficiency**	**Feed**	**X-pol. in principal planes (dB)**	**T/R module**	**Comment**
[22]	1-5.3	-	136%	Dual LP	0.09-0.46	90%	Same	-7	UWB	Beam scanning is reduced to 45° in the diagonal plane
[27]	1-8	-	155%	Dual LP	0.067-0.54	>90%	Same	-17	UWB	X-pol. is 12 dB higher than co-pol. in the diagonal plane
[33]	1.8-18	-	164%	Dual LP	0.05-0.5	-	Same	-25	UWB	Poor VSWR when scanned in the H-plane
[9]	-	9.8 / 17	3.1% / 7.1%	Dual LP	0.33/0.58	-	Same	-15	Wideband	Limited bandwidth in each operating state
switchable-frequency antenna in Chapter 3	-	1.8 / 5.7	8.6% / 11.5%	Single LP	<0.5/0.36	67%/81%	Separate	-15	Narrow band	Limited bandwidth in each operating state
Reconfigurable wideband antenna in Chapter 4	-	1.8 to 3.7 / 4.5 to 8.2	69.1% / 58.3%	Dual LP	<0.5/0.33	67%/88%	Separate	-12/-15	With only an octave band	Vertical transition is needed for expansion to larger array for beamscanning

4.3 Reconfigurable Dual-Polarized Single-Sided-Radiation Antenna Element with Wide Bandwidth in *S*- and *C*-band Operating States

One-sided radiation antenna arrays are needed in some applications. For the antenna/array in Figure 4.5, a metal plate is placed as a reflecting ground at the backside of the antenna to create unidirectional radiation. In order to find the optimum distance between the antenna and the ground plane, the total phase of the returning wave should be smaller than 90^o or larger than 270^o over the entire frequency range. As shown in Figure 4.18(a), the total phase delay (φ_{total}) is equal to the reflection phase of the ground plane (φ_{ground}) plus the round trip phase delay of the wave between the antenna and the ground plane (φ_{delay}). By first-order approximation, the total phase delay can be estimated by (4-6);

$$\varphi_{total} = \varphi_{ground} + \varphi_{delay} = 180^0 + 2 \times \frac{2\pi d \times f}{c_o} \quad (4\text{-}6)$$

where d is the distance between the antenna and the ground plane, f is the frequency, and c_o is the speed of light. From Figure 4.18, it is seen that the total phase delay from 2 to 8 GHz is approximately in the green region for d = 15 mm.

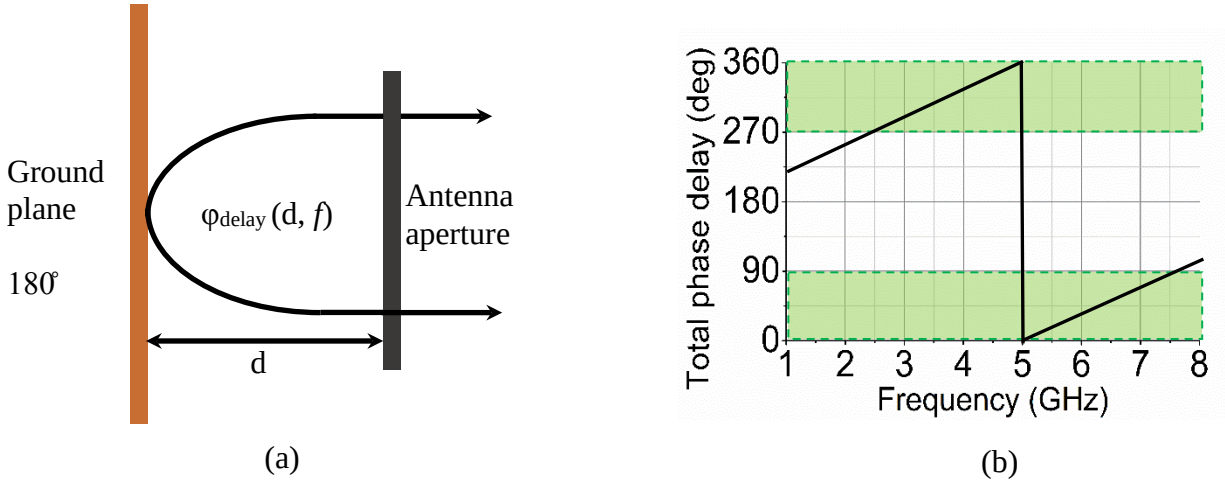

Figure 4.18. (a) Phase delay diagram between the antenna and the ground plane. (b) Total phase delay vs. frequency for d = 15mm.

4.3.1 Simulation and Measurement Results of the Reconfigurable Dual-Polarized Wideband Antenna Element with PEC

By placing a reflecting conductor 15 mm away from the aperture of the reconfigurable antenna/array in Figure 4.9, an antenna/array with unidirectional radiation is obtained. Simulation and measurement results for this antenna/array is presented in this section.

4.3.1.1 S-Parameters

The simulated and measured S-parameters of the unidirectional antenna/array shown in Figure 4.19 and Figure 4.20 are close to the S-parameters of the double-sided radiation antenna/array shown in Figure 4.10 to Figure 4.13. Worst-case isolations between two ports when the switches are OFF (S_{12}) and ON (S_{37}) are shown in Figure 4.20(a) and (b), respectively.

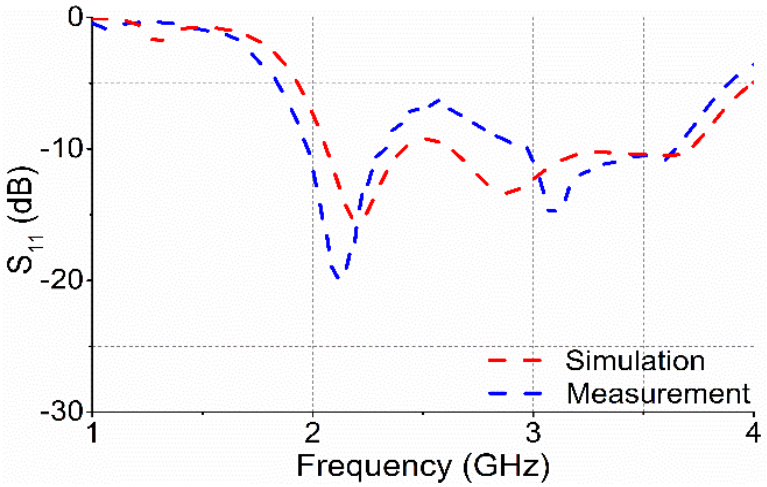

(a)

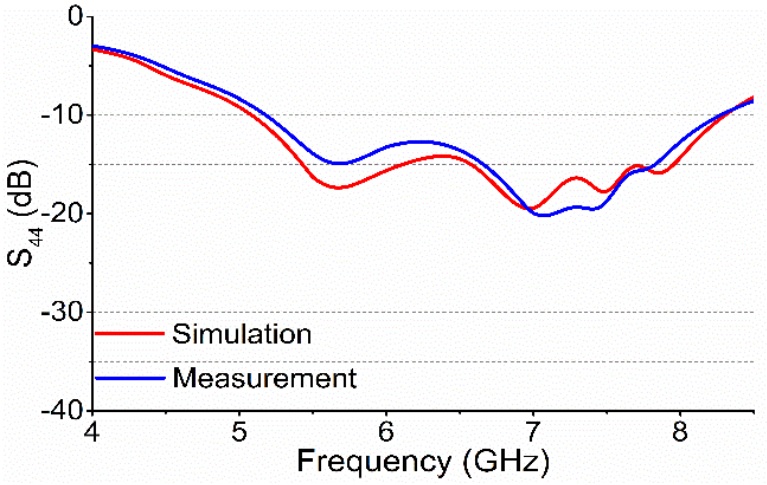

(b)

Figure 4.19. Simulated and measured (a) S_{11} when the switches are OFF, (b) S_{44} when the switches are ON for the unidirectional wideband antenna/array.

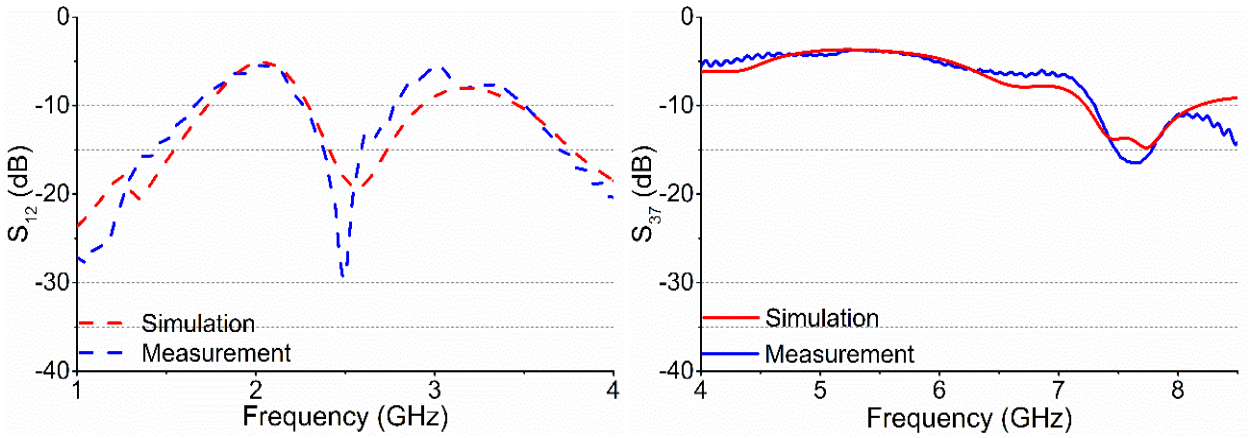

Figure 4.20. Simulated and measured mutual coupling for the unidirectional wideband antenna/array. (a) S_{12} when the switches are OFF, (b) S_{37} when the switches are ON.

4.3.1.2 Radiation Patterns

Figure 4.21 shows the H-plane measurement setup of the unidirectional antenna/array in the *C*-band state. This setup is similar to the double-sided radiation antenna/array except for the supporting structure that holds the antenna and the ground plane. Simulated and measured radiation patterns at *S*- and *C*-band operating states are illustrated in Figure 4.22(a) and (b), respectively. A front-to-back ratio of 12 and 16 dB at 3.5 and 8 GHz is achieved by placing the ground plane at the back of the antenna/array. The X-pol. levels at *S* and *C* bands are consistent with those of the double-sided radiation antenna/array presented in section 4.2.

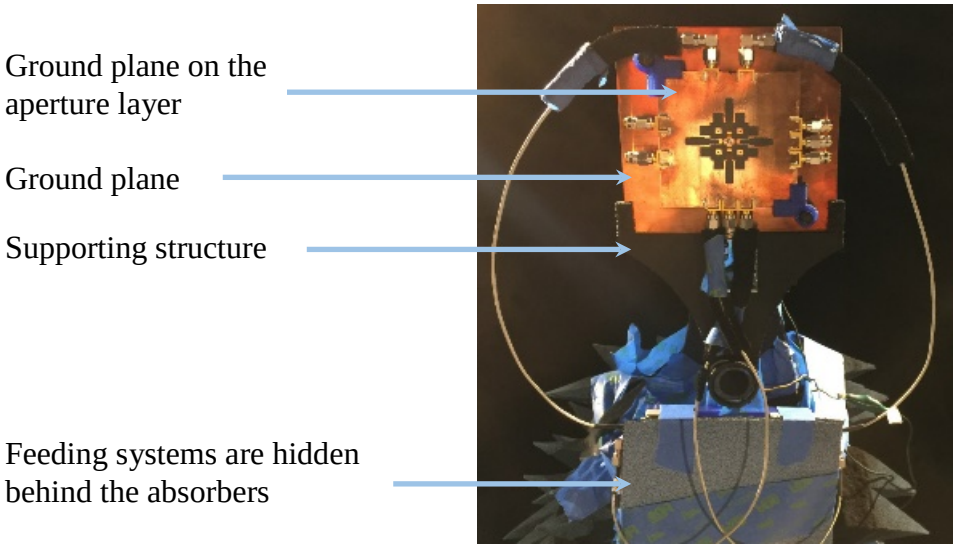

Figure 4.21. H-plane radiation pattern measurement setup for the unidirectional wideband antenna/array in the *C*-band state.

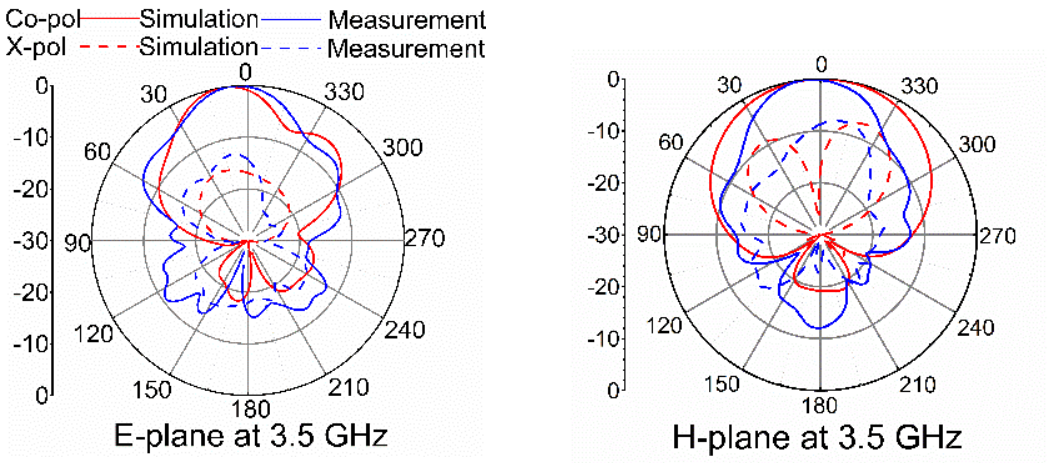

(a)

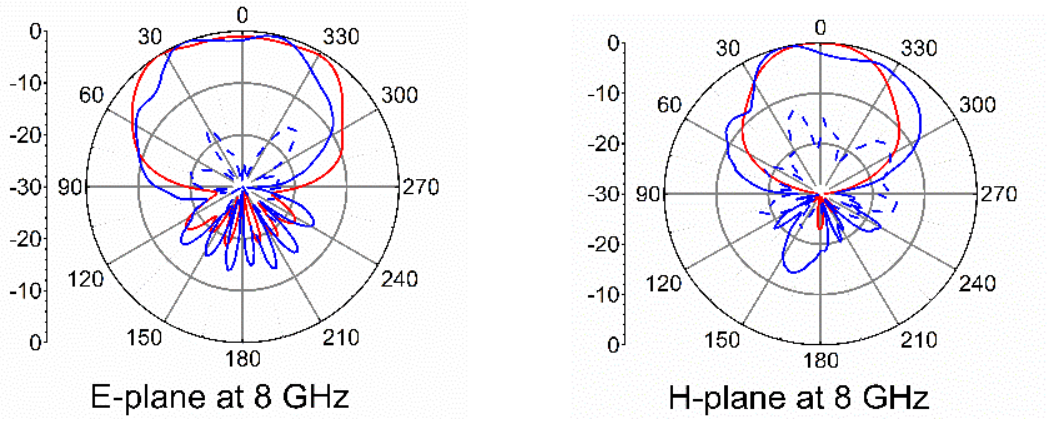

(b)

Figure 4.22. Co- and X-pol. radiation patterns of the unidirectional wideband antenna/array at (a) *S*-band operating state at 3.5 GHz, and (b) *C*-band operating state at 8 GHz.

4.3.1.3 Realized Gain

The gain of a single-sided radiating antenna is 3 dB higher than that of a double-sided radiating antenna because the backside radiation is reflected by the ground plane. The simulated

and measured realized gain of the reconfigurable dual-polarized single-sided radiation wideband antenna/array is demonstrated in Figure 4.23. In the *S*-band state, the realized gain vs. frequency is 3 dB higher than the gain of the double-sided antenna/array over the *S*-band. In the *C*-band state, there is a null in the realized gain vs. frequency at 5 GHz as shown in Figure 4.23(b). The radiation patterns at this frequency are illustrated in Figure 4.24 which show a dip at boresight; the null in the gain is caused by the null in the radiation pattern at boresight. This null in the radiation pattern is not only due to L_g as described earlier but also due to the larger reflecting ground plane. Based on the studies in [68], the null should disappear for a very large antenna array. To prove this, an HFSS simulation was performed using periodic boundary conditions to emulate a larger array using the antenna/array presented in this section as a unit cell. The simulation setup for a 4×4 array is illustrated in Figure 4.25(a). The radiation pattern of this 8×8 *C*-band array (4×4 *S*-band array) at 5 GHz is shown in Figure 4.25(b). This array exhibits 12.6 dBi realized gain. Since the array lattice and element spacing are not optimized in Figure 4.25(a) to be less than $\lambda_0/2$, two grating lobes are observed. Nevertheless, the null at the boresight no longer exists. The radiation efficiencies for the unidirectional antenna is close to the double-sided case which is higher than 67%/88% in the *S*-/*C*-band state.

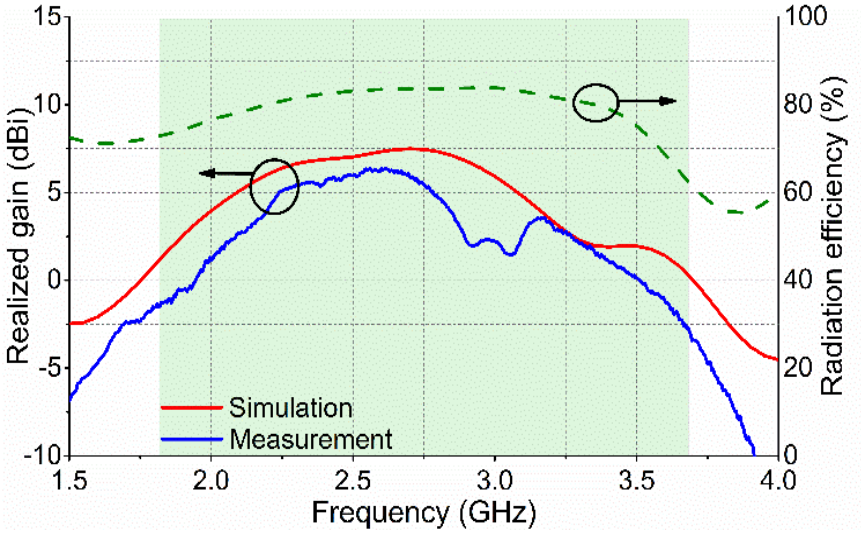

(a)

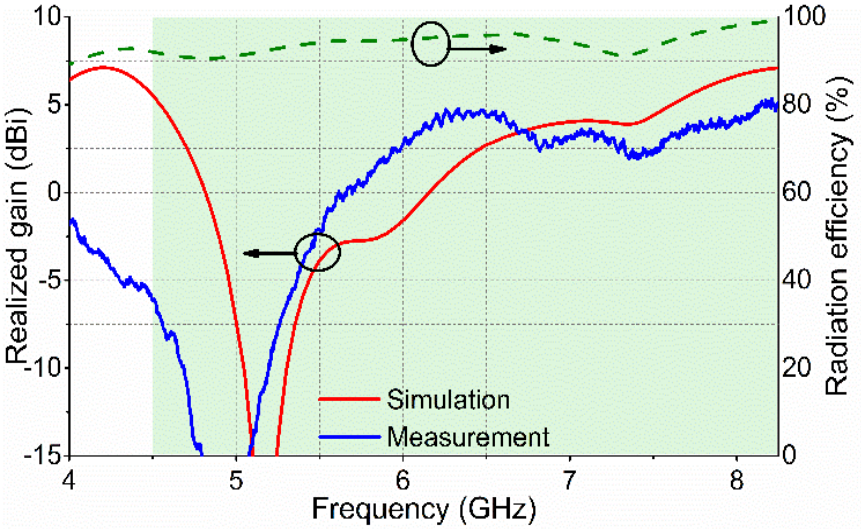

(b)

Figure 4.23. Simulated and measured realized gain and radiation efficiency of the reconfigurable dual-polarized single-sided radiation wideband antenna/array at (a) *S*- and (b) *C*-band operating states.

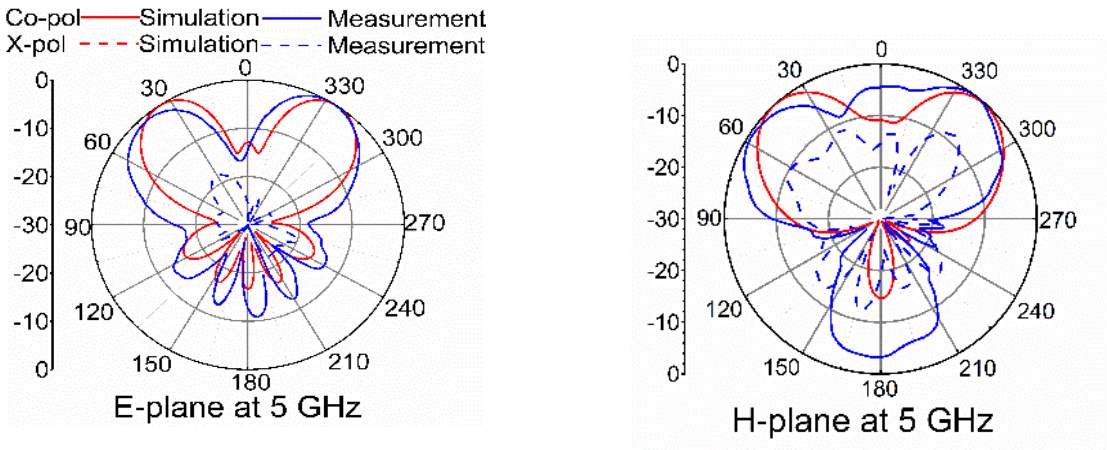

Figure 4.24. Co- and X-pol. radiation patterns of the reconfigurable dual-polarized single-sided radiation wideband antenna/array at *C*-band operating state at 5 GHz.

4.3.2 Simulation Results of an Optimum Dual-Polarized Single-Sided-Radiation Antenna Element with Wide Bandwidth in *S*- and *C*-band Operating States

In the previous section, it was shown that the null in the gain vs. frequency for the reconfigurable dual-polarized single-sided radiation wideband antenna/array is due to the size of the ground plane. In this section, an antenna element with smaller substrate size (L_g=58 mm) and four defects at the corners of the ground on the aperture layer is demonstrated in Figure 4.26. After studying the effect of each parameter on the S-parameters and gain of the dual-polarized single-sided-radiation wideband antenna element, an antenna with optimum dimensions is presented in Figure 4.26. The simulated S_{11} and Active-S_4 in the *S*- and *C*-band operating states are shown in Figure 4.27. It is seen that this antenna element covers *S* and *C* bands with no frequency gap between two operating states. As illustrated in Figure 4.28, the worst case isolations in the *S* and *C*-band operating states are S_{12}<-5 dB and S_{37}<-4 dB, respectively. For this dual-polarized single-

sided-radiation antenna element, the radiation patterns at 3.5/6.0 GHz are demonstrated in Figure 4.29. The X-pol level at 3.5/6.0 GHz is 18.0/26.0 dB with the front to back ratio of 20.0/26.0 dB. Figure 4.30 shows the realized gain vs. frequency in the *S*/*C* band. The variation of the gain over the frequency is less than 4 and 3 dBi in the *S* and *C* bands.

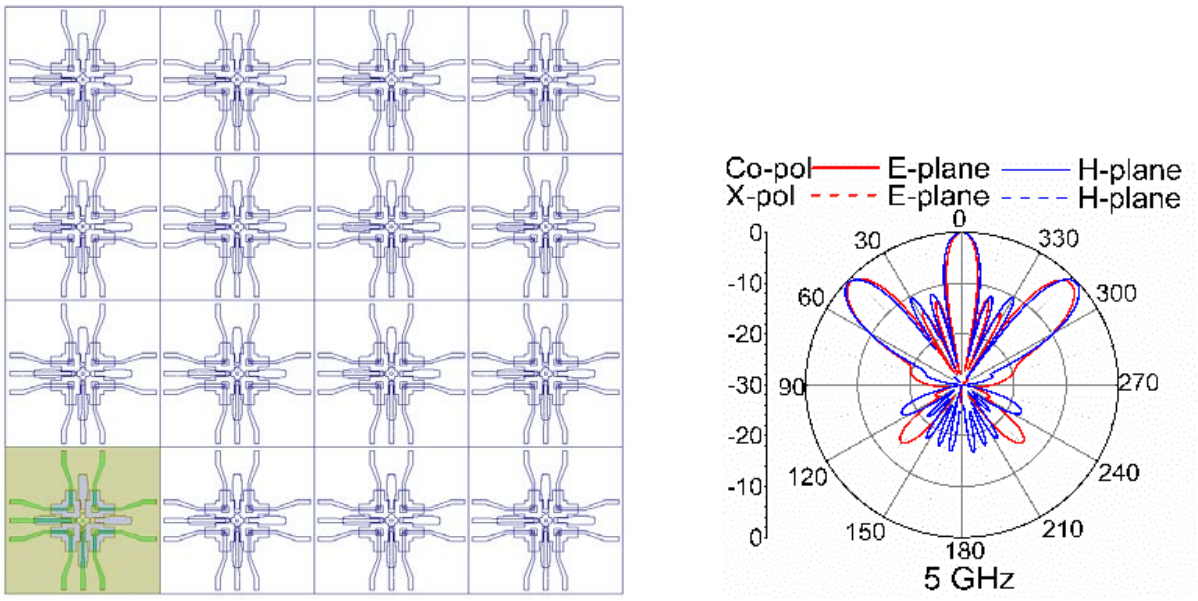

(a) (b)

Figure 4.25. Co- and X-pol. radiation patterns of an 8×8 C-band array (4×4 S-band array) at 5 GHz.

This reconfigurable optimum dual-polarized single-sided-radiation wideband antenna element has the following specifications:

- It covers *S* and *C* band in two operating states with no frequency gap

- It operates in two orthogonal polarizations at each operating state
- One-sided radiation is achieved by using a reflecting ground
- Low gain variation over the frequency of operation is obtained
- Only eight PIN diode switches with one bias line are required to switch between two modes of operation

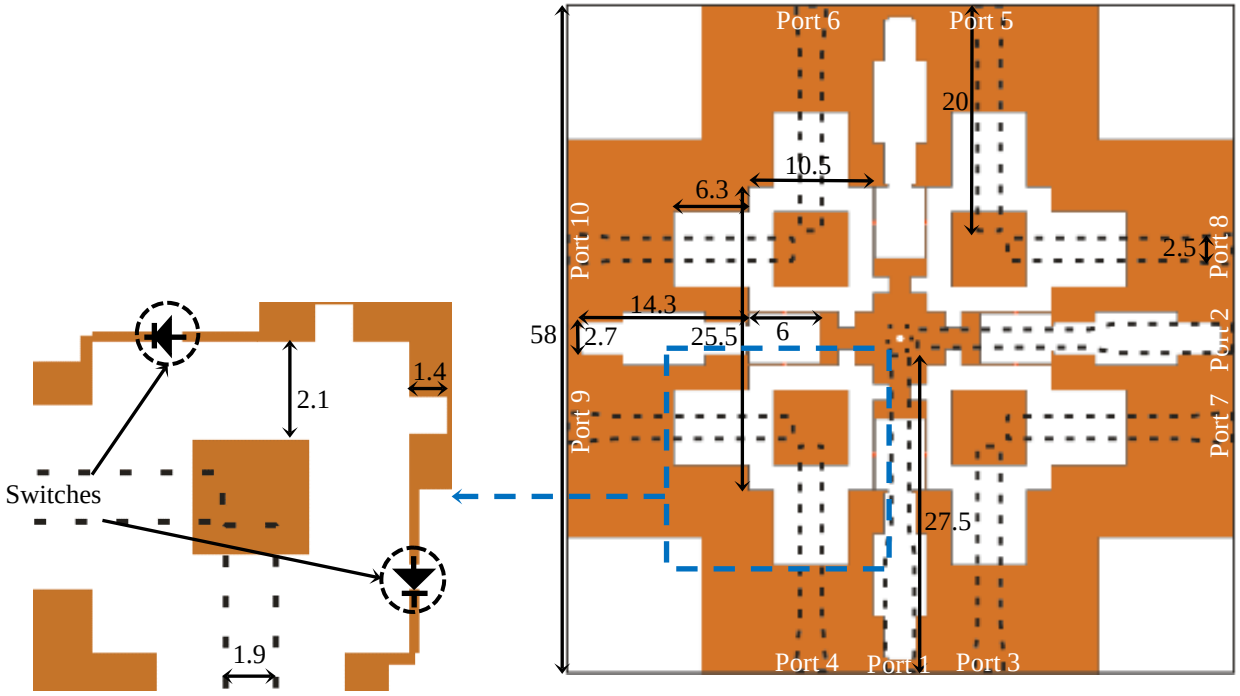

Figure 4.26. Unidirectional antenna/array with smaller substrate size and defected corners (all dimensions are in mm).

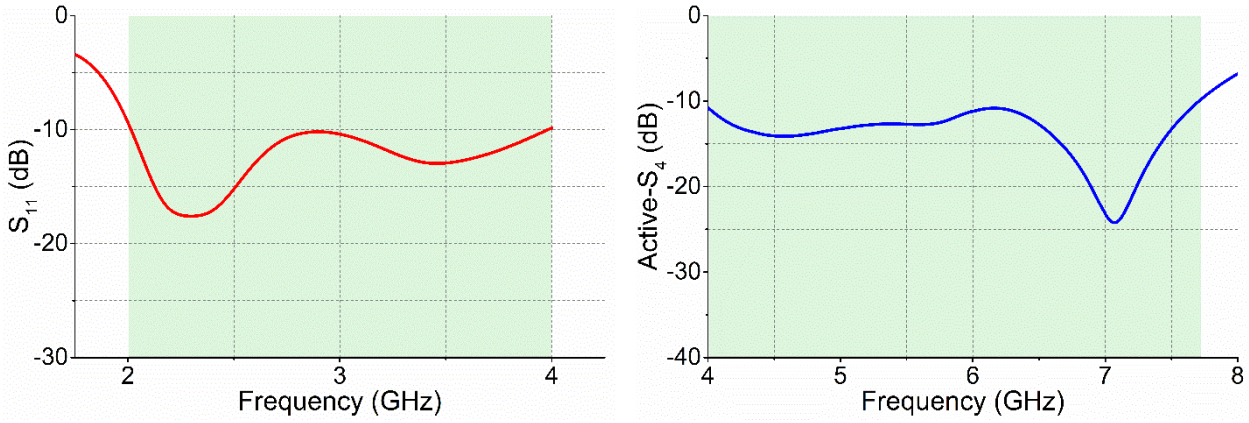

Figure 4.27. Simulated (a) S_{11} in the *S*-band operating state and (b) Active-S_4 in the *C*-band operating state for the optimum one-sided radiation antenna element.

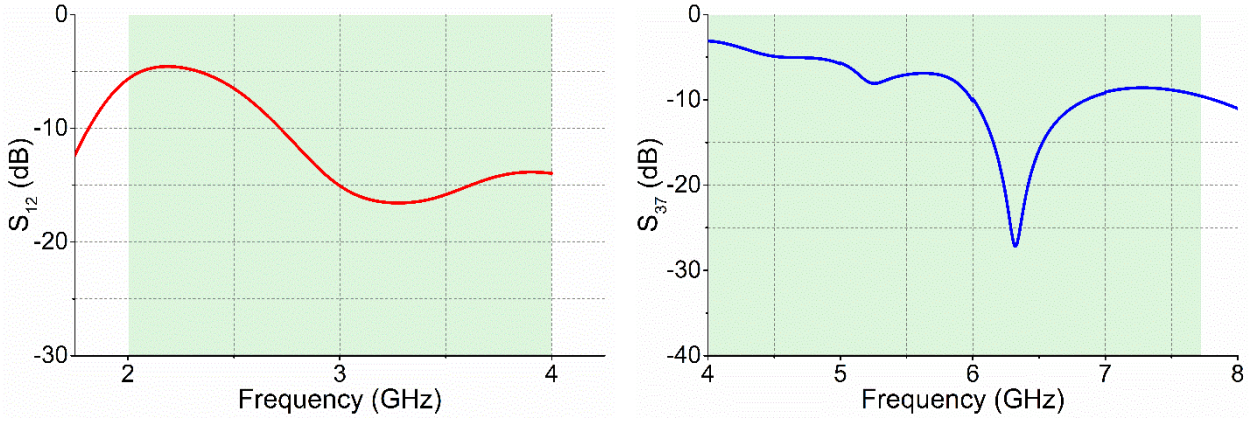

Figure 4.28. Simulated (a) S_{12} in the *S*-band operating state and (b) S_{37} in the *C*-band operating state for the optimum one-sided radiation antenna element.

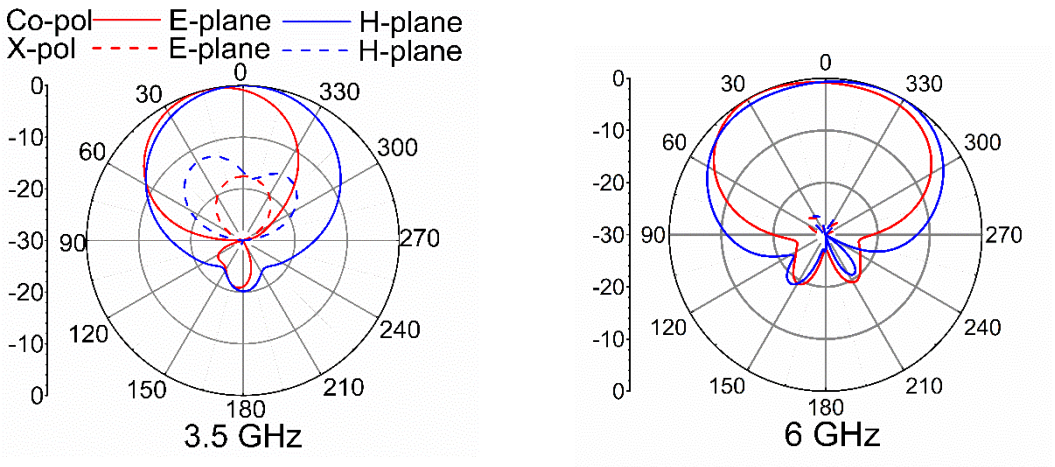

(a) (b)

Figure 4.29. Simulated radiation patterns of the optimum one-sided radiation antenna element in the (a) *S*-band operating state at 3.5 GHz and (b) *C*-band operating state at 6 GHz.

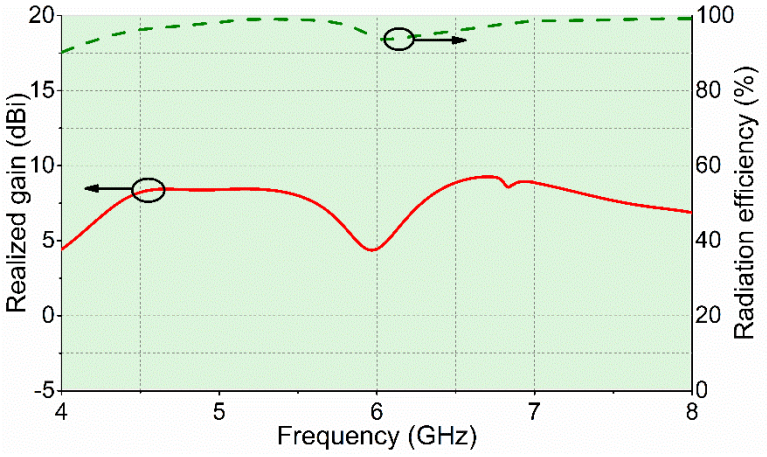

(a)

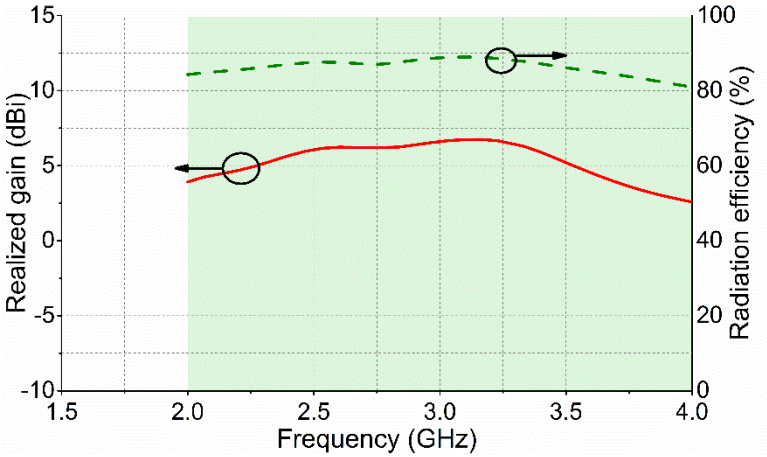

(b)

Figure 4.30. Simulated realized gain and radiation efficiency of the optimum one-sided radiation antenna element in the (a) *S*- and (b) *C*-band operating state.

4.4 Conclusion

First, a reconfigurable double slot-ring antenna element for bandwidth enhancement in the *C*-band operating state has been presented. 32 PIN diode switches are used in the antenna structure

to switch between two frequency bands. A balanced double stub loaded microstrip line feeds two concentric slot-rings that operate at lower band. Four small slot-rings form a 2×2 array at higher band. At lower band, the gain and FBW of the double slot-ring antenna element are significantly improved from the switchable-frequency band antenna element presented in section 3.1.1. At higher band, the antenna performance is not compromised.

Then, a novel reconfigurable dual-polarized antenna element incorporating modified Koch fractal geometries to provide wide bandwidth has been presented. Eight PIN diode switches were placed inside the slots to activate the selected aperture slot-rings to achieve frequency reconfigurability (*S*- and *C*-band operating states). By exciting the antenna ports appropriately, the radiation patterns can be switched between horizontal or vertical polarizations, realizing polarization agility. The antenna shows a FBW of 69.1%/58.3%, maximum realized gain of 2.4/3.1 dBi, and minimum radiation efficiency of 67%/88% in the *S*-/*C*-band states, respectively. This antenna/array can be extended to a large array with element spacing around $\lambda_0/2$ at the center frequency of each operating state which is studied in Chapter 5. A vertical transition is needed in the feeding network of the large array; it is realizable by using a coaxial to microstrip transition. In addition, due to the separate feeding for each band, only narrow-band T/R modules are needed.

CHAPTER 5: RECONFIGURABLE WIDEBAND ANTENNA ARRAY COVERING *S* AND *C* BANDS

Phased array antennas are widely used for military applications, advanced radar and wireless communications. A phased array antenna that is able to operate at different frequency bands and with different polarization states can significantly reduce the time and cost required to design each individual phased array with a specific frequency band and a particular polarization state. The advantages of reconfigurable wideband antenna element to multi-band/switchable-band antenna arrays or UWB antenna arrays were discussed in Chapter 1, 3 and 4. In this chapter, a reconfigurable dual-polarized shared-aperture antenna array is presented for phased array applications.

5.1 2×2 Reconfigurable Dual-Polarized *S*-Band Array Covering *S* and *C* Bands

Wideband and UWB antenna arrays were compared to the reconfigurable wideband arrays in section 1.3. Single-polarized tightly coupled dipole antenna (TCDA) and eared antenna with 60^o and 45^o beam scanning capability were demonstrated in [70] and [71], respectively. These wideband antenna arrays with less than an octave bandwidth, only require narrowband T/R modules. In [22], a dual-polarized planar UWB CSA with 45^o beam scanning capability was shown with X-pol. level as high as -7 dB in the principal planes. Dual-polarized Vivaldi antenna array for remote sensing applications were demonstrated in [26] with the FBW of 155% and beam scanning of 30^o.

A frequency and polarization reconfigurable shared-aperture phased array antenna with full band coverage in each operating state is demonstrated in this section. A 2×2 *S*-band antenna array which can be reconfigured to a 4×4 *C*-band antenna array by activating 32 PIN diode switches is fabricated and measured. The separate feeding mechanism for each frequency band allows for the use of narrow-band T/R modules. This antenna array is modular with separate feeding lines for each frequency band and each polarization. The FBW of this antenna array in the *S*-/*C*-band state is 69.1%/58.3%, respectively. In Chapter 4, a single *S*-band antenna element containing four *C*-band antennas with microstrip feeding was demonstrated. In this section, a coax-to-microstrip transition is used in the feeding network of the antenna array. This antenna array exhibits single-sided radiation with a ground plane placed below the radiating aperture and relatively flat gain over the entire band in each operating state. In addition, due to the shared aperture design and proper arrangement of the array lattice, the antenna array can scan its main beam to ±60^{o} and ±35^{o} in the principal planes in the *S*- and *C*-band operating states, respectively. This is the first reconfigurable antenna array which can continuously cover two adjacent frequency bands with full band coverage. This concept can be extended to tri-band antenna array with full coverage of the *S*, *C* and *X* bands.

5.1.1 Antenna Configuration and Design Procedure

The configuration of the dual-polarized 2×2 *S*-band array which can be reconfigured to a 4×4 *C*-band array is shown in Figure 5.1(a), with port numbers labeled. A single *S*-band antenna is shown in Figure 5.1(b) with eight p.i.n diode switches (DSM8100-000, 0201 package)

highlighted in dashed circles. The details of the *C*-band antenna element and p.i.n. diode switch placement are illustrated in Figure 5.1(c). A metal ground plane is placed 15 mm, i.e. $\lambda_0/4$ at 5 GHz, under the antenna aperture layer to create a single-sided radiation pattern. The coaxial to microstrip transition is used to bring the feeding ports of the array to the backside of the ground plane, as shown in Figure 5.1(d) and (e), which is critical to minimize the antenna element spacing and form a larger array. As illustrated in Figure 5.1(e), the center conductor of the coax lines is soldered to the microstrip lines while the outer conductor is soldered to the narrow strip ground on the radiating aperture.

As illustrated in Figure 5.1(b), a modified Koch fractal geometry is incorporated into the antenna element to achieve wide bandwidth. As discussed in detail in Chapter 4, this fractal shape is able to generate two or more resonant modes in addition to the fundamental mode of the slot-ring, which can result in one octave bandwidth in both *S*- and *C*- band operating states. Unlike the design in Figure 4.5, a narrow strip ground is used as the perimeter for the *S*-band antenna element as shown in Figure 5.1. First, it helps remove a null in the gain of the antenna array in the *C*-band state of the design in section 4.3. Figure 5.2 shows the aperture layer for three cases: W_{st} = 2 mm, W_{st} = 7 mm and the array with ground extended to the edge of the substrate. Figure 5.3(a) and (b) demonstrate the antenna gain for these three cases in the *S*- and *C*-band states, respectively. It is seen that for Case III (black dashed line), there is a null in the gain at 6 GHz. This null is mitigated for smaller values of W_{st}, i.e. case I and II. Second, for smaller values of W_{st}, the mutual coupling between the adjacent *S*-band elements is reduced in the *C*-band operating state. Figure 5.4(a) and (b) illustrate the variation of S_{a1d1} and S_{a6b8} with respect to W_{st} in the *S*- and *C*-band operating

states, respectively. From Figure 5.4, the overall mutual coupling between adjacent *S*-band elements is reduced by 5 dB in the *C*-band state, while it does not change significantly in the *S*-band state. Finally, the effects of W_{st} on the S_{a1a1} and S_{b4b4} are presented in Figure 5.5. Smaller values of W_{st} result in larger FBW in the *C*-band state as well as smaller frequency gap between the *S*- and *C*-band operating states.

Generally, four steps should be followed to design a wideband slot-ring antenna array operating at two adjacent frequency bands:

1) As for the starting point, obtain the dimensions of the *S*-band antenna element including the fractal geometries based on the guidelines in section 4.2.1.

2) Find the optimum value of W_{st} to obtain relatively-flat gain in the *C*-band state and minimum frequency gap between the *S*- and *C*-band states.

3) Fine-tune the dimensions of fractal shapes to fit in the array lattice which will be discussed in Section III.

4) Slightly adjust the position of coaxial to microstrip transition and the length of microstrip feedlines to achieve desired FBW in both *S*- and *C*-band states.

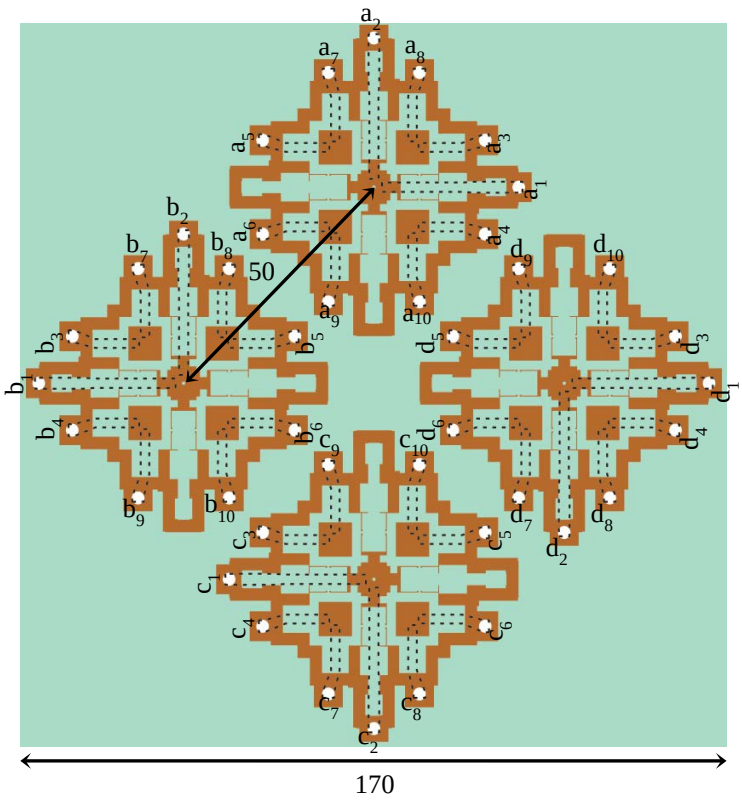
a2
a7
a8
a5
a3
a1
b2
a6
a4
b7
b8
50
d9
d10
a9
a10
b3
b5
d5
d3
b1
d1
b4
b6
c9
c10
d6
d4
b9
b10
d7
d8
c3
c5
d2
c1
c4
c6
c7
c8
c2
170

(a)

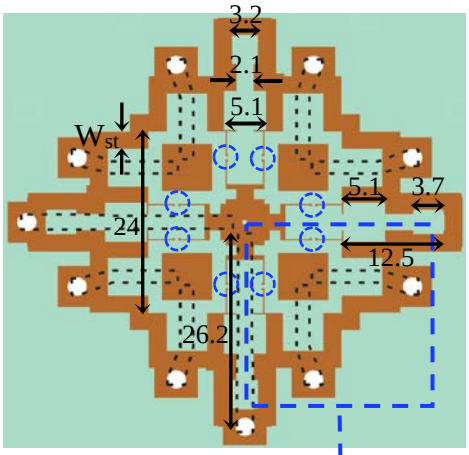
3.2
2.1
5.1
Wst
5.1
3.7
24
12.5
26.2

(b)

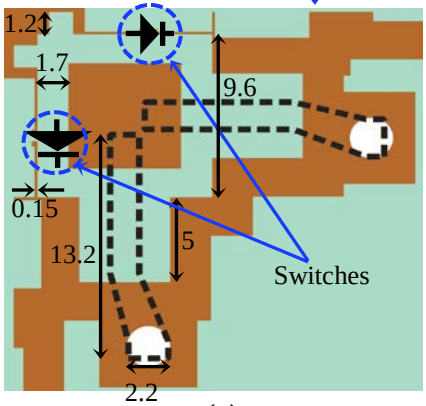
1.2
1.7
9.6
0.15
13.2
5
Switches
2.2

(c)

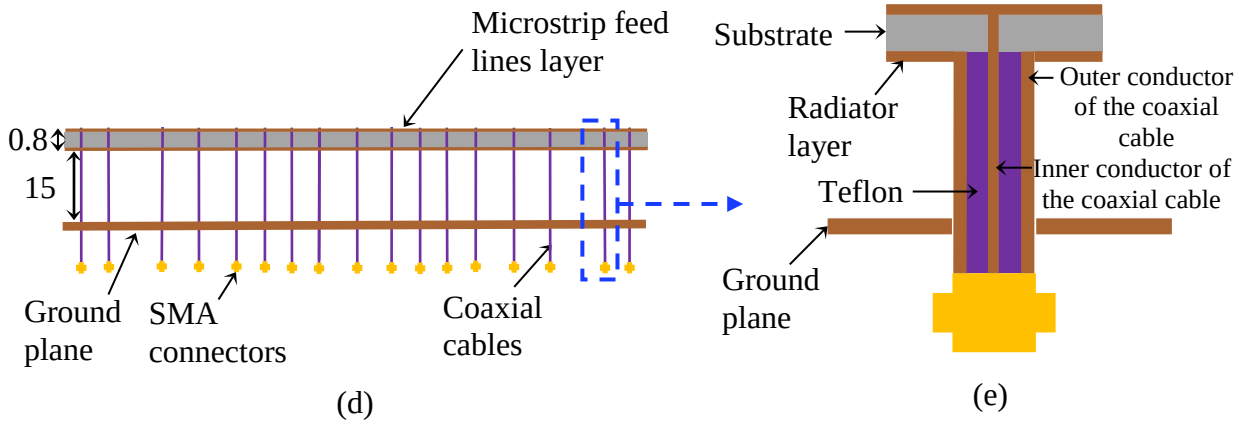

Figure 5.1 (a) Configuration of the 2×2 reconfigurable dual-polarized *S*-band array (4×4 *C*-band array). (b) Close-up view of the *S*-band unit cell. (c) Close-up view of the *C*-band unit cell. (d) Side view of the 2×2 reconfigurable dual-polarized *S*-band array (all dimensions are in mm).

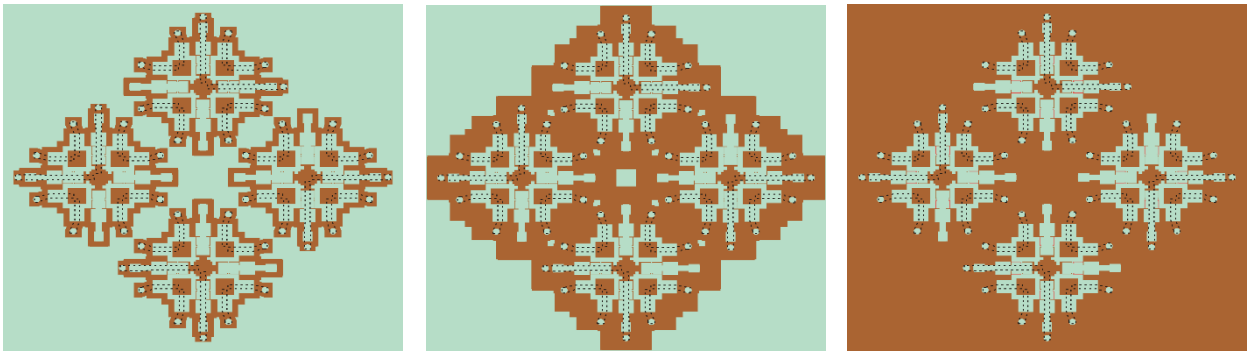

Case I: W_{st} = 2 mm

Case I: W_{st} = 7 mm

Case III: ground is extended to the edge of the board

Figure 5.2 2×2 dual-polarized reconfigurable S-band array with different widths of the ground strip on the radiator layer.

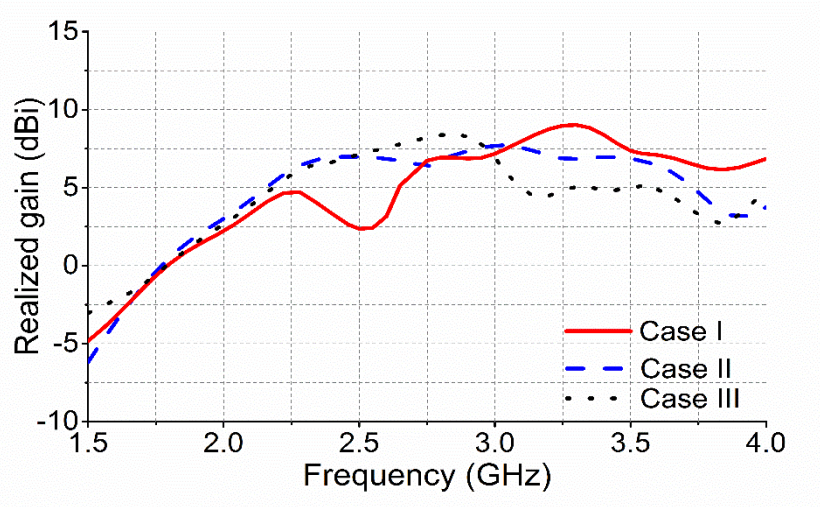

(a)

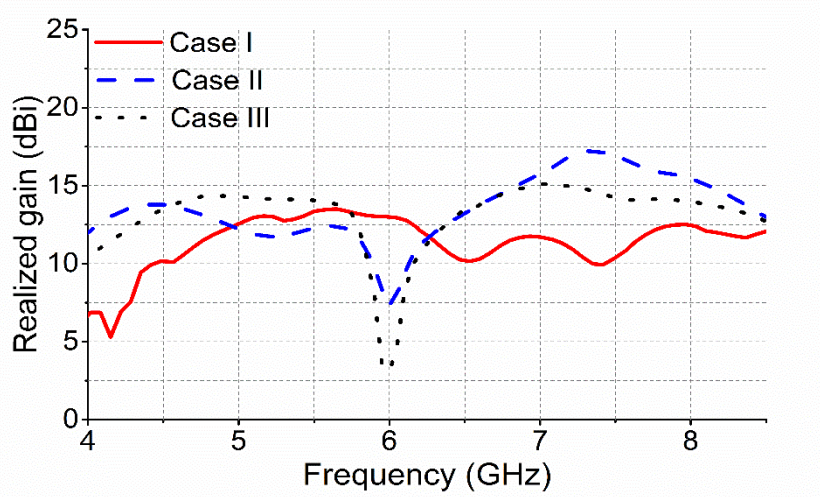

(b)

Figure 5.3 Effects of W_{st} on the realized gain at (a) *S*- and (b) *C*-band state.

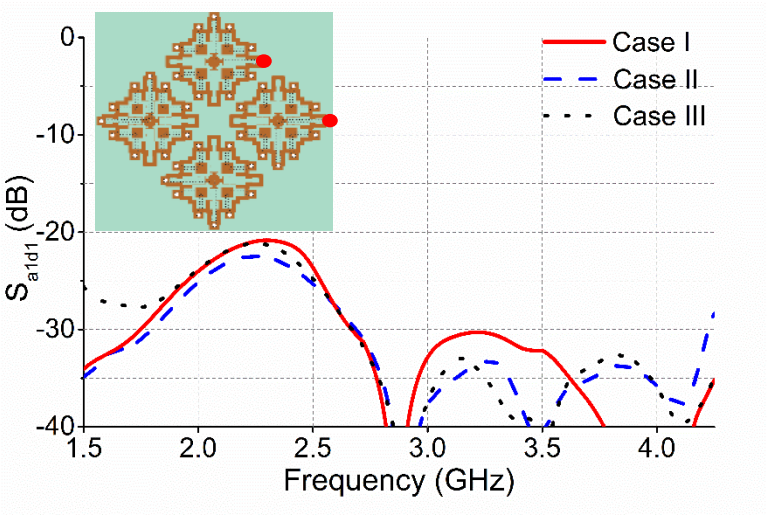

(a)

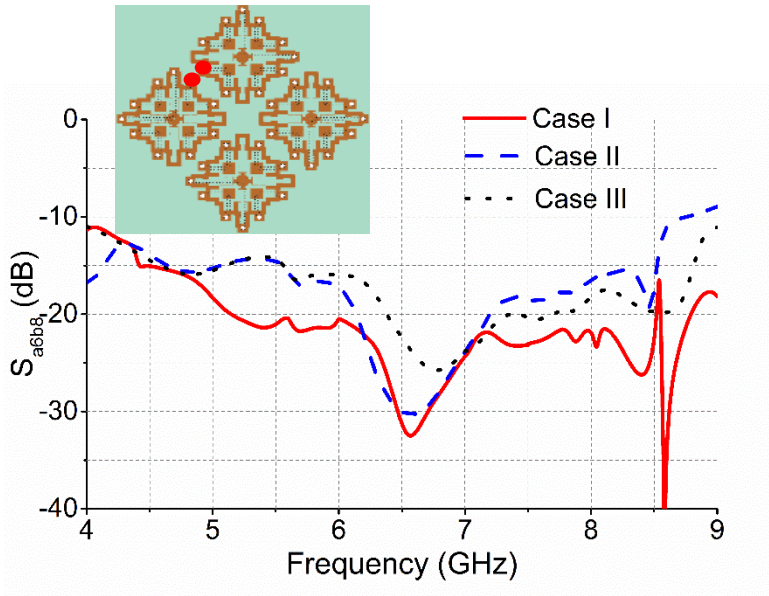

(b)

Figure 5.4 Effects of W_{st} on (a) S_{a1d1} at *S*-band state and (b) S_{a6b8} at *C*-band state.

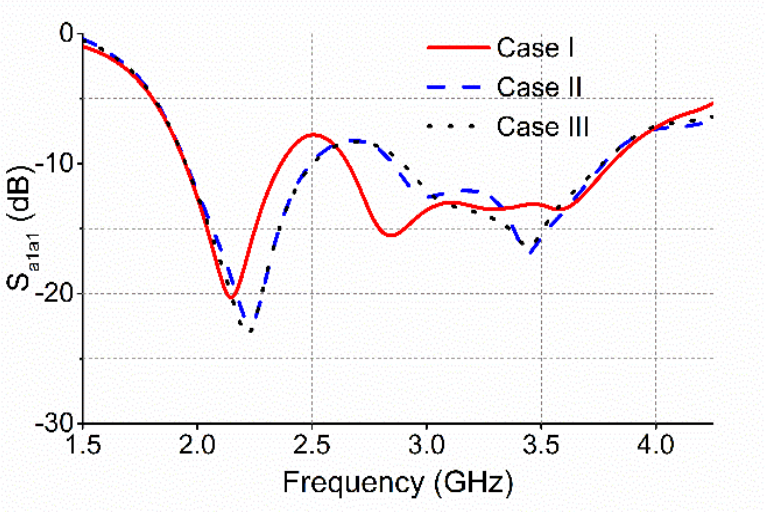

(a)

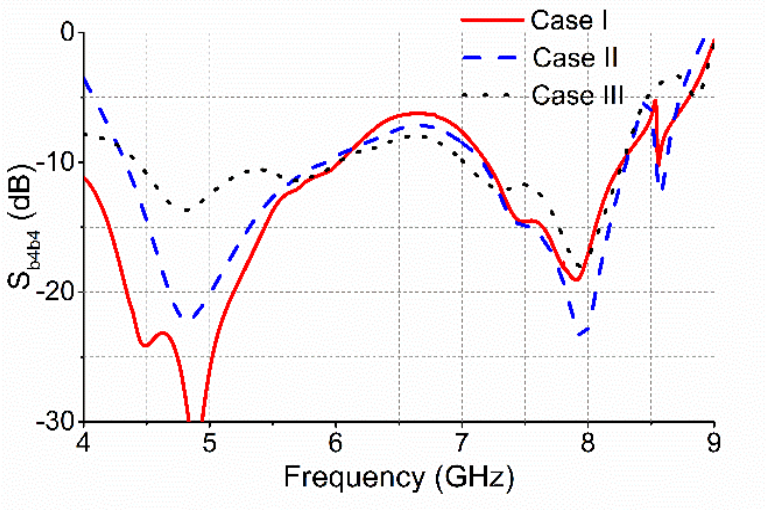

(b)

Figure 5.5 Effects of W_{st} on (a) S_{a1a1} at *S*-band state and (b) S_{b4b4} at *C*-band state.

32 p.i.n diode switches in the antenna array are controlled by a single DC bias voltage supplied at the center of each *S*-band antenna element where the electric field is minimum. A 100-Ω resistor is used to limit the DC current of all the p.i.n diodes. When the switches are OFF, the

antenna is excited by ports a_1, b_1, c_1, and d_1 (horizontal polarization) or ports a_2, b_2, c_2, and d_2 (vertical polarization) operating in the *S*-band state. By turning on all the p.i.n diode switches, a 4×4 antenna array is formed to operate at the *C*-band state. Ports $a_3/b_3/c_3/d_3$, $a_4/b_4/c_4/d_4$, $a_5/b_5/c_5/d_5$, $a_6/b_6/c_6/d_6$ (horizontal polarization) or ports $a_7/b_7/c_7/d_7$, $a_8/b_8/c_8/d_8$, $a_9/b_9/c_9/d_9$, $a_{10}/b_{10}/c_{10}/d_{10}$ (vertical polarization) are excited in this state. The DC power consumption is 0 W in the *S*-band state since the switches are reverse biased. In the *C*-band state, the total DC power consumption is 5.8 mW in which 2.1 mW is dissipated in the 100-Ω resistor and 3.7 mW is consumed by the p.i.n diodes in the ON state. The p.i.n diode switches are modeled with *RLC* equivalent circuit which is presented in 2.2.2. Black dashed lines in Figure 5.1 illustrates the microstrip feeding lines for the *S*- and *C*-band arrays. The *S*-band horizontal (vertical) polarization feed lines of the antenna elements “a” and “d” are mirrored to that of the elements “b” and “c” in order to improve cross polarization (X-pol.) level at *S*-band operating state. The final antenna dimensions are listed in Figure 5.1.

5.1.2 Antenna Array Configuration

Selection of an appropriate array lattice configuration is an important part in the design of a phased array. The spacing between elements is limited by the requirement of avoiding grating lobes in both operating states while scanning the main beam. Figures 5.6 and 5.7 show the rectangular and triangular array lattices with the grating lobe diagrams [72]. The visible region is limited to a unit circle in the grating lobe diagram. As can be seen in Figures 5.6 and 5.7, the narrower spacing in the array lattice in one direction leads to wider-spaced grating lobes in

corresponding direction in the grating lobe diagram. Furthermore, increasing the frequency or the element spacing enlarges the unit circle diameter on an existing grating lobe diagram. When the main beam is scanned to (θ_0, φ_0), the center of the unit circle in the grating lobe diagram is moved to ($\sin\theta_0\cos\varphi_0$, $\sin\theta_0\sin\varphi_0$) which is shown with red circle in Figures 5.6 and 5.7 [72]. When the red circle encloses only one main beam, there are no grating lobes at this scan angle.

Triangular lattices permit larger maximum element spacing compared to rectangular lattices [73]. Hence, the *S*-band elements in this paper are arranged with triangular lattice. Specifically, as shown in Figure 5.8, a triangular lattice is selected for the *S*-band elements with spacing C_1=0.86λ_0 and C_2=0.61λ_0, i.e. α=45^o, at 3.7 GHz. Therefore, the spacing in the grating lobe diagram are:

$$\frac{\lambda}{C_1 \sin\alpha} = 1.64 \quad and \quad \frac{\lambda}{C_2 \sin\alpha} = 2.32 \tag{5-1}$$

Then, the maximum scan angle in the *S*-band state is obtained from:

$$(\sin\theta_0 \cos\varphi_0)\,|_{\varphi_0=0} = 0.64 \rightarrow \theta_{max} = 40.1^o \tag{5-2}$$

In the *C*-band state, the *C*-band elements are arranged in a rectangular lattice inside the *S*-band elements. If we consider the 2×2 rectangular array of the *C*-band elements as a sub-array, then the arrangement of these sub-arrays form a triangular lattice. The spacing between the *C*-band elements in the sub-array is C_3=C_4=0.35λ_0, while the spacing between the sub-arrays in the

triangular lattice is C_1=1.72λ_0 and C_2=1.23λ_0, i.e. α=45°, at 7.4 GHz. This arrangement of *C*-band elements leads to much more complicated grating lobe diagram than the *S*-band array. Therefore, it is not shown here. Instead, the maximum scanning angle in the *S*- and *C*-band states are computed using both HFSS and MATLAB simulations in Section 5.1.4.5.

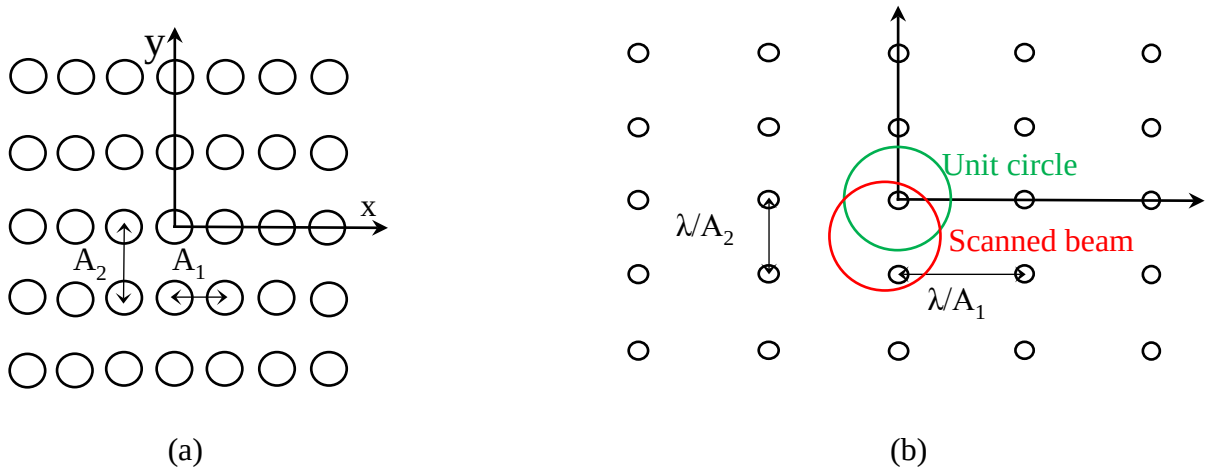

Figure 5.6. Rectangular array; (a) array lattice and (b) grating lobe diagram [72].

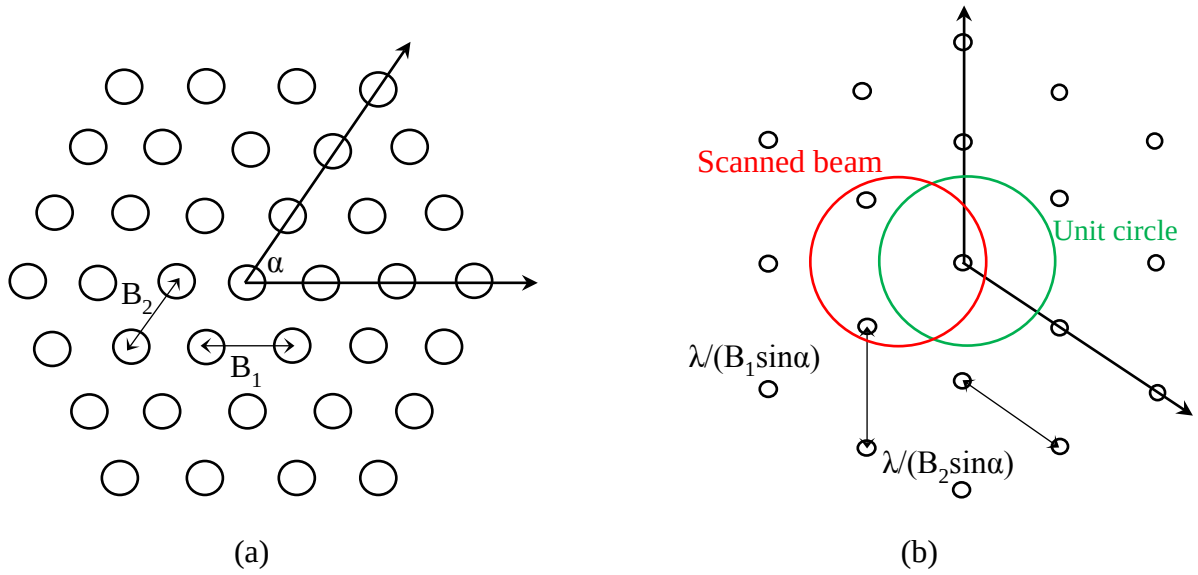

Figure 5.7. Triangular array (*S*-band operating state); (a) array lattice and (b) grating lobe diagram [72].

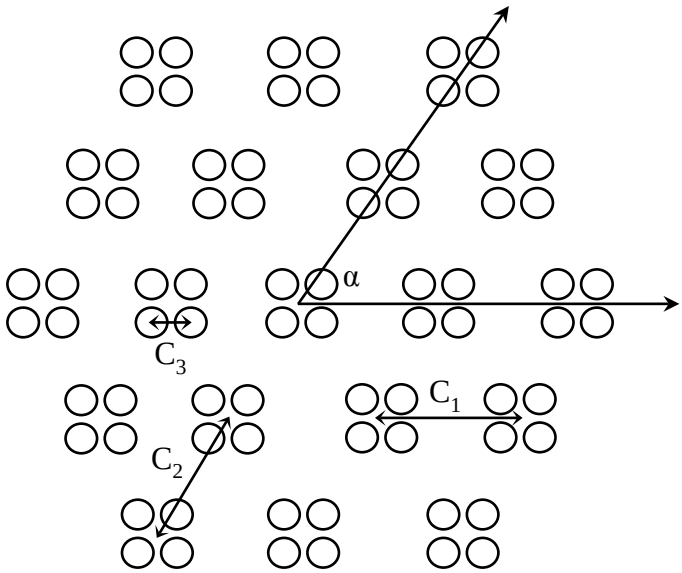

Figure 5.8. Hexagonal-rectangular array (*C*-band operating state).

5.1.3 Antenna Array Fabrication

Figure 5.9(a) and (b) show the fabricated antenna radiator aperture and microstrip feed lines on both sides of a Rogers RT/Duroid 5880 substrate (ε_r=2.2 and $tan\delta$=0.0009) with a thickness of 0.79 mm. Conductive silver paint (SPI 05002-AB from Structure Probe, Inc.) is used to make the electrical connection between the p.i.n diode switches and the antenna. 40 via holes with a diameter of 0.58 mm are drilled in the substrate for the coaxial to microstrip transition. Four via holes with the same diameter are drilled at the center of the four *S*-band antenna elements for DC biasing. A double-layer ground plane as shown in Figure 5.10(a) and (b) is designed to facilitate the replacement of malfunctioned p.i.n diodes easier. As shown in Figure 5.10(c), the holes inside *Ground II* are slightly larger than the SMA connectors so that it can be removed when p.i.n. diode replacement is needed. The holes in *Ground I* is just slightly larger than outer dimension of the coaxial lines to ensure that there is no energy leakage to the back side. In addition, the four square apertures inside *Ground I* allows for the access to re-solder the p.i.n. diodes. The combination of the two ground planes is able to provide a ground plane as simulated in HFSS with the benefit of easy repair capabilities.

An antenna mounting structure is designed and fabricated by a 3-D printer in order to hold the radiator layer, ground planes and the coaxial cables in place. Figure 5.11(a), (b) and (c) show the antenna array with the supporting structure from the top, bottom and side view, respectively. The supporting structure is made of three major parts: Top part that holds the antenna substrate; bottom part that holds the coaxial cables with the SMA connectors; four arms that connect the top

and bottom parts together (the 2-layer ground plane is also held by the four arms). Hexagonal holes are made in the bottom part of the supporting structure to prevent the SMA connectors from rotation during tightening the connections. Steps for fabrication and assembling of the antenna array are listed as follows:

1) Radiator and microstrip feed lines are etched on both sides of the substrate using printed circuit board (PCB) fabrication. Then, 44 via holes are drilled in the substrate.

2) 40 holes with the diameter of 3.2 and 7.9 mm are cut in the *Ground I* and *Ground II*, respectively. Four square apertures are cut in the *Ground I*. Additional four holes are also cut in the *Ground II* for biasing purposes.

3) 32 p.i.n diode switches are soldered onto the antenna. 40 coaxial cables are vertically connected to the substrate through *Ground I*. It is noted that the *Ground I* cannot be removed from the antenna structure after this step unless all 40 coaxial cables are removed. Four DC bias wires are vertically connected to the middle of each *S*-band element.

4) *Ground II* is placed on *Ground I* by moving SMA connectors through the holes inside *Ground II*. The antenna radiating aperture, double-layer ground plane and 40 coaxial lines are firmly held together by the mounting structure.

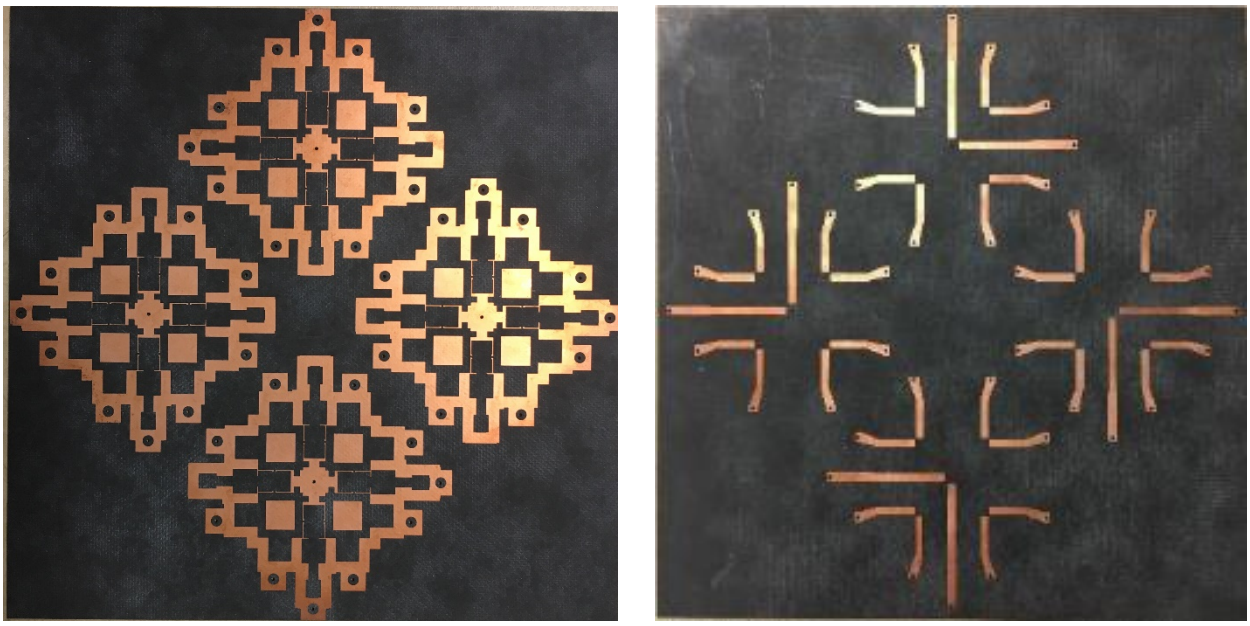

(a) (b)

Figure 5.9. (a) Aperture layer and (b) microstrip feed line layer of the 2×2 reconfigurable dual-polarized *S*-band antenna array in fabrication.

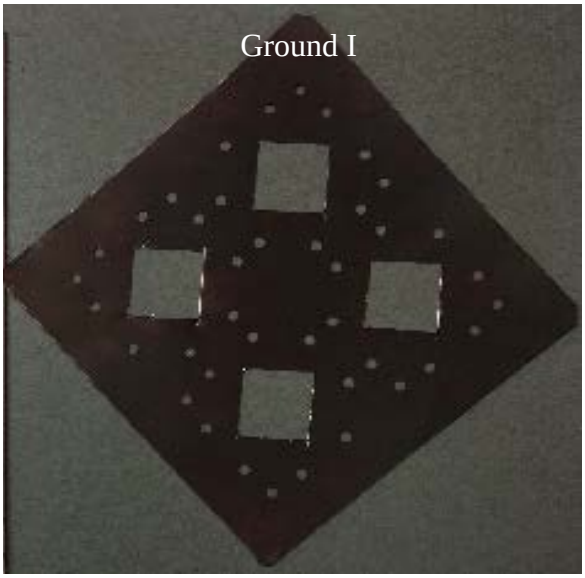

(a)

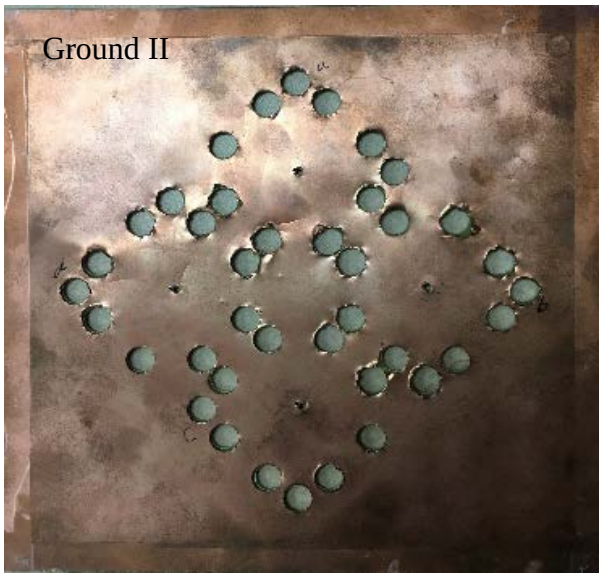

(b)

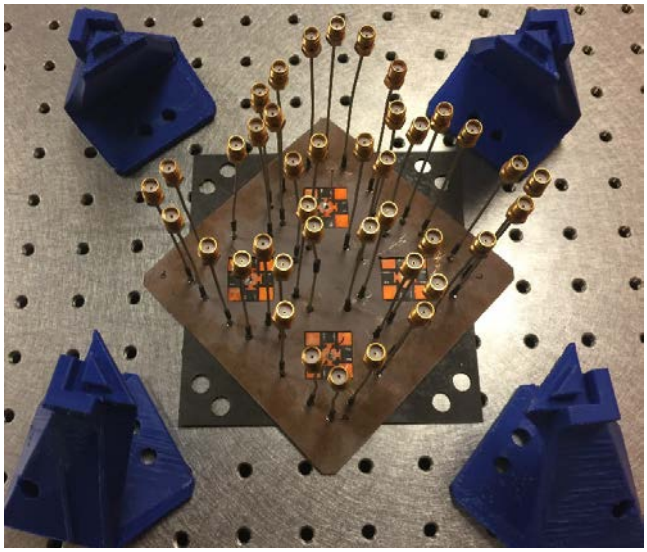

(c)

Figure 5.10. (a) *Ground I* and (b) *Ground II* before assembly. (c) Antenna aperture layer, *Ground I* and coaxial vertical cables in the middle. The blue plastics are part of the 3-D printed antenna array mounting structure.

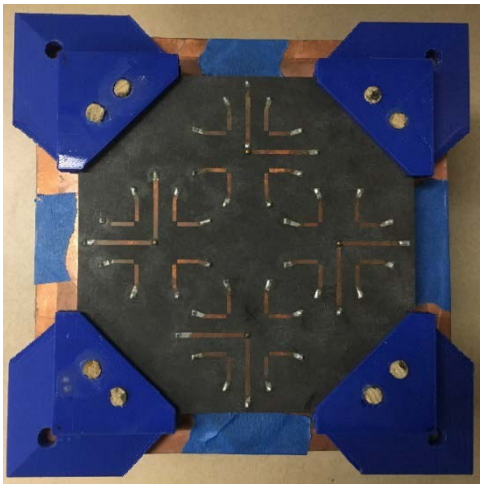

(a)

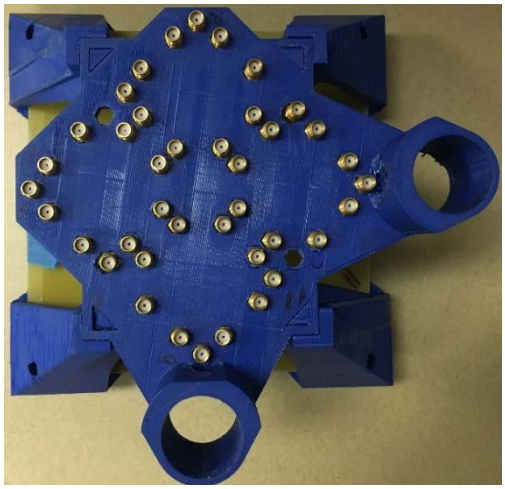

(b)

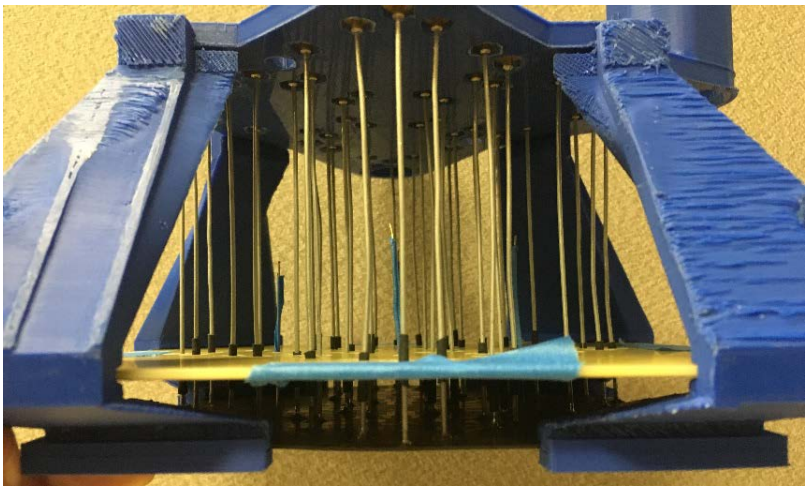

(c)

Figure 5.11. (a) Top, (b) bottom and (c) side view of the reconfigurable antenna array with the antenna mounting structure.

5.1.4 Simulation and Measurement Results

S-parameters, radiation patterns, gains and nonlinearity of the antenna array are measured in an anechoic chamber at both operating states.

5.1.4.1 S Parameters

The simulated and measured S_{a1a1} and S_{b4b4} for the antenna array in the *S*- and *C*-band operating states are illustrated in Figure 5.12(a) and (b), respectively. In the *S*-band state, the antenna shows 64.3% FBW when the switches are OFF. When the switches are ON, S_{a1a1} is higher than -1 dB showing that most of the energy is reflected back. In the *C*-band state, 66.7% FBW is obtained when the switches are ON. S_{b4b4} is approximately -5 dB when the switches are turned OFF in the *C*-band state. Due to the symmetric design of the antenna array, the return losses for all other ports are consistent with the results in Figure 5.12. The measured reflection coefficients for all eight ports of the 2×2 *S*-band antenna array (four ports in the horizontal polarization and four ports in the vertical polarization) when the switches are ON or OFF are illustrated in Figure 5.13(a). In the *C*-band state, the reflection coefficients for all 32 ports were measured when the switches are ON or OFF. Again, excellent consistency was observed. In Figure 5.13(b), the reflection coefficients for the eight *C*-band ports within the subarray "*a*" are shown.

This antenna array contains 40 ports, therefore, the isolation between different ports is another important parameter. In HFSS simulations and measurements, it is found that The coupling level between any two ports which are located inside different sub-arrays is below -18dB owing

to the narrow strip ground. Figure 5.14(a)-(c) presents three cases when the isolation is relatively worse. S_{a1a2} represents the isolation between the two polarization states at *S* band, which is less than -10 dB within most of the frequency band and rises to -5 dB at the lower edge of the band 2 GHz. S_{a1a3} (S_{a1a4}) represents the isolation between the adjacent ports at different bands, which is less than -8 dB at both *S*- and *C*-band operation states. S_{a1ai} (*i*=5-10) is less than -13 dB at both operating states. S_{a4a10} represents the isolation between the two polarization states at *C* band. The highest level is found to be -5 dB at *C* band.

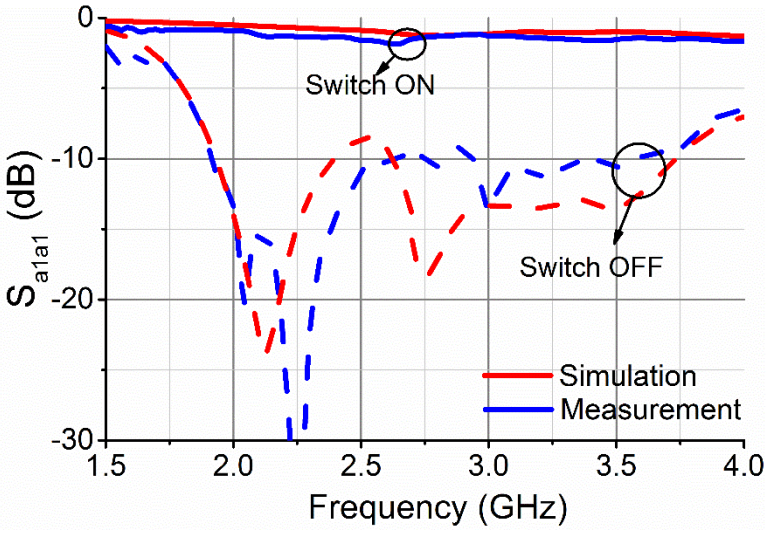

(a)

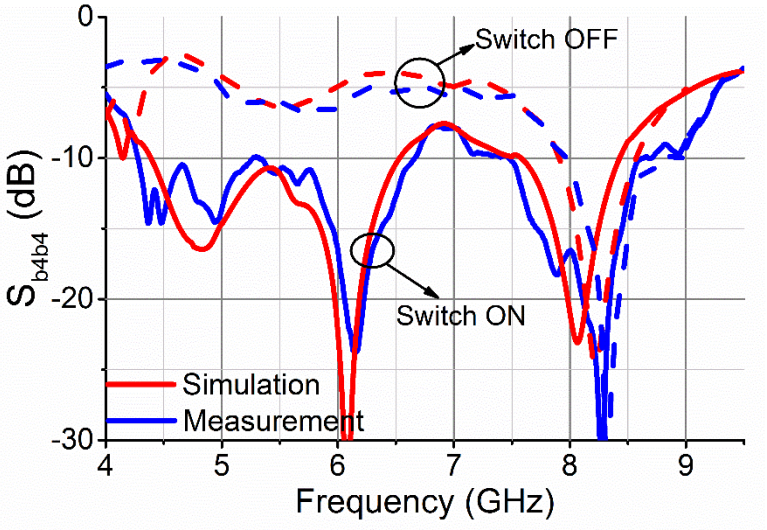

(b)

Figure 5.12. Simulated and measured (a) S_{a1a1} and (b) S_{b4b4} when the switches are ON (solid lines) or OFF (dash lines).

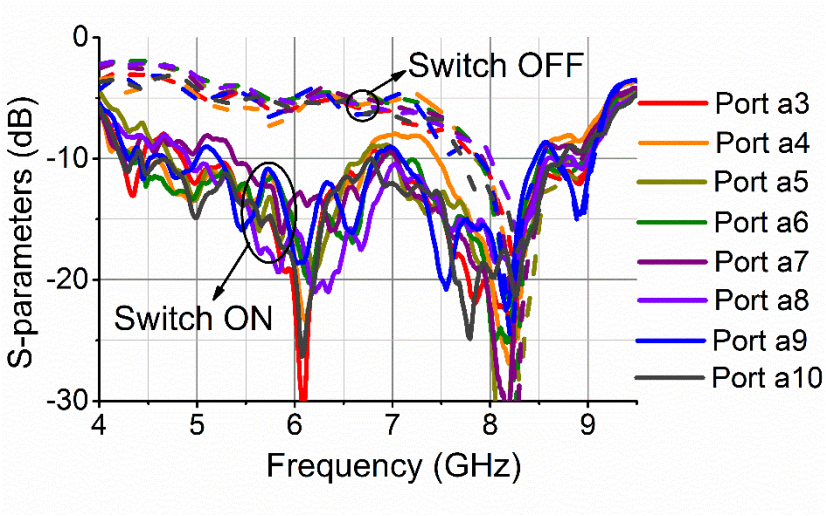

(a)

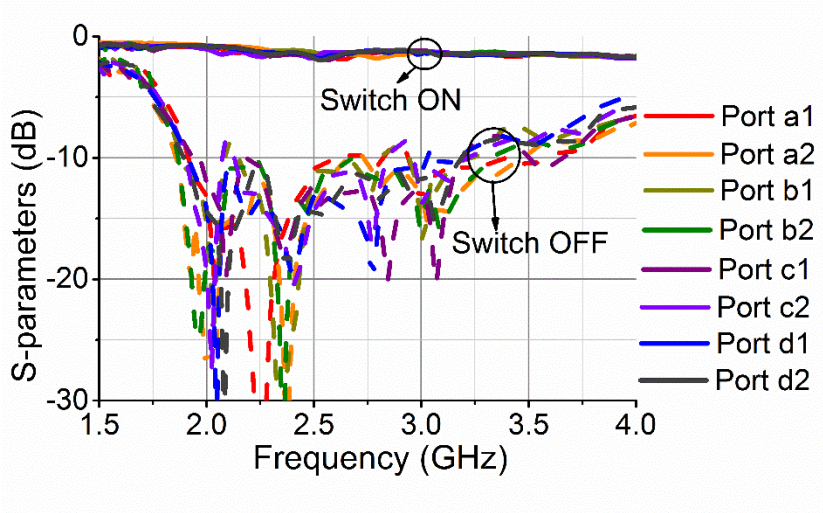

(b)

Figure 5.13. Measured S-parameters for (a) all eight *S*-band ports and (b) eight *C*-band ports of the antenna element “a”, when the switches are ON (solid lines) or OFF (dash lines).

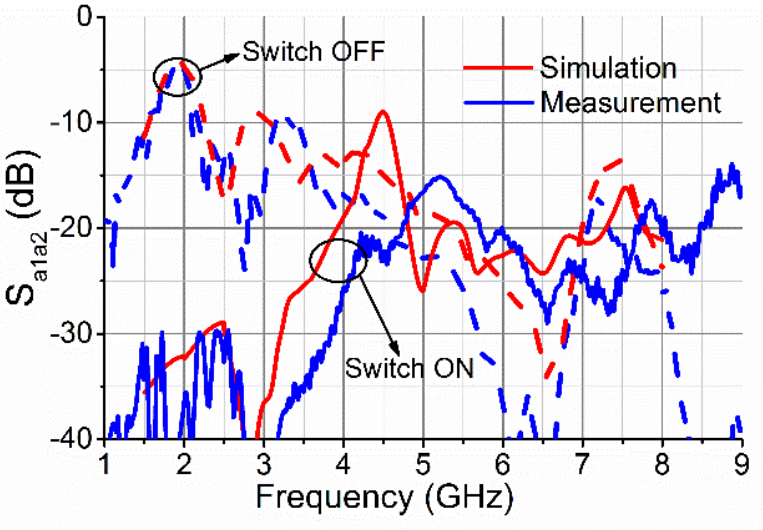
Switch OFF
Simulation
Measurement
Switch ON
S_{a1a2} (dB)
Frequency (GHz)
0
-10
-20
-30
-40
1
2
3
4
5
6
7
8
9

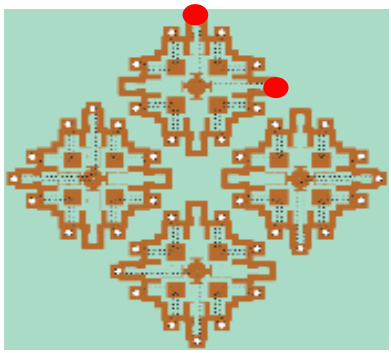

(a)

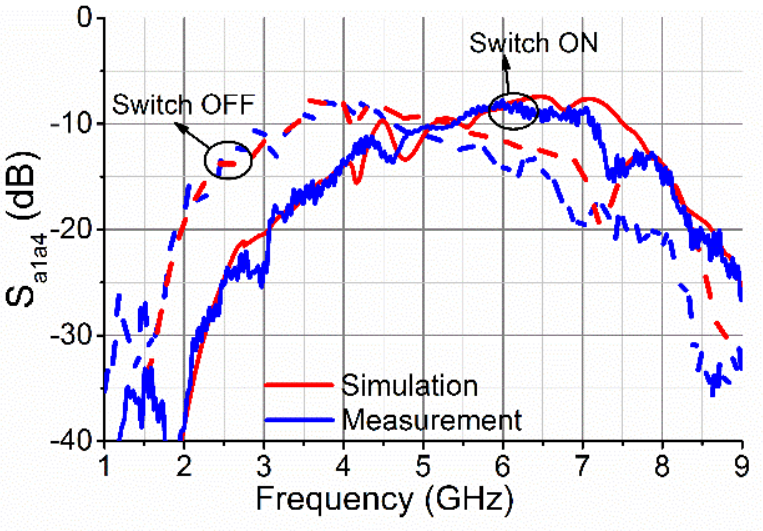
Switch ON
Switch OFF
Simulation
Measurement
S_{a1a4} (dB)
Frequency (GHz)
0
-10
-20
-30
-40
1
2
3
4
5
6
7
8
9

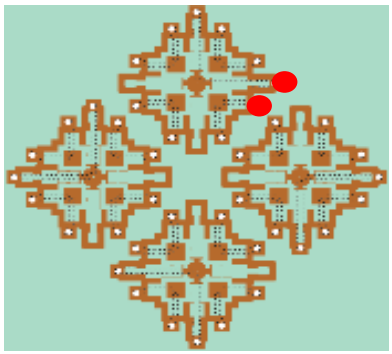

(b)

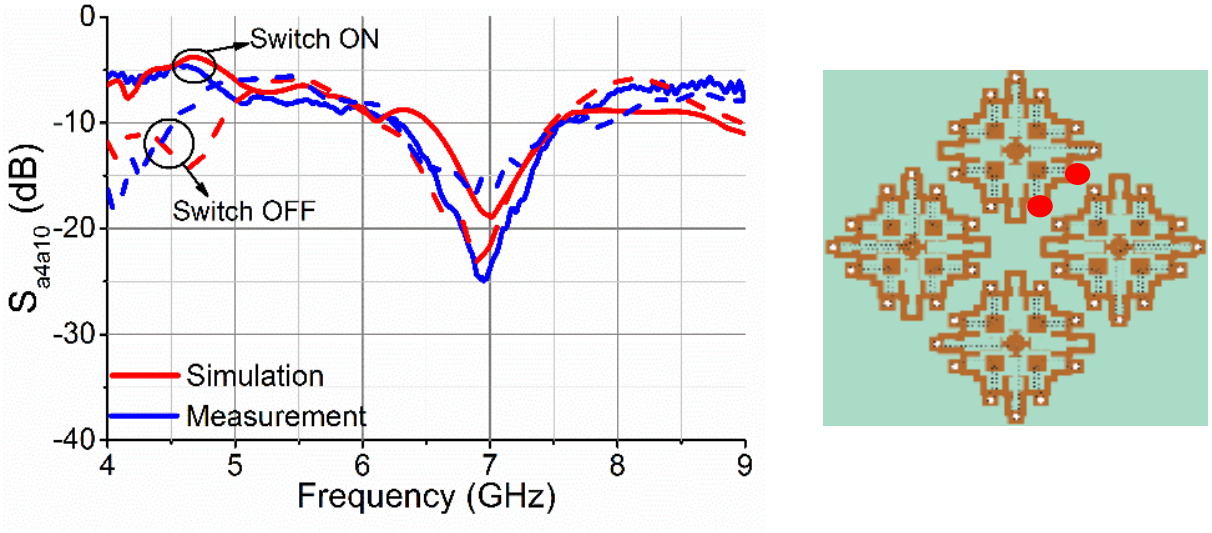

(c)

Figure 5.14. Simulated and measured mutual coupling between different ports. (a) S_{a1a2}, (b) S_{a1a4} and (c) S_{a4a10} when the switches are ON (solid lines) or OFF (dash lines).

5.1.4.2 Radiation Pattern

In the *S*-band state, in order to achieve the maximum radiation at boresight, a phase difference of 180° is required between the ports on the opposite sides of the array, i.e. ports a_1, d_1 (a_2, d_2) and ports b_1, c_1 (b_2, c_2) are 180° out of phase in the horizontal (vertical) polarization. A two-way power divider (RFLT2W2G08G from RF-Lambda) with two 180°-hybrids. (RFHB02G08GPI from RF-Lambda) are used to provide the required phase differences for the *S*-band array as shown in Figure 5.15. To achieve the maximum radiation at boresight in the *C*-band state, a phase difference of 180° is required between the ports on the opposite sides of the sub-array, i.e. ports $a_3/b_5/c_5/d_3/a_4/b_6/c_6/d_4$ ($a_7/b_7/c_9/d_9/a_8/b_8/c_{10}/d_{10}$) and ports $a_5/b_3/c_3/d_5/a_6/b_4/c_4/d_6$

($a_9/b_9/c_7/d_7/a_{10}/b_{10}/c_8/d_8$) are 180^o out of phase in the horizontal (vertical) polarization as illustrated in Figure 5.16(b). In this state, one two-way power divider, four four-way power dividers (RFLT4W2G08G from RF -Lambda) and two 180^o-hybrids are needed to provide the required phase differences. The simulated and measured co-polarization (co-pol.) and X-pol. radiation patterns in the E plane (y-z plane) and H plane (x-z plane) at both operating states are shown in Figures 5.17 and 5.18. In the *S*- and *C*-band states, the radiation patterns at 2.0/3.3 GHz and 4.5/7.3 GHz were measured in an anechoic chamber, respectively. At each frequency, the radiation patterns are normalized with respect to the maximum values. Good agreement between measured and simulated patterns is observed. The measured X-pol. level is 15 and 25 dB lower than the co-pol in the *S*- and *C*-band operating states, respectively. The biasing wires at the center of each *S*-band element is made to be perpendicular to the antenna aperture in order to minimize the X-pol. level. Well-behaved linear polarization and broadside radiation patterns are observed in Figures 5.17 and 5.18 over the entire *S* and *C* bands.

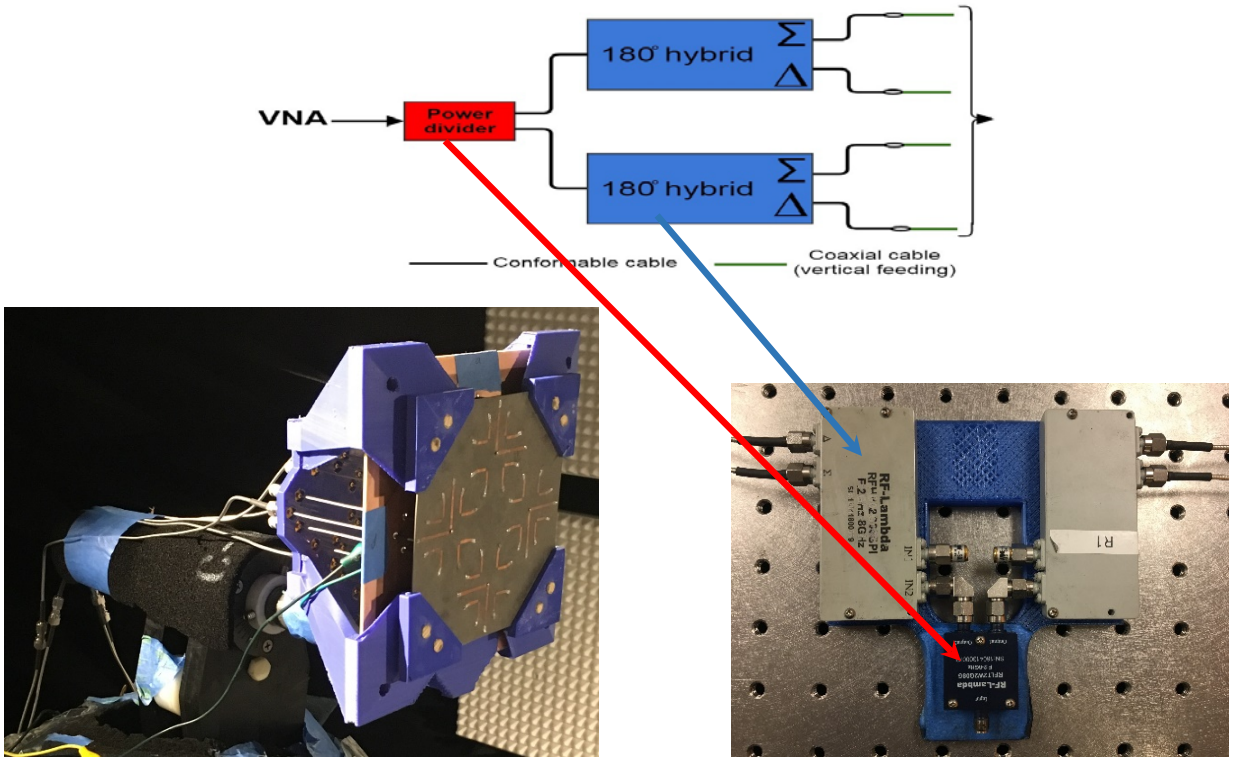

Figure 5.15. E-plane radiation pattern measurement setup of the 2×2 *S*-band array.

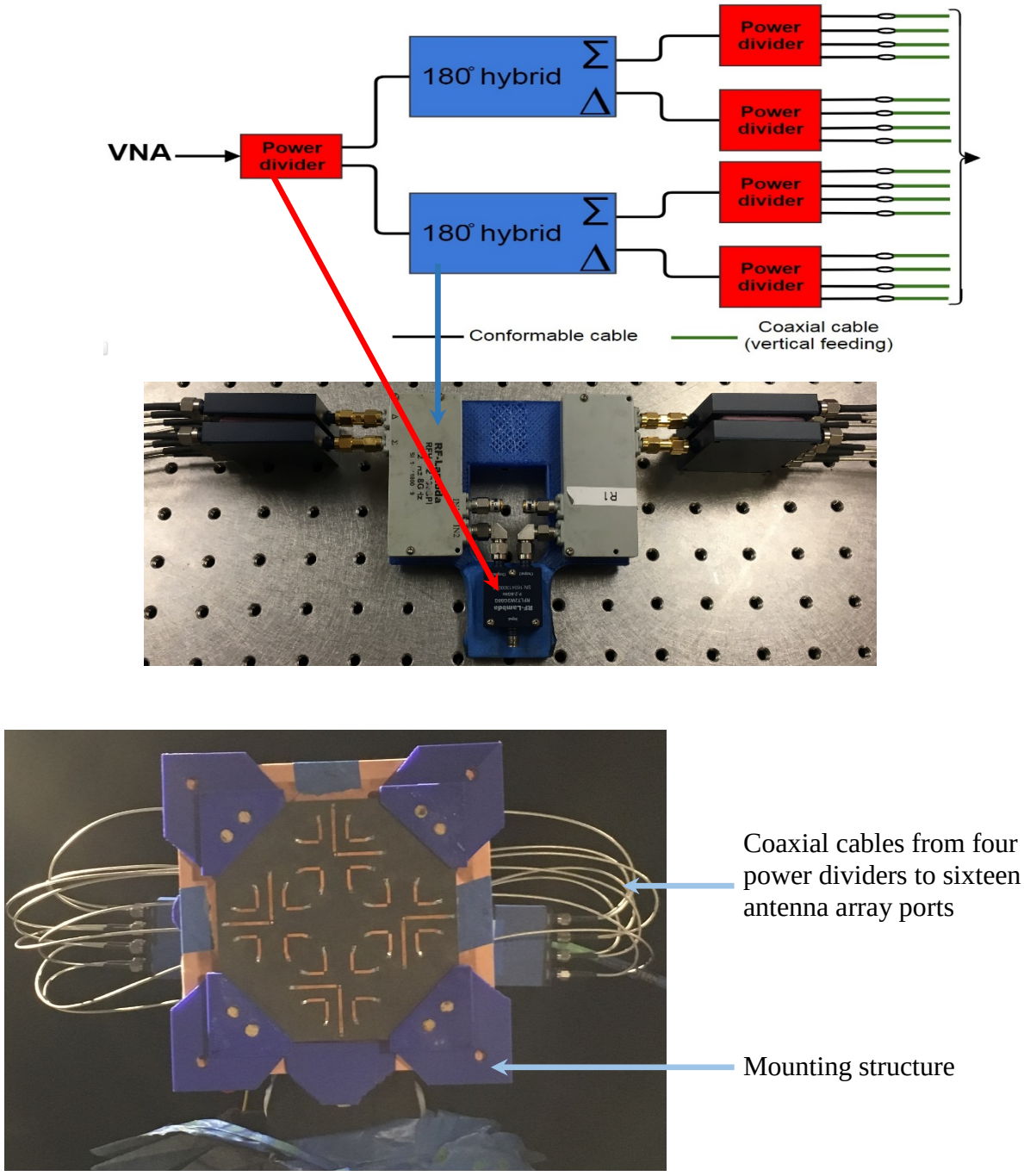

Figure 5.16. E-plane radiation pattern measurement setup of the 4×4 *C*-band array.

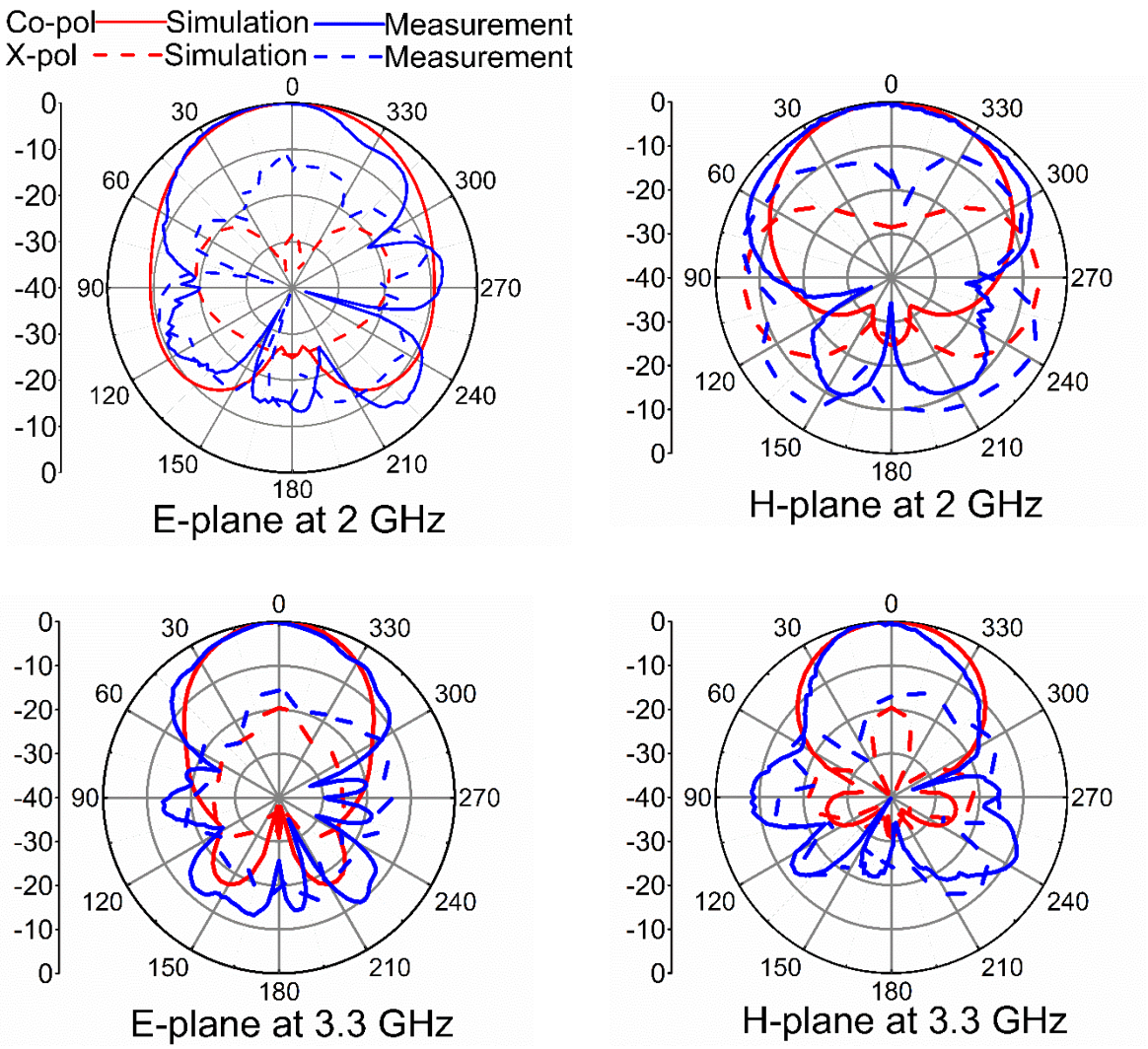

Figure 5.17. Co- and X-pol. radiation patterns of the reconfigurable dual-polarized antenna array at *S*-band operating state at 2 and 3.3 GHz.

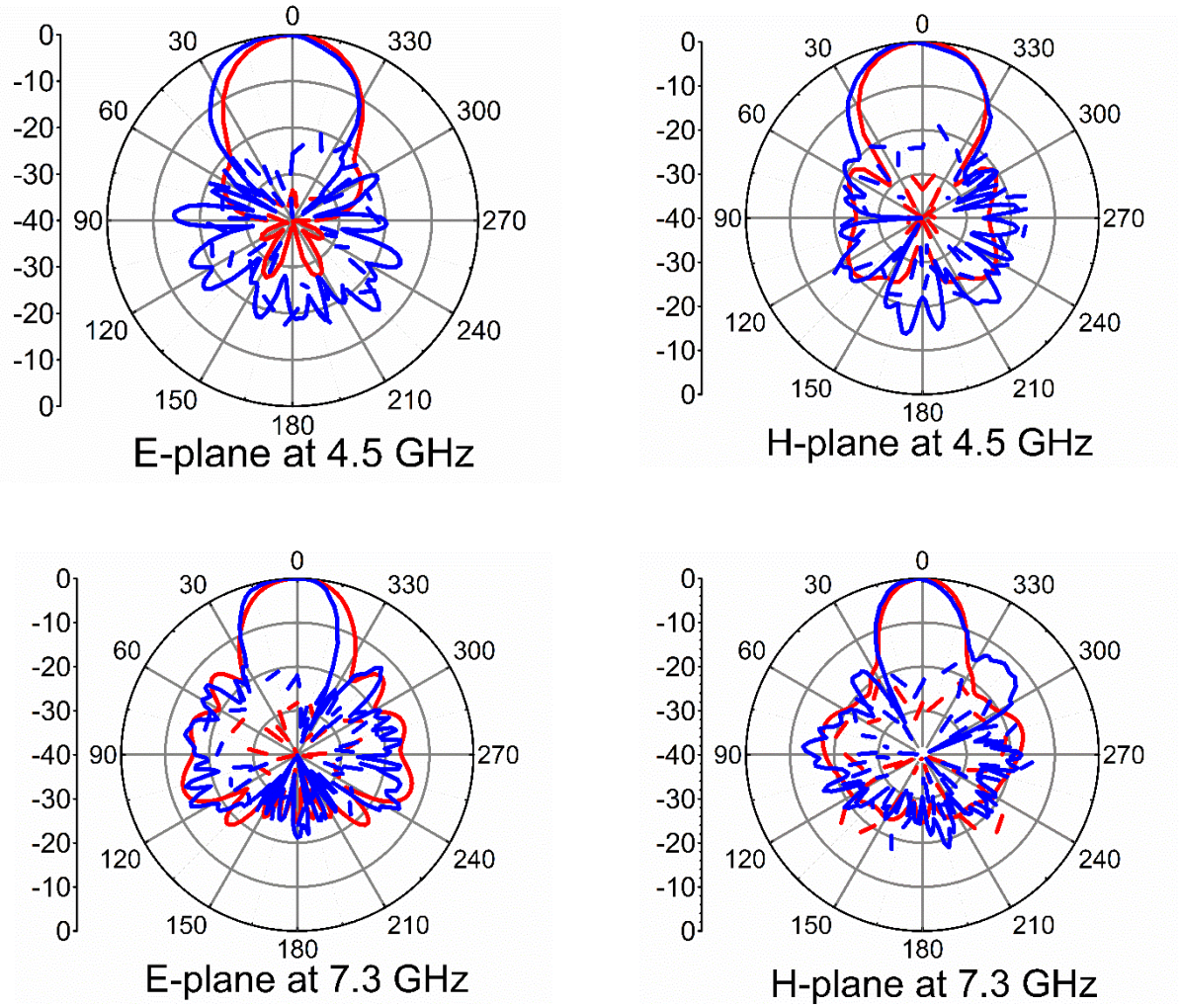

Figure 5.18. Co- and X-pol. radiation patterns of the reconfigurable dual-polarized antenna array at *C*-band operating state at 4.5 and 7.3 GHz.

5.1.4.3 Realized Gain

Simulated and measured realized gains, radiation efficiencies and total efficiencies in the *S*- and *C*-band states are demonstrated in Figure 5.19(a) and (b), respectively. As it is seen from

this figure, the realized gain of the 4×4 *C*-band array is approximately 6 dB higher than that of the 2×2 *S*-band array which is due to the array factor of the *C*-band array. Realized gain includes the mismatch loss from the active ports and also the mutual coupling from the active ports to the non-active ports. The radiation efficiency of an antenna (η) is equal to the absolute gain divided by the directivity while the total efficiency is the realized gain divided by the directivity. The radiation efficiencies of the 2×2 array in the *S* band and 4×4 array in the *C* band are higher than 72% and 85%, respectively. It is noted that in the *S*-band state, eight p.i.n diodes are included in the electric current path with a single *S*-band antenna element. However, only two p.i.n diodes are involved in forming a *C*-band antenna element in the *C*-band state. Therefore, the antenna radiation efficiency in the *C* band is higher than that in the *S* band. The total efficiency of the antenna/array versus frequency in the *S* and *C* bands are also shown in Figure 5.19(a) and (b), respectively. More details on calculating the realized gain and total efficiency of the antenna element in the *S*- and *C*-band operating states can be found in 4.2.2.3. The variations of the realized gain over the frequency are 8.3 and 6.5 dB in the *S*- and *C*-band operating state, respectively.

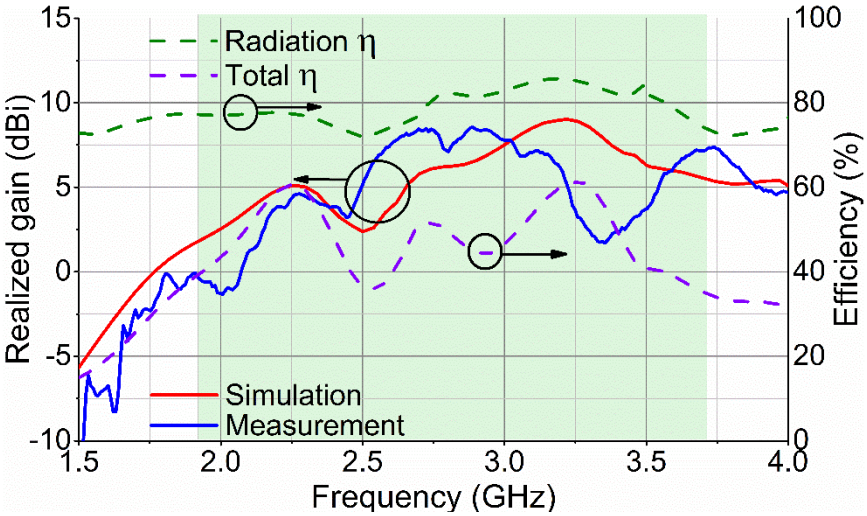

(a)

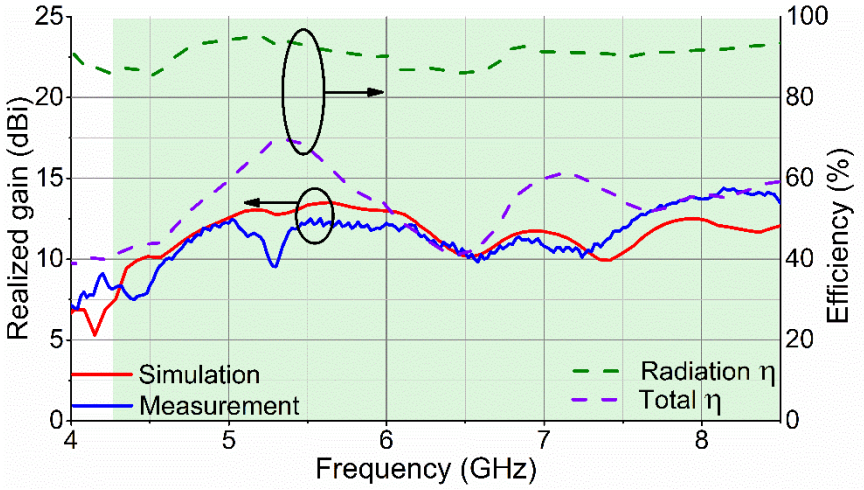

(b)

Figure 5.19. Simulated and measured realized gain, simulated radiation efficiency and total efficiency of the reconfigurable dual-polarized antenna array at (a) *S*- and (b) *C*-band operating states.

5.1.4.4 Nonlinearity

The nonlinearity performance of the antenna array is tested by measuring IIP_3 of a subarray. The 2×2 *C*-band array is characterized in the *C*-band state for two reasons. First, since the radiation pattern of a single *C*-band antenna is slightly tilted from the boresight, a 2×2 *C*-band array is able to direct the main beam towards the boresight due to the symmetry inside it. Second, a 2×2 *C*-band array exhibits 6 dB higher gain than a single *C*-band element which is critical to ensure that received power at the spectrum analyzer is much higher than the noise floor. The power delivered to a single *C*-band antenna element, which is 25% of that delivered to the 2×2 *C*-band array, is considered as the input power in Figure 5.20. As shown in Figure 5.20(a), two amplifiers (Amps) (ZX60-83LN-s+ from Mini-Circuits), two isolators (ISOs) (RFLI-402-4 from RF-Lambda), and one two-way power divider are used. The losses inside the feeding network and cables, which were described in 5.1.4.2, are de-embedded from the measurement results. In the *S*-band state, a single *S*-band antenna element is characterized without the amplifiers and the feeding network, since the radiation pattern of an *S*-band antenna element is towards the boresight.

As shown in Figure 5.20(b)-(d), the measured IIP_3 at f_0 = 2.5 GHz in the *S*-band operating state is 53.8 dBm (10V reverse bias), 57.2 dBm (25V reverse bias) and 59.7 dBm (50V reverse bias), respectively. The measured IIP_3 at f_0 = 6 GHz in the *C*-band operating state is 54.5 dBm (10mA forward bias current), as shown in Figure 5.20(e).

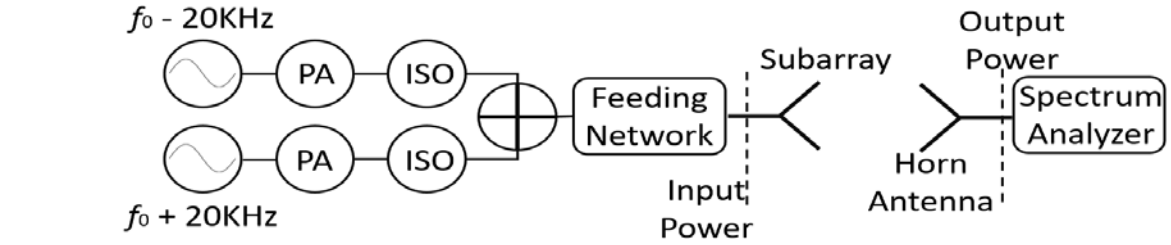

(a)

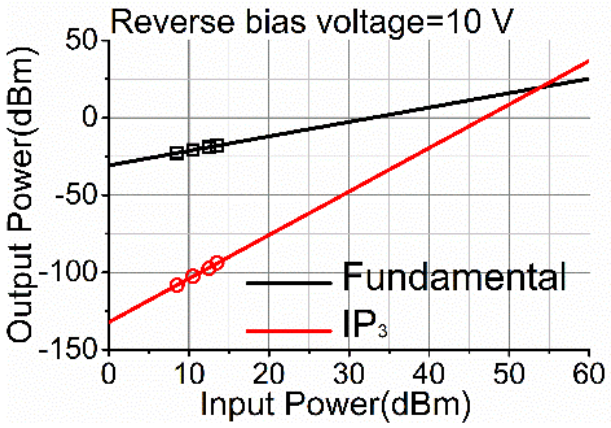

(b)

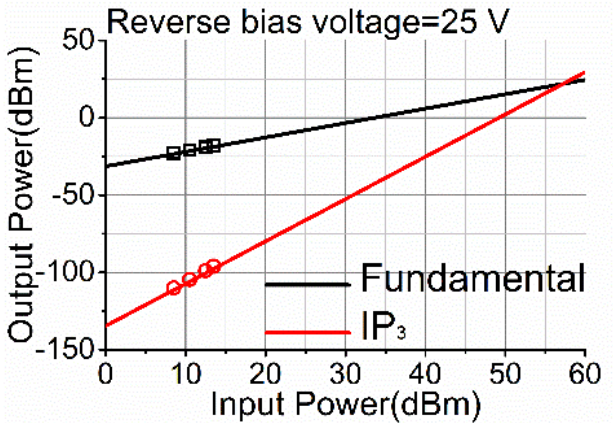

(c)

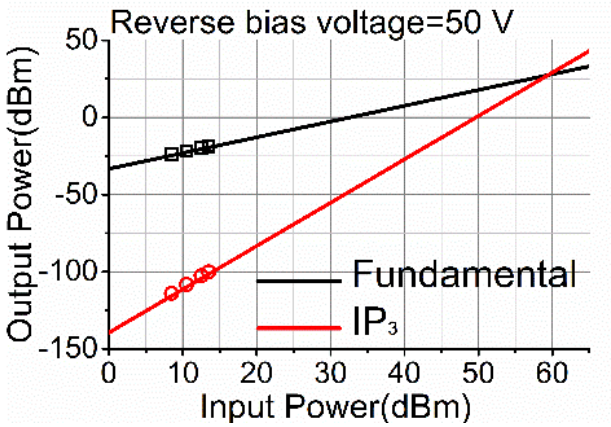

(d)

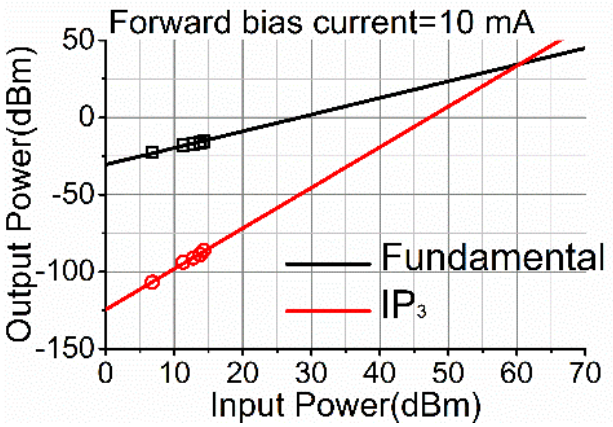

(e)

Figure 5.20. (a) Measurement setup for IIP_3. IIP_3 of *S*-band operation state with (b) 10V reverse bias, (c) 25V reverse bias, (d) 50V reverse bias and (e) of *C*-band operation state with a 10mA forward bias current.

5.1.4.5 Beam Scanning

The beam scanning of a 10×10 *S*-band array which can be reconfigured to a 20×20 *C*-band array is studied in this section. In the *S*-band operating state, the 2-D and 3-D radiation patterns of a single *S*-band element are extracted from HFSS simulations and multiplied by the array factor of a triangular lattice using MATLAB. Figure 5.21 demonstrates the beam scanning up to ±60^{o} in the principal planes and ±40^{o} in the diagonal plane at 3.7 GHz, without grating lobes. From Figure 5.21(c), it is observed that the grating lobes start to appear when the main beam is scanned to ±40^{o}, which was predicted from the calculations in 5.1.2. In the *C*-band state, the 2-D and 3-D radiation patterns of a 2×2 *C*-band sub-array are extracted from HFSS and multiplied by the array factor of a triangular lattice in MATLAB. 2-D radiation patterns of the reconfigurable dual-polarized antenna array at *C*-band operating state are illustrated in Figure 5.22. The maximum beam scan angle in the principal planes and diagonal plane is ±35^{o} and ±25^{o} at 7.6 GHz, respectively. Fig. 21 shows the 3-D plot when the main beam of the *C*-band array is scanned to 40^{o} in either E- or H-plane at 7.6 GHz. It is seen that grating lobes start to show up but in other planes. The beam scan angles can be increased at *C* band if the antenna element is smaller in terms of wavelength by using a higher-dielectric-constant

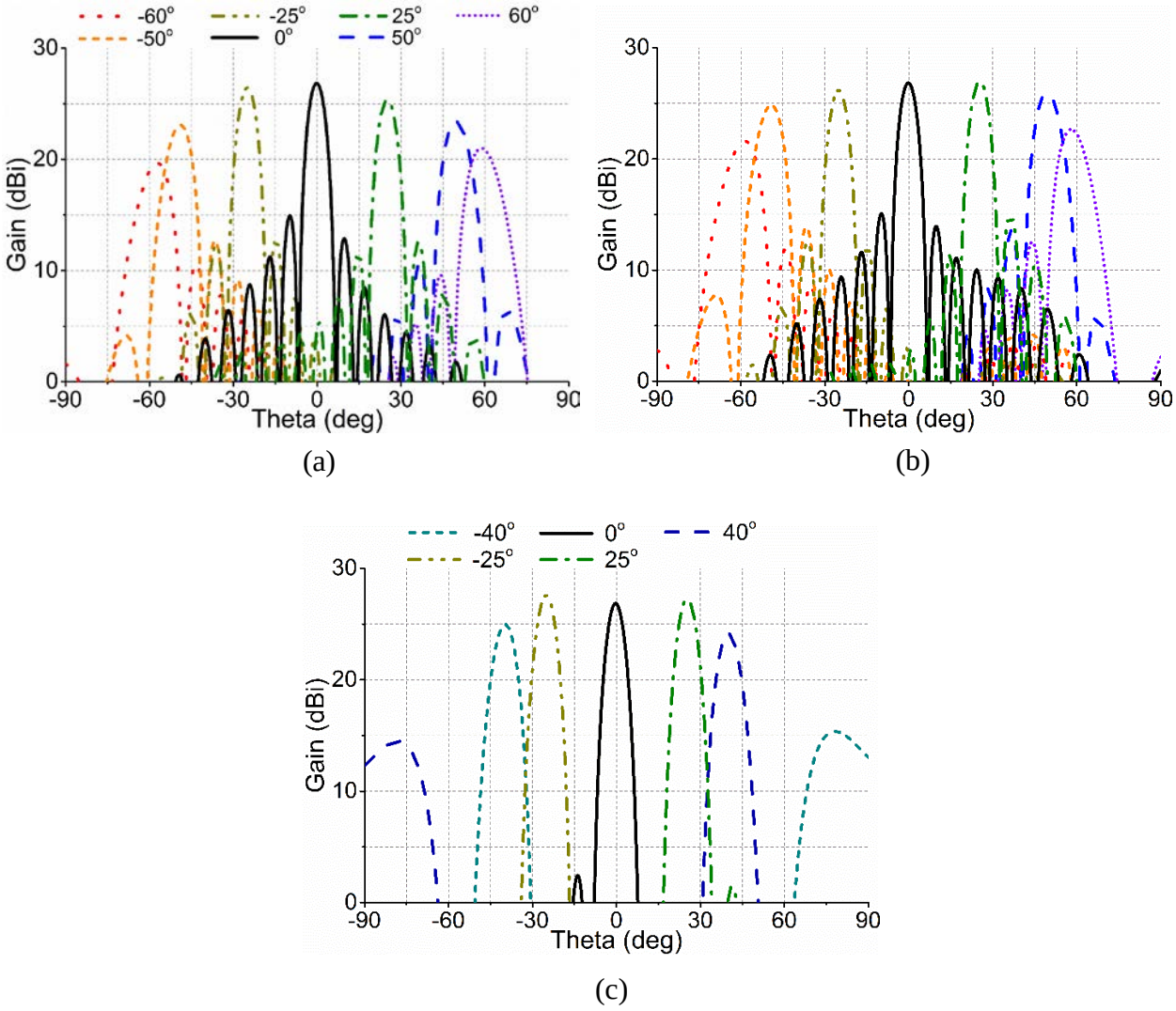

Figure 5.21. Beam steering of the reconfigurable dual-polarized antenna array at *S*-band operating state at 3.7 GHz in the (a) H plane, (b) E plane, and (c) diagonal plane.

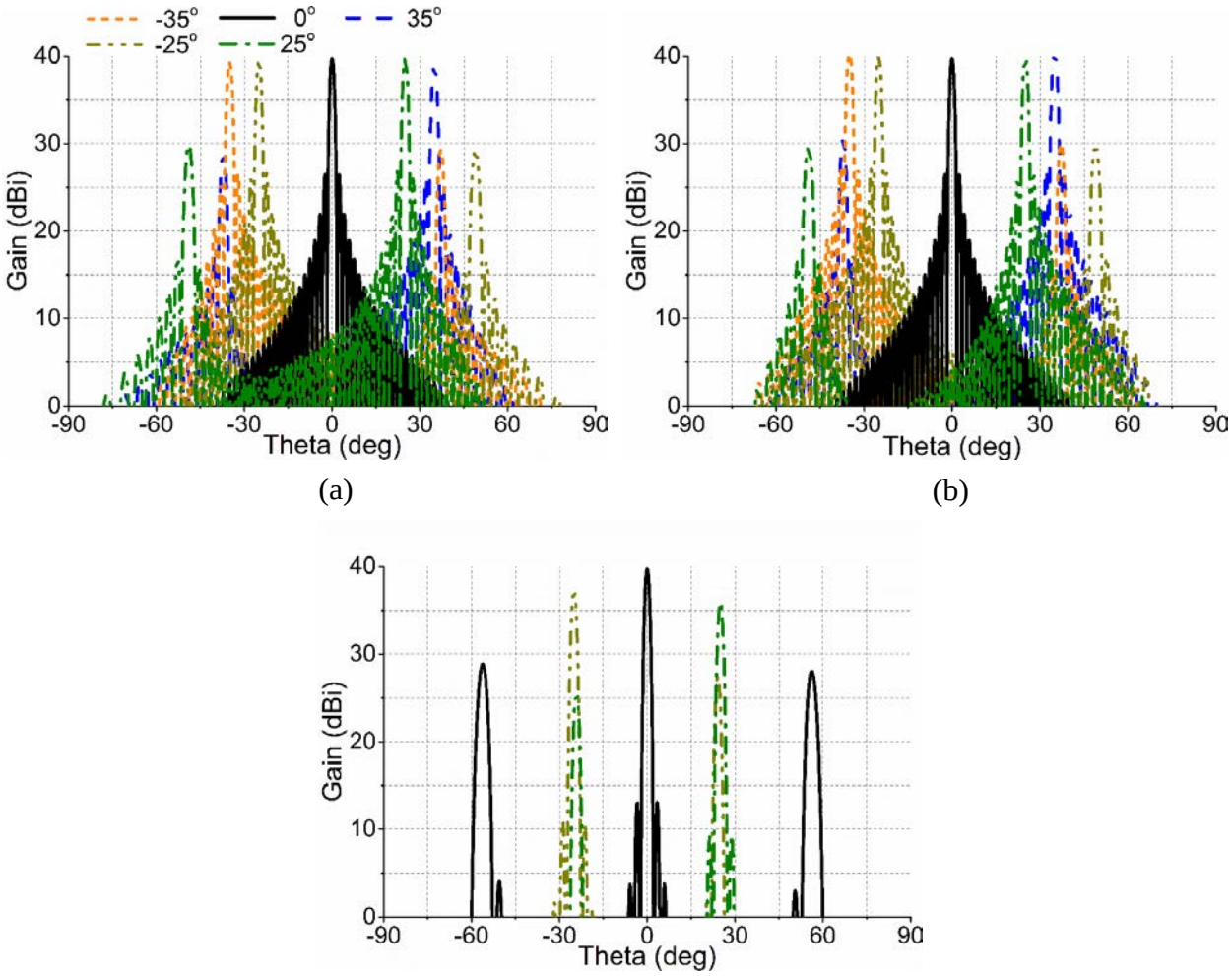

Figure 5.22. Beam steering of the reconfigurable dual-polarized antenna array at *C*-band operating state at 7.6 GHz in the (a) H plane, (b) E plane, and (c) diagonal plane.

To highlight the advantages of the reconfigurable dual-polarized phased array antenna in this paper compared with other wideband, UWB or multi-band phased array antennas in Table 5-1,

key antenna parameters such as array profile, FBW, polarization, scanning volume, radiation efficiency, modularity, X-pol. level, and the type of T/R modules are presented.

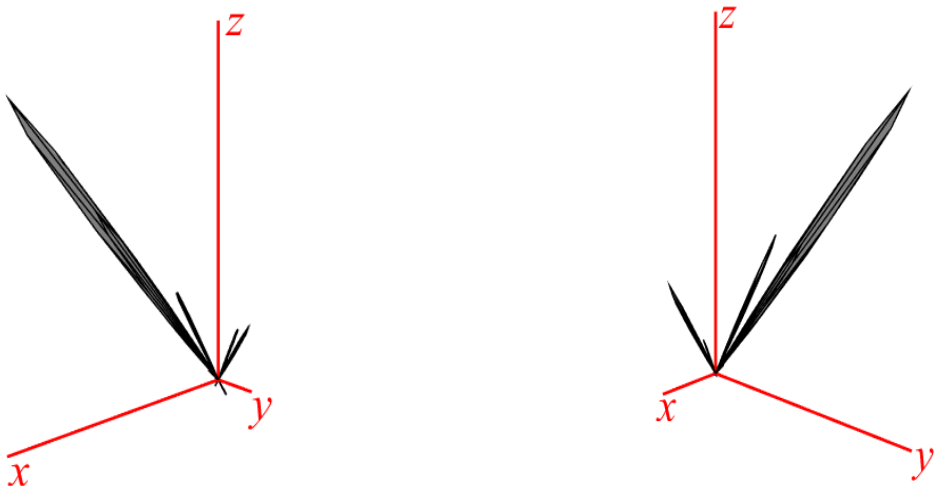

(a) (b)

Figure 5.23 3-D plot of the scanned beam to 40° at *C*-band operating state at 7.6 GHz in the (a) H and (b) E plane.

Table 5-1. Comparison between the reconfigurable dual-polarized phased array antenna in this paper and wideband, UWB or multi-band phased array antennas.

	Profile	**FBW**	**Pol.**	**Scan volume in principal planes**	**Radiation efficiency**	**Modularity**	**X-pol. in principal planes (dB)**	**T/R module**	**Comment**
[70]	$0.53\times\lambda_H$	44%	Single LP	60°	93%	No	-17	With less than octave bandwidth	-

	Profile	**FBW**	**Pol.**	**Scan volume in principal planes**	**Radiation efficiency**	**Modularity**	**X-pol. in principal planes (dB)**	**T/R module**	**Comment**
[22]	$0.46\times\lambda_H$	133%	Dual LP	45°	90%	Yes (with precise machining)	-7	UWB	-
[25]	$1.03\times\lambda_H$	143%	Dual LP	60°	90%	No	-25	UWB	Poor VSWR when scanned in the principal planes
[27]	$3.5\times\lambda_H$	155%	Dual LP	45°	90%	Yes	-17	UWB	High X-pol. and poor VSWR when scanned in the diagonal plane
[34]	$0.50\times\lambda_H$	160% (VSWR <3)	Dual LP	45°	-	Yes	-15	UWB	Poor VSWR when scanned in the H-plane
[14]	-	5%/22%	Single LP	60°	-	Yes	-25	With one octave bandwidth	Limited to single polarization. Limited bandwidth
Reconfigurable wideband antenna array in Chapter 5	$0.42\times\lambda_H$	64%/67% in the *S*-/*C*-band state	Dual LP	60°/35° in the *S*-/*C*-band state	72%/85% in the *S*-/*C*-band state	Yes	-15/-25 in the *S*-/*C*-band state	With octave bandwidth	-

5.2 Conclusion

A novel reconfigurable dual-polarized antenna array covering *S* and *C* bands in two operating states has been presented. Separate feeding for each band allows for the use of high-performance single-band T/R modules instead of UWB T/R modules. Vertical coaxial to microstrip transition is used to form a 2×2 *S*-band (4×4 *C*-band) antenna array. 32 p.i.n diode switches are mounted on the aperture layer of the antenna array to switch the operating state. The polarization reconfigurability is achieved by exciting either horizontal or vertical ports appropriately. This antenna array shows 64.3% and 66.7% FBW with constant radiation patterns

and relatively-flat realized gains over the frequency. The minimum radiation efficiencies are found to be 72% and 85% in the *S*- and *C*-band states, respectively. Triangular and rectangular-triangular array lattices allow for ±60^{o} and ±35^{o} beam scanning with no grating lobes in the principal planes at 3.7 and 7.6 GHz, respectively. The IIP_3 of the antenna array is better than 54 dBm in both operating states.

CHAPTER 6: RECONFIGURABLE WIDEBAND ANTENNA ELEMENT COVERING *S*, *C* AND *X* BANDS

To further extend the idea of reconfigurable wideband antenna element presented in Chapter 4, an antenna element covering three frequency bands is presented in this chapter. The number of parameters to optimize in a tri-band antenna array is increased compared to the dual-band design. To optimize the tri-band antenna array with good response in each state, we have to consider each of these parameters. This chapter is divided into two sections. In the first section, a tri-band antenna element with microstrip feeding is studied. This antenna element is able to cover three adjacent bands with separate feeding. In the second sub-section, a tri-band antenna element with vertical coaxial feeding is designed and simulated.

6.1 Tri-band Antenna Element with microstrip feeding

Figure 6.1 shows the schematic view of the tri-band fractal-shaped antenna element with microstrip feeding. After careful optimization, this antenna element should demonstrate 67%/67%/40% fractional bandwidth (FBW) in the *S*-/*C*-/*X*-band operating states, respectively, with relatively flat gain vs. frequency in each state.

6.1.1 Parametric Study of the Tri-Band Antenna Element

Several parameters are defined in Figure 6.1 for the tri-band antenna element. The effects of each parameter on the return loss in *S*, *C*, and *X* bands is studied. The effects of some selected parameters on the antenna is illustrated in Figure 6.2. The length of the slot-ring in the *S*-band (L_S),

C-band (L_C), and *X*-band (L_X), and the length of fractal shapes (L_{fS}, L_{fC}) are changing and their effects on the antenna performance is shown.

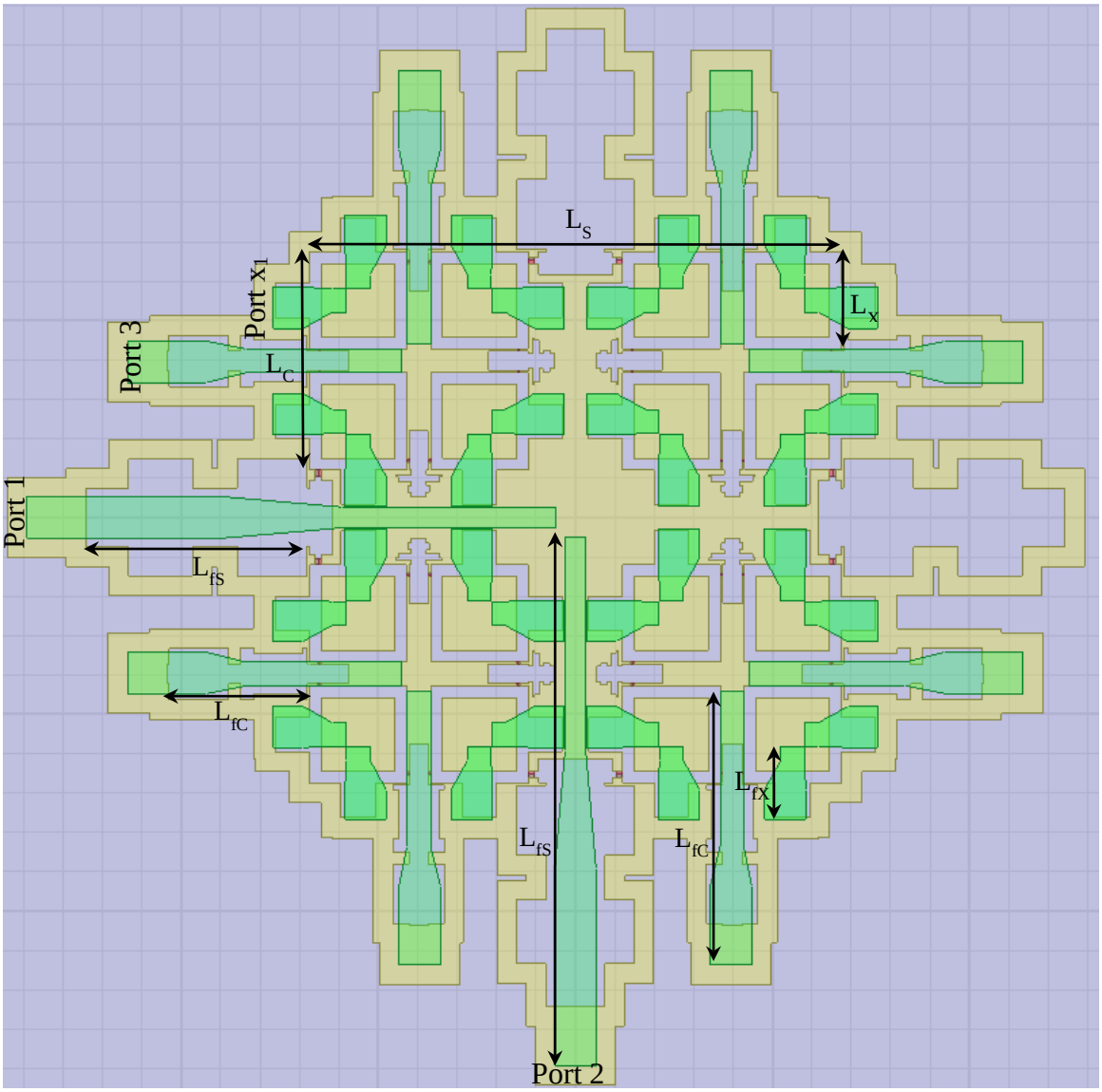

Figure 6.1. Schematic view of the tri-band antenna/array.

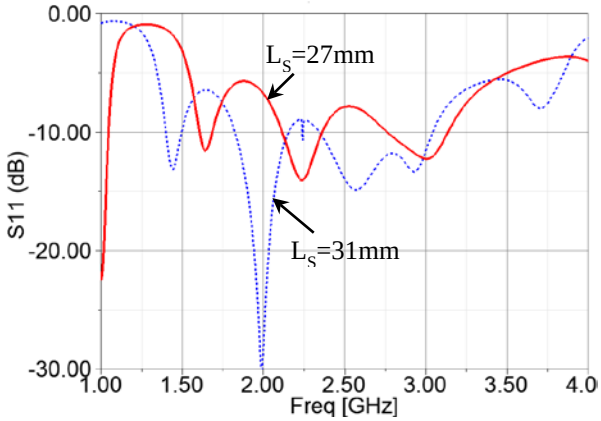
0.00
-10.00
-20.00
-30.00
S11 (dB)
1.00
1.50
2.00
2.50
3.00
3.50
4.0
Freq [GHz]
L_S=27mm
L_S=31mm

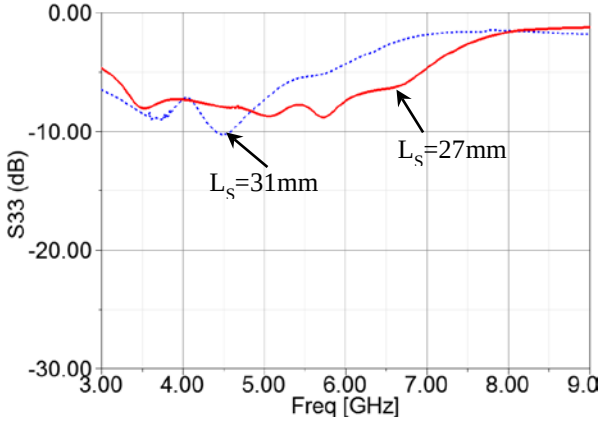
0.00
-10.00
-20.00
-30.00
S33 (dB)
3.00
4.00
5.00
6.00
7.00
8.00
9.0
Freq [GHz]
L_S=31mm
L_S=27mm

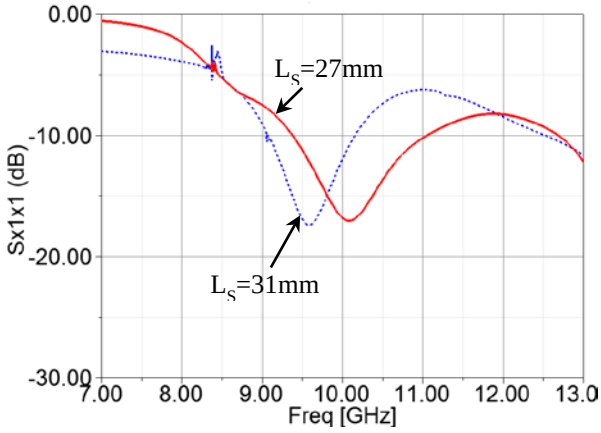
0.00
-10.00
-20.00
-30.00
Sx1x1 (dB)
7.00
8.00
9.00
10.00
11.00
12.00
13.0
Freq [GHz]
L_S=27mm
L_S=31mm

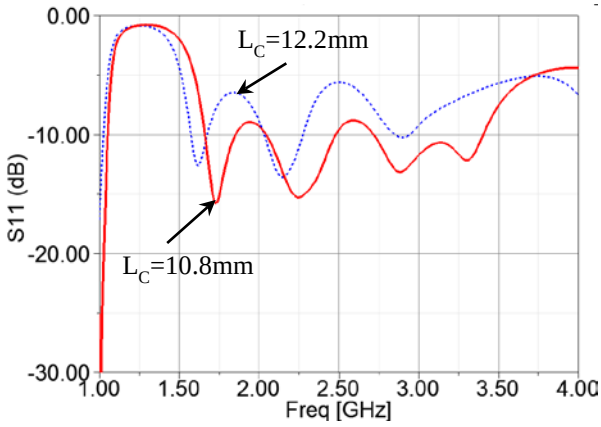
0.00
-10.00
-20.00
-30.00
S11 (dB)
1.00
1.50
2.00
2.50
3.00
3.50
4.00
Freq [GHz]
L_C=12.2mm
L_C=10.8mm

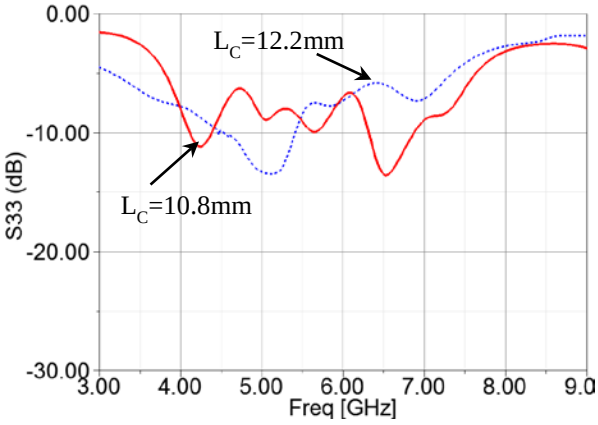
0.00
-10.00
-20.00
-30.00
S33 (dB)
3.00
4.00
5.00
6.00
7.00
8.00
9.0
Freq [GHz]
L_C=12.2mm
L_C=10.8mm

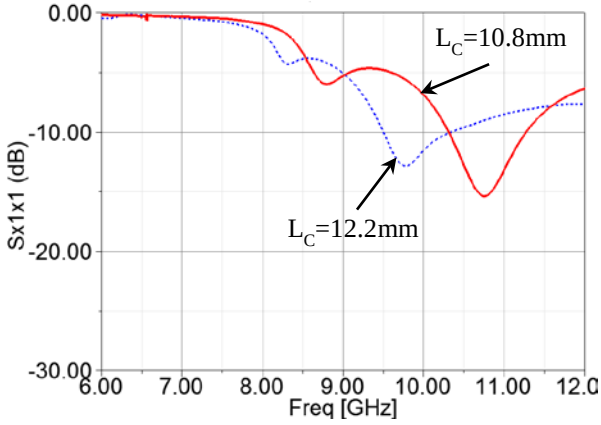
0.00
-10.00
-20.00
-30.00
Sx1x1 (dB)
6.00
7.00
8.00
9.00
10.00
11.00
12.0
Freq [GHz]
L_C=10.8mm
L_C=12.2mm

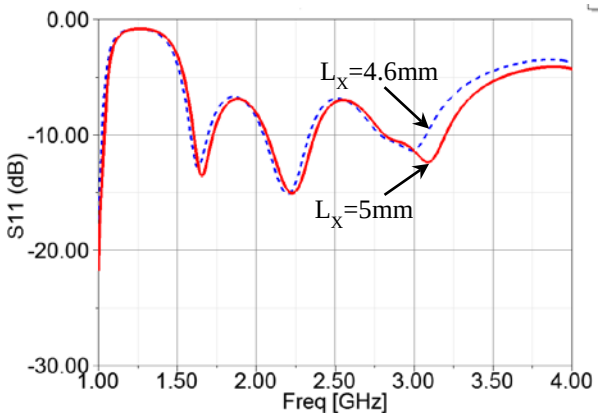
0.00
-10.00
-20.00
-30.00
S11 (dB)
1.00
1.50
2.00
2.50
3.00
3.50
4.00
Freq [GHz]
L_X=4.6mm
L_X=5mm

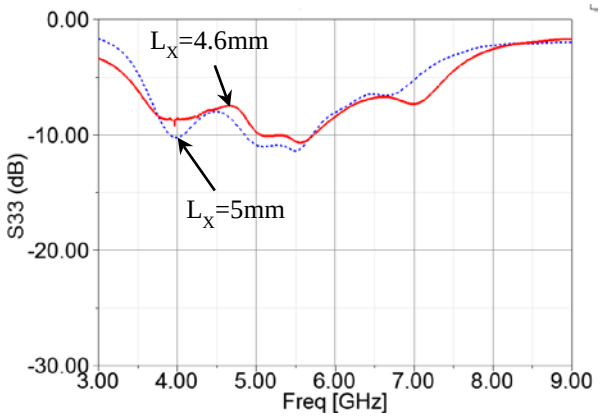
0.00
-10.00
-20.00
-30.00
S33 (dB)
3.00
4.00
5.00
6.00
7.00
8.00
9.00
Freq [GHz]
L_X=4.6mm
L_X=5mm

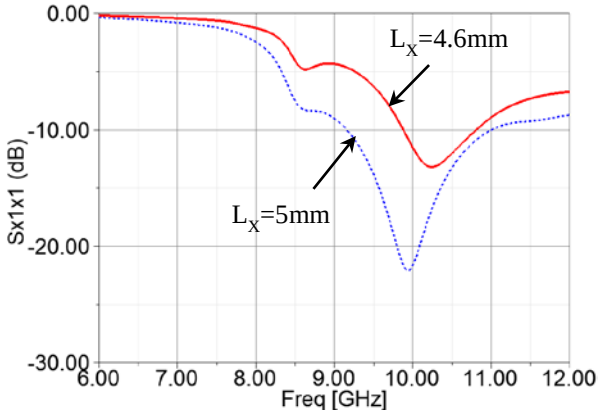
0.00
-10.00
-20.00
-30.00
Sx1x1 (dB)
6.00
7.00
8.00
9.00
10.00
11.00
12.00
Freq [GHz]
L_X=4.6mm
L_X=5mm

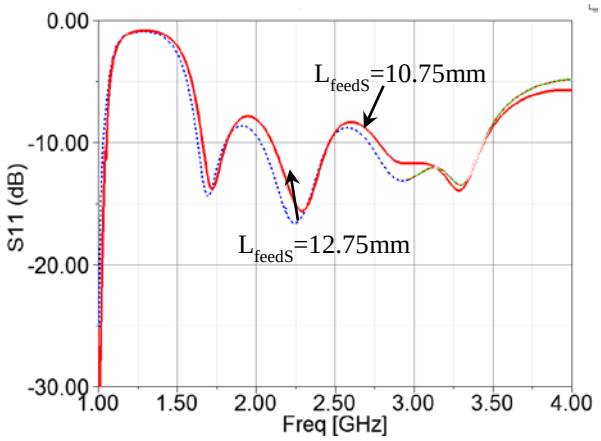
0.00
-10.00
-20.00
-30.00
S11 (dB)
1.00
1.50
2.00
2.50
3.00
3.50
4.00
Freq [GHz]
L_{feedS}=10.75mm
L_{feedS}=12.75mm

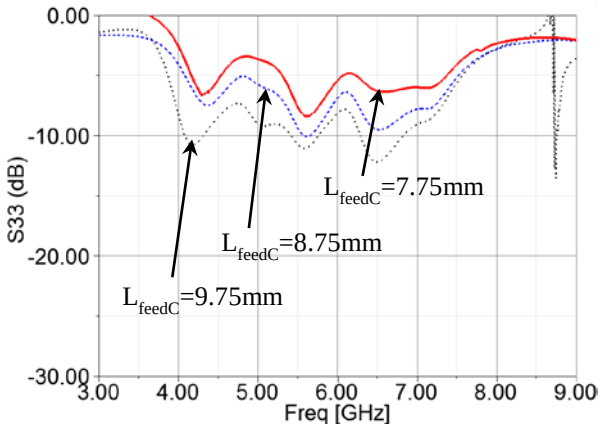
0.00
-10.00
-20.00
-30.00
S33 (dB)
3.00
4.00
5.00
6.00
7.00
8.00
9.00
Freq [GHz]
L_{feedC}=7.75mm
L_{feedC}=8.75mm
L_{feedC}=9.75mm

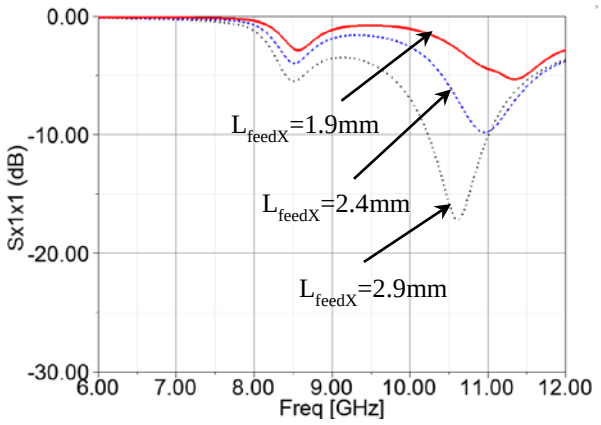
0.00
-10.00
-20.00
-30.00
Sx1x1 (dB)
6.00
7.00
8.00
9.00
10.00
11.00
12.00
Freq [GHz]
L_{feedX}=1.9mm
L_{feedX}=2.4mm
L_{feedX}=2.9mm

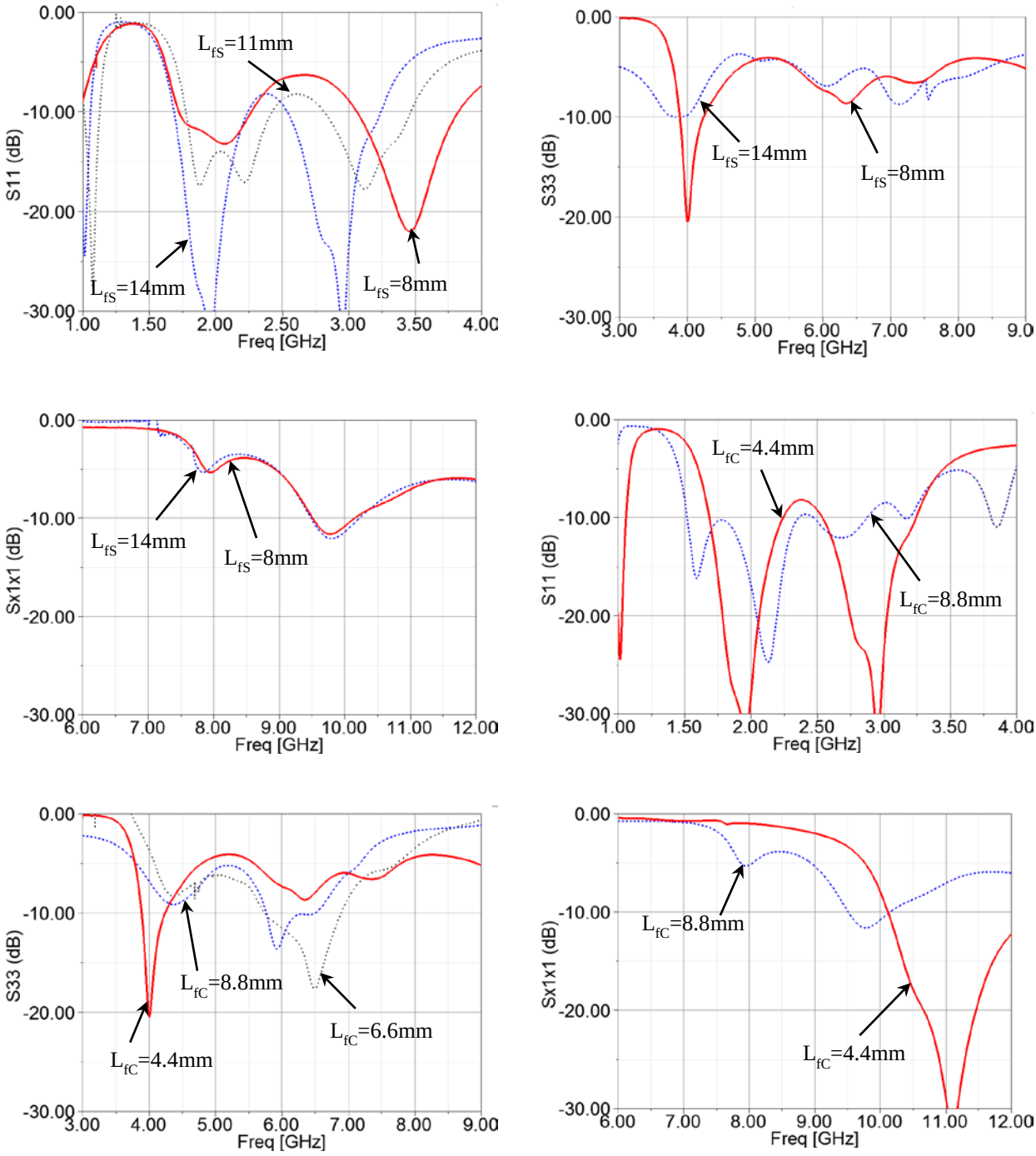

Figure 6.2. Parametric study of the tri-band antenna element for different values of L_S, L_C, Lx, L_{feedS}, L_{feedC}, L_{feedX}, L_{fS}, L_{fC}.

6.1.2 Effects of Distance Between the Ground Plane and Radiator On the Gain of Tri-Band Antenna

Figure 6.3 shows the tri-band antenna from the side view. d_G is the distance between the ground plane and the radiator with the optimum value of 15 mm (λ/4 at 5 GHz) for the dual-band antenna array which only covers *S* and *C* bands (section 4.3). Figure 6.4 shows the gain vs. frequency in the *S*, *C* and *X* band operating states. It is seen that the dip in the gain is disappeared for smaller values of d_G. This is mainly due to the change in the radiation pattern of the antenna array in the *X*-band operating state.

Decreasing d_G has negligible effects on the gain and radiation pattern of the tri-band antenna/array in the *S*-band operating state because the distance between the radiator and ground plane at 2 GHz slightly changes when d_G = 15 mm or d_G = 12.5 mm.

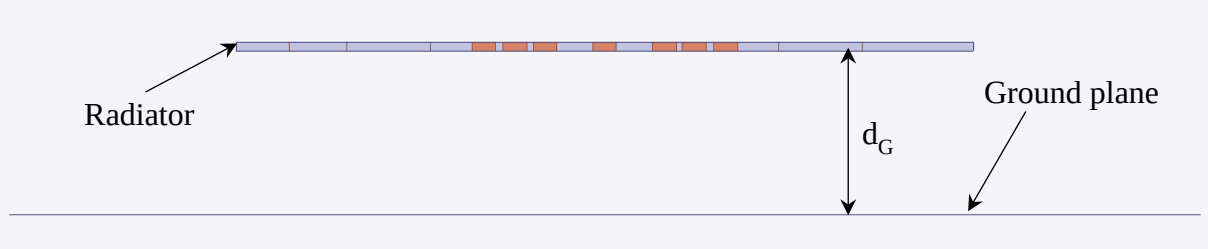

Figure 6.3. Tri-band antenna/array from the side view

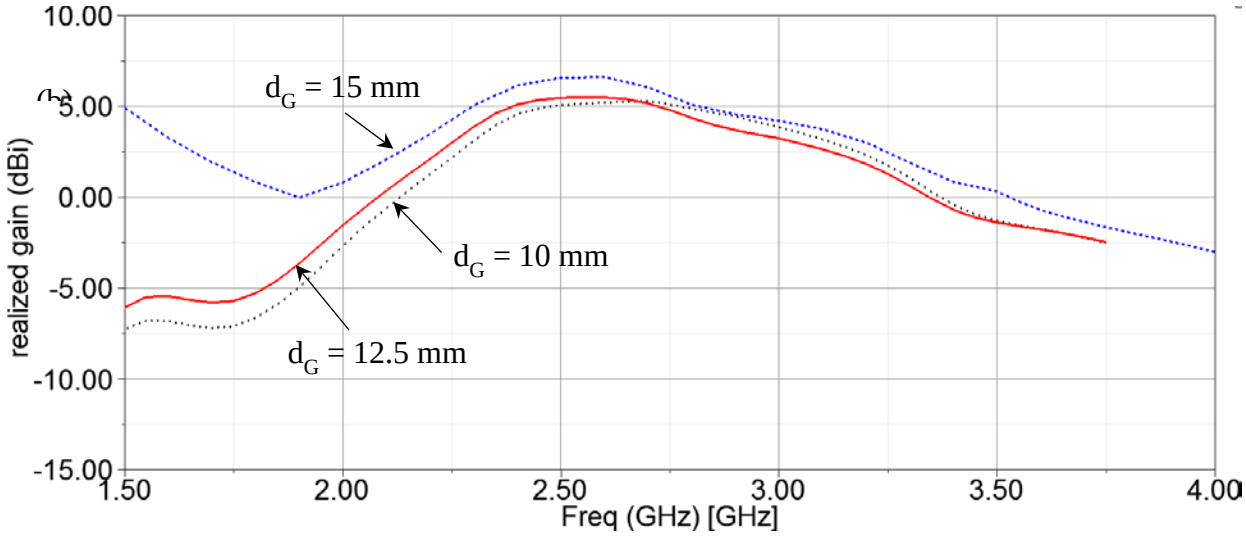
10.00
5.00
0.00
-5.00
-10.00
-15.00
realized gain (dBi)
1.50
2.00
2.50
3.00
3.50
4.00
Freq (GHz) [GHz]
d_G = 15 mm
d_G = 10 mm
d_G = 12.5 mm

(a)

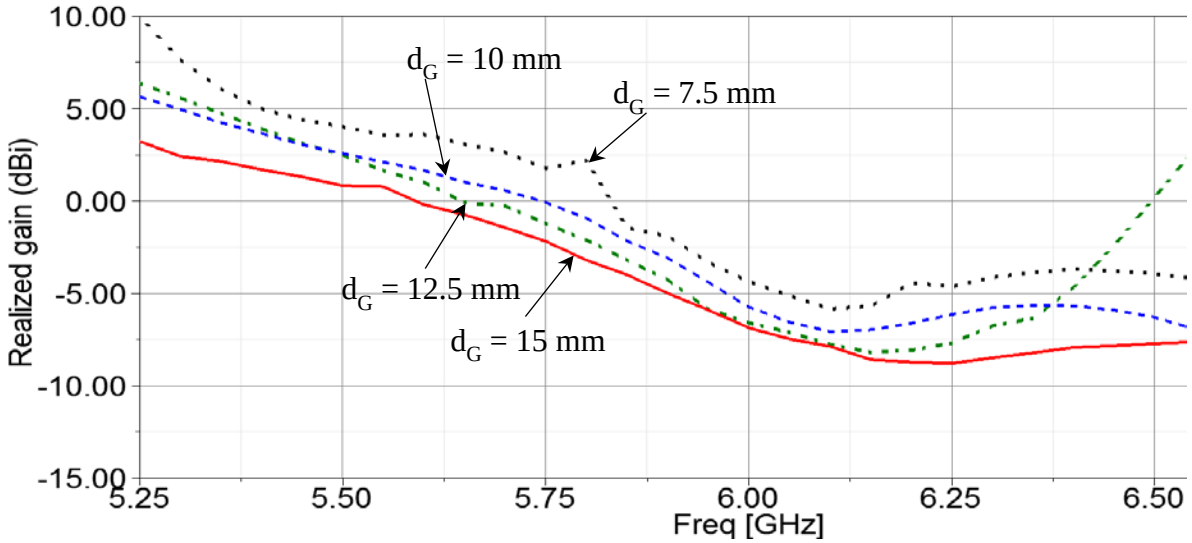
10.00
5.00
0.00
-5.00
-10.00
-15.00
Realized gain (dBi)
5.25
5.50
5.75
6.00
6.25
6.50
Freq [GHz]
d_G = 10 mm
d_G = 7.5 mm
d_G = 12.5 mm
d_G = 15 mm

(b)

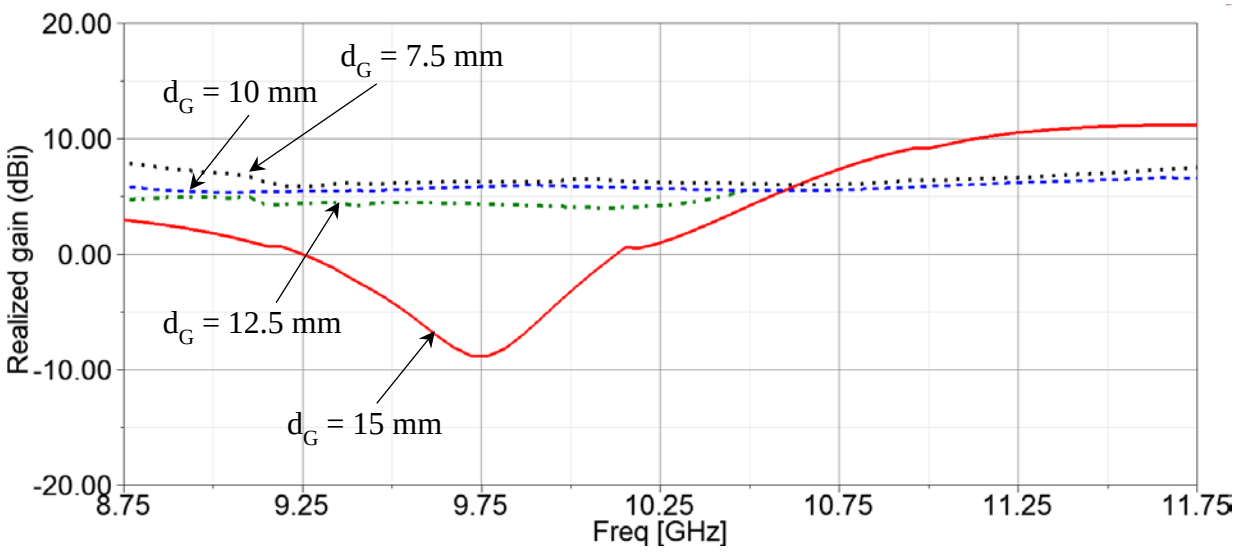

(c)

Figure 6.4. The effects of distance between the ground plane and the radiator (d_G) on the realized gain of the tri-band antenna/array in the (a) *S*-, (b) *C*- and (c) *X*-band operating state.

6.1.3 Simulation Results of an Optimum Dual-Polarized Single-Sided-Radiation Tri-band Antenna Element h microstrip feeding

Figure 6.5 shows the simulated S-parameters of the optimum microstrip-fed tri-band antenna element with wide bandwidth in all operating states. In the *S*/*C*/*X* band operating state, the antenna/array shows 75%/63%/26% FBW, respectively, for Active-S parameters less than -9 dB. The realized gain and radiation patterns of the antenna/array in the *S*-, *C*- and *X*-band states are illustrated in Figures 6.6, Figure 6.7, and Figure 6.8, respectively. In the *S* and *C* bands, the gain variation vs. frequency is approximately 8 dB which is probably due to the large number of microstrip feed lines in a single *S*-band antenna element (42 feed lines). As the number of feed

lines decreases, the gain in the *C* band is becoming more flat over the frequency. In the *X*-band operating state, the gain variation is less than 3 dB as illustrated in Figure 6.8.

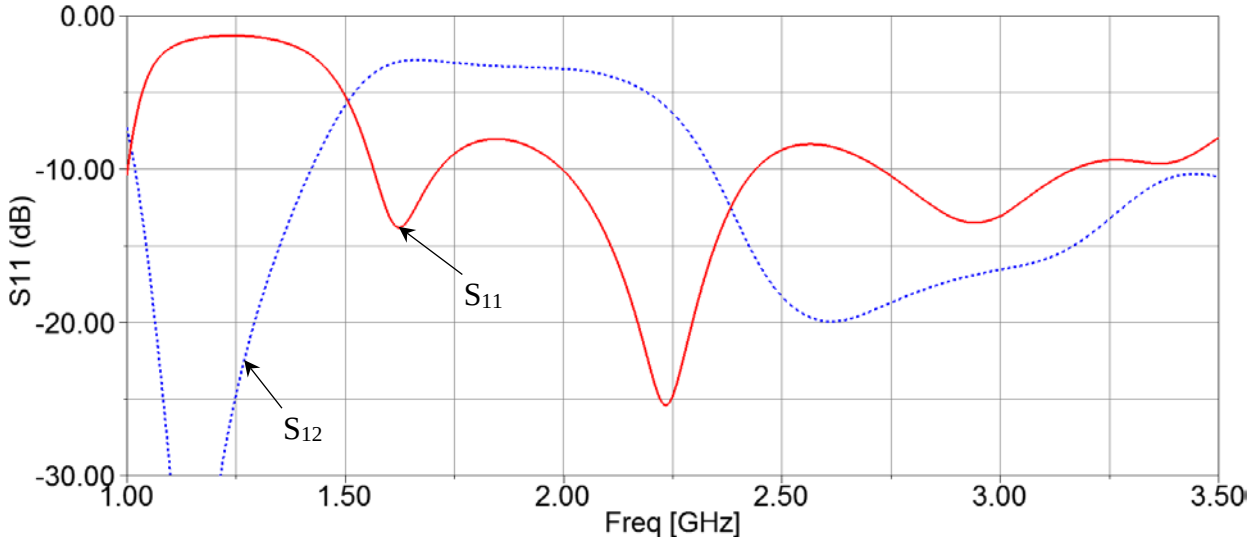

(a)

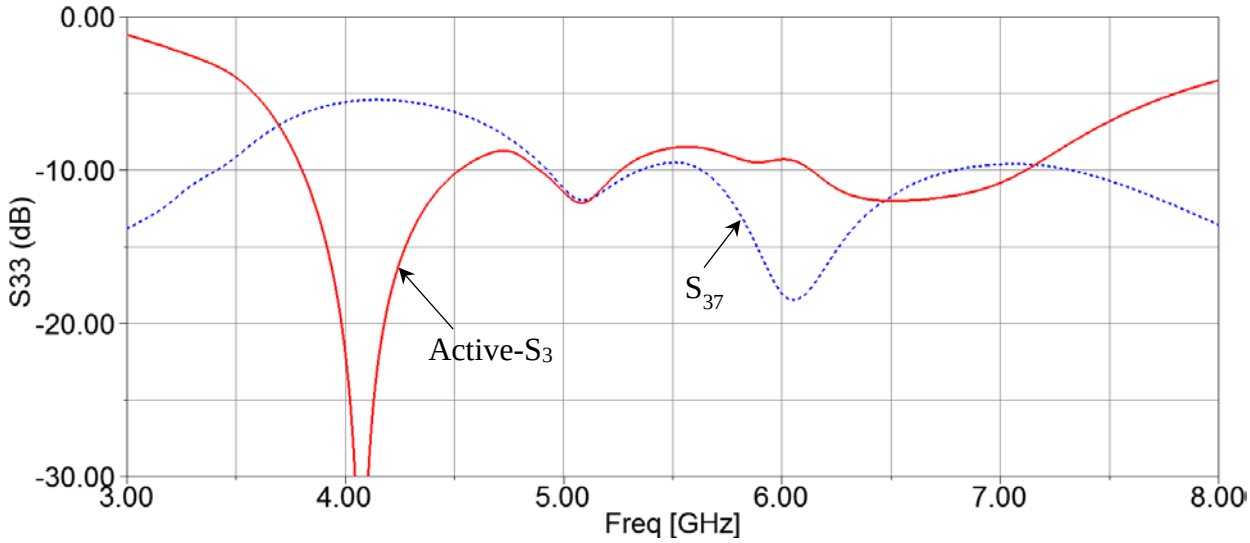

(b)

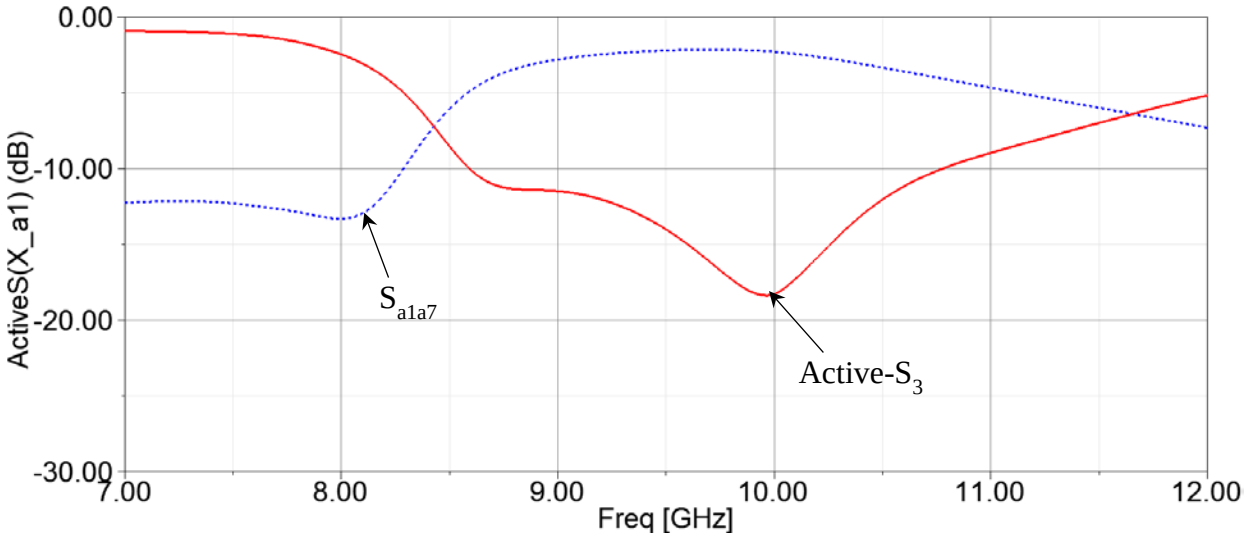

(c)

Figure 6.5 S-parameters of the optimum tri-band antenna/array in the (a) *S*-, (b) *C*- and (c) *X*-band operating state.

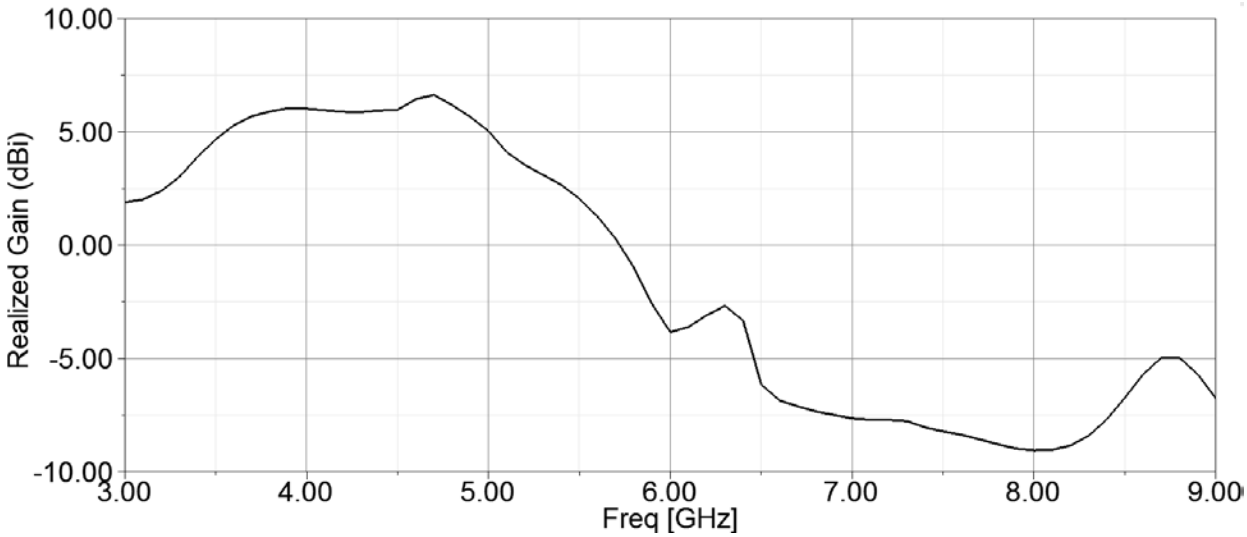

(a)

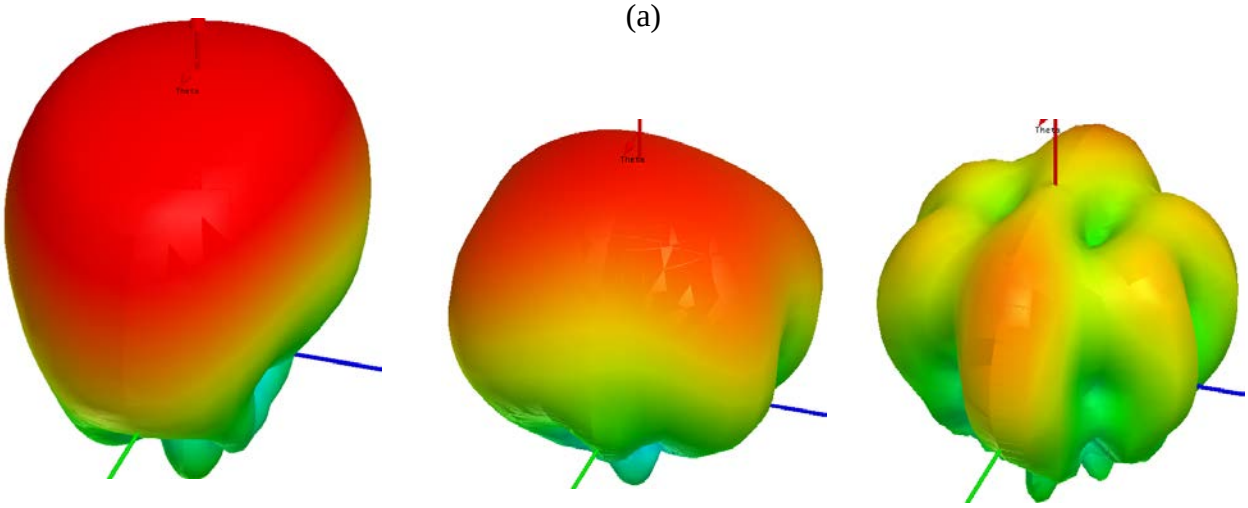

4 GHz 5 GHz 7 GHz

(b)

Figure 6.6 Gain and radiation patterns of the optimum tri-band antenna element in the *C*-band operating state.

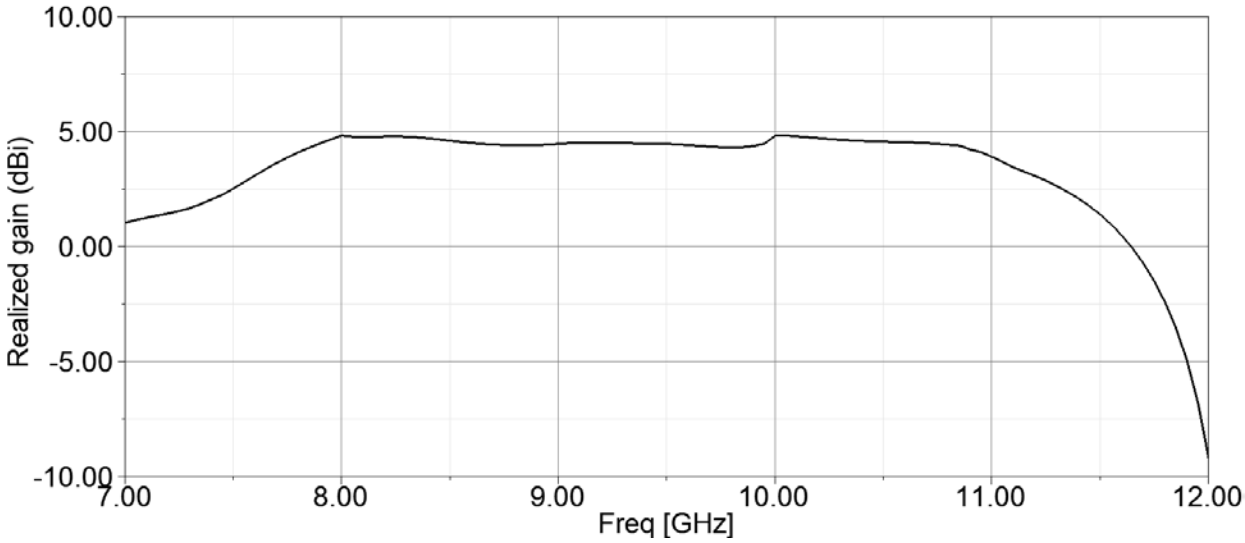

(a)

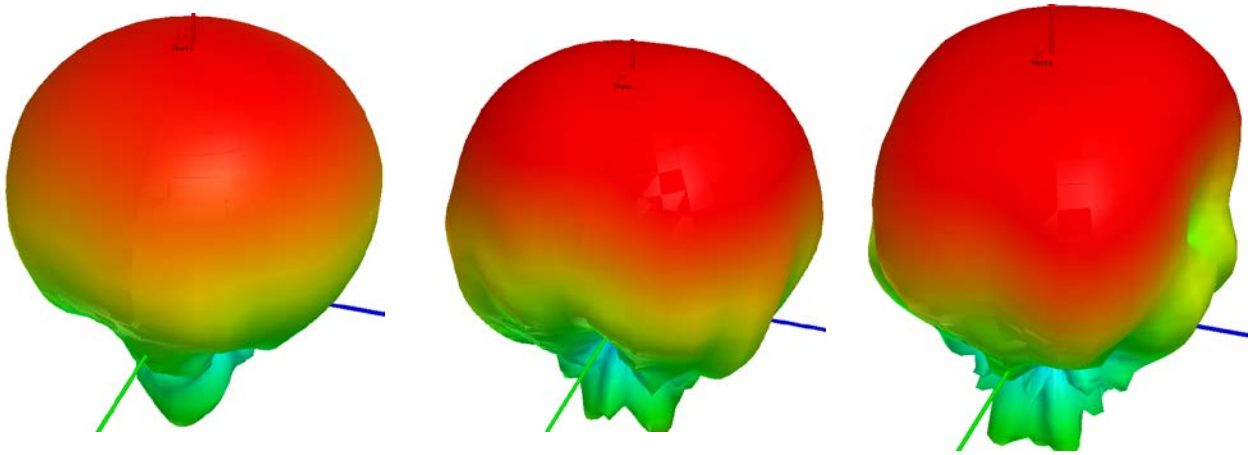

7 GHz 9 GHz 10.5

(b)

Figure 6.7 Gain and radiation patterns of the optimum tri-band antenna element in the x-band operating state.

6.1 Tri-band Antenna Element with vertical coaxial feeding

Figure 6.8 shows the schematic view of the tri-band antenna element with vertical coaxial feeding. Ant I, II and III are defined in Figures 6.8 and 6.9 with different number of coaxial cables. In the *S*- and *C*-band states, by adding more coaxial cables to the antenna structure, the S_{11} and Active-S_3 are degraded as shown in Figure 6.10(a) and (b), respectively. In the *X*-band state, adding *S* and *C*-band coaxial cables does not affect the Active-S_{X1} significantly.

To attack the problem mentioned above, a reconfigurable antenna/array with compact CPW feeding is presented in [74]. The next step in this design is to further optimize the tri-band antenna/array with CPW-fed vertical coaxial feeding.

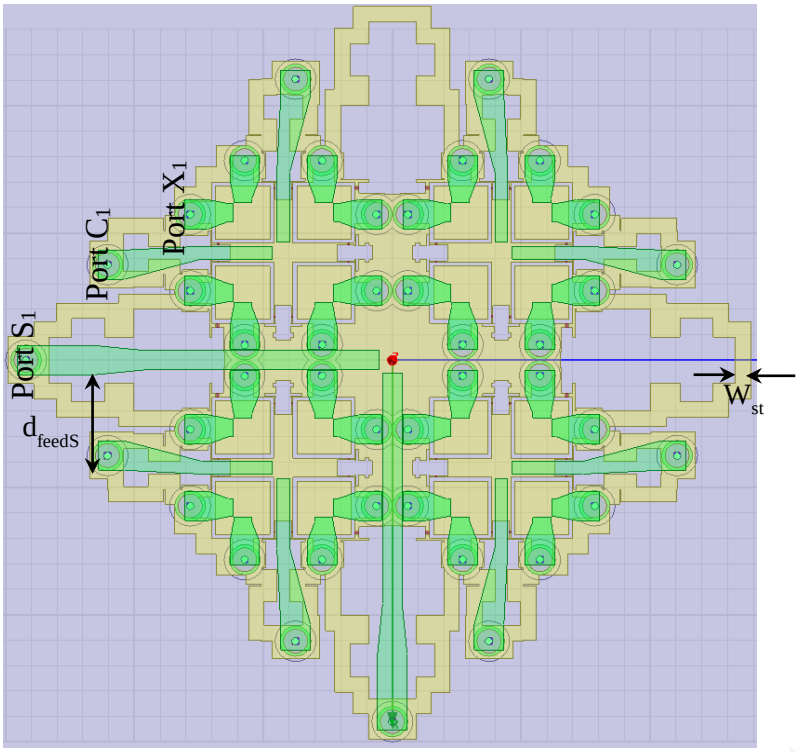

(a)

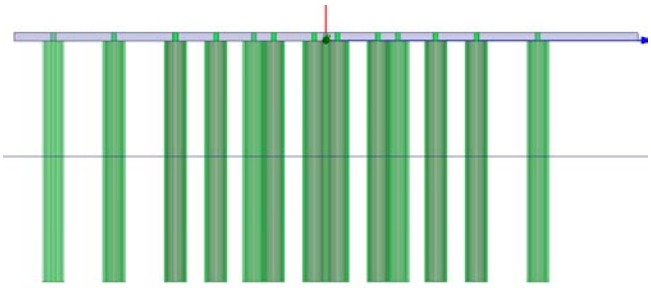

(b)

Ant I

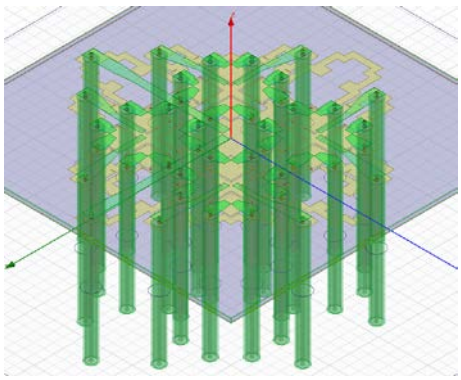

(c)

Figure 6.8 Schematic view of the tri-band antenna/array with vertical coaxial feeding from (a) top, (b) side and (c) trimetric view.

Ant II

Ant III

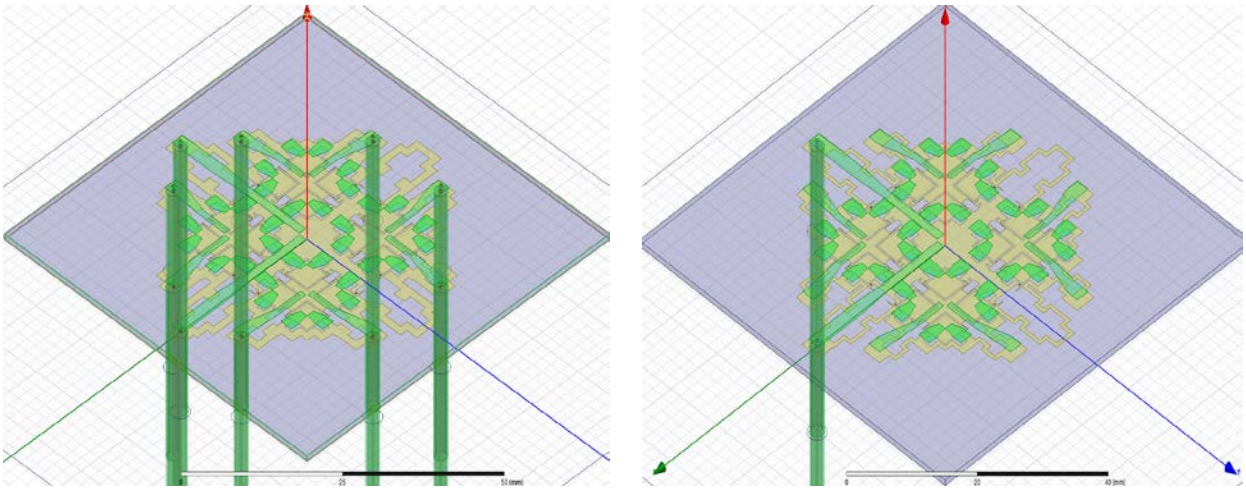

(a)

(b)

Figure 6.9 Schematic view of the tri-band antenna/array with reduced number of vertical coaxial feeding (a) Ant II, (b) Ant III.

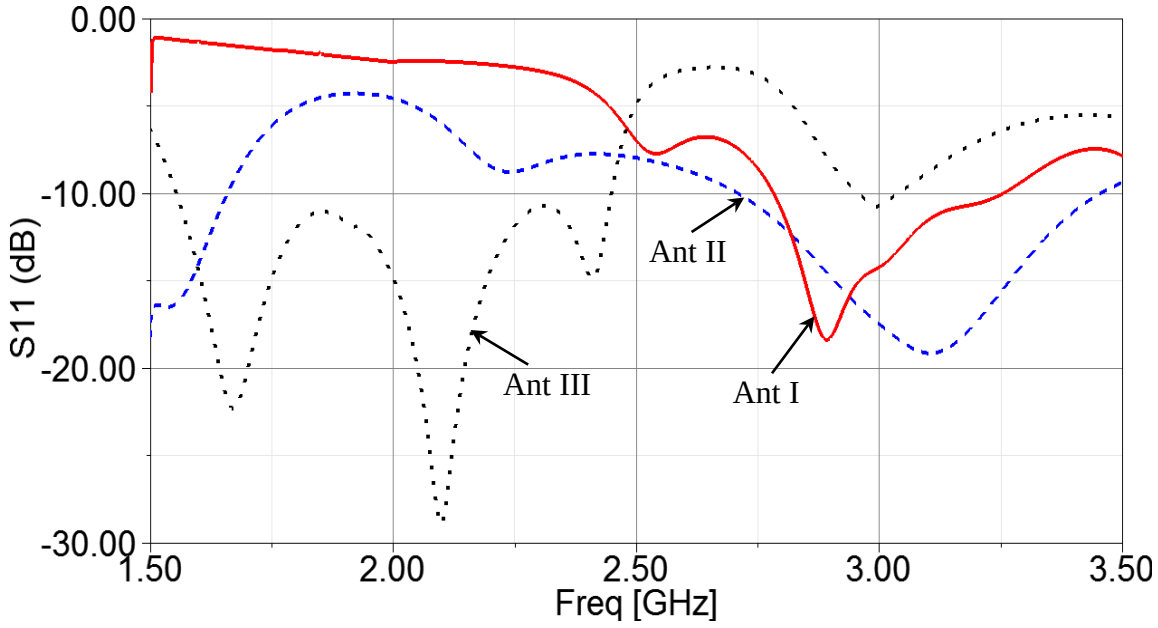

(a)

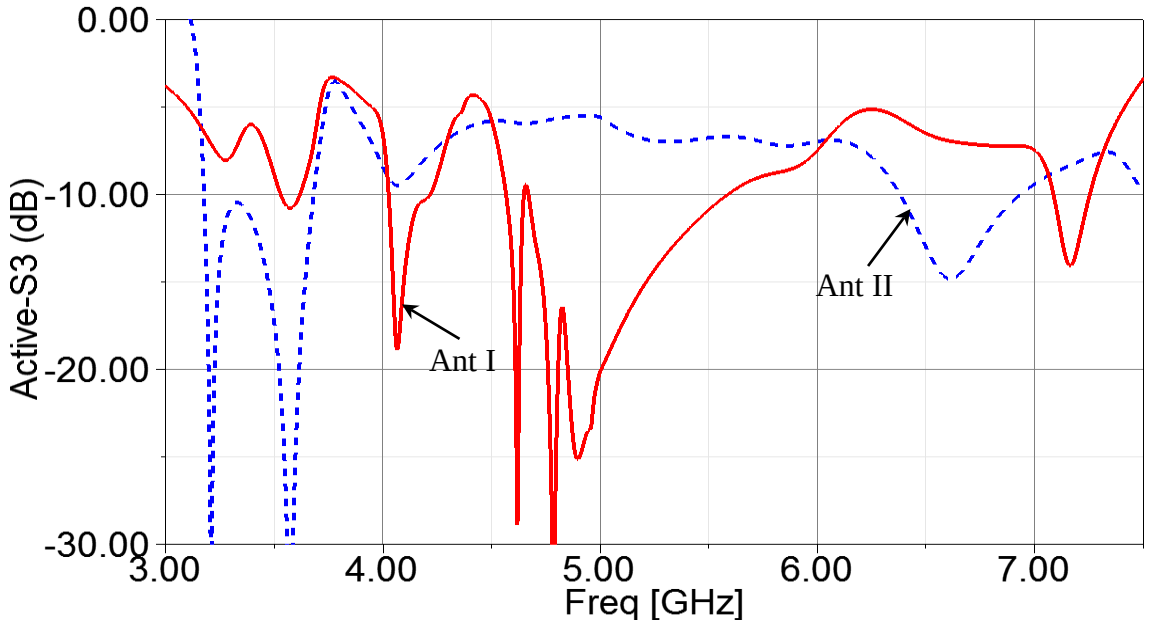

(b)

Figure 6.10 . S-parameters of Ant I, Ant II and Ant III in the (a) *S*-, (b) *C*-band operating state.

Table 6-1 compares the reconfigurable dual-polarized tri-band antenna element in this chapter with the antenna/arrays in Chapter 3, 4 and 5. FBW, polarization, scanning volume, efficiency, X-pol. Level, and the type of T/R modules are considered in this table.

Table 6-1 Comparison between the reconfigurable dual-polarized tri-band antenna element with microstrip feeding in this chapter with the antenna/arrays in Chapter 3, 4 and 5.

	Covered freq. bands	**FBW**	**Pol.**	**Scan volume in principal planes**	**Radiation efficiency**	**X-pol. in principal planes (dB)**	**T/R module**	**Comment**
Antenna array in Chapter 3	-	8.6%/11.5% in the *L*-/*C*-band state	Single LP	60º/60º in the *L*-/*C*-band state	67%/81% in the *L*-/*C*-band state	-15/-25 in the *S*-/*C*-band state	Narrow band	Limited bandwidth in each operating state
Antenna array in Chapter 4	*S* and *C*	67%/64% in the *S*-/*C*-band state	Dual LP	Single element	67%/88% in the *S*-/*C*-band state	-12/-15 in the *S*-/*C*-band state	With only octave bandwidth	Vertical transition is needed for e0xpansion to larger array for beamscanning
Antenna array in Chapter 5	*S* and *C*	64%/67% in the *S*-/*C*-band state	Dual LP	60º/35º in the *S*-/*C*-band state	72%/85% in the *S*-/*C*-band state -	-15/-25 in the *S*-/*C*-band state	With only octave bandwidth	-
Antenna array in Chapter 6	*S* and *C* and *X*	64%/67%/40% in the *S*-/*C*-/*X*-band state	Dual LP	Single element	72%/85%/% in the *S*-/*C*-/*X*-band state	-15/-25 in the *S*-/*C*-band state	With only octave bandwidth	-

6.2 Conclusion

A reconfigurable dual-polarized tri-band antenna element covering *S*, *C* and *X* bands has been presented. 42 microstrip lines are incorporated into a single *S*-band element for feeding the antenna/array. 40 PIN diode switches are used in this antenna element to switch the operating state of the antenna between the *S*-, *C*- and *X*-band states. Simulations show that this antenna has 75%/63%/26% FBW in the *S*/*C*/*X* bands. Single-sided radiation patterns with maximum radiation

toward boresight is obtained. A tri-band antenna/array with vertical coaxial feeding has also been presented. The effects of 42 coaxial cables on the antenna/array performance were studied. This antenna element can be used in a large array.

APPENDIX:
CALCULATING ARRAY FACTOR

The following code is originally written by “Seunghwan Yoon, Arizona State University, 08/12/2002” and revised by revised in “12/03/2002”. This code is modified for the purpose of this dissertation. Triangular array is added to the code as an option for the array type. This Matlab code can be slightly modified to calculate the array factor of the reconfigurable wideband antenna array in *S* and *C* band operating states.

```
%     ARRAYS
%
%    This is a MATLAB based program that computes the
%    radiation characteristics of:
%
%     I.   LINEAR ARRAYS (UNIFORM & BROADSIDE NONUNIFORM)
%     II.  PLANAR ARRAY (BROADSIDE UNIFORM)
%     II.  TRIANGULAR ARRAY (BROADSIDE UNIFORM)
%
%     THE UNIFORM AND BROADSIDE NONUNIFORM LINEAR ARRAYS HAVE N ELEMENTS
%     PLACED EQUIDISTANTLY ALONG THE Z-AXIS.
%
%     BROADSIDE PLANAR UNIFORM ARRAY HAS M x N ELEMENTS PLACED
%     EQUIDISTANTLY ALONG THE X AND Y AXES
%
%     OPTION I.  LINEAR ARRAYS
%
%       OPTION A.  UNIFORM
%         ** CHOICES: ARRAY TYPE
%
%         1. BROADSIDE (MAXIMUM ALONG THETA = 0 DEGREES)
%         2. SCANNING (MAXIMUM ALONG THETA = THETA_MAX)
%
%         ** INPUT PARAMETERS:
%
%            1. NUMBER OF ELEMENTS
%            2. SPACING BETWEEN THE ELEMENTS (IN WAVELENGTHS)
%            3. DIRECTION OF ARRAY MAXIMUM (THETA_MAX IN DEGREES)
%
%         ** PROGRAM OUTPUT:
%
%            1. NORMALIZED ARRAY FACTOR
%            2. DIRECTIVITY (DIMENSIONLESS & IN dB) USING NUMERICAL
%               INTEGRATION OF THE ARRAY FACTOR
%
%     OPTION II.  PLANAR ARRAY
%         ** CHOICES: ARRAY TYPE
```

```
%
%         1. RECTANGULAR
%         2. TRIANGULAR
%
%         ** ARRAY INPUT PARAMETERS:
%
%         1. NUMBER OF ARRAY ELEMENTS IN X-DIRECTION
%         2. SPACING BETWEEN THE ELEMENTS IN X-DIRECTION (IN
%            WAVELENGTHS)
%         3. NUMBER OF ARRAY ELEMENTS IN Y-DIRECTION
%         4. SPACING BETWEEN THE ELEMENTS IN Y-DIRECTION (IN
%            WAVELENGTHS)
%         5. MAXIMUM BEAM DIRECTION - ANGLE THETA (IN DEGREES)
%         6. MAXIMUM BEAM DIRECTION - ANGLE PHI (IN DEGREES)
%         7. THE PHI ANGLE (IN DEGREES) AT WHICH THE 2-D ANTENNA
%            PATTERN NEEDS TO BE EVALUATED (PHIEVAL IN DEG.)
%
%
%         ** PROGRAM OUTPUT:
%
%         1. NORMALIZED ARRAY FACTOR EVALUATED AT A GIVEN ANGLE
%           (PHIEVAL)
%         2. DIRECTIVITY (IN dB) USING NUMERICAL INTEGRATION OF THE
%            ARRAY FACTOR
%         3. HALF-POWER BEAMWIDTH (IN DEGREES) FOR ALL MAXIMA THAT
%            OCCUR IN THE ELEVATION PLANE OF THE 2-D ANTENNA PATTERN
%
%     OPTION III.  TRIANGULAR ARRAY
%         ** CHOICES: EQUATION TYPE
%
%         1. EXPONENTIAL FUNCTION FORM
%         2. BESSEL FUNCTION FORM
%
%
%     ALL THE INPUT PARAMETERS ARE IN TERMS OF THE WAVELENGTH.
%     ****************************************************************

function[]=TriAF_times_SingleElement_Sband(AES_2D,AES_3D);

close all;
clc;

option_a=0;
while((option_a~=1)&(option_a~=2)),
disp(strvcat('OUTPUT DEVICE OPTION FOR THE OUTPUT PARAMETERS',...
   'OPTION (1):SCREEN','OPTION (2):OUTPUT FILE'));
option_a=input('OUTPUT DEVICE =');
end
if option_a==2, %OUTPUT FILE
   filename=input('INPUT THE DESIRED OUTPUT FILENAME <in single quotes> =
',...
```

```
      's');
   fid=fopen(filename,'wt');
end
disc=181;
MM=disc;
NN=disc;
theta_low=0;
theta_up=180;
phi_low=0;
phi_up=360;


% CHOICE OF LINEAR OR PLANAR ARRAY OR CIRCULAR ARRAY

option_b=0;
while ((option_b~=1)&(option_b~=2)&(option_b~=3)),
disp(strvcat('LINEAR OR PLANAR ARRAY','OPTION (1):LINEAR ARRAY','OPTION
(2):PLANAR ARRAY','OPTION (3):CIRCULAR ARRAY'));
option_b=input('OPTION NUMBER =');
end;

if option_b==1, % LINEAR ARRAY

M=1800;
%MM=180;
%NN=180;
k=2*pi;
theta=linspace(0,pi,M+1);
theta3=linspace(theta_low*pi/180,theta_up*pi/180,MM+1);
phi3=linspace(phi_low*pi/180,phi_up*pi/180,NN+1);
[THETA,PHI]=meshgrid(theta3,phi3);
dtheta=pi/M;

% CHOICE OF ARRAY TYPE
% (BROADSIDE,SCANNING)
option_d=0;
while ((option_d~=1)&(option_d~=2)),
disp(strvcat('ARRAY NAMES','OPTION (1):BROADSIDE ARRAY(MAXIMUM ALONG THETA =
90 DEGREES)','OPTION (2):SCANNING ARRAY'));
option_d=input('OPTION NUMBER =');
end;

if option_d==1, % BROADSIDE
Nelem=0;
while (Nelem<1),
Nelem=floor(input('NUMBER OF ELEMENTS ='));
end
d=input('SPACING d BETWEEN THE ELEMENTS (IN WAVELENGTHS) =');
beta=0;
psi=k.*d.*cos(theta)+beta;
```

```
psi3=k.*d.*cos(THETA)+beta;
AF=sinc((Nelem.*psi./2)/pi)./sinc((psi./2)/pi);   % I used sinc function.
AF3=sinc((Nelem.*psi3./2)/pi)./sinc((psi3./2)/pi);  %
sinc(x)=sin(pi*x)/(pi*x).  not, sin(x)/x.


elseif option_d==2, % SCANNING
Nelem=0;
while (Nelem<1),
Nelem=floor(input('NUMBER OF ELEMENTS ='));
end
d=input('SPACING d BETWEEN THE ELEMENTS (IN WAVELENGTHS) =');
thmax=input('ANGLE WHERE MAXIMUM OCCURS (THETA = 0 OR 180 DEG.)=');
beta=-k*d*cos(thmax*pi/180);
psi=k*d*cos(theta)+beta;
psi3=k*d*cos(THETA)+beta;
AF=sinc((Nelem.*psi./2)/pi)./sinc((psi./2)/pi);
AF3=sinc((Nelem.*psi3./2)/pi)./sinc((psi3./2)/pi);
end;


U=(abs(AF)./max(abs(AF))).^2;
Prad=2*pi*sum(U.*sin(theta).*dtheta);
D=4*pi*U/Prad;
DdB=10.*log10(D+eps);
Do=max(D);
DodB=max(DdB);
if Nelem==1|max(AF)<2*min(AF)
hp=0;
thmax=0;
else
% [hp,thmax]=hpbw(U,M);
end
No_maxima=length(thmax);


elseif option_b==2, % PLANAR ARRAY
%M=180;
%N=180;
k=2*pi;
dtheta=pi/MM;
dphi=2*pi/NN;

% CHOICE OF ARRAY TYPE
% (Rectangular or Triangular)
option_e=0;
while ((option_e~=1)&(option_e~=2)),
disp(strvcat('ARRAY NAMES','OPTION (1):RECTANGULAR ARRAY','OPTION
(2):TRIANGULAR ARRAY'));
option_e=input('OPTION NUMBER =');
```

```
end;

if option_e==1, % RECTANGULAR
Mx=0;
while (Mx<2),
Mx=floor(input('NUMBER OF ELEMENTS IN THE X-DIRECTION ='));
end
Ny=0;
while (Ny<2),
Ny=floor(input('NUMBER OF ELEMENTS IN THE Y-DIRECTION ='));
end

dx=input('SPACING dx BETWEEN THE ELEMENTS (IN WAVELENGTHS) =')-1e-10;
dy=input('SPACING dy BETWEEN THE ELEMENTS (IN WAVELENGTHS) =')-1e-10;
thmax2=input('MAXIMUM BEAM DIRECTION - ANGLE THETA (IN DEGREES - INTEGER
#)=');
phimax2=input('MAXIMUM BEAM DIRECTION - ANGLE PHI (IN DEGREES - INTEGER
#)=');
phieval=input('THE PATTERN IS EVALUATED AT AN ANGLE PHI (IN DEGREES - INTEGER
#)=');
dtor=pi/180;
betax=-k*dx*sin(dtor*thmax2)*cos(dtor*phimax2);
betay=-k*dy*sin(dtor*thmax2)*sin(dtor*phimax2);

theta=linspace(theta_low*pi/180,theta_up*pi/180,MM+1);
phi=linspace(phi_low*pi/180,phi_up*pi/180,NN+1);

[THETA,PHI]=meshgrid(theta,phi);
AF3=af10(THETA,PHI,Mx,Ny,dx,dy,betax,betay);

Prad=sum(sum(abs(AF3).^2.*sin(THETA)*dtheta*dphi));
D1=4*pi*abs(AF3).^2/Prad;
D1dB=10.*log10(D1);
Do=4*pi*max(max(abs(AF3).^2))/Prad;
DodB=10.*log10(Do);

theta=linspace(0,pi,10*MM+1);
phi=phieval*dtor;
AF=af10(theta,phi,Mx,Ny,dx,dy,betax,betay);
D=4*pi*abs(AF).^2/Prad;
DdB=10.*log10(D);
U=(abs(AF)./max(abs(AF))).^2;

phi180=phieval*dtor-pi;
AF180=af10(theta,phi180,Mx,Ny,dx,dy,betax,betay);
D180=4*pi*abs(AF180).^2/Prad;
D180dB=10.*log10(D180);
U180=(abs(AF180)./max(abs(AF180))).^2;

elseif option_e==2, % TRIANGULAR
```

```
Mx=0;
while (Mx<1),
Mx=floor(input('NUMBER OF ELEMENTS IN THE X-DIRECTION ='));
end
Ny=0;
while (Ny<1),
Ny=floor(input('NUMBER OF ELEMENTS IN THE Y-DIRECTION ='));
end

dx=input('SPACING dx BETWEEN THE ELEMENTS (IN WAVELENGTHS) =')-1e-10;
dy=input('SPACING dy BETWEEN THE ELEMENTS (IN WAVELENGTHS) =')-1e-10;
thmax2=input('MAXIMUM BEAM DIRECTION - ANGLE THETA (IN DEGREES - INTEGER
#)=');
phimax2=input('MAXIMUM BEAM DIRECTION - ANGLE PHI (IN DEGREES - INTEGER
#)=');
phieval=input('THE PATTERN IS EVALUATED AT AN ANGLE PHI (IN DEGREES - INTEGER
#)=');
dtor=pi/180;
betax=-k*dx*sin(dtor*thmax2)*cos(dtor*phimax2);
betay=-k*dy*sin(dtor*thmax2)*sin(dtor*phimax2);

theta=linspace(theta_low*pi/180,theta_up*pi/180,MM+1);
phi=linspace(phi_low*pi/180,phi_up*pi/180,NN+1);

[THETA,PHI]=meshgrid(theta,phi);
AF3=aft10(THETA,PHI,Mx,Ny,dx,dy,betax,betay);

Prad=sum(sum(abs(AF3).^2.*sin(THETA)*dtheta*dphi));
D1=4*pi*abs(AF3).^2/Prad;
D1dB=10.*log10(D1);
Do=4*pi*max(max(abs(AF3).^2))/Prad;
DodB=10.*log10(Do);

theta=linspace(0,pi,10*MM+1);
phi=phieval*dtor;
AF=aft10(theta,phi,Mx,Ny,dx,dy,betax,betay);
D=4*pi*abs(AF).^2/Prad;
DdB=10.*log10(D);
U=(abs(AF)./max(abs(AF))).^2;

phi180=phieval*dtor-pi;
AF180=aft10(theta,phi180,Mx,Ny,dx,dy,betax,betay);
D180=4*pi*abs(AF180).^2/Prad;
D180dB=10.*log10(D180);
U180=(abs(AF180)./max(abs(AF180))).^2;
end

elseif option_b==3, % CIRCULAR ARRAY
   option_f=0;
while ((option_f~=1)&(option_f~=2)),
```

```
disp(strvcat('FUNCTIONS','OPTION (1):EXPONENTIAL FUNCTION FORM','OPTION
(2):BESSEL FUNCTION FORM'));
option_f=input('OPTION NUMBER =');
end;

%M=180;
%N=180;
k=2*pi;
dtheta=pi/MM;
dphi=2*pi/NN;

Nelem=0;
while (Nelem<2),
Nelem=floor(input('NUMBER OF ELEMENTS ='));
end
rad=input('RADIUS (IN WAVELENGTHS) =');
if option_f==2, % BESSEL
m=-1;
while (m<0),
   m=floor(input('Residuals[>2]='));
end
end

theta0=input('MAXIMUM BEAM DIRECTION - ANGLE THETA (IN DEGREES - INTEGER
#)=');
phi0=input('MAXIMUM BEAM DIRECTION - ANGLE PHI (IN DEGREES - INTEGER #)=');
phieval=input('THE PATTERN IS EVALUATED AT AN ANGLE PHI (IN DEGREES - INTEGER
#)=');

if option_f==1, % EXPONENTIAL
dtor=pi/180;
theta=linspace(theta_low*pi/180,theta_up*pi/180,MM+1);
phi=linspace(phi_low*pi/180,phi_up*pi/180,NN+1);
[THETA,PHI]=meshgrid(theta,phi);
AF3=afc(THETA,PHI,theta0,phi0,Nelem,rad);
Prad=sum(sum(abs(AF3).^2.*sin(THETA)*dtheta*dphi));
D1=4*pi*abs(AF3).^2/Prad;
D1dB=10.*log10(D1);
Do=4*pi*max(max(abs(AF3).^2))/Prad;
DodB=10.*log10(Do);

theta=linspace(0,pi,10*MM+1);
phi=phieval*dtor;
AF=afc(theta,phi,theta0,phi0,Nelem,rad);
D=4*pi*abs(AF).^2/Prad;
DdB=10.*log10(D);
U=(abs(AF)./max(abs(AF))).^2;
AFdB=10.*log10(U);

phi180=phieval*dtor-pi;
```

```
AF180=afc(theta,phi180,theta0,phi0,Nelem,rad);
D180=4*pi*abs(AF180).^2/Prad;
D180dB=10.*log10(D180);
U180=(abs(AF180)./max(abs(AF180))).^2;

end

if option_f==2, % BESSEL
dtor=pi/180;
theta=linspace(theta_low*pi/180,theta_up*pi/180,MM+1);
phi=linspace(phi_low*pi/180,phi_up*pi/180,NN+1);
[THETA,PHI]=meshgrid(theta,phi);
AF3=afc3(THETA,PHI,theta0,phi0,Nelem,rad,m);
Prad=sum(sum(abs(AF3).^2.*sin(THETA)*dtheta*dphi));
D1=4*pi*abs(AF3).^2/Prad;
D1dB=10.*log10(D1);
Do=4*pi*max(max(abs(AF3).^2))/Prad;
DodB=10.*log10(Do);

AF30=afc3(THETA,PHI,theta0,phi0,Nelem,rad,0);
Prad0=sum(sum(abs(AF30).^2.*sin(THETA)*dtheta*dphi));
D10=4*pi*abs(AF30).^2/Prad0;
D1dB0=10.*log10(D10);
Do0=4*pi*max(max(abs(AF30).^2))/Prad0;
DodB0=10.*log10(Do0);


theta=linspace(0,pi,10*MM+1);
phi=phieval*dtor;
AF=afc3(theta,phi,theta0,phi0,Nelem,rad,m);
D=4*pi*abs(AF).^2/Prad;
DdB=10.*log10(D);
U=(abs(AF)./max(abs(AF))).^2;
AFdB=10.*log10(U);

AF0=afc3(theta,phi,theta0,phi0,Nelem,rad,0);
D0=4*pi*abs(AF0).^2/Prad0;
DdB0=10.*log10(D0);
U0=(abs(AF0)./max(abs(AF0))).^2;
AFdB0=10.*log10(U0);

phi180=phieval*dtor-pi;
AF180=afc3(theta,phi180,theta0,phi0,Nelem,rad,m);
D180=4*pi*abs(AF180).^2/Prad;
D180dB=10.*log10(D180);
U180=(abs(AF180)./max(abs(AF180))).^2;

end
end
```

```
if option_a==2
   diary(filename);
end

scale=0;
while ((scale~=1)&(scale~=2)),
disp(strvcat('DIMENSIONLESS OR dB SCALE IN 3D DIRECTIVITY PLOT','OPTION
(1):DIMENSIONLESS SCALE','OPTION (2):dB SCALE'));
scale=input('OPTION NUMBER =');
end;




% Let's go output!!!
disp(strvcat('************************************************************'));
disp(strvcat('PROGRAM OUTPUT'));
disp(strvcat('************************************************************'));
disp(strvcat('INPUT SPECIFICATION'));
disp(strvcat('------------------------------------------------------------'));

if option_b==1
if option_d==1
disp(strvcat('UNIFORM BROADSIDE ARRAY'));
end
if option_d==2
disp(strvcat('UNIFORM SCANNING ARRAY'));
end
disp(['NUMBER OF ARRAY ELEMENTS = ',num2str(Nelem)]);
disp(['SPACING BETWEEN THE ELEMENTS (IN WAVELENGTHS) = ',num2str(d)]);
if option_d~=1
disp(['MAXIMUM NEEDS TO OCCUR AT = ',num2str(thmax)]);
end
disp('OUTPUT CHARACTERISTICS OF THE ARRAY');
disp('------------------------------------------------------------');


disp(['DIRECTIVITY = ',num2str(DodB),' dB']);
disp(['DIRECTIVITY = ',num2str(Do),' dimensionless']);
disp(['NUMBER OF MAXIMA BETWEEN 0 AND 180 DEGREES = ',num2str(No_maxima)]);
% for i=1:No_maxima;
% disp(['HPBW FOR MAXIMUM # =',num2str(i),'    ',num2str(hp(i)),' degrees
THMAX = ',num2str(thmax(i)),' degrees']);
% end

end

if option_b==2
if option_e==1
disp(strvcat('RECTANGULAR ARRAY'));
```

```
end
if option_e==2
disp(strvcat('TRIANGULAR ARRAY'));
end
disp(['NUMBER OF ELEMENTS IN X-DIRECTION = ',num2str(Mx)]);
disp(['SPACING BETWEEN THE ELEMENTS IN X-DIRECTION (IN WAVELENGTHS) =
',num2str(dx)]);
disp(['NUMBER OF ELEMENTS IN Y-DIRECTION = ',num2str(Ny)]);
disp(['SPACING BETWEEN THE ELEMENTS IN Y-DIRECTION (IN WAVELENGTHS) =
',num2str(dy)]);
disp(['MAXIMUM BEAM DIRECTION - THETA (IN DEGREES) = ',num2str(thmax2)]);
disp(['MAXIMUM BEAM DIRECTION - PHI (IN DEGREES) = ',num2str(phimax2)]);
disp(['THE 2D ANTENNA PATTERN IS EVALUATED AT AN ANGLE PHI (IN DEGREES) =
',num2str(phieval)]);
disp(strvcat('OUTPUT CHARACTERISTICS OF THE ARRAY'));
disp(strvcat('-------------------------------------------------------'));
disp(['PROGRESSIVE PHASE SHIFT IN X-DIRECTION = ',num2str(betax/dtor),'
degrees']);
disp(['PROGRESSIVE PHASE SHIFT IN Y-DIRECTION = ',num2str(betay/dtor),'
degrees']);
disp('DIRECTIVITY BASED ONLY ON THE FIELDS ABOVE THE XY-PLANE')
disp(['DIRECTIVITY = ',num2str(DodB+10*log10(2)),' dB']);
disp(['DIRECTIVITY = ',num2str(Do*2),' dimensionless']);
% if max(AF3)<2*min(AF3)
% hp=0;
% thmax=0;
% else
% [hp,thmax]=hpbw(U,10*MM);
% end
% No_maxima=length(thmax);
disp('DIRECTIVITY BASED ON THE FIELDS ABOVE AND BELOW THE XY-PLANE')
disp(['DIRECTIVITY = ',num2str(DodB),' dB']);
disp(['DIRECTIVITY = ',num2str(Do),' dimensionless']);
% disp(['EVALUATION PLANE: NUMBER OF MAXIMA BETWEEN 0 AND 180 DEGREES =
',num2str(No_maxima)]);
% for i=1:No_maxima;
% disp(['HPBW FOR MAXIMUM #',num2str(i),'    ',num2str(hp(i)),' degrees
THMAX = ',num2str(thmax(i)),' degrees']);
% end
end

if option_b==3
disp(strvcat('UNIFORM CIRCULAR ARRAY'));
disp(['NUMBER OF ELEMENTS = ',num2str(Nelem)]);
disp(['RADIUS (IN WAVELENGTHS) = ',num2str(rad)]);
disp(['MAXIMUM BEAM DIRECTION - THETA (IN DEGREES) = ',num2str(theta0)]);
disp(['MAXIMUM BEAM DIRECTION - PHI (IN DEGREES) = ',num2str(phi0)]);
disp(['THE 2D ANTENNA PATTERN IS EVALUATED AT AN ANGLE PHI (IN DEGREES) =
',num2str(phieval)]);
disp(strvcat('OUTPUT CHARACTERISTICS OF THE ARRAY'));
disp(strvcat('-------------------------------------------------------'));
```

```
disp('DIRECTIVITY BASED ONLY ON THE FIELDS ABOVE THE XY-PLANE')
disp(['DIRECTIVITY = ',num2str(DodB+10*log10(2)),' dB']);
disp(['DIRECTIVITY = ',num2str(Do*2),' dimensionless']);
% if max(AF3)<2*min(AF3)
% hp=0;
% thmax=0;
% else
% [hp,theta0]=hpbw(U,10*MM);
% end
No_maxima=length(theta0);
disp('DIRECTIVITY BASED ON THE FIELDS ABOVE AND BELOW THE XY-PLANE')
disp(['DIRECTIVITY = ',num2str(DodB),' dB']);
disp(['DIRECTIVITY = ',num2str(Do),' dimensionless']);
disp(['EVALUATION PLANE: NUMBER OF MAXIMA BETWEEN 0 AND 180 DEGREES =
',num2str(No_maxima)]);
% for i=1:No_maxima;
% disp(['HPBW FOR MAXIMUM #',num2str(i),'    ',num2str(hp(i)),' degrees
THMAX = ',num2str(theta0(i)),' degrees']);
% end
end
```

```
disp(' AN OUTPUT FILE CALLED  ............   ArrFac.dat');
disp(' ================================================');

diary off;

AFdB=10.*log10(U);
if option_b==1,
for i=1:901
   thetarec(i)=theta(i*2-1);
   AFdBrec(i)=AFdB(i*2-1);
end
for i=902:1801
   thetarec(i)=2*pi-theta(3601-i*2+3);
   AFdBrec(i)=AFdB(3601-i*2+3);

end
elseif option_b==2|option_b==3,
for i=1:MM+1
   thetarec(i)=theta(i*10-9);
   AFdBrec(i)=AFdB(i*10-9);
end
for i=MM+2:2*MM+1
   thetarec(i)=2*pi-thetarec(2*MM+2-i);
   AFdBrec(i)=AFdBrec(2*MM+2-i);
```

```
end

end

fidaf=fopen('ArrFac.dat','wt');
fprintf(fidaf,'%7.3f        %9.5f\n',[thetarec.*180/pi; AFdBrec]);
fprintf(fidaf,'%7.3f        %9.5f\n',[thetarec.*180/pi; AFdBrec]);
fclose(fidaf);



% PLOT THE GRAPHS
% ARRAY FACTOR

clf;
plot(theta*180/pi,AFdB,'m','linewidth',2);
xlabel(['\theta',' (degrees)']),ylabel('ARRAY FACTOR(dB)')
grid on;
axis([0 180 max(min(AFdB)-1,-60) 1]);
% t1=text(1,1,['HPBW = ',num2str(max(hp)),' (degrees)']);
% set(t1,'units','normalized','position',[1 1.05],'horizontalalign','right');

if option_b==1&option_d==1
   s1=title('UNIFORM BROADSIDE','Fontsize',15);
   set(gca,'units','normalized');
   set(s1,'position',[0 1],'horizontalalign','left');
end
if option_b==1&option_d==2
   s4=title('UNIFORM SCANNING','Fontsize',15);
      set(gca,'units','normalized');
   set(s4,'position',[0 1],'horizontalalign','left');
end
if option_b==2&option_e==1
   s7=title('RECTANGULAR PLANAR','Fontsize',15);
      set(gca,'units','normalized');
   set(s7,'position',[0 1],'horizontalalign','left');
end
if option_b==2&option_e==2
   s7=title('TRIANGULAR PLANAR','Fontsize',15);
      set(gca,'units','normalized');
   set(s7,'position',[0 1],'horizontalalign','left');
end
if option_b==3&option_f==1
   s8=title('UNIFORM CIRCULAR(EXPONENTIAL)','Fontsize',15);
      set(gca,'units','normalized');
   set(s8,'position',[0 1],'horizontalalign','left');
end
if option_b==3&option_f==2
   hold on;
   plot(theta*180/pi,AFdB0,'b--','linewidth',2);
```

```
   legend('principal+residuals','principal')
   s9=title('UNIFORM CIRCULAR(BESSEL)','Fontsize',15);
      set(gca,'units','normalized');
   set(s9,'position',[0 1],'horizontalalign','left');
end

figure;


diff=Do-min(D);
subplot(2,1,1)
plot(theta*180/pi,D,'r','linewidth',2);
xlabel(['\theta',' (degrees)']),ylabel('DIRECTIVITY(dimensionless)')
grid on;
axis([0 180 floor(min(D)-0.1*diff-.1) ceil(Do+0.1*diff+.1)]);
t2=text(1,1,['D_0 = ',num2str(Do),' (dimensionless)']);
set(t2,'units','normalized','position',[1 1.05],'horizontalalign','right');

if option_b==1&option_d==1
   s1=title('UNIFORM BROADSIDE','Fontsize',15);
    set(gca,'units','normalized');
   set(s1,'units','normalized','position',[0 1],'horizontalalign','left');
end
if option_b==1&option_d==2
   s4=title('UNIFORM SCANNING','Fontsize',15);
      set(gca,'units','normalized');
   set(s4,'units','normalized','position',[0 1],'horizontalalign','left');
end
if option_b==2&option_e==1
   s7=title('RECTANGULAR PLANAR','Fontsize',15);
      set(gca,'units','normalized');
      set(s7,'units','normalized','position',[0 1],'horizontalalign','left');
end
if option_b==2&option_e==2
   s7=title('TRIANGULAR PLANAR','Fontsize',15);
      set(gca,'units','normalized');
      set(s7,'units','normalized','position',[0 1],'horizontalalign','left');
end
if option_b==3&option_f==1
   s8=title('UNIFORM CIRCULAR(EXPONENTIAL)','Fontsize',15);
      set(gca,'units','normalized');
      set(s8,'units','normalized','position',[0 1],'horizontalalign','left');
end
if option_b==3&option_f==2
%         hold on;
%         plot(theta*180/pi,D0,'b--','linewidth',2);
%         legend('principal+residuals','principal')
   s9=title('UNIFORM CIRCULAR(BESSEL)','Fontsize',15);
      set(gca,'units','normalized');
      set(s9,'units','normalized','position',[0 1],'horizontalalign','left');
end
```

```
diffdB=DodB-min(DdB);
subplot(2,1,2)
plot(theta*180/pi,DdB,'b','linewidth',2);
%if option_b==3&option_f==2
%         hold on;
%         plot(theta*180/pi,D0,'r--','linewidth',2);
%         legend('principal+residuals','principal');
%end
t3=text(1,1,['D_0 = ',num2str(DodB),' (dB)']);
set(t3,'units','normalized','position',[1 1.05],'horizontalalign','right');
xlabel(['\theta',' (degrees)']),ylabel('DIRECTIVITY(dB)')
grid on;
axis([0 180 max(-50,10*floor(min(DdB)/10)) 10*ceil(DodB/10)]);


if option_b==1;
     for i=1:Nelem;
         Ncoef(i)=1;
     end
   figure;
   x=(1-Nelem)*d/2:d:(Nelem-1)*d/2;
   y=(1-Nelem)/2:1:(Nelem-1)/2;
   [AX,H1,H2]=plotyy(x,Ncoef(ceil(abs(y)+0.1)),x,beta.*y.*180./pi);
   set(get(AX(1),'Ylabel'),'String','AMPLITUDE','color','r');
set(get(AX(2),'Ylabel'),'String','PHASE (degrees)','color','b');
set(AX(1),'ycolor','r');
set(AX(2),'ycolor','b');
set(H1,'Linestyle','-','color','r','linewidth',2,'marker','s');
set(H2,'Linestyle',':','color','b','linewidth',2,'marker','o');

xlabel(['ARRAY LENGTH',' (\lambda)']);
%axis([],'color','r');
%axis([(1-Nelem)*d/2 (Nelem-1)*d/2 0 max(Ncoef)+0.1],'color','r');
grid on;
l2=legend('PHASE',2);
[hle,l3]=legend('AMPLITUDE',1); set(hle,'color',[1 1 1]);

if option_b==1&option_d==1
   s1=title('UNIFORM BROADSIDE','Fontsize',15);
   % set(gca,'units','normalized');
   set(s1,'units','normalized','position',[0 1],'horizontalalign','left');
end
if option_b==1&option_d==2
   s4=title('UNIFORM SCANNING','Fontsize',15);
      set(gca,'units','normalized');
   set(s4,'units','normalized','position',[0 1],'horizontalalign','left');
end
```

```
end

if option_b==2

for i=1:Mx*Ny;
    Ncoef(i)=1;

end

figure;
   x=(1-Mx)*dx/2:dx:(Mx-1)*dx/2;
   y=(1-Mx)/2:1:(Mx-1)/2;
   subplot(2,1,1)
   [AX,H1,H2]=plotyy(x,Ncoef(ceil(abs(y)+0.1)),x,betax.*y.*180./pi);
  set(get(AX(1),'Ylabel'),'String','AMPLITUDE(X)','color','r');
  set(get(AX(2),'Ylabel'),'String','PHASE (degrees)','color','b');
  set(AX(1),'ycolor','r');
set(AX(2),'ycolor','b');
set(H1,'Linestyle','-','color','r','linewidth',2,'marker','s');
set(H2,'Linestyle',':','color','b','linewidth',2,'marker','o');
xlabel(['ARRAY LENGTH ',' (\lambda)']);
%axis([(1-Mx)*dx/2 (Mx-1)*dx/2 0 max(Ncoef)+0.1]);
grid on;
l2=legend('PHASE',2);
[hle,l3]=legend('AMPLITUDE',1); set(hle,'color',[1 1 1]);

if option_b==2&option_e==1
   s7=title('RECTANGULAR PLANAR','Fontsize',15);
      set(gca,'units','normalized');
   set(s7,'units','normalized','position',[0 1],'horizontalalign','left');
end
if option_b==2&option_e==2
  s7=title('TRIANGULAR PLANAR','Fontsize',15);
      set(gca,'units','normalized');
   set(s7,'units','normalized','position',[0 1],'horizontalalign','left');
end

x1=(1-Ny)*dy/2:dy:(Ny-1)*dy/2;
   y1=(1-Ny)/2:1:(Ny-1)/2;
   subplot(2,1,2)
   [AX,H1,H2]=plotyy(x1,Ncoef(ceil(abs(y1)+0.1)),x1,betay.*y1.*180./pi);
 set(get(AX(1),'Ylabel'),'String','AMPLITUDE(Y)','color','r');
 set(get(AX(2),'Ylabel'),'String','PHASE (degrees)','color','b');
 set(AX(1),'ycolor','r');
set(AX(2),'ycolor','b');
set(H1,'Linestyle','-','color','r','linewidth',2,'marker','s');
set(H2,'Linestyle',':','color','b','linewidth',2,'marker','o');
xlabel(['ARRAY LENGTH ',' (\lambda)']);
%axis([(1-Ny)*dy/2 (Ny-1)*dy/2 0 max(Ncoef)+0.1]);
grid on;
```

```
l2=legend('PHASE',2);
[hle,l3]=legend('AMPLITUDE',1); set(hle,'color',[1 1 1]);

end


figure;
if option_b==1,
polar_dB(theta*180/pi,DdB,max(-
40,6*floor(min(DdB)/6)),10*ceil(DodB/10),10,'r-')
hold on
polar_dB(-theta*180/pi,DdB,max(-
40,6*floor(min(DdB)/6)),10*ceil(DodB/10),10,'r-')
title('Polar plot of Directivity (\phi = 90 degrees)','Fontsize',15)
else
   polar_dB(theta*180/pi,DdB,-10,30,4,'r-.')
   hold on
polar_dB(-theta*180/pi,D180dB,-10,30,4,'r-.')
title(['Polar plot of Directivity (\phi= ',num2str(phieval),'
degrees)'],'Fontsize',15)
end

% hold on
% polar_dB(theta*180/pi,Dp0t0,-20,40,3,'b-')
%    hold on
% polar_dB(-theta*180/pi,D180p0t0,-20,40,3,'b-')
% title(['Polar plot of Directivity (\phi= ',num2str(phieval),'
degrees)'],'Fontsize',15)
%
% figure;
% DtdB=Dp0t0+DdB;
% Dt180dB=D180p0t0+D180dB;
% polar_dB(theta*180/pi,DtdB,-20,40,3,'r-')
%    hold on
% polar_dB(-theta*180/pi,Dt180dB,-20,40,3,'r-')
% title(['Polar plot of total Directivity (\phi= ',num2str(phieval),'
degrees)'],'Fontsize',15)


hold on
AE1=AES_2D(1:905);
AE2=AES_2D(906:1811);
AE4=flipud(AES_2D(1811:2716));
AE3=flipud(AES_2D(2717:3621));
AE_T=[AE1;AE2];
AE=AE_T';
AE_T180=[AE3;AE4];
AE180=AE_T180';
polar_dB(theta*180/pi,AE,-10,30,4,'b-.')
hold on
```

```
polar_dB(-theta*180/pi,AE180,-10,30,4,'b-.')

hold on
if option_b==1,
    APdB=AE+DdB;
    AP180dB=AE180+DdB;
polar_dB(theta*180/pi,APdB,max(-
40,6*floor(min(DdB)/6)),10*ceil(DodB/10)+10,12,'k-')
hold on
polar_dB(-theta*180/pi,AP180dB,max(-
40,6*floor(min(DdB)/6)),10*ceil(DodB/10)+10,12,'k-')
title('Polar plot of array pattern (\phi = 90 degrees)','Fontsize',12)
else
    APdB=AE+DdB;
    AP180dB=AE180+D180dB;
   polar_dB(theta*180/pi,APdB,-10,30,4,'k-')
   hold on
polar_dB(-theta*180/pi,AP180dB,-10,30,4,'k-')
title(['2D radiation pattern (\phi= ',num2str(phieval),'
degrees)'],'Fontsize',15)
end
APT=APdB';
APT180=AP180dB';
save('APS','APT');
save('AP180S','APT180');

% hold on
% APH1=AP_2D(1:906);
% APH2=AP_2D(906:1812);
% APH4=flipud(AP_2D(1812:2717));
% APH3=flipud(AP_2D(2716:3622));
% APH_T=[APH1;APH2];
% APdBH=APH_T';
% APH_T180=[APH3;APH4];
% AP180dBH=APH_T180';
% polar_dB(theta*180/pi,APdBH,-30,20,10,'r-')
% hold on
% polar_dB(-theta*180/pi,AP180dBH,-30,20,10,'r-')
%
% figure;
% if option_b==1,
% polar_dB(theta*180/pi,DdB-max(DdB),max(-60,6*floor(min(DdB)/6)),0,12,'-')
% hold on
% polar_dB(-theta*180/pi,DdB-max(DdB),max(-60,6*floor(min(DdB)/6)),0,12,'-')
% title('Polar plot of Relative Directivity (0< \phi <360
degrees)','Fontsize',15)
% else
%    polar_dB(theta*180/pi,DdB-max(max(DdB),max(D180dB)),max(-
60,6*floor(min(DdB)/6)),0,12,'-')
%    hold on
```

```
% polar_dB(-theta*180/pi,D180dB-max(max(DdB),max(D180dB)),max(-
60,6*floor(min(DdB)/6)),0,12,'-')
% title(['Polar plot of Relative Directivity (\phi= ',num2str(phieval),'
degrees)'],'Fontsize',15)
% end


%Spherical Plot3D

D3=4*pi*abs(AF3).^2/Prad;
D3dB=10.*log10(D3);
D3dB=D3dB-min(min(D3dB));
save('D3dB','D3dB')
AE_mat_dB=reshape(AES_3D,[182,182]);
AE_mat_dB=AE_mat_dB-min(min(AE_mat_dB));
AE_mat=10.^(AE_mat_dB./10);

figure;
[x,y,z]=sph2cart(PHI,pi/2-THETA,D3dB);
surf(x,y,z);
title('Array Factor(Spherical Plot3D)','Fontsize',15);

figure;
[x,y,z]=sph2cart(PHI,pi/2-THETA,AE_mat_dB);
surf(x,y,z);
title('Element Factor(Spherical Plot3D)','Fontsize',15);

% figure;
% [xx,yx,zx]=sph2cart(PHI,pi/2-THETA,DDp0t0);
% surf(xx,yx,zx);
% title('Directivity of square array(Spherical Plot3D)','Fontsize',15);

AP_3D_dB=D3dB+AE_mat_dB;
AP_3D_dB=AP_3D_dB-min(min(AP_3D_dB));
AP_3D=10.^(AP_3D_dB./10);
figure;
[xx,yx,zx]=sph2cart(PHI,pi/2-THETA,AP_3D_dB);
surf(xx,yx,zx);
title('Directivity of total array(Spherical Plot3D)','Fontsize',15);

if scale==1
   DD=D3;
   AE=AE_mat;
   AP=AP_3D;
%  DDp0t0=DDp0t0;
%  DDt=D3t;
end
if scale==2
   DD=D3dB;
   AE=AE_mat_dB;
```

```
   AP=AP_3D_dB;
%  DDp0t0=DDp0t0;
%  DDt=D3t;
end
disc=size(DD,1);
spherical_plot(DD,THETA,PHI,disc)
discE=size(AE,1);
spherical_plot(AE,THETA,PHI,discE)
discP=size(AP,1);
spherical_plot(AP,THETA,PHI,discP)
% spherical_plot(DDp0t0,THETA,PHI,disc)
% spherical_plot(DDt,THETA,PHI,disc)

if scale==1
      ss=title('3D Total pattern(Dimensionless)','Fontsize',15);
   else
      ss=title('3D Spherical plot of Directivity (dB)','Fontsize',15);
end
title('3D Total pattern','Fontsize',15)
```

```
%%%%%%%%%%%%%%%%%%%%%%%%%%%%%%%%%%%%%%%%%%%%%%%%%%%%%%%%%%%%%%%%%%%%%%%%%%%%%
%%%%%%%%%%%%%
%%%%%%%%%%%%%%%%%%%%%%%%%%%%%%%%%%%% Subroutines
%%%%%%%%%%%%%%%%%%%%%%%%%%%%%%%%%%%%%%%%%
%%%%%%%%%%%%%%%%%%%%%%%%%%%%%%%%%%%%%%%%%%%%%%%%%%%%%%%%%%%%%%%%%%%%%%%%%%%%%
%%%%%%%%%%%%%
% HPBWCALC
% function[hp,thmax]=hpbw(U,M)
% tol=0.001;
% imax=0;
% j=0;
% for i=1:M+1;
%    if abs(U(i)-1)<tol & floor((j+2)/2)==imax+1,
%       imax=imax+1;
%       thmax(imax)=(i-1)/10;
%    end
%    if i>1 & abs(U(i)-1)<tol & U(i)>U(i-1) & j~=0,
%       thmax(imax)=(i-1)/10;
%    end
%    if i>1,
%       y(1)=U(i)-0.5;
%       y(2)=U(i-1)-0.5;
%       x(1)=(i-1)/10;
%       x(2)=(i-2)/10;
%       sign=y(1)*y(2);
```

```
%       if sign<0,
%          j=j+1;
%          root(j)=x(2)-y(2)*(x(2)-x(1))/(y(2)-y(1));
%          if j>=2 & y(2)>y(1),
%             hp(imax)=root(j)-root(j-1);
%          elseif j==1 & y(2)>y(1),
%             hp(imax)=2.*root(j);
%          end
%       end
%    end
% end
% if thmax(imax)>root(j),
%    hp(imax)=2.*(180-root(j));
% end


% FACT(IARG)
function[f7]=fact(iarg)
f7=1;
for j=1:iarg;
f7=j*f7;
end

% PLANAR(THETA,PHI,MX,NY,DX,DY,BETAX,BETAY)
function[f10]=af10(theta,phi,Mx,Ny,dx,dy,betax,betay)
k=2*pi;
psix=k.*dx.*sin(theta).*cos(phi)+betax;
psiy=k.*dy.*sin(theta).*sin(phi)+betay;
AFx=sinc((Mx.*psix./2)./pi)./sinc((psix./2)./pi);
AFy=sinc((Ny.*psiy./2)./pi)./sinc((psiy./2)./pi);
f10=AFx.*AFy;

% PLANAR_TRI(THETA,PHI,MX,NY,DX,DY,BETAX,BETAY)
function[f11]=aft10(theta,phi,Mx,Ny,dx,dy,betax,betay)
k=2*pi;
psix=k.*dx.*sin(theta).*cos(phi)+betax;
psiy=k.*dy.*sin(theta).*sin(phi)+betay;
AFx=sinc((Mx.*psix./2)./pi)./sinc((psix./2)./pi);
AFy=sinc((Ny.*psiy./2)./pi)./sinc((psiy./2)./pi);
Dis_factor=1+(exp(1i.*(psix./2)).*exp(1i.*(psiy./2)));
f11=AFx.*AFy.*Dis_factor;

% CIRCULAR(THETA,PHI,THETA0,PHI0,NELEM,RAD)
function[fc]=afc(theta,phi,theta0,phi0,Nelem,rad)
k=2*pi;
dtor=pi/180;
%n=linspace(1,Nelem,Nelem);
%AF=sum(exp(i.*(k.*rad.*sin(theta).*cos(phi-phin(n))+alpha(n))));
AF=0;
for n=1:Nelem
   phin(n)=2*pi*n/Nelem;
```

```
alpha(n)=-k.*rad.*sin(dtor.*theta0).*cos(dtor.*phi0-phin(n));
AF=AF+exp(i.*(k.*rad.*sin(theta).*cos(phi-phin(n))+alpha(n)));
end
AFabs=abs(AF);
fc=AFabs;


% bessel with residuals
function[fc3]=afc3(theta,phi,theta0,phi0,Nelem,rad,m)
if theta0==0|phi0==0,
   theta0=theta0+0.000001;
   phi0=phi0-0.000001;
end
k=2*pi;
dtor=pi/180;
rho0=rad.*sqrt((sin(theta).*cos(phi)-
sin(theta0).*cos(phi0)).^2+(sin(theta).*sin(phi)-sin(theta0).*sin(phi0)).^2);
zeta=atan((sin(theta).*sin(phi)-
sin(theta0).*sin(phi0))./(sin(theta).*cos(phi)-sin(theta0).*cos(phi0)));
AFpri=besselj(0,k.*rho0);
AFres=0;
for n=1:m
AFres=AFres+(i^(n.*Nelem))*besselj(n.*Nelem,k.*rho0).*cos(n.*Nelem.*zeta);
end
AFres=2*AFres;
AF=AFpri+AFres;
AFabs=abs(AF);
fc3=AFabs;


% spherical plot
function spherical_plot(r,THETA,PHI,disc)
%theta = linspace(theta_low,theta_up,disc);
%phi   = linspace(phi_low,phi_up,disc);

%[THETA,PHI] = meshgrid(theta,phi);

% spherical to rectangular conversion
x = abs(r).*sin(THETA).*cos(PHI);
y = abs(r).*sin(THETA).*sin(PHI);
z = abs(r).*cos(THETA);

% do the plot
figure; surf(x,y,z); view(135,20);
C = [.8 .8 .8]; colormap(C); axis off equal;

% Draw x, y, and z axes
set(line([1e-8;max(max(x))+3],[1e-8;1e-8],[1e-8;1e-8]),'Color','r');
set(line([1e-8;1e-8],[1e-8;max(max(y))+3],[1e-8;1e-8]),'Color','r');
set(line([1e-8;1e-8],[1e-8;1e-8],[1e-8;max(max(z))+3]),'Color','r');
```

```
% Label x, y, and z axes
text(max(max(x))+4,0,0,'x','FontSize',14,'FontName','Times','FontAngle','ital
ic','Color','r');
text(0,max(max(y))+4,0,'y','FontSize',14,'FontName','Times','FontAngle','ital
ic','Color','r');
text(0,0,max(max(z))+4,'z','FontSize',14,'FontName','Times','FontAngle','ital
ic','Color','r');

% Fill surface using patches
patch_1 = zeros(3,disc+1);  patch_2 = zeros(3,disc+1);
patch_1(1,1:disc) = x(1,:); patch_2(1,1:disc) = x(disc,:);
patch_1(2,1:disc) = y(1,:); patch_2(2,1:disc) = y(disc,:);
patch_1(3,1:disc) = z(1,:); patch_2(3,1:disc) = z(disc,:);
patch(patch_1(1,:),patch_1(2,:),patch_1(3,:),C);
patch(patch_2(1,:),patch_2(2,:),patch_2(3,:),C);



%------------------------------------------------------------------------
-
%       polar_dB(theta,rho,rmin,rmax,rticks,line_style)
%
%   POLAR_DB is a MATLAB function that plots 2-D patterns in
%   polar coordinates where:
%          0      <= THETA (in degrees) <= 360
%       -infinity <  RHO   (in dB)      <  +infinity
%
%   Input Parameters Description
%   ----------------------------
%   - theta (in degrees) must be a row vector from 0 to 360 degrees
%   - rho (in dB) must be a row vector
%   - rmin (in dB) sets the minimum limit of the plot (e.g., -60 dB)
%   - rmax (in dB) sets the maximum limit of the plot (e.g.,   0 dB)
%   - rticks is the # of radial ticks (or circles) desired. (e.g., 4)
%   - linestyle is solid (e.g., '-') or dashed (e.g., '--')
%
%   Credits:
%       S. Bellofiore
%       S. Georgakopoulos
%       A. C. Po
%       C. Bishoplycarpou
%       C. Wangsvick
%
%   Tabulate your data accordingly, and call polar_dB to provide the
%   2-D polar plot
%
%   Note:  This function is different from the polar.m (provided by
%          MATLAB) because RHO is given in dB, and it can be negative
%------------------------------------------------------------------------
-
```

```
function hpol = polar_dB(theta,rho,rmin,rmax,rticks,line_style)

% Convert degrees into radians
theta = theta * pi/180;

% Font size, font style and line width parameters
font_size  = 16;
font_name  = 'Times';
line_width = 1.5;

if nargin < 5
    error('Requires 5 or 6 input arguments.')
elseif nargin == 5
    if isstr(rho)
        line_style = rho;
        rho = theta;
        [mr,nr] = size(rho);
        if mr == 1
            theta = 1:nr;
        else
            th = (1:mr)';
            theta = th(:,ones(1,nr));
        end
    else
        line_style = 'auto';
    end
elseif nargin == 1
    line_style = 'auto';
    rho = theta;
    [mr,nr] = size(rho);
    if mr == 1
        theta = 1:nr;
    else
        th = (1:mr)';
        theta = th(:,ones(1,nr));
    end
end
if isstr(theta) | isstr(rho)
    error('Input arguments must be numeric.');
end
if any(size(theta) ~= size(rho))
    error('THETA and RHO must be the same size.');
end

% get hold state
cax = newplot;
next = lower(get(cax,'NextPlot'));
hold_state = ishold;
```

```
% get x-axis text color so grid is in same color
tc = get(cax,'xcolor');

% Hold on to current Text defaults, reset them to the
% Axes' font attributes so tick marks use them.
fAngle  = get(cax, 'DefaultTextFontAngle');
fName   = get(cax, 'DefaultTextFontName');
fSize   = get(cax, 'DefaultTextFontSize');
fWeight = get(cax, 'DefaultTextFontWeight');
set(cax, 'DefaultTextFontAngle', get(cax, 'FontAngle'), ...
    'DefaultTextFontName',   font_name, ...
    'DefaultTextFontSize',   font_size, ...
    'DefaultTextFontWeight', get(cax, 'FontWeight') )

% only do grids if hold is off
if ~hold_state

% make a radial grid
    hold on;
  % v returns the axis limits
  % changed the following line to let the y limits become negative
    hhh=plot([0 max(theta(:))],[min(rho(:)) max(rho(:))]);
    v = [get(cax,'xlim') get(cax,'ylim')];
    ticks = length(get(cax,'ytick'));
    delete(hhh);

% check radial limits (rticks)

    if rticks > 5   % see if we can reduce the number
        if rem(rticks,2) == 0
            rticks = rticks/2;
        elseif rem(rticks,3) == 0
            rticks = rticks/3;
        end
    end

% define a circle
    th = 0:pi/50:2*pi;
    xunit = cos(th);
    yunit = sin(th);
% now really force points on x/y axes to lie on them exactly
    inds = [1:(length(th)-1)/4:length(th)];
    xunits(inds(2:2:4)) = zeros(2,1);
    yunits(inds(1:2:5)) = zeros(3,1);

    rinc = (rmax-rmin)/rticks;

% label r
  % change the following line so that the unit circle is not multiplied
  % by a negative number.  Ditto for the text locations.
```

```
    for i=(rmin+rinc):rinc:rmax
                is = i - rmin;
        plot(xunit*is,yunit*is,'-','color',tc,'linewidth',0.5);
        text(0,is+rinc/20,['   ' num2str(i)],'verticalalignment','bottom' );
    end
% plot spokes
    th = (1:6)*2*pi/12;
    cst = cos(th); snt = sin(th);
    cs = [-cst; cst];
    sn = [-snt; snt];
    plot((rmax-rmin)*cs,(rmax-rmin)*sn,'-','color',tc,'linewidth',0.5);

% plot the ticks
    george=(rmax-rmin)/30; % Length of the ticks
        th2 = (0:36)*2*pi/72;
        cst2 = cos(th2); snt2 = sin(th2);
    cs2 = [(rmax-rmin-george)*cst2; (rmax-rmin)*cst2];
    sn2 = [(rmax-rmin-george)*snt2; (rmax-rmin)*snt2];
    plot(cs2,sn2,'-','color',tc,'linewidth',1); % 0.5
        plot(-cs2,-sn2,'-','color',tc,'linewidth',1); % 0.5


% annotate spokes in degrees
  % Changed the next line to make the spokes long enough
    rt = 1.1*(rmax-rmin);
    for i = 1:max(size(th))
        text(rt*cst(i),rt*snt(i),int2str(abs(i*30-
90)),'horizontalalignment','center' );
        if i == max(size(th))
            loc = int2str(90);
        elseif i*30+90<=180
            loc = int2str(i*30+90);
                else
                        loc = int2str(180-(i*30+90-180));
        end
        text(-rt*cst(i),-rt*snt(i),loc,'horizontalalignment','center' );
    end
% set viewto 2-D
    view(0,90);

% set axis limits
  % Changed the next line to scale things properly
    axis((rmax-rmin)*[-1 1 -1.1 1.1]);
end

% Reset defaults.
set(cax, 'DefaultTextFontAngle', fAngle , ...
    'DefaultTextFontName',   font_name, ...
    'DefaultTextFontSize',   fSize, ...
    'DefaultTextFontWeight', fWeight );
```

```
% transform data to Cartesian coordinates.
  % changed the next line so negative rho are not plotted on the other side

  for i = 1:length(rho)
    if (rho(i) > rmin)
      if theta(i)*180/pi >=0 & theta(i)*180/pi <=90
          xx(i) = (rho(i)-rmin)*cos(pi/2-theta(i));
          yy(i) = (rho(i)-rmin)*sin(pi/2-theta(i));
      elseif theta(i)*180/pi >=90
          xx(i) = (rho(i)-rmin)*cos(-theta(i)+pi/2);
          yy(i) = (rho(i)-rmin)*sin(-theta(i)+pi/2);
      elseif theta(i)*180/pi < 0
          xx(i) = (rho(i)-rmin)*cos(abs(theta(i))+pi/2);
          yy(i) = (rho(i)-rmin)*sin(abs(theta(i))+pi/2);
      end
    else
      xx(i) = 0;
      yy(i) = 0;
    end
  end

% plot data on top of grid
if strcmp(line_style,'auto')
    q = plot(xx,yy);
else
    q = plot(xx,yy,line_style);
end
if nargout > 0
    hpol = q;
end
if ~hold_state
    axis('equal');axis('off');
end

% reset hold state
if ~hold_state, set(cax,'NextPlot',next);
end
```

REFERENCES

[1] S. He and J. Xie, "Analysis and Design of a Novel Dual-Band Array Antenna With a Low Profile for 2400/5800-MHz WLAN Systems," *IEEE Transactions on Antennas and Propagation,* vol. 58, no. 2, pp. 391-396, Feb 2010.

[2] W. K. Toh, X. Qing and Z. N. Chen, "A Planar Dualband Antenna Array," *IEEE Transactions on Antennas and Propagation,* vol. 59, no. 3, pp. 833-838, March 2011.

[3] Z. Wang, G. X. Zhang, Y. Yin and J. Wu, "Design of a Dual-Band High-Gain Antenna Array for WLAN and WiMAX Base Station," *IEEE Antennas and Wireless Propagation Letters,* vol. 13, pp. 1721-1724, 2014.

[4] Y. Cui, R. Li and P. Wang, "Novel Dual-Broadband Planar Antenna and Its Array for 2G/3G//LTE Base Stations," *IEEE Transactions on Antennas and Propagation,* vol. 61, no. 3, pp. 1132-1139, March 2013.

[5] A. B. Smolders,, R. M. C. Mestrom, , A. C. F. Reniers and M. Geurts, "A Shared Aperture Dual-Frequency Circularly Polarized Microstrip Array Antenna," *IEEE Antennas and Wireless Propagation Letters,* vol. 12, pp. 120-133, 2013.

[6] Z. Yang and K. F. Warnick, "Multiband Dual-Polarization High-Efficiency Array Feed for Ku/Reverse-Band Satellite Communications," *IEEE Antennas and Wireless Propagation Letters,* vol. 13, pp. 1325-1328, 2014.

[7] S. Ye, J. Geng, X. Liang, Y. Jay Guo and R. Jin, "A Compact Dual-Band Orthogonal Circularly Polarized Antenna Array With Disparate Elements," *IEEE Transactions on Antennas and Propagation*, vol. 63, no. 4, pp. 1359-1364, 2015.

[8] A. I. Sandhu, E. Arnieri, G. Amendola and L. Boccia, "Radiating Elements for Shared Aperture Tx/Rx Phased Arrays at K/Ka Band," *IEEE Transactions on Antennas and Propagation*, vol. 64, no. 6, pp. 2270-2282, 2016.

[9] S. E. Valavan, D. Tran, A. G. Yarovoy and A. G. Roederer, "Dual-Band Wide-Angle Scanning Planar Phased Array in X/Ku-Bands," *IEEE Transactions on Antennas and Propagation*, vol. 62, no. 5, pp. 2514-2521, 2014.

[10] N. Haider, D. Caratelli and A. G. Yarovoy, "Frequency Reconfiguration of a Dual-Band Phased Array Antenna With Variable-Impedance Matching," *IEEE Transactions on Antennas and Propagation*, vol. 63, no. 8, pp. 3477-3485, 2015.

[11] D. M. Pozar and S. D. Targonski, "A shared-aperture dual-band dual-polarized microstrip array," *IEEE Transactions on Antennas and Propagation,* vol. 49, no. 2, pp. 150-157, 2001.

[12] C. X. Mao, S. Gao, Y. Wang, Q. Luo and Q. X. Chu, "A Shared-Aperture Dual-Band Dual-Polarized Filtering-Antenna-Array With Improved Frequency Response," *IEEE Transactions on Antennas and Propagation,* vol. 65, no. 4, pp. 1836-1844, 2017.

[13] J. D. Zhang, L. Zhu, N. W. Liu and W. Wu, "Dual-Band and Dual-Circularly Polarized Single-Layer Microstrip Array Based on Multiresonant Modes," *IEEE Transactions on Antennas and Propagation*, vol. 65, no. 3, pp. 1428-1433, 2017.

[14] K. Naishadham, R. Li, L. Yang, T. Wu, W. Hunsicker and M. Tentzeris, "A Shared-Aperture Dual-Band Planar Array With Self-Similar Printed Folded Dipoles," *IEEE Transactions on Antennas and Propagation*, vol. 61, no. 2, pp. 606-613, 2013.

[15] J. R. De Luis and F. De Flaviis, "Frequency Agile Switched Beam Antenna Array System," *IEEE Transactions on Antennas and Propagation*, vol. 58, no. 10, pp. 3196-3204, 2010.

[16] N. Haider, D. P. Tran and A. G. Yarovoy, "A new concept for frequency reconfigurable phased-array element," in *Loughborough Antennas & Propagation Conference*, Loughborough, 2011.

[17] Q. Li, T. Li, Z. Li and J. Fang, "Unidirectional frequency reconfigurable bow-tie antenna array with AMC reflector," in *11th European Conference on Antennas and Propagation (EUCAP)*, paris, 2017.

[18] N. Haider, A. G. Yarovoy and A. G. Roederer, "L/S-Band Frequency Reconfigurable Multiscale Phased Array Antenna With Wide Angle Scanning," *IEEE Transactions on Antennas and Propagation*, vol. 65, no. 9, pp. 4519-4528, 2017.

[19] M. Shirazi, J. Huang, T. Li and X. Gong, "A Switchable-Frequency Slot-Ring Antenna Element for Designing a Reconfigurable Array," *IEEE Antennas and Wireless Propagation Letters*, vol. 17, no. 2, pp. 229-233, 2017.

[20] M. H. Novak, F. A. Miranda and J. L. Volakis, "Ultra-wideband phased array for small satellite communications," *IET Microwaves, Antennas & Propagation,* vol. 11, no. 9, pp. 1234-1240, 2017.

[21] E. Yetisir, N. Ghalichechian and J. L. Volakis, "Ultrawideband Array With 70° Scanning Using FSS Superstrate," *IEEE Transactions on Antennas and Propagation,* vol. 64, no. 10, pp. 4256-4265, 2016.

[22] S. S. Holland and M. N. Vouvakis, "The Planar Ultrawideband Modular Antenna (PUMA) Array," *IEEE Transactions on Antennas and Propagation,* vol. 60, no. 1, pp. 130-140, 2012.

[23] J. Zhong, E. A. Alwan and J. L. Volakis, "7.2 to 1 ultra-wideband dual-linear polarized phased array with 60° scanning," in *IEEE International Symposium on Antennas and Propagation & USNC/URSI National Radio Science Meeting,* San Diego, 2017.

[24] J. Zhong, E. A. Alwan and J. L. Volakis, "Ultra-wideband dual-linear polarized phased array with 60° scanning for simultaneous transmit and receive systems," in *International Workshop on Antenna Technology: Small Antennas, Innovative Structures, and Applications (iWAT),* Athens, 2017.

[25] M. H. Novak and J. L. Volakis, "Ultrawideband Antennas for Multiband Satellite Communications at UHF–Ku Frequencies," *IEEE Transactions on Antennas and Propagation,* vol. 63, no. 4, pp. 1334-1341, 2015.

[26] J. B. Yan, S. Gogineni, B. Camps-Raga and J. Broze, "A Dual-Polarized 2–18-GHz Vivaldi Array for Airborne Radar Measurements of Snow," *IEEE Transactions on Antennas and Propagation,* vol. 64, no. 2, pp. 781-785, 2016.

[27] R. W. Kindt and W. R. Pickles, "Ultrawideband All-Metal Flared-Notch Array Radiator," *IEEE Transactions on Antennas and Propagation,* vol. 58, no. 11, pp. 3568-3575, 2010.

[28] R. W. Kindt, "Prototype Design of a Modular Ultrawideband Wavelength-Scaled Array of Flared Notches," *IEEE Transactions on Antennas and Propagation,* vol. 60, no. 3, pp. 1320-1328, 2012.

[29] E. de Lera Acedo, E. Garcia, V. GonzÁlez-Posadas, J. L. Vazquez-Roy, R. Maaskant and D. Segovia, "Study and Design of a Differentially-Fed Tapered Slot Antenna Array," *IEEE Transactions on Antennas and Propagation,* vol. 58, no. 1, pp. 68-78, 2010.

[30] Y. Zhang and A. K. Brown, "Bunny Ear Combline Antennas for Compact Wide-Band Dual-Polarized Aperture Array," *IEEE Transactions on Antennas and Propagation,* vol. 59, no. 8, pp. 3071-3075, 2011.

[31] S. S. Holland and M. N. Vouvakis, "The Banyan Tree Antenna Array," *IEEE Transactions on Antennas and Propagation,* vol. 59, no. 11, pp. 4060-4070, 2011.

[32] Z. Guo, S. Yang, Z. Shi and Y. Chen, "A miniaturized wideband dual-polarized linear array with balanced antipodal Vivaldi antenna," in *IEEE MTT-S International Microwave Workshop Series on Advanced Materials and Processes for RF and THz Applications (IMWS-AMP)*, Chengdu, 2016.

[33] M. W. Elsallal and J. C. Mather, "An ultra-thin, decade (10:1) Bandwidth, modular “BAVA” array with low cross-polarization," in *IEEE International Symposium on Antennas and Propagation (APSURSI)*, Spokane, 2011.

[34] W. Elsallal and e. al., "Charateristics of decade-bandwidth, Balanced Antipodal Vivaldi Antenna (BAVA) phased arrays with time-delay beamformer systems," in *IEEE International Symposium on Phased Array Systems and Technology*, Waltham, 2013.

[35] B. A. Cetiner, G. R. Crusats, L. Jofre and N. Biyikili, "RF MEMS integrated frequency reconfigurable annular slot antenna," *IEEE Transactions on Antennas Propagation*, vol. 58, no. 3, pp. 626-632, 2010.

[36] R. B. S. Nikolaou, C. Lugo, I. Carrasquillo, D. C. Thompson, G. E. Ponchak, J. Papapolymerou and M. M. Tentzeris, "Pattern and frequency reconfigurable annular slot antenna using PIN diodes," *IEEE Transactions on Antennas and Propagation*, vol. 54, no. 2, p. 439–448, 2006.

[37] N. Behdad and K. Sarabandi, "A Varactor Tuned Dual-Band Slot Antenna," *IEEE Transactions on Antennas and Propagation*, vol. 54, no. 2, p. 401–408, 2006.

[38] T. Aboufoul, A. Alomainy and C. Parini, "Reconfigurable UWB monopole antenna for cognitive radio applications using GaAs FET switches," *IEEE Antennas Wireless Propagation Letters*, vol. 11, p. 392–393, 2012.

[39] H. Cong, P. J. Zampardi, K. Buisman, C. Cismaru, M. Sun and K. e. a. Stevens, "A GaAs Junction Varactor With a Continuously Tunable Range of 9:1 and an OIP3 of 57 dBm," *IEEE Electron Device Letters*, vol. 31, pp. 108-110, 2010.

[40] G. M. Rebeiz, C. D. Patel, S. K. Han, K. Chih-Hsiang and K. M. J. Ho, "The Search for a Reliable MEMS Switch," *Microwave Magazine, IEEE*, vol. 14, pp. 57-67, 2013.

[41] J. Aguilera and R. Berenguer, Design and Test of Integrated Inductors for RF Applications, Boston, MA: Springer, 2003.

[42] Í. Gutiérrez, J. Meléndez and E. Hernández, Design and Characterization of Integrated Varactors for RF Applications, John Wiley & Sons, Ltd, 2007.

[43] D. McMahill, "Coplanar Waveguide Analysis/Synthesis Calculator," CGIC, 2009. [Online]. Available: http://wcalc.sourceforge.net/cgi-bin/coplanar.cgi.

[44] MaCOM, "cdn.macom," [Online]. Available: https://cdn.macom.com/datasheets/MAVR-000120-1411.pdf.

[45] D. N. P. Thalakotuna, D. K. Karmokar, K. P. Esselle, M. Heimlich and L. Materkovits, "Modelling PIN diode switches in reconfigurable leaky-wave antenna design," in *IEEE Antennas and Propagation Society International Symposium (APSURSI)*, 2013.

[46] M. Shirazi, T. Li and X. Gong, "Effects of PIN diode switches on the performance of reconfigurable slot-ring antenna," in *IEEE 16th Annual Wireless and Microwave Technology Conference (WAMICON)*, Cocoa Beach, 2015.

[47] S. Kurth, "RF-MEMS Varactor for High Power Applications," [Online]. Available: http://electronix.ru/forum/index.php?act=Attach&type=post&id=35481.

[48] Tyndall, "RF MEMS," 2015. [Online]. Available: https://www.tyndall.ie/index.cfm?action=page_pdf&pageId=354.

[49] A. Razi, A. K. Hua and A. Majidi, "NQ-GPLS: N-Queen Inspired Gateway Placement and Learning Automata-based Gateway Selection in Wireless Mesh Network," in *Proceedings of the 15th ACM International Symposium MobiWaC*, New Yprk, 2017.

[50] M. Shirazi and A. Vosoughi, "Fisher Information Maximization for Distributed Vector Estimation in Wireless Sensor Networks," *IEEE Transactions on Signal and Information Processing over Networks*, 2018.

[51] A. Sani and A. Vosoughi, "Distributed Vector Estimation for Power- and Bandwidth-Constrained Wireless Sensor Networks," *IEEE Transactions on Signal Processing*, vol. 64, no. 15, pp. 3879-3894, 2016.

[52] M. Shirazi, A. Sani and A. Vosoughi, "Sensor selection and power allocation via maximizing Bayesian fisher information for distributed vector estimation," in *51st Asilomar Conference on Signals, Systems, and Computers*, Pacific Grove, CA, 2017.

[53] G. Ardeshiri, A. Jamshidi and A. Keshavarz-Haddad, "Performance analysis of Decode and Forward Relay network in Diffusion based Molecular Communication," in *ranian Conference on Electrical Engineering (ICEE)*, Tehran, 2017.

[54] H. Yazdani and A. Vosoughi, "On cognitive radio systems with directional antennas and imperfect spectrum sensing," in *IEEE International Conference on Acoustics, Speech and Signal Processing (ICASSP)*, New Orleans, LA, 2017.

[55] A. Jabalameli and A. Behal, "A constrained linear approach to identify a multi-timescale adaptive threshold neuronal model," in *IEEE 5th International Conference on Computational Advances in Bio and Medical Sciences (ICCABS)*, Miami, FL, 2015.

[56] S. Masoudi, C. H. Wright, N. Rahnavard, J. C. Gatlin and J. S. Oakey, "Multiple Microtubule Tracking in Microscopy Time- Lapse Images using Piecewise-Stationary Multiple Motion Model Kalman Smoother," in *2018 Rocky Mountain Bioengineering Symposium*, Fargo, ND, 2018.

[57] S. Masoudi and e. al, "Early detection of apnea-bradycardia episodes in preterm infants based on coupled hidden Markov model," in *IEEE International Symposium on Signal Processing and Information Technology*, Athens, 2013.

[58] S. Manaffam and A. Jabalameli, "RF-localize: An RFID-based localization algorithm for Internet-of-Things," in *Annual IEEE Systems Conference (SysCon)*, Orlando, FL, 2016.

[59] D. M. Pozar and S. D. Targonski, "A shared-aperture dual-band dual- polarized microstrip array," *IEEE Transactions on Antennas and Propagation*, vol. 49, no. 2, pp. 150-157, 2001.

[60] T. Li, M. Shirazi and X. Gong, "S-band continuously-tunable slot-ring antennas for reconfigurable antenna array applications," in *International Workshop on Antenna Technology (iWAT)*, Cocoa Beach, 2016.

[61] A. Sani and A. Vosoughi, "Bandwidth and power constrained distributed vector estimation in wireless sensor networks," in *MILCOM 2015 - 2015 IEEE Military Communications Conference*, Tampa, FL, 2015.

[62] M. Shirazi and A. Vosoughi, "Bayesian Cramér-Rao Bound for distributed vector estimation with linear observation model," in *IEEE 25th Annual International Symposium on Personal, Indoor, and Mobile Radio Communication (PIMRC)*, Washington, DC, 2014.

[63] M. Kahrizi, T. K. Sarkar and Z. A. Maricevic, "Analysis of a wide radiating slot in the groundplane of a microstrip line," *IEEE Transactions on Antennas and Propagation*, vol. 41, no. 1, pp. 29-37, 1993.

[64] W. L. Chen, G. M. Wang and C. X. Zhang, "Bandwidth enhancement of a microstrip-line-fed printed wide-slot antenna with a fractal-shaped slot," *IEEE Transactions on Antennas and Propagation*, vol. 57, no. 7, p. 2176–2179, 2006.

[65] S. Yun, D. Y. Kim and S. Nam, "Bandwidth and Efficiency Enhancement of Cavity-Backed Slot Antenna Using a Substrate Removal," *IEEE Antennas and Wireless Propagation Letters*, vol. 11, pp. 1458-1461, 2012.

[66] N. Behdad and K. Sarabandi, "Wideband double-element ring slot antenna," *Electronics Letters*, vol. 40, no. 7, pp. 408-409, 2004.

[67] W. Lee, H. Kim and Y. H. Yoon, "Reconfigurable slot antenna with wide bandwidth," in *IEEE International Symposium on Antennas and Propagation*, 2006.

[68] T. Li and X. Gong, "Effects of the ground plane size on radiation pattern of reconfigurable slot-ring antennas," in *IEEE International Symposium on Antennas and Propagation & USNC/URSI National Radio Science Meeting*, Vancouver, 2015.

[69] C. Balanis, "Pattern distortion due to edge diffractions," *IEEE Transactions on Antennas and Propagation*, vol. 18, no. 4, pp. 561-563, 1970.

[70] J. A. Kasemodel, C. C. Chen and J. L. Volakis, "Wideband Planar Array With Integrated Feed and Matching Network for Wide-Angle Scanning," *IEEE Transactions on Antennas and Propagation*, vol. 61, no. 9, pp. 4528-4537, 2013.

[71] F. M. Tanyer-Tigrek, I. E. Lager and L. P. Ligthar, "On the Array Performance of Printed, Ultra-Wideband “Eared” Antennas," *IEEE Antennas and Propagation Magazine,* vol. 53, no. 5, pp. 57-64, 2011.

[72] T. A. Milligan, "Arrays," in *Modern Antenna Design*, Wiley-IEEE Press, 2005, pp. 102-135.

[73] E. D. Sharp, "A triangular arrangement of planar-array elements that reduces the number needed," *IRE Transactions on Antennas and Propagation*, vol. 9, p. 126–129, 1961.

[74] J. Huang, M. Shirazi and X. Gong, "A wide-band dual-polarized reconfigurable slot-ring antenna/array with a compact CPW feeding structure," in *IEEE International Symposium on Antennas and Propagation & USNC/URSI National Radio Science Meeting*, San Diego, CA, 2017.

[75] M. Shirazi and A. Vosoughi, "Bayesian Cramér-Rao bound for distributed estimation of correlated data with non-linear observation model," in *48th Asilomar Conference on Signals, Systems and Computers*, Pacific Grove, CA, 2014.

[76] G. Ardeshiri, H. Yazdani and A. Vosough, "Optimal Local Thresholds for Distributed Detection in Energy Harvesting Wireless Sensor Networks," in *arXiv:1811.01909*, 2018.